Optical detection of (bio)molecules

Kun Jia

▶ To cite this version:

Kun Jia. Optical detection of (bio)molecules. Micro and nanotechnologies/Microelectronics. Université de Technologie de Troyes, 2013. English. NNT : 2013TROY0032 . tel-03355928

HAL Id: tel-03355928
https://theses.hal.science/tel-03355928

Submitted on 27 Sep 2021

Thèse
de doctorat
de l'UTT

Kun JIA

Détection Optique des (Bio)molécules

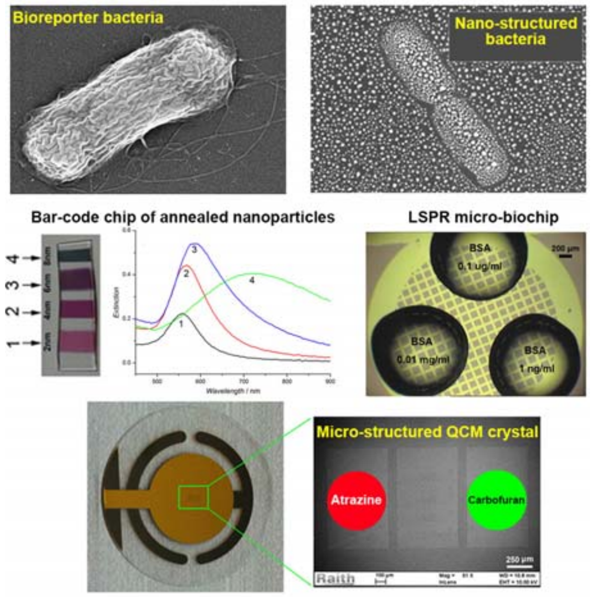

**Spécialité :
Optique et Nanotechnologies**

2013TROY0032

Année 2013

utt
université de technologie
Troyes

THESE

pour l'obtention du grade de

DOCTEUR de l'UNIVERSITE
DE TECHNOLOGIE DE TROYES

Spécialité : OPTIQUE ET NANOTECHNOLOGIES

présentée et soutenue par

Kun JIA

le 10 décembre 2013

Détection optique des (bio)molécules

JURY

M. P.-M. ADAM	PROFESSEUR DES UNIVERSITES	Président
Mme E. R. IONESCU	ENSEIGNANT CHERCHEUR UTT - HDR	Directrice de thèse
Mme N. JAFFREZIC-RENAULT	DIRECTRICE DE RECHERCHE CNRS	Rapporteur
M. T. LEICHLE	CHARGE DE RECHERCHE CNRS	Examinateur
M. E. LESNIEWSKA	PROFESSEUR DES UNIVERSITES	Rapporteur
M. R. MARKS	PROFESSOR	Examinateur

Personnalité invitée

M. J.-L. BIJEON	PROFESSEUR UTT

Acknowledgements

Completing my PhD degree is probably the most challenging activity so far in my life. The best and worst moments of my doctoral journey have been shared with many people. It has been a great privilege to spend several years in the Laboratory of Nanotechnology and Instrumental Optics (LNIO) at University of Technology of Troyes (UTT), and its members will always remain dear to me.

My first debt of gratitude must go to my advisor, Dr. Elena Rodica Ionescu. She patiently provides the vision, encouragement and advice necessary for me to proceed through the doctorial projects and complete my dissertation. Her great passions and strong confidences in science have profoundly shaped my personality as a junior researcher. She has been a considerate and supportive adviser to me throughout my graduate school career, and she has always given me great freedom to pursue independent work.

I would like to thank our collaborators of Professor Robert Marks from Ben-Gurion University in Israel and Professor Pierre Michel Adam, Professor Jean Louis Bijeon, Dr. Timothée Toury at UTT. They have participated in almost all the experimental discussions and given invaluable suggestions and comments to the articles writing, which gives me very important ability to make complicated science much easier to understand.

Special thanks to my committee: Dr. Nicole Jaffrezic-Renault for her kind suggestions, especially on the bacterial bioluminescence work; Prof. Eric Lesniewska for his valuable and critical comments on the plasmonic based biosensors, and Dr. Thierry Leichlé for his constructive suggestions on bacteria cells templated plasmonic nanosensors experiments, which allow me to expand the novel applications of my research work. Their comments and guidance have contributed to improvement on quality of this PhD thesis and I owe them my heartfelt appreciation.

I also thank many wonderful teachers and engineers in our department like Dr. Anne-Laure Baudrion, Régis Deturche, Serguei Kochecheev, Rafael Salas and Jérémie Béal for their constantly and timely training and help on the operation of various experimental instruments. The special thanks should be given to Xavier Gassmann for his long-term assistance in my utilization of the public chemistry lab.

My PhD student fellows of LNIO, Huan, Xuan, Mohammad, Yubing, Wei, Maher, Julie, Komla, Joseph and the others more; my special friends of Evgeni, Daria, Liova from Ben-Gurion University in Israel as well as Marco and Priya from Universita' di Udine in Italy, also deserve my sincerest thanks, their friendship and assistance has meant more to me than I could ever express. I could not complete my work without invaluable friendly assistance of these smart friends.

I wish to thank my parents, my sister and my girlfriend. Their love provided my inspiration and was always my driving force. I owe them everything and wish I could show them just how much I love and appreciate them. Finally, I would like to thank the China Scholarship Council (CSC) for funding my PhD study in such a lovely place in France and the various research grants and projects at LNIO like Stratégique program 2009-2012, OSEO innovation 2012-2014, France-Israel binational research network programs 2009-2011, and region Champagne-Ardenne grant NANO’MAT platform to give me a wider vision for future research career.

Table of Contents

Lists of Figures

Nomenclature

E. coli	Escherichia coli
OD	Optical density
RLU	Relative light units
AUC	Area under curve
HPLC	High performance liquid chromatography
LC/MS	Liquid chromatography/mass spectrometry
SEM	Scanning electron microscope
FESEM	Field emission scanning electron microscope
TEM	Transmission electron microscope
QCM	Quartz crystal microbalance
LSPR	Localized surface plasmon resonance
SERS	Surface enhanced Raman spectroscopy
BSA	Bovine serum albumin
PBS	Phosphate buffed saline
IgG	Immunoglobulin G
BPE	1, 2-bis(4-pyridyl)ethylene
MUA	11-Mercaptoundecanoic acid
NHS	N-Hydroxysuccinimide
EDC	Ethyl(dimethylaminopropyl) carbodiimide
PCB	Polychlorinated biphenyl
UV-Vis-NIR	Ultraviolet-visible-near infrared
LB	Luria Bertani
NPs	Nanoparticles

Abstract

Optical biosensors have witnessed unprecedented developments over recent years, mainly due to the lively interplay between biotechnology, optical physics and materials chemistry. In this thesis, two different optical biosensing platforms have been designed for sensitive and specific detection of (bio)molecules. Specifically, the first optical detection system is constructed on the basis of bioluminescence derived from engineered *Escherichia coli* bacterial cells. Upon stressed by the toxic compounds, the bacterial cells produce light via a range of complex biochemical reactions *in vivo* and the resulted bioluminescent evolution thus can be used for toxicant detection. The bacterial bioluminescent assays are able to provide competitive sensitivity, while they are limited in the specificity. Therefore, the second optical detection platform is built on the localized surface plasmon resonance (LSPR) immunosensors. In this optical biosensor, the noble metal (gold and silver) nanoparticles with tunable plasmonic properties are used as transducer for probing the specific biomolecules interactions occurred in the nano-bio interface. These nanoparticles were obtained after a high temperature thermal treatment of an initially thin-metallic film deposited on a glass substrate through a TEM grid or on a bacteria layer fixed on the glass. After appropriate optimization on metal nanostructures morphology and surface biomodification, the applicable sensitivity and specificity can be both guaranteed in this LSPR immunosensor.

Résumé

Les biocapteurs optiques ont connu une évolution sans précédent au cours des dernières années, principalement en raison de la forte interaction entre la biotechnologie, l’optique et la chimie des matériaux. Dans cette thèse, deux différentes plates-formes de biocapteurs optiques ont été conçues pour la détection sensible et spécifique des biomolécules. Plus précisément, le premier système de détection optique est construit sur la base de la bioluminescence de cellules bactériennes *d'Escherichia coli* génétiquement modifiées. L’émission de lumière induite par cette interaction peut donc être utilisée pour la détection des substances toxiques. Le second système utilise des nanoparticules de métaux précieux (or et argent) aux propriétés plasmoniques accordables qui permettent de sonder les interactions des biomolécules spécifiques à l'interface nano-bio par la résonance plasmonique de surface (LSPR). Ces nanoparticules ont été obtenues par traitement thermique à haute température d’un film métallique déposé sur du verre à l’aide d’une grille de TEM ou déposé sur une couche de bactéries fixée sur le verre. Après une optimisation appropriée des nanostructures métalliques en termes de morphologie et de fonctionnalisation, une sensibilité élevée et une grande spécificité peuvent être simultanément obtenues avec ces immunocapteurs plasmonique. Ces deux plateformes ont été utilisées pour détecter des pesticides comme le carbofuran et l’atrazine.

General introduction

Optical biosensor is a highly interdisciplinary subject requires diverse expertise from biotechnology, optical physics, materials chemistry and engineering. Compared to the classical physicochemical analysis techniques, these emerging optical biosensors are able to provide applicable sensitivity and specificity in a more cost-effective and time-efficient way. Consequently, the optical biosensors have been widely used in a range of different fields such as environmental monitoring, food and water quality control, drug development and medical diagnostic. Given the importance and ongoing research interests in this field, the work reported in this PhD thesis mainly focuses on the development of two different optical biosensor platforms based on bacterial bioluminescence and localized surface plasmon resonance.

In the Chapter 1, the fundamentals of optical biosensors have been introduced, where includes the definition, classification and basic principle of two different groups: catalytic and affinity based optical biosensors. Further, the bioluminescence assays using genetically modified bacterial cells have been presented as the typical example for the catalytic optical biosensors, while the surface plasmon biosensors using noble metal (gold and silver) nanostructures have been demonstrated as the symbolic option for affinity based optical biosensors. In both cases, the principle, construction and recent applications of these optical biosensors are discussed.

In the Chapter 2, the experimental works involving two strains of genetically modified *E. coli* bacterial cells have been reported. These bacterial cells are genetically modified to produce light (to be luminescent) when exposed to certain toxicants, this toxicant induced bioluminescence thus serves as the underline principle for the optical biosensor or bioassays. However, these engineered bacterial cells also show considerable background bioluminescence in the absent of any toxicants when cultured for certain time, which will compromise their analytical efficiency in the biosensors or bioassays applications. Therefore, we have developed two independent protocols to reduce the bacteria background bioluminescence in order to increase the sensitivity. Specifically, the first protocol is named as the “fresh-overnight” test, which contains an essential step of overnight cold incubation of bacterial suspension with toxicant solution at 4 °C for 9 hr, finally leads to more sensitive detection of a model herbicide atrazine down to 10 fg/mL. The second protocol is made up of three consecutive steps of incubation, centrifugation/washing and bioluminescent test at 30 °C. After appropriate incubation of bacterial suspension with toxicant solution for certain time, a centrifuge followed by replacement of aged bacterial medium with fresh one is conduced to significantly decline the bioluminescent interference resulted from bacterial metabolites, thus the trace concentration of carbofuran (0.5 pg/mL) can be detected using this newly developed protocol.

In the Chapter 3, the immunosensor based on localized surface plasmon resonance of gold and silver nanostructures have been developed to ensure the analytical specificity for biomolecules detection, which is quite a challenge for the bacterial bioluminescent assays reported in Chapter 2. This part start with the protocol of samples preparation, which is the metal evaporation followed by high temperature annealing to create ultra-stable gold nanoparticles on glass substrate. Then this robust sample preparation protocol is adapted with different masks to fabricate the different zones of gold nanoparticles of varying sizes on single glass substrate and well-organized micro/nano-structures. Using these samples, the optimized gold nanostructure has been rapidly selected out and subsequently used for high throughput detection of several antigen dilutions using single substrate. The protocol of antibody immobilization on gold surface has also been validated via another complementary technique based on quartz crystal microbalance acoustic biosensor. Finally, the overall LSPR biosensor sensitivity is enhanced by using gold/silver bi-metallic NPs and dopamine based functional coatings, which enables the sensitive and specific detection of bovine serum albumin down to 0.01 ng/mL.

In the Chapter 4, an interesting surface enhanced Raman spectroscopy (SERS) substrate has been fabricated based on the previous experience in bacterial cells and gold nanoparticles. The bacterial cells are used as the templates to facilitate the organization of Au nanoparticles into controlled structures containing plenty of “hot spots”, which contribute to the enormously enhanced SERS intensity compared to Au nanoparticles prepared without bacterial cells templates. This SERS active substrate is therefore able to detect the model Raman dye of 1, 2-bis(4-pyridyl)ethylene (BPE) of extremely low concentration at 10^{-12} M.

Finally, the overall experimental works in this thesis as well as some perspectives concerning the future work in the optical biosensors have been summarized in the conclusion part in the end.

Chapter 1 Principle of optical biosensor

Because of growing concerns over different toxic compounds in the environment and their deleterious effects on human health, it is imperative to develop the cost-effective, rapid and facile analytic methods that can be used for sensitive and specific detection. Taken the pesticides as the example, tremendous synthetic pesticides and fertilizers have been introduced to farmland to increase agriculture production, since the initiation of green evolution in agriculture occurred between 1940s and 1970s.[1] The mostly used toxicant pesticides include organophosphates (OP), organochlorines (OC) and carbamate (CB).[2] The toxicity of these pollutants has been documented in many articles. For instance, the toxic triazine is one of the typical organochlorines herbicides that is frequently appeared in many nature watercourses due to their widespread usage.[3] Their toxicity is basically attributed to the specific inhibition of the photosynthetic electron transport based on a toxicity study using algae in aquatic systems.[4]

With respect to the detection of these toxic compounds, the available analytical methodologies can be divided into two different groups: conventional physicochemical analyses and biosensors or biological assays. The former one, exemplified by the liquid chromatography/mass spectroscopy (LC/MS), is able to provide high sensitivity and specificity; however the complicated and usually expensive instruments are not well equipped in many laboratories, together with the requirements of laborious sample pre-preparation steps and professional technicians, which hinder the wider application of these methods. On the contrary, the biosensors or biological assays are cost-effective, rapid and capable of analyzing the bioavailability of pollutants and their effects on living systems.[5] This is particularly important in environmental and ecotoxicology studies, as the real samples are usually mixed with various pollutants, thus the synergistic or antagonistic effects of co-exist toxicants in real environmental samples would be more important than the individual pollutant concentration.[6]

Therefore, the sensitive and more economic analytical strategies based on the biosensors (and bioassays) have witnessed increasing development during recent decades. The biosensor is defined as an analytical device that uses specific biochemical reactions mediated by active enzymes, immunosystems, oligonucleotides, tissues, organelles or whole cells to detect target compounds by a range of different readouts such as electrical, optical, mechanical and magnetic signals.[7] A biosensor usually contains two parts: the biological sensing element, and the transducer that converts the biochemical information into the measurable signals.[8] Even though numerous kinds of biosensors do exist, this thesis is confined to sensors and systems where the information is gathered by the measurement of photons, in other words optical biosensors.

1.1 Optical biosensors

1.1.1 Classification: catalytic and affinity-based optical biosensors

Optical biosensors are a powerful detection and analysis tool that has vast applications in biomedical research, healthcare, pharmaceuticals, environmental monitoring, homeland security, and the battlefield.[9] Generally, there are two detection protocols that can be implemented in optical biosensing: fluorescence-based detection and label-free detection. In fluorescence-based detection, either target molecules or biorecognition molecules are labeled with fluorescent tags, such as dyes. Fluorescence is by far the method most often applied and comes in a variety of schemes. Parameters that are being measured in such sensors include intensity, decay time, anisotropy, quenching efficiency, luminescence energy transfer, and so on. While fluorescent based techniques are able to provide promising sensitivity (even down to single molecule level), they suffer from laborious labeling processes that may also interfere with the function of a biomolecule. Moreover, the photobleaching is a well-known challenge for the conventional organic fluorescent dyes. Although this photobleaching problem can be solved by using the inorganic semiconductors nanocrystals (quantum dots, QDs), there are additional cytotoxicity concerns associated with application of QDs in biological systems.[10] In contrast, in label-free detection, target molecules are not labeled or altered, and are detected in their natural forms. This type of detection is relatively easy and cheap to perform, and allows for quantitative and kinetic measurement of molecular interaction. Therefore, an ideal biosensor-based platform should be label-free, sensitive and biocompatible.

This chapter focuses on the label-free optical biosensors or bioassays, which can be further classified into two major groups: the catalytic and affinity-based optical biosensors. In the former one, the biocomponents are used to recognize (bio)chemical species and then transform them into a product through a (bio)chemical reaction. While in the affinity-based biosensors, the principle is to detect the specific binding of analyte to a biorecognition element.

1.1.2 Catalytic optical biosensors

One of the representative catalytic optical biosensors is the enzyme-based detection, which make use of specific enzymes or their combinations. It also includes biosensors based on measurement of the rate of inhibition of a catalytic reaction by an inhibitor such as a heavy metal ion or a pesticide. As the typical example, the enzymatic glucose biosensors are the most frequently investigated ones, which are based on the following reactions:

$$\text{D-glucose} + O_2 \xrightarrow{\text{GOx}} \text{D-gluconolactone} + H_2O_2 \qquad (1)$$

$$\text{D-gluconolactone} + H_2O \rightarrow \text{D-gluconate} + H^+ \qquad (2)$$

The concentration of glucose thus can be related to (a) the amount of oxygen consumed[11] (b) the amount of hydrogen peroxide produced[12] or (c) the decrease in pH due to the conversion of D-gluconolactone to D-gluconic acid.[13]

The other interesting catalytic optical biosensor is the whole-cell based bacterial biosensors, where the microorganisms are genetically engineered to produce luminescent signals when exposed to toxicants.[14] The bioluminescence generation is enabled by the different enzymes, substrate and cofactors that are produced by bacterial cells *in vivo*. The principle as well as the applications of these engineered bacterial cells based biosensor will be discussed later.

1.1.3 Affinity-based optical biosensors

According to the specific biomolecules interaction involved, this kind of optical biosensors can be further grouped as immunosensors (which rely on the specific interaction between antibody and antigen), genosensors (which utilize the affinity between complementary oligonucleotides) and biosensors based on ligand analyte binding to biological receptor. Among these different groups, the immunosensors are the most frequently used one, due to their high specificity and diverse formats. Specifically, there are 4 different immunosensors formats widely used, including direct, competitive, sandwich and displacement immunosensors as shown in **Figure 1.1**.

The direct format is fairly straightforward and doesn’t need a label biomolecule, which is the simplest configuration and reported in several studies.[15] In the competitive format,[16] an unlabeled antigen (the analyte) and its labeled form compete for a limited number of binding sites of the immobilized antibody. This method requires a labeled antigen and can be inversed to enable the detection and assay of antibodies via the competitive binding of labeled and unlabeled antibodies, respectively, to an immobilized antigen. The sandwich bioassays are widely used and require relatively large antigens that contain at least two epitopes (the recognition site of antibody) to be bound to the immobilized capture antibody and to the labeled second antibody.[17] The last displacement immunosensor is less common format which requires an initial saturation of all the antibody binding sites with a fluorescently labeled antigen.[18] Upon introduction of the unlabeled antigen, displacement of the labeled antigen occurs and is measured in this sensor as a decrease in the optical intensity.

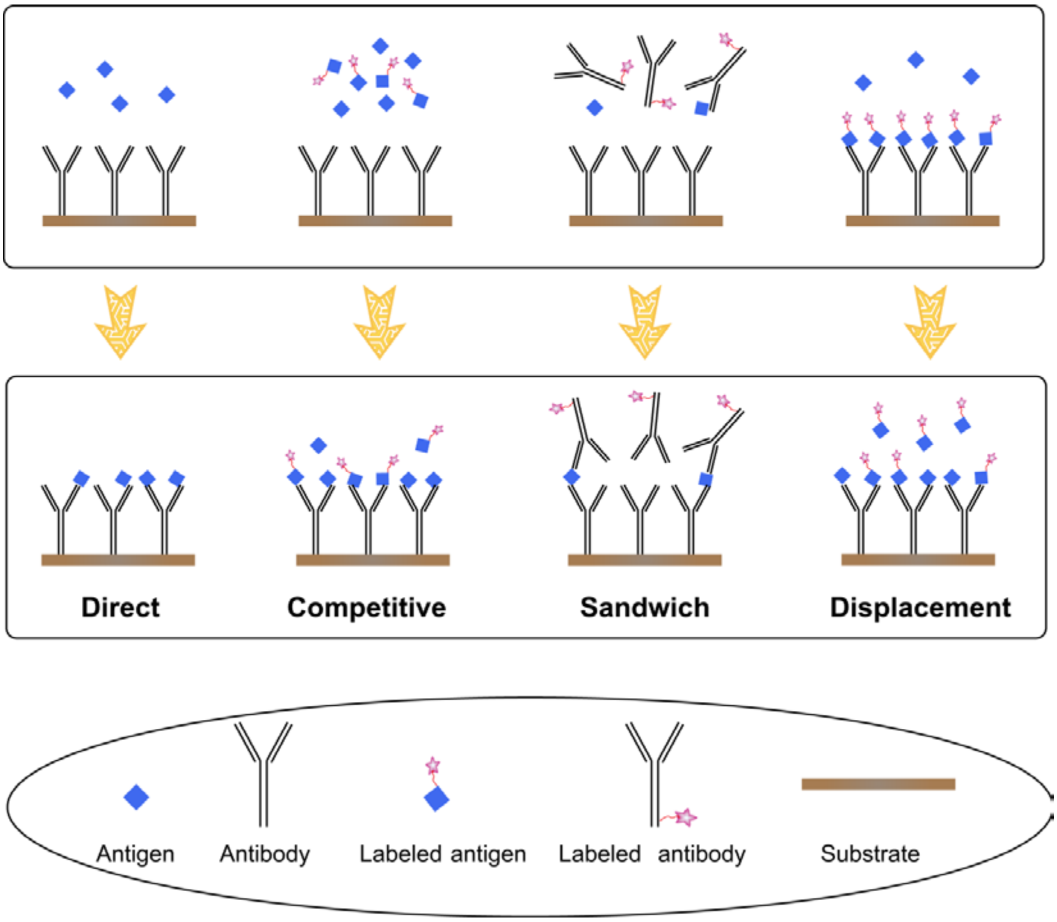

Figure 1.1 Typical formats of optical immunosensors or immunoassays before (upper panel) and after (lower panel) equilibration of immunoreactions.

The immunoreaction information from these different formats can be probed by various optical detection methods. However, the present work will mainly focus on the nanophotonics field, more specifically on the localized surface plasmonic resonance based biosensors, thanks to the rich optical properties of noble metal nanoparticles and increasing advancements made in this domain during recent years. All these details will be presented in later part.

1.2 Optical biosensors based on bacterial bioluminescence

1.2.1 Brief history of bioluminescent assay

Bioluminescence is the light production process mainly enabled by luciferases inside the living organisms, which is prevalent in numerous marine creatures and some terrestrial invertebrates as well. Biochemically, all known luciferases are oxygenases that oxidize its corresponding substrate (generally named luciferin, literally means the "light-bearing" molecules) in the presence of oxygen.[19] Although the bioluminescence can be established in various organism, the bacterial bioluminescence, occurred naturally in 11 bacterial species from four genera (*Vibrio*, *Photobacterium, Shewanella and Photorhabdus*), is especially important due to the ubiquitous and simplicity of bacterial cells.[20] Initiated about 20 years ago,[21] the bioluminescent bacterial sensor-reporters, which consist of living microbe genetically engineered to produce specific outputs proportional to the content of exposed target chemicals or toxic stress, offer an interesting alternative to the environmental monitoring applications.

Due to the diversity of sensing parts (promoter gene)[22] and reporting elements (fluorescent protein or luciferase),[23] together with the intrinsic properties of living cells, the whole-cell bioassays using engineered bacterial cells are able to detect the effects of only bioavailable part of toxicant and also can quantify the total toxicity of several toxicants mixtures to living cells, the possible evaluation of bioavailability via these bacterial bioreporter is therefore regarded as their most prominent advantage over other traditional biosensing techniques using biomolecules (e.g. antibody, enzyme, nucleotide, etc.) as sensing element.[24] Moreover, bacterial bioluminescence, enabled by the *lux* genes, is one special kind of chemiluminescence occurred in the living microbial cells without requirement of external optical excitation, thus the absence of background luminescent signal from host-cells indicates the bacteria bioluminescent detection efficiency is solely determined by the optical detector used. As the results, the bioluminescent assay can achieve extremely high sensitivity due to the self-illumination nature of bioluminescence. Therefore, genetically modified microorganisms have been widely used in the screening of environmental toxicants, such as organic pollutants,[25] heavy metals,[26] pesticides,[27] and antibiotics.[28]

1.2.2 Genetically engineered bacteria cells

Oftentimes, the recombinant bacterial cells have been constructed by transforming the plasmids fused with promoter probe (such as *recA* or *grpE*) and reporter gene (*luxCDABE*, *luxAB* or *luc*) into host cells (e.g. *E. coli*); the promoter probe is responsible for the specific recognition of the analyte, while the expression of the reporter gene leads to the production of bioluminescence via the synthesis of luciferase and its corresponding substrate.[29] A generation description of this complex biochemical reaction leading to bioluminescence based on *luxCDABE* is shown in **Figure 1.2**.

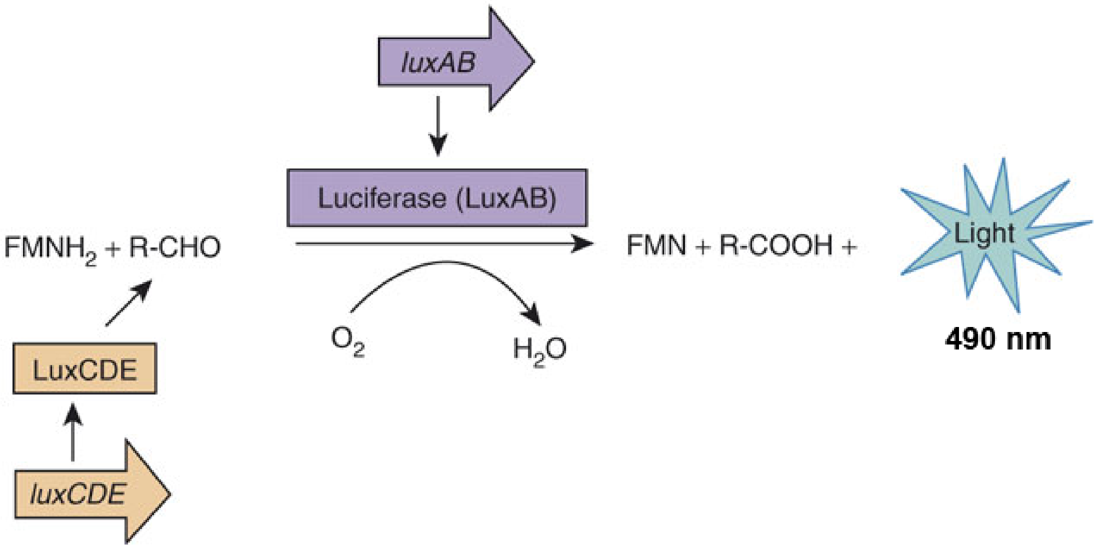

Figure 1.2 The biochemical reaction involved in bacterial bioluminescence generation. *LuxAB* form the α- and β-subunits of the luciferase enzyme that catalyzes the oxidation of reduced flavin mononucleotide ($FMNH_2$) and a long-chain fatty aldehyde (R-CHO), generated by the *LuxCDE* proteins. This results in the emission of a blue-green light at 490 nm.

Depending on the toxicants to be detected, a large number of engineered bacteria strains harbouring different promoter genes have been constructed, while the reporter genes used in majority studies is the lux bioreporter, as shown in **Table 1.1**.

Table 1.1 The genetically modified bacterial cells contain different promoters.

Target	**Microorganism**	**Promoter: reporter**	**Reference**
Toluene	*E. coli DH5α pTOLLUX*	*Pu::lux*	30
Tetracycline	*E. coli K12 pTetlux1*	*tetA::lux*	31
Mercury	*E. coli HMS174*	*mer::lux*	32
Urinary mercury	*E. coli MC1061*	*mer::lux*	33
Copper	*P. fluorescens DF57*	*Tn5::luxAB*	34
Phosphorus	*Synechococcus PCC 7942*		35
Herbal tinctures	*E. coli DE135*	*uspA::lux*	36
Methyl viologen	*E. coli PGRFM*	*pgi::lux*	37
Chlorine dioxide	*P. fluorescens 5RL*	*sal::lux*	38
2,4-Dichlorophenol	*V. fischeri*	*lux*	39
3,4-Dichlorophenol	*V. fischeri*	*lux*	39
2,3,5,6-Tetrachlorophenol	*V. fischeri*	*lux*	39
naphthalene in soil	*P. fluorescens HK44 pUTK21*	*lux*	40
Chloramphenicol	*E. coli EMS310*	*cspA::luc*	41
Ofloxacin	*E. coli EMS50*	*sulA::lucR1*	41
Tributyltin	*E. coli*	*lux AB*	42
Halogenated organic acids	*E. coli*	*luxCDABE*	43
various pollutants	*E. coli*	*fab A::lux*	44
Phenolic waste water	*P. fischeri,* *P. putida*	*BS566::luxCDABE*	44
Mitomycin	*E. coli*	*recA::lux*	45
UV	*E. coli*	*recA::lux*	45

1.2.3 Applications of *luxCDABE* reporter based biosensors and assays

Based on the previous discussion, the most frequently used bioreporter lux genes responsible for encoding the luciferase enzyme are the *luxCDABE* gene. The bacterial responses to toxicants or toxic effects are mainly determined by the promoter genes. Especially the capability of toxic effects and toxicant bioavailability detection are exclusively found in these whole-cell based biosensors, while it is quite difficult to obtain this important information from other conventional physicochemical analysis and even optical biosensors based on biomolecules. For example, the protein damage can be sensed by using the strain *E. coli* TV 1061 (*grpE::luxCDABE*) sensitive to cellular metabolism changes, which is attributed to fact that the promoter *grpE* is one of about 20 promoters that are activated under conditions when the cells experience protein damage (e.g. upon addition of ethanol or phenol). Followed this activation, the reporter gene is therefore transcribed into necessary components that are responsible for light production.[46] The other toxic effects such as oxidative stress, cell membrane damage and genotoxicity can also be detected by specific engineered bacterial cells. For instance, another strain frequently used is based on the fusion of a DNA-damage inducible promoter *recA* and reporter gene (*luxCDABE*), thus this strain is responsive to the genotoxical materials.[47]

Therefore, a great range of the bioassays based on *E. coli* bacterial bioluminescence have been reported for detection of various different toxicants including heavy metal, organic pollutants (PCB: polychlorinated biphenyl) and toxic effects such as DNA damages, protein damage, cell membrane damage and oxidative stress. All these *luxCDABE* bioreporter based bioluminescent sensors or assays are summarized in **Table 1.2**, where includes the detection target, biorecognition element (promoter), lower limit of detection (LOD) and experimental setup used. It should be noted that **Table 1.2** is modified from the published work of M. Woutersen et al.[48]

Table 1.2 Toxicants detection using bioluminescence biosensors or assays based on genetically modified bacterial cells containing *luxCDABE* bioreporter.[48]

Target/stress		**Strain**	**Promoter**	**LOD**	**Setup**
Organic pollutants	Naphthalene	*P. fluorescens HK44*	*nahG*	45 µg/L	culture plate
	Salicylate	*E. coli DNT5*	*nagR-nagAa*	164 µg/L	culture plate
	PCBs	*Ralstonia eutropha ENV307 (pUTK60)*	*orf0-bphA1*	150 µg/L	culture plate
	Phenol	*P. fluorescens OS8*	*dmpR*	80 µg/L	culture plate
Heavy Metals	Cd, Pb, Zn	*E. coli MG1655*	*zntA*	1.1 µg/L	culture plate
	Hg, Cd	*E. coli MC1061*	*merRB*	0.002 µg/L	culture plate
	Hg, Cd, Pb	*P. fluorescens OS8*	*cadRA*	10 µg/L	culture plate
	Hg, Cd, Zn	*Bacillus subtilis*	*cadCA*	2 µg/L	culture plate
DNA damage	Trimethroprin	*E. coli DPD2794*	*recA*	500 µg/L	culture plate
	Mitomycin C	*E. coli DPD2797*	*recA*	0.1 µg/L	culture plate
	Mitomycin C	*E. coli DPD1710*	*recA*	1 µg/L	culture plate
	4-nitrophenol	*E. coli Sal94*	*recA*	250 µg/L	culture plate
Protein Damage	0.3% ethanol	*E. coli TV1061*	*grpE*	0.1 mg/L	sol-gel wells
	pentachlorophenol	*E. coli WM1202*	*dnaKp*	19 mg/L	culture plate
	phenol	*E. coli WM1302*	*dnaKp*	50 mg/L	culture plate
	pentachlorophenol	*E. coli TV1076*	*grpE*	0.07 mg/L	culture plate
Cell membrane damage	Triton X-100	*E. coli DPD2544*	*fabA*	0.19 mg/L	culture plate
	4-bromophenol	*E. coli DPD2540*	*fabA*	0.14 mg/L	culture plate
	4-nitrophenol	*E. coli DPD2543*	*fabA*	0.08 mg/L	culture plate
	phenol	*E. coli DPD2546*	*fabA*	100 mg/L	Bioreactor
Oxidative stress	H_2O_2	*E. coli DPD2511*	*katG*	0.1 mg/L	culture plate
	Paraquat	*E. coli DPD2515*	*micF*	0.01 mg/L	gold plates
	2-propanol	*E. coli DK1*	*katG*	0.15%	sol-gel well plate
	H_2O_2	*E. coli DK1*	*katG*	0.03 mg/L	Microfluid chip
	Paraquat	*E. coli EBHJ*	*sodA*	0.015 mg/L	culture plate

1.3 Optical biosensors based on plasmonics

1.3.1 Fundamentals of plasmonics

Surface plasmons are defined as the collective oscillation of the conductive electrons in metal induced by electromagnetic wave.[49] Specifically, this plasmon oscillation is resulted from the electron gas displacement with respect to the fix ionic nucleus due to the electric field of incident light, as demonstrated in **Figure 1.3**. Although the plasmon can be observed in many types of metals, materials like gold (Au),[50] silver (Ag),[51] copper (Cu) and aluminum (Al)[52] are capable to support surface plasmons when driven by the UV-Vis-NIR light, due to their large negative real and small positive imaginary dielectric constant over a range of frequency spectrum. In addition, the surface plasmon resonance can be either propagated (**Figure 1.3**A) or localized (**Figure 1.3**B), the former one is established at the interface between thin metal films and dielectric substrate,[53] while the later one is basically observed on the metal nanostructures.[54] Interestingly, in some special cases, the co-existence of both modes, SPR and LSPR, is realized for certain plasmonic nanostructures such as the nanoholes arrays on the thin film[55] and nanoporous gold thin membrane.[56] In the case of metal nanoparticles (diameter of R) that are much smaller than the wavelength (λ) of incident light ($2\pi R << \lambda$), the plasmon is highly confined at the surface of metal nanoparticles and is damping rapidly with the distance away from the nanoparticle surface, thus this specific phenomenon is named as localized surface plasmon resonance (LSPR). Owing to the large amount of methodologies that are capable to precisely synthesis tremendous nanostructures with different compositions, sizes and shapes,[57-61] together with the rapid advancement of high performance computing simulation methods,[62-64] LSPR have received burgeoning research interests over the last two decades and found wide applications in optical devices,[65] photonic circuits,[66] plasmon enhanced spectroscopy,[67] (bio)chemical sensing,[68-69] medical theranostics[70] as well as in photovoltaics[71] and photocatalysts.[72]

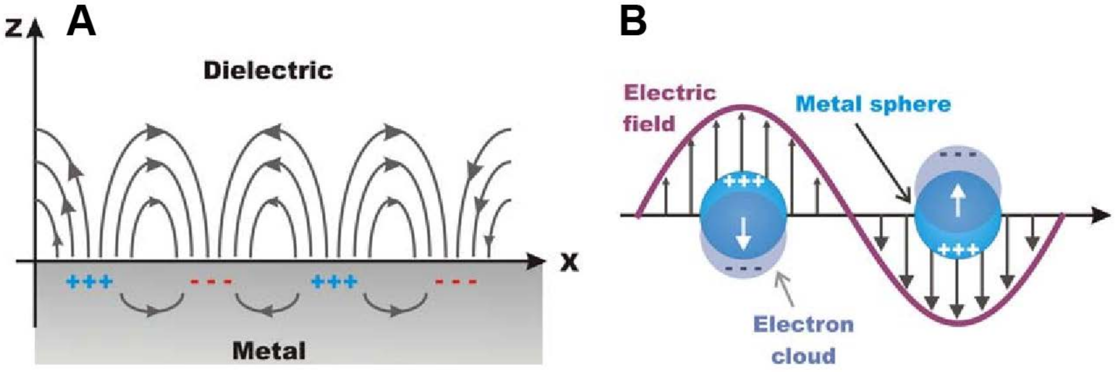

Figure 1.3 Illustration of propagating surface plasmon resonance (A) presented in the interface between thin metal film and dielectric substrate and localized surface plasmon resonance (B) occurred in the highly localized space surrounding nanoparticles surface.[49]

1.3.2 Plasmonic properties of noble metal nanoparticles

The LSPR spectra of metal nanostructures can be recorded in a transmission extinction measurement setup using the conventional optical instruments in either solution phase or solid state, from which the plasmonic properties including resonant wavelength, maximum optical density and peak shape can be readily resolved. These plasmonic properties are highly dependent on the physical dimensions (size, shape, interparticle distance, aspect ratio, etc.,) and chemical compositions of metal nanoparticles.[73] Besides of the geometric dimension dependence of plasmonic peak, the refractive index of local medium surrounding the nanoparticles also plays an important role in determining the plasmonic properties. This refractive index dependent plasmonic response is thus explored as the basic sensing mechanism for the emerging LSPR biosensors, where the specific biochemical reaction contributes to an increasing of local refractive index, which in turn leads to a red-shift of resonant wavelength and/or increasing of maximum optical density (OD) value.[74] In order to better understand how the nanoparticles dimensions and local refractive index influence the plasmonic properties, one must turn to the classical scattering theory.

Due to their rich optical properties, the coinage nanoparticles have been widely used since ancient times, for example, the stained glass of the windows of mediaeval churches exhibits different colors depending on the doping concentration of gold nanoparticles;[75] the Lycurgus cup is a stunning decorative Roman artefact from about AD400, which contains gold/silver alloy nanoparticles dispersed uniformly in glass thus leading to a green color in reflection light but a brilliant red color as light pass through its sections.[76] However, the modern scientific evaluation of gold colloid particles started from midnineteenth century, when Michael Faraday firstly described that "a mere variation in the size of particle gave rise to a variety of resultant colors in the gold colloid solutions".[77] Inspired by the pioneering work of Faraday, in the early 20th century, Gustav Mie firstly developed an analytical solution for the Maxwell's equation, in which the light scattering and absorption of small metal spherical nanoparticles ($2\pi R << \lambda$) can be resolved.[78] From the Mie theory, the extinction (scattering plus absorption) of a homogeneous conducting sphere excited by an incident plane wave can be simply described as:

$$\sigma_{ext} = \frac{32\pi^4 {\varepsilon_m}^2 V^2}{\lambda^4} \frac{(\varepsilon_1 - \varepsilon_m)^2 + (\varepsilon_2)^2}{(\varepsilon_1 + 2\varepsilon_m)^2 + (\varepsilon_2)^2} \tag{3}$$

where σ_{ext} is the extinction cross-section, ε_m is the dielectric function of medium, the complex dielectric function of metal is described as $\tilde{\varepsilon} = \varepsilon_1 + i\varepsilon_2$, λ and V are the wavelength and particle volume, respectively.

It should be noted that the above expression for total extinction cross-section is obtained by assuming the metal nanoparticle shape is strictly spherical and its size (diameter R) is much smaller than the wavelength (λ). From this model, it is clear that the extinction is dependent on nanoparticle size (i.e. the volume V) and will be maximized once the condition $\varepsilon_1 = -2\varepsilon_m$ is qualified, which demonstrates the LSPR extinction peak is also dependent on the surrounding medium refractive index.

By using the Drude model based on the electronic structure of metals, the real part (ε_1) of frequency-dependent dielectric function can be described as:

$$\varepsilon_1 = 1 - \frac{\omega_p^2}{\omega^2+\gamma^2} \tag{4}$$

where ω_p is the plasma frequency and γ is the damping parameter of the bulk metal, ω is the angular frequency. Since in the visible and near-infrared frequencies $\gamma \ll \omega_p$, the above equation is simplified as follow:

$$\varepsilon_1 = 1 - \frac{\omega_p^2}{\omega^2} \tag{5}$$

Using this expression for ε_1 and converting the angular frequency (ω) to wavelength (λ) via $\lambda = 2\pi c/\omega$, c is the speed of light, the resonant wavelength (λ_{max}) of the extinction can be obtained as follows:

$$\lambda_{max} = \lambda_p\sqrt{2n_m^2 + 1} \tag{6}$$

where n_m($n_m^2 = \varepsilon_m$) is the refractive index of medium, λ_p is the plasmon wavelength, from the equation (6), it is clear that the resonant wavelength is almost linearly varied versus medium refractive index.

However the Mie theory mentioned above is only valid for small metal sphere particles, while the light extinction of spheroidal particle with any aspect ratio can be resolved using the generalized Gans Theory, which is developed in 1912 by Richard Gans.[79] From this modified model, the aspect ratio of spheroidal particles also has influence onto the plasmonic spectra; the increasing of aspect ratio generally leads to a red-shift of plasmonic peak, as well as the increased plasmonic sensitivity to dielectric constant of local environments. For the nanoparticles beyond spheres and spheroids, the shape of nanoparticles plays an important role in determining the final plasmonic properties, and the shape dependent plasmonic changes can only be revealed via the numerical simulation methods such as finite difference time domain (FDTD), discrete dipole approximation (DDA) and finite element method (FEM). The details about the principles and the applications of these numerical simulation methods are summarized in some recent review articles.[80-82]

The metal nanoparticles or nanostructures are used as the transducers in the LSPR biosensors, from which the specific biochemical binding events have been converted into quantifiable optical signals. In order to obtain the best analytical sensitivity in this LSPR biosensor configuration, the optimization of optical properties of metal nanoparticles or nanostructures is essentially important. Fortunately, a large plasmonic tunability of noble metal nanoparticles or nanostructures can be achieved by using controlled synthesis and lithographic based methodologies combined with advanced numerical simulations. In this work, we will mainly focus on the gold nanoparticles (Au NPs) synthesis and their uses in plasmonic based biosensors.

1.3.3 Synthesis and assembly of gold nanoparticles

A large number of articles involving preparation of noble metal nanoparticles and nanostructures have been reported over the recent years [39, 40]. Basically, these well documented methods can be roughly classified into two categories: the “top-down” physical manipulation protocols and “bottom-up” chemical transformation recipes.

The Au NPs have firstly been prepared by using citrate reduction of $HAuCl_4$ in H_2O, which was pioneered by Turkevich in 1951 and is still widely used today.[59] In this method, citrate acts as both the reducing agent and the stabilizer during the reaction, and it is possible to obtain Au NPs of varying size ranging from 16 to 147 nm by simply adjusting the concentration ratio between citrate and $HAuCl_4$. In order to get Au NPs with uniform size and shape distribution, the Brust-Schiffrin method that developed in 1994 is capable to synthesis alkanethiol-stabilized Au NPs in single phase.[60] The Au NPs obtained from the Brust-Schiffrin method have some promising advantages such as the thermal and oxidation stability, reduced dispersity and precise size control (especially in extremely small size of 1.5 to 5.2 nm), and the Au NPs obtained via this method are normally stabilized with functional thiol ligands, which facilities the further modification of Au NPs.

The Au NPs are also assembled into more complex nanostructures via the different templates. Of special interests, the DNA or oligonucleotides have been widely used for templating the assembly of Au NPs, because the DNA or oligonucleotides can be readily synthesized using commercial PCR techniques, and various functional groups can be easily integrated to allow for interaction with Au NPs. The DNA templated Au nanostructures were pioneered by Mirkin and Alivisatos groups independently in 1996,[83-84] since then various DNA-Au NPs conjugated nanostructures such as discrete DNA-Au clusters[85-87] and extended DNA-Au assemblies[88-92] have been prepared. Other different kinds of biological templates such as peptides, proteins and even microorganism like virus and bacteria have also been utilized to realize the complex Au assembly.[93-96] Besides these versatile biological templates, the other inorganic or organic templates have also been widely used, such as carbon nanotube, supramolecular assemblies and block copolymer.[97-100] The different Au NPs and assembled Au nanostructures obtained from these templating methods are demonstrated in **Figure 1.4**.

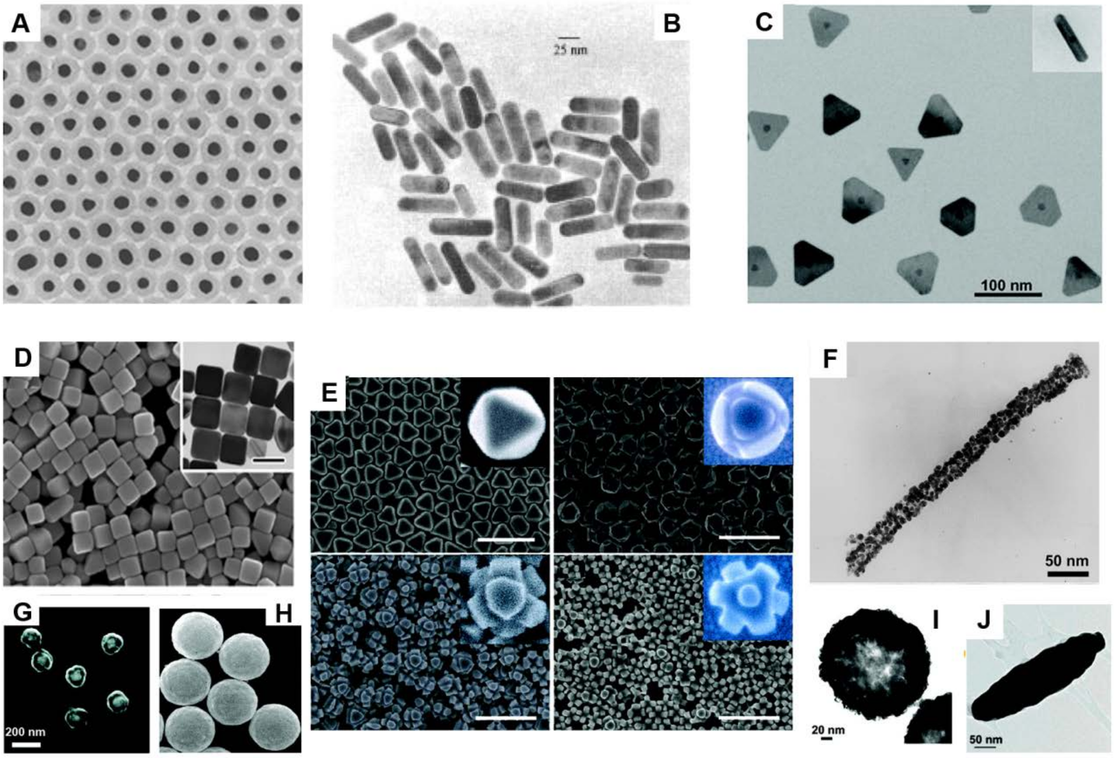

Figure 1.4 Different gold based nanostructures synthesized by using template growth like silica shells grown on Au nanoparticles cores (A), Au nanorods (B), Ag nanoprism grown on sphere Au cores via plasma mediated reduction of Ag^+(C), Au nanocubes (D), site specific oxidation of Ag octahedral on Au triangle core leading to the final eight-armed octopod structure (E), selective deposition of Au NPs on the outside surface of tobacco mosaic virus template (F), a spherical Au NP embedded within a nanoshell separated by a silica layer (G), Au NP in a nested and concentric nanoshell (H), Au NP in a asymmetric nanoshell (I) and anisotropic hybrid nanorice composed of α-Fe_2O_3 core and Au shell (J).This figure is modified from the published work.[100]

Despite the tremendous kinds of Au nanoparticle or nanostructures have been prepared by using chemical bottom-up methods, it is quite challenging to obtain the patterns with precisely organized particles at nanoscale range. And the well-organized nanoparticles pattern with known uniform size, shape and interparticle spacing are very important to understand the basic properties of localized surface plasmon resonance versus nanoparticles morphology. In this sense, the physical “top-down” protocols serve as the promising candidate for these requirements. One of the typical “top-down” method is the electron beam lithography (EBL),[101-102] which uses the electron beam to scan the photoresist protected substrate in a programmed manner, followed by developing, metal evaporation and lift-off of the photoresist, finally the strictly controlled nanoparticle patterns are obtained, some typical EBL gold patterns containing nanodots, nanotriangles, nanosquares were showed in **Figure 1.5**.

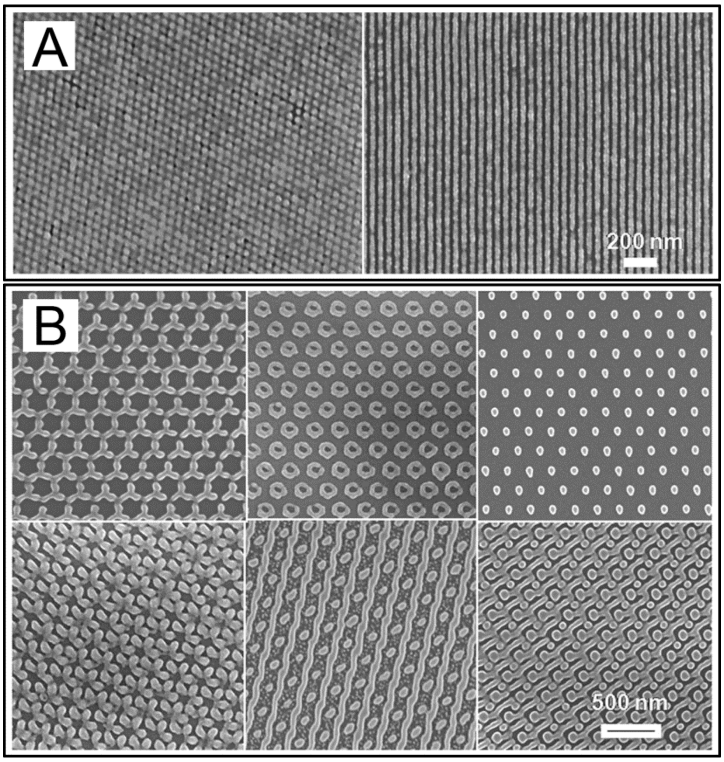

Figure 1.5 Typical simple dot/line patterns (A) and more complex patterns (B) fabricated via EBL.[102]

1.3.4 Applications of plasmonic based biosensors

Thanks to the rich optical properties of Au NPs, the nanophotonics have witnessed rapidly developments in recent years, especially in the application of plasmonic based optical biosensors. Although a similar technique of surface plasmon resonance (SPR) sensor has been commercialized for more than 20 years and still dominated as the an important optical biosensor,[103] the emerging localized surface plasmon resonance based biosensor are receiving ongoing interests, mainly due to its ability to confine the electromagnetic wave in nanoscale range around the nanoparticles. There are two important consequences associated with this precise light manipulation: the LSPR spectra are highly sensitive to localized dielectric environments and the local electronic field is strongly enhanced. The former one is conventionally explored as the basic mechanism for the molecular LSPR sensor,[104] while the later one is generally utilized in the resonant based LSPR sensor and some plasmon enhanced spectroscopy, represented by the surface enhanced Raman spectroscopy (SERS) nanosensor.[105]

In the LSPR based biosensors, the specific biochemical interaction is transduced by the local refractive index changes around Au NPs, which leads to the modulation of plasmonic resonant peak. With the continuous advancement on the understanding of plasmonic properties and controlled synthesis of plasmonic nanostructures, tremendous studies of LSPR biosensors have been reported to detect various kinds of biomolecule interactions, the details can be found in a range of excellent review articles.[53, 69, 74, 104-108] Specifically, the immunological LSPR biosensor based on the antibody-antigen interaction is of paramount interests, mainly due to the strong and highly specific binding ability of antibody. In this type of LSPR immunosensor, the capture antibody is normally immobilized onto the plasmonic surface via the self-assembly monolayer (SAM) based on thiol chemistry, followed by passivation of nonspecific binding sites, thus the specific recognition towards target analyte (antigen) is probed in a dose dependent resonant wavelength shift. One typical example was shown in **Figure 1.6,** where LSPR real time detection of ADDL (amyloid-β derived diffusible ligands), a biomarker for Alzheimer’s disease, is realized.[109]

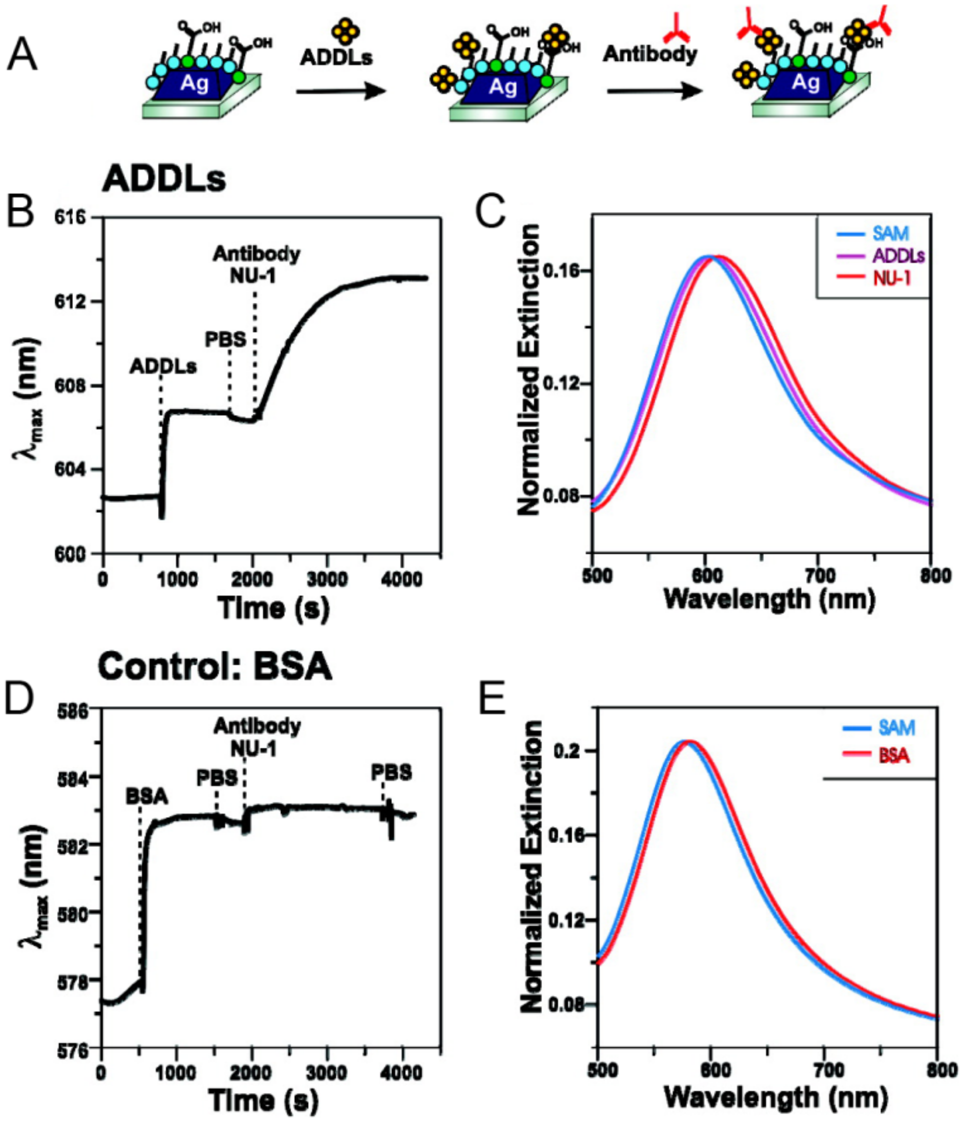

Figure 1.6 LSPR sensor for biomarker detection (A), real time sensorgram and LSPR spectra corresponding to ADDLs binding (B,C) and control experiment using BSA (D, E), respectively.[109]

Interestingly, since the LSPR decay length is in the same range of typical protein size and the plasmonic properties in this localized sensing volume are extremely sensitive, thus the protein conformation change can also be precisely monitored using LSPR biosensor. For instance, a quantitative demonstration of the conformation change of calmodulin (CaM) via LSPR spectra was revealed by Van Duyne and coauthors.[110] In this configuration, the protein CaM was covalently linked to the cutinase (Cut) that is immobilized on the plasmonic surface to supply the accommodation for CaM and to provide conformation flexibility. Upon binding of Ca^{2+} ions, the conformation of CaM-Cut complex is changed, which results in a changing of local dielectric constant due to different protein packing density on the plasmonic surface. Therefore, the conformation changes and the concentration of small ions can be obtained by monitoring the plasmonic spectra in real time as indicated in **Figure 1.7**.

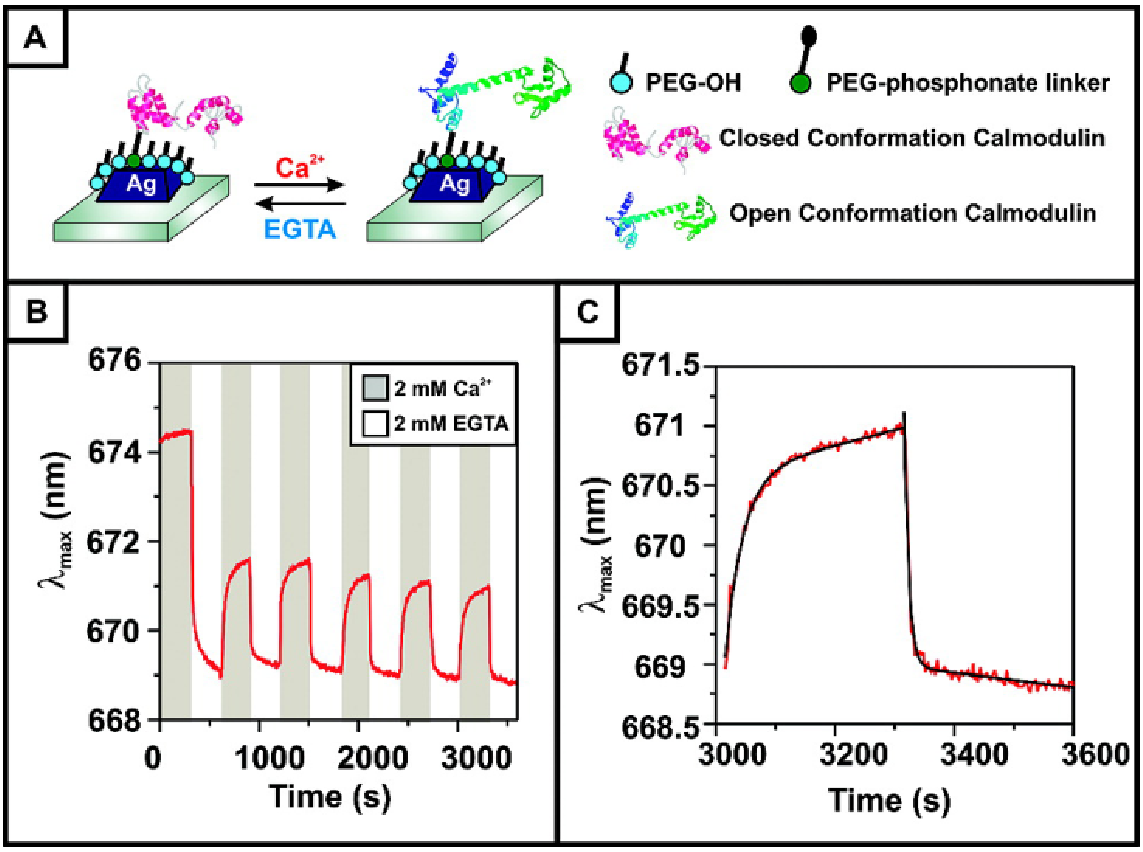

Figure 1.7 Schematic of reversible conformation changing of CutCaMCut complex (A) and real time LSPR resonant wavelength changing as the buffer is transferred between same concentration of Ca^{2+} and EGTA (B), closeup of LSPR spectra changing corresponding to single Ca^{2+}/EGTA cycle (C).[110]

Although the LSPR biosensor is able to detect the trace concentration of biomolecules as well as the minute conformation changes of proteins, it is quite a challenge to obtain the chemical structure information of analyte from the LSPR biosensors that detect local refractive index changes. To this end, another plasmon based optical biosensor of SERS, namely surface enhanced Raman spectroscopy, is not only able to show the dose dependent responsive as conventional LPSR biosensors, but also provide fingerprint structure information for the analyte target, therefore the target biomolecules can be virtually “seen” by the SERS nanosensors. Given these promising features of SERS nanosensors, there are increasing work conducted, involving mechanism study, substrate preparation, instrumental measurement and so on, these details can also be found in several comprehensive reviews articles[111-115] and excellent books.[116-119] Herein, an interesting plasmonic biosensor containing dual transducing channels for parallel acquisitions of LSPR transmission and SERS spectra is described as the conclusion example for this chapter. As shown in **Figure 1.8**, the LSPR and SERS are combined in highly tunable plasmonic metamaterials biochip which is made up of split-ring resonator arrays.[120] The conformation and structure information are probed by SERS spectra, while the quantitative binding information is obtained by LSPR transmission measurement. By simultaneous probing the conformational states and binding affinity of biomolecule, the authors are able to fingerprint and detect the interaction between binding domain of nucleolin cancer biomarker (RGG_9 peptide) and K^+-induced AS1411 G-quadruplexes with a picomolar sensitivity.

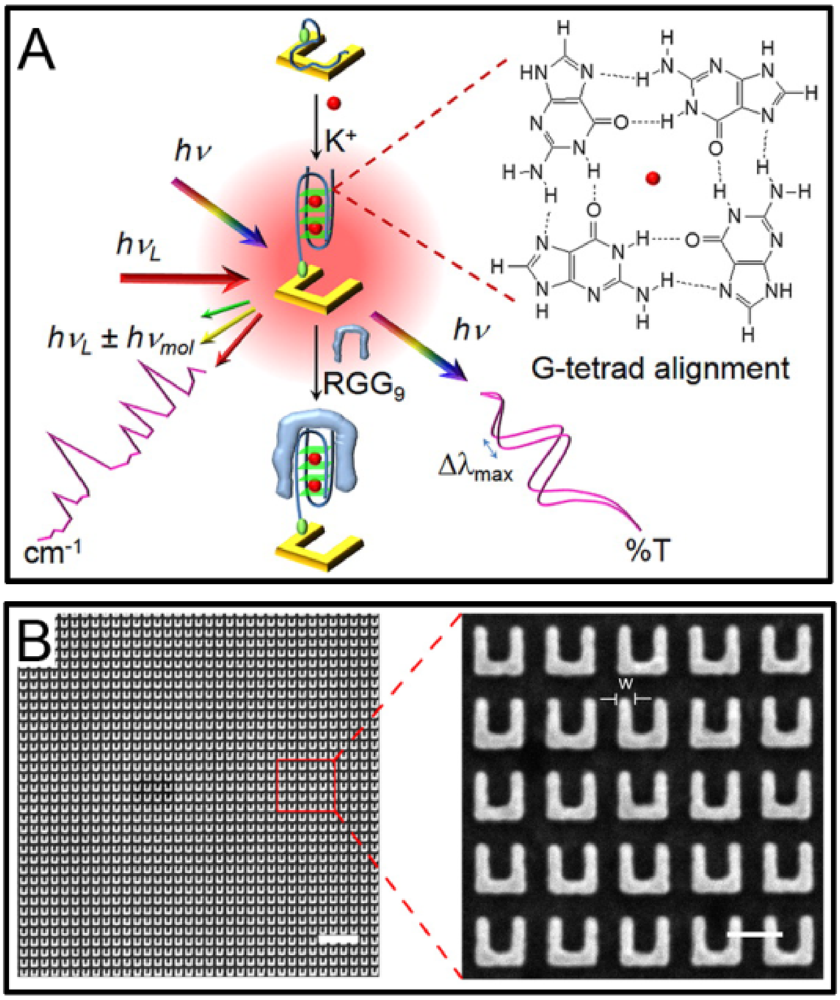

Figure 1.8 Schematic illustration of vis–NIR metamaterials as a dual transducing mode nanosensor for the detection and identification of biomolecules (A) and representative SEM micrographs of substrate with average width w = 45.2 ± 2.6 nm measured from 25 structures (from left to right, the scale bars are 1 μm and 200 nm, respectively). Designed to operate in the vis-NIR spectrum, the plasmonic metamaterials will provide direct access to characteristic fingerprints of biomolecules, thus enabling a unique platform to execute both conformational information and quantitative binding data simultaneously by transmission LSPR and SERS spectroscopies. The nanosensor is functionalized with AS1411, an effective anticancer drug that is currently in clinical trials for cancer treatment. Under K^+-induced conditions, AS1411 folds into a G-quadruplex, which can effectively capture the binding region of a nucleolin biomarker RGG_9. The figures was adapted from the publish work.[120]

1.4 Summary

With the increasing demands from ecotoxicology, environmental and medical analysis fields, the biosensors have seen continuous growth both in academic research and industries applications since the first glucose biosensors was developed and later commercialized. Among the tremendous different biosensing systems, optical biosensors are receiving ongoing research interests during the recent decades, especially for those based on the label free optical detection. Based on the detection principle, the label free optical biosensor can be divided into catalytic and affinity-based biosensors. The principle of former one is to probe the specific biomolecules interactions via a biochemical reaction, while the later one directly detects the analyte binding to biorecognition elements by various methods.

As one typical example for the catalytic label-free optical biosensors, the bioluminescent assays based on engineered bacterial cells have been discussed in terms of fundamentals of bacterial bioluminescence, engineered bacterial cells construction as well as biosensor or bioassays applications towards a wide range of toxicants or toxic effects. For the affinity-based optical biosensors, we have mainly focused on the immunosensors using plasmonic Au NPs, mainly due to their versatile optical properties. In this part, the basic information of plasmonic, gold nanoparticles synthesis and application of two plasmonic based biosensors of LSPR and SERS nanosensors have been discussed. Particularly, some innovative platforms have been designed to realize the simultaneous recording of LSPR and SERS signals, which will definitely improve the overall analytical performance of these surface plasmon based biosensors.

References:

1. Gaud, W. S., The green revolution: accomplishments and apprehensions. *Discurso perante a Society for International Development, Washington, DC* **1968**.

2. Karami-Mohajeri, S.; Abdollahi, M., Toxic influence of organophosphate, carbamate, and organochlorine pesticides on cellular metabolism of lipids, proteins, and carbohydrates A systematic review. *Human & Experimental Toxicology* **2011,** *30* (9), 1119-1140.

3. Graymore, M.; Stagnitti, F.; Allinson, G., Impacts of atrazine in aquatic ecosystems. *Environment International* **2001,** *26* (7), 483-495.

4. Faust, M.; Altenburger, R.; Backhaus, T.; Blanck, H.; Boedeker, W.; Gramatica, P.; Hamer, V.; Scholze, M.; Vighi, M.; Grimme, L., Predicting the joint algal toxicity of multi-component *s*-triazine mixtures at low-effect concentrations of individual toxicants. *Aquatic Toxicology* **2001,** *56* (1), 13-32.

5. Antunes, S. C.; Pereira, J. L.; Cachada, A.; Duarte, A. C.; Gonçalves, F.; Sousa, J. P.; Pereira, R., Structural effects of the bioavailable fraction of pesticides in soil: Suitability of elutriate testing. *Journal of Hazardous Materials* **2010,** *184* (1), 215-225.

6. DeLorenzo, M. E.; Scott, G. I.; Ross, P. E., Toxicity of pesticides to aquatic microorganisms: a review. *Environmental Toxicology and Chemistry* **2001,** *20* (1), 84-98.

7. Thévenot, D. R.; Toth, K.; Durst, R. A.; Wilson, G. S., Electrochemical biosensors: recommended definitions and classification. *Biosensors and Bioelectronics* **2001,** *16* (1), 121-131.

8. Turner, A. P., Biosensors--sense and sensitivity. *Science* **2000,** *290* (5495), 1315-1317.

9. Fan, X.; White, I. M.; Shopova, S. I.; Zhu, H.; Suter, J. D.; Sun, Y., Sensitive optical biosensors for unlabeled targets: A review. *Analytica Chimica Acta* **2008,** *620* (1), 8-26.

10. Michalet, X.; Pinaud, F.; Bentolila, L.; Tsay, J.; Doose, S.; Li, J.; Sundaresan, G.; Wu, A.; Gambhir, S.; Weiss, S., Quantum dots for live cells, in vivo imaging, and diagnostics. *Science* **2005,** *307* (5709), 538-544.

11. Trettnak, W.; Leiner, M. J.; Wolfbeis, O. S., Optical sensors. Part 34. Fibre optic glucose biosensor with an oxygen optrode as the transducer. *Analyst* **1988,** *113* (10), 1519-1523.

12. Heo, J.; Crooks, R. M., Microfluidic biosensor based on an array of hydrogel-entrapped enzymes. *Analytical Chemistry* **2005,** *77* (21), 6843-6851.

13. McCurley, M. F., An optical biosensor using a fluorescent, swelling sensing element. *Biosensors and Bioelectronics* **1994,** *9* (7), 527-533.

14. Belkin, S., Microbial whole-cell sensing systems of environmental pollutants. *Current Opinion in Microbiology* **2003,** *6* (3), 206-212.

15. Sapsford, K. E.; Charles, P. T.; Patterson, C. H.; Ligler, F. S., Demonstration of four immunoassay formats using the array biosensor. *Analytical Chemistry* **2002,** *74* (5), 1061-1068.

16. Owaku, K.; Goto, M.; Ikariyama, Y.; Aizawa, M., Protein A Langmuir-Blodgett film for antibody immobilization and its use in optical immunosensing. *Analytical Chemistry* **1995,** *67* (9), 1613-1616.

17. Hong, B.; Kang, K. A., Biocompatible, nanogold-particle fluorescence enhancer for fluorophore mediated, optical immunosensor. *Biosensors and Bioelectronics* **2006,** *21* (7), 1333-1338.

18. Sheikh, S. H.; Mulchandani, A., Continuous-flow fluoro-immunosensor for paclitaxel measurement. *Biosensors and Bioelectronics* **2001,** *16* (9), 647-652.

19. Hastings, J., Chemistries and colors of bioluminescent reactions: a review. *Gene* **1996,** *173* (1), 5-11.

20. Thouand, G.; Daniel, P.; Horry, H.; Picart, P.; Durand, M. J.; Killham, K.; Knox, O. G.; DuBow, M. S.; Rousseau, M., Comparison of the spectral emission of lux recombinant and bioluminescent marine bacteria. *Luminescence* **2003,** *18* (3), 145-155.

21. King, J.; DiGrazia, P.; Applegate, B.; Burlage, R.; Sanseverino, J.; Dunbar, P.; Larimer, F.; Sayler, G. a., Rapid, sensitive bioluminescent reporter technology for naphthalene exposure and biodegradation. *Science* **1990,** *249* (4970), 778-781.

22. Marqués, S.; Aranda-Olmedo, I.; Ramos, J. L., Controlling bacterial physiology for optimal expression of gene reporter constructs. *Current Opinion in Biotechnology* **2006,** *17* (1), 50-56.

23. Drepper, T.; Eggert, T.; Circolone, F.; Heck, A.; Krauß, U.; Guterl, J.-K.; Wendorff, M.; Losi, A.; Gärtner, W.; Jaeger, K.-E., Reporter proteins for in vivo fluorescence without oxygen. *Nature Biotechnology* **2007,** *25* (4), 443-445.

24. Magrisso, S.; Erel, Y.; Belkin, S., Microbial reporters of metal bioavailability. *Microbial Biotechnology* **2008,** *1* (4), 320-330.

25. Valdman, E.; Battaglini, F.; Leite, S.; Valdman, B., Naphthalene detection by a bioluminescence sensor applied to wastewater samples. *Sensors and Actuators B: Chemical* **2004,** *103* (1), 7-12.

26. Jouanneau, S.; Durand, M.-J.; Courcoux, P.; Blusseau, T.; Thouand, G., Improvement of the identification of four heavy metals in environmental samples by using predictive decision tree models coupled with a set of five bioluminescent bacteria. *Environmental Science & Technology* **2011,** *45* (7), 2925-2931.

27. Jia, K.; Eltzov, E.; Marks, R. S.; Ionescu, R. E., Bioluminescence enhancement through an added washing protocol enabling a greater sensitivity to carbofuran toxicity. *Ecotoxicology and Environmental Safety* **2013,** *96*, 61-66.

28. Eltzov, E.; Ben-Yosef, D. Z.; Kushmaro, A.; Marks, R., Detection of sub-inhibitory antibiotic concentrations via luminescent sensing bacteria and prediction of their mode of action. *Sensors and Actuators B: Chemical* **2008,** *129* (2), 685-692.

29. Meighen, E. A., Molecular biology of bacterial bioluminescence. *Microbiological Reviews* **1991,** *55* (1), 123-142.

30. Li, Y.-F.; Li, F.-Y.; Ho, C.-L.; Liao, V. H.-C., Construction and comparison of fluorescence and bioluminescence bacterial biosensors for the detection of bioavailable toluene and related compounds. *Environmental Pollution* **2008,** *152* (1), 123-129.

31. Virolainen, N. E.; Pikkemaat, M. l. G.; Elferink, J. A.; Karp, M. T., Rapid detection of tetracyclines and their 4-epimer derivatives from poultry meat with bioluminescent biosensor bacteria. *Journal of Agricultural and Food Chemistry* **2008,** *56* (23), 11065-11070.

32. Rasmussen, L. D.; Turner, R. R.; Barkay, T., Cell-density-dependent sensitivity of a mer-lux bioassay. *Applied and Environmental Microbiology* **1997,** *63* (8), 3291-3293.

33. Roda, A.; Guardigli, M.; Pasini, P.; Mirasoli, M.; Michelini, E.; Musiani, M., Bio-and chemiluminescence imaging in analytical chemistry. *Analytica Chimica Acta* **2005,** *541* (1), 25-35.

34. Tom-Petersen, A.; Hosbond, C.; Nybroe, O., Identification of copper-induced genes in Pseudomonas fluorescens and use of a reporter strain to monitor bioavailable copper in soil. *FEMS Microbiology Ecology* **2001,** *38* (1), 59-67.

35. Schreiter, P. P.-Y.; Gillor, O.; Post, A.; Belkin, S.; Schmid, R. D.; Bachmann, T. T., Monitoring of phosphorus bioavailability in water by an immobilized luminescent cyanobacterial reporter strain. *Biosensors and Bioelectronics* **2001,** *16* (9), 811-818.

36. Watt, K.; Christofi, N.; Young, R., The detection of antibacterial actions of whole herb tinctures using luminescent Escherichia coli. *Phytotherapy Research* **2007,** *21* (12), 1193-1199.

37. Niazi, J. H.; Kim, B. C.; Ahn, J.-M.; Gu, M. B., A novel bioluminescent bacterial biosensor using the highly specific oxidative stress-inducible pgi gene. *Biosensors and Bioelectronics* **2008,** *24* (4), 670-675.

38. del Busto-Ramos, M.; Budzik, M.; Corvalan, C.; Morgan, M.; Turco, R.; Nivens, D.; Applegate, B., Development of an online biosensor for in situ monitoring of chlorine dioxide gas disinfection efficacy. *Applied Microbiology and Biotechnology* **2008,** *78* (4), 573-580.

39. Stolper, P.; Fabel, S.; Weller, M. G.; Knopp, D.; Niessner, R., Whole-cell luminescence-based flow-through biodetector for toxicity testing. *Analytical and Bioanalytical Chemistry* **2008,** *390* (4), 1181-1187.

40. Paton, G. I.; Reid, B. J.; Semple, K. T., Application of a luminescence-based biosensor for assessing naphthalene biodegradation in soils from a manufactured gas

plant. *Environmental Pollution* **2009,** *157* (5), 1643-1648.

41. Shapiro, E.; Baneyx, F., Stress-activated bioluminescent *Escherichia coli* sensors for antimicrobial agents detection. *Journal of Biotechnology* **2007,** *132* (4), 487-493.

42. Thouand, G.; Horry, H.; Durand, M.; Picart, P.; Bendriaa, L.; Daniel, P.; DuBow, M., Development of a biosensor for on-line detection of tributyltin with a recombinant bioluminescent Escherichia coli strain. *Applied Microbiology and Biotechnology* **2003,** *62* (2-3), 218-225.

43. Tauber, M.; Rosen, R.; Belkin, S., Whole-cell biodetection of halogenated organic acids. *Talanta* **2001,** *55* (5), 959-964.

44. Bechor, O.; Smulski, D. R.; Van Dyk, T. K.; LaRossa, R. A.; Belkin, S., Recombinant microorganisms as environmental biosensors: pollutants detection by *Escherichia coli* bearing *fabA′ :: lux* fusions. *Journal of Biotechnology* **2002,** *94* (1), 125-132.

45. Rosen, R.; Davidov, Y.; LaRossa, R. A.; Belkin, S., Microbial sensors of ultraviolet radiation based on recA’:: lux fusions. *Applied Biochemistry and Biotechnology* **2000,** *89* (2-3), 151-160.

46. Van Dyk, T. K.; Majarian, W. R.; Konstantinov, K. B.; Young, R. M.; Dhurjati, P. S.; Larossa, R. A., Rapid and sensitive pollutant detection by induction of heat shock gene-bioluminescence gene fusions. *Applied and Evironmental Microbiology* **1994,** *60* (5), 1414-1420.

47. Vollmer, A. C.; Belkin, S.; Smulski, D. R.; Van Dyk, T. K.; LaRossa, R. A., Detection of DNA damage by use of Escherichia coli carrying *recA':: lux, uvrA':: lux*, or *alkA':: lux* reporter plasmids. *Applied and Environmental Microbiology* **1997,** *63* (7), 2566-2571.

48. Woutersen, M.; Belkin, S.; Brouwer, B.; van Wezel, A. P.; Heringa, M. B., Are luminescent bacteria suitable for online detection and monitoring of toxic compounds in drinking water and its sources? *Analytical and Bioanalytical Chemistry* **2011,** *400* (4), 915-929.

49. Willets, K. A.; Van Duyne, R. P., Localized surface plasmon resonance spectroscopy and sensing. *Annu. Rev. Phys. Chem.* **2007,** *58*, 267-297.

50. Chen, C.-F.; Tzeng, S.-D.; Chen, H.-Y.; Lin, K.-J.; Gwo, S., Tunable plasmonic response from alkanethiolate-stabilized gold nanoparticle superlattices: Evidence of near-field coupling. *Journal of the American Chemical Society* **2008,** *130* (3), 824-826.

51. Zhao, L.; Kelly, K. L.; Schatz, G. C., The extinction spectra of silver nanoparticle arrays: influence of array structure on plasmon resonance wavelength and width. *The Journal of Physical Chemistry B* **2003,** *107* (30), 7343-7350.

52. Chan, G. H.; Zhao, J.; Schatz, G. C.; Duyne, R. P. V., Localized surface plasmon resonance spectroscopy of triangular aluminum nanoparticles. *The Journal of*

Physical Chemistry C **2008,** *112* (36), 13958-13963.

53. Homola, J.; Yee, S. S.; Gauglitz, G., Surface plasmon resonance sensors: review. *Sensors and Actuators B: Chemical* **1999,** *54* (1), 3-15.

54. Hutter, E.; Fendler, J. H., Exploitation of localized surface plasmon resonance. *Advanced Materials* **2004,** *16* (19), 1685-1706.

55. Live, L. S.; Murray-Méthot, M.-P.; Masson, J.-F., Localized and Propagating Surface Plasmons in Gold Particles of Near-Micron Size. *The Journal of Physical Chemistry C* **2008,** *113* (1), 40-44.

56. Yu, F.; Ahl, S.; Caminade, A.-M.; Majoral, J.-P.; Knoll, W.; Erlebacher, J., Simultaneous excitation of propagating and localized surface plasmon resonance in nanoporous gold membranes. *Analytical Chemistry* **2006,** *78* (20), 7346-7350.

57. Grand, J.; Adam, P.-M.; Grimault, A.-S.; Vial, A.; de la Chapelle, M. L.; Bijeon, J.-L.; Kostcheev, S.; Royer, P., Optical extinction spectroscopy of oblate, prolate and ellipsoid shaped gold nanoparticles: experiments and theory. *Plasmonics* **2006,** *1* (2-4), 135-140.

58. Sobhan, M. A.; Withford, M. J.; Goldys, E. M., Enhanced stability of gold colloids produced by femtosecond laser synthesis in aqueous solution of CTAB. *Langmuir* **2009,** *26* (5), 3156-3159.

59. Turkevich, J.; Stevenson, P. C.; Hillier, J., A study of the nucleation and growth processes in the synthesis of colloidal gold. *Discussions of the Faraday Society* **1951,** *11,* 55-75.

60. Brust, M.; Walker, M.; Bethell, D.; Schiffrin, D. J.; Whyman, R., Synthesis of thiol-derivatised gold nanoparticles in a two-phase liquid-liquid system. *J. Chem. Soc., Chem. Commun.* **1994,** (7), 801-802.

61. Xie, J.; Zheng, Y.; Ying, J. Y., Protein-directed synthesis of highly fluorescent gold nanoclusters. *Journal of the American Chemical Society* **2009,** *131* (3), 888-889.

62. Morton, S. M.; Silverstein, D. W.; Jensen, L., Theoretical studies of plasmonics using electronic structure methods. *Chemical Reviews* **2011,** *111* (6), 3962-3994.

63. Yang, W.-H.; Schatz, G. C.; Van Duyne, R. P., Discrete dipole approximation for calculating extinction and Raman intensities for small particles with arbitrary shapes. *Journal of Chemical Physics* **1995,** *103* (3), 869-875.

64. Bian, R. X.; Dunn, R. C.; Xie, X. S.; Leung, P., Single molecule emission characteristics in near-field microscopy. *Physical Review Letters* **1995,** *75* (26), 4772.

65. Barth, M.; Schietinger, S.; Fischer, S.; Becker, J.; Nusse, N.; Aichele, T.; Lochel, B.; Sonnichsen, C.; Benson, O., Nanoassembled plasmonic-photonic hybrid cavity for tailored light-matter coupling. *Nano Letters* **2010,** *10* (3), 891-895.

66. Ozbay, E., Plasmonics: merging photonics and electronics at nanoscale dimensions. *Science* **2006,** *311* (5758), 189-193.

67. Han, X. X.; Zhao, B.; Ozaki, Y., Surface-enhanced Raman scattering for

protein detection. *Analytical and Bioanalytical Chemistry* **2009,** *394* (7), 1719-1727.

68. Anker, J. N.; Hall, W. P.; Lyandres, O.; Shah, N. C.; Zhao, J.; Van Duyne, R. P., Biosensing with plasmonic nanosensors. *Nature Materials* **2008,** *7* (6), 442-453.

69. Sagle, L. B.; Ruvuna, L. K.; Ruemmele, J. A.; Van Duyne, R. P., Advances in localized surface plasmon resonance spectroscopy biosensing. *Nanomedicine* **2011,** *6* (8), 1447-1462.

70. Ma, Y.; Liang, X.; Tong, S.; Bao, G.; Ren, Q.; Dai, Z., Gold nanoshell nanomicelles for potential magnetic resonance imaging, light-triggered drug release, and photothermal therapy. *Advanced Functional Materials* **2012**, *23* (7), 815-822.

71. Atwater, H. A.; Polman, A., Plasmonics for improved photovoltaic devices. *Nature Materials* **2010,** *9* (3), 205-213.

72. Warren, S. C.; Thimsen, E., Plasmonic solar water splitting. *Energy & Environmental Science* **2012,** *5* (1), 5133-5146.

73. Kelly, K. L.; Coronado, E.; Zhao, L. L.; Schatz, G. C., The optical properties of metal nanoparticles: the influence of size, shape, and dielectric environment. *The Journal of Physical Chemistry B* **2003,** *107* (3), 668-677.

74. Sepúlveda, B.; Angelomé, P. C.; Lechuga, L. M.; Liz-Marzán, L. M., LSPR-based nanobiosensors. *Nano Today* **2009,** *4* (3), 244-251.

75. Haes, A. J.; Stuart, D. A.; Nie, S.; Van Duyne, R. P., Using solution-phase nanoparticles, surface-confined nanoparticle arrays and single nanoparticles as biological sensing platforms. *Journal of Fluorescence* **2004,** *14* (4), 355-367.

76. Freestone, I.; Meeks, N.; Sax, M.; Higgitt, C., The Lycurgus cup—a roman nanotechnology. *Gold Bulletin* **2007,** *40* (4), 270-277.

77. Faraday, M., The Bakerian lecture: experimental relations of gold (and other metals) to light. *Philosophical Transactions of the Royal Society of London* **1857,** *147*, 145-181.

78. Mie, G. B., Contributions to the optics of diffuse media, especially colloidal metal. *Annals of Physics* **1908**, *25*, 377-445.

79. Farias, T.; Köylü, Ü.; Carvalho, M., Range of validity of the Rayleigh-Debye-Gans theory for optics of fractal aggregates. *Applied Optics* **1996,** *35* (33), 6560-6567.

80. Gray, S. K., Theory and Modeling of Plasmonic Structures. *The Journal of Physical Chemistry C* **2012,** *117* (5), 1983-1994.

81. Halas, N. J.; Lal, S.; Chang, W.-S.; Link, S.; Nordlander, P., Plasmons in strongly coupled metallic nanostructures. *Chemical Reviews* **2011,** *111* (6), 3913-3961.

82. McMahon, J. M.; Li, S.; Ausman, L. K.; Schatz, G. C., Modeling the effect of small gaps in surface-enhanced Raman spectroscopy. *The Journal of Physical Chemistry C* **2011,** *116* (2), 1627-1637.

83. Mirkin, C. A.; Letsinger, R. L.; Mucic, R. C.; Storhoff, J. J., A DNA-based method for rationally assembling nanoparticles into macroscopic materials. *Nature*

1996, *382* (6592), 607-609.

84. Alivisatos, A. P.; Johnsson, K. P.; Peng, X.; Wilson, T. E.; Loweth, C. J.; Bruchez, M. P.; Schultz, P. G., Organization of'nanocrystal molecules' using DNA. *Nature* **1996,** *382* (6592), 609-611.

85. Bidault, S.; García de Abajo, F. J.; Polman, A., Plasmon-based nanolenses assembled on a well-defined DNA template. *Journal of the American Chemical Society* **2008,** *130* (9), 2750-2751.

86. Mastroianni, A. J.; Claridge, S. A.; Alivisatos, A. P., Pyramidal and chiral groupings of gold nanocrystals assembled using DNA scaffolds. *Journal of the American Chemical Society* **2009,** *131* (24), 8455-8459.

87. Lo, P. K.; Altvater, F.; Sleiman, H. F., Templated synthesis of DNA nanotubes with controlled, predetermined lengths. *Journal of the American Chemical Society* **2010,** *132* (30), 10212-10214.

88. Storhoff, J. J.; Lazarides, A. A.; Mucic, R. C.; Mirkin, C. A.; Letsinger, R. L.; Schatz, G. C., What controls the optical properties of DNA-linked gold nanoparticle assemblies? *Journal of the American Chemical Society* **2000,** *122* (19), 4640-4650.

89. Kanaras, A. G.; Wang, Z.; Brust, M.; Cosstick, R.; Bates, A. D., Enzymatic disassembly of DNA-gold nanostructures. *Small* **2007,** *3* (4), 590-594.

90. Huo, F.; Lytton-Jean, A. K.; Mirkin, C. A., Asymmetric functionalization of nanoparticles based on thermally addressable DNA interconnects. *Advanced Materials* **2006,** *18* (17), 2304-2306.

91. Kim, J.-Y.; Lee, J.-S., Synthesis and thermally reversible assembly of dna-gold nanoparticle cluster conjugates. *Nano Letters* **2009,** *9* (12), 4564-4569.

92. Xiong, H.; van der Lelie, D.; Gang, O., Phase behavior of nanoparticles assembled by DNA linkers. *Physical Review Letters* **2009,** *102* (1), 015504.

93. McMillan, R. A.; Paavola, C. D.; Howard, J.; Chan, S. L.; Zaluzec, N. J.; Trent, J. D., Ordered nanoparticle arrays formed on engineered chaperonin protein templates. *Nature Materials* **2002,** *1* (4), 247-252.

94. Hu, M.; Qian, L.; Briñas, R. P.; Lymar, E. S.; Hainfeld, J. F., Assembly of nanoparticle–protein binding complexes: from monomers to ordered arrays. *Angewandte Chemie* **2007,** *119* (27), 5203-5206.

95. Lamm, M. S.; Sharma, N.; Rajagopal, K.; Beyer, F. L.; Schneider, J. P.; Pochan, D. J., Laterally spaced linear nanoparticle arrays templated by laminated β-sheet fibrils. *Advanced Materials* **2008,** *20* (3), 447-451.

96. Sun, J.; DuFort, C.; Daniel, M.-C.; Murali, A.; Chen, C.; Gopinath, K.; Stein, B.; De, M.; Rotello, V. M.; Holzenburg, A., Core-controlled polymorphism in virus-like particles. *Proceedings of the National Academy of Sciences* **2007,** *104* (4), 1354-1359.

97. Rance, G. A.; Marsh, D. H.; Bourne, S. J.; Reade, T. J.; Khlobystov, A. N., van der Waals interactions between nanotubes and nanoparticles for controlled assembly of

composite nanostructures. *ACS Nano* **2010,** *4* (8), 4920-4928.

98. Correa-Duarte, M. A.; Pérez-Juste, J.; Sanchez-Iglesias, A.; Giersig, M.; Liz-Marzan, L. M., Aligning Au nanorods by using carbon nanotubes as templates. *Angewandte Chemie International Edition* **2005,** *44* (28), 4375-4378.

99. Rasch, M. R.; Rossinyol, E.; Hueso, J. L.; Goodfellow, B. W.; Arbiol, J.; Korgel, B. A., Hydrophobic gold nanoparticle self-assembly with phosphatidylcholine lipid: Membrane-loaded and Janus vesicles. *Nano Letters* **2010,** *10* (9), 3733-3739.

100. Jones, M. R.; Osberg, K. D.; Macfarlane, R. J.; Langille, M. R.; Mirkin, C. A., Templated techniques for the synthesis and assembly of plasmonic nanostructures. *Chemical Reviews* **2011,** *111* (6), 3736-3827.

101. Vieu, C.; Carcenac, F.; Pepin, A.; Chen, Y.; Mejias, M.; Lebib, A.; Manin-Ferlazzo, L.; Couraud, L.; Launois, H., Electron beam lithography: resolution limits and applications. *Applied Surface Science* **2000,** *164* (1), 111-117.

102. Lee, H.-S.; Kim, B.-S.; Kim, H.-M.; Wi, J.-S.; Nam, S.-W.; Jin, K.-B.; Kim, K.-B.; Arai, Y. In *Electron beam projection nanopatterning using crystal lattice images obtained from high resolution transmission electron microscopy*, SPIE OPTO: Integrated Optoelectronic Devices, International Society for Optics and Photonics: 2009; pp 72221B-72221B-7.

103. Homola, J., Present and future of surface plasmon resonance biosensors. *Analytical and Bioanalytical Chemistry* **2003,** *377* (3), 528-539.

104. Zheng, Y. B.; Kiraly, B.; Weiss, P. S.; Huang, T. J., Molecular plasmonics for biology and nanomedicine. *Nanomedicine* **2012,** *7* (5), 751-770.

105. Stewart, M. E.; Anderton, C. R.; Thompson, L. B.; Maria, J.; Gray, S. K.; Rogers, J. A.; Nuzzo, R. G., Nanostructured plasmonic sensors. *Chemical Reviews* **2008,** *108* (2), 494-521.

106. Zhao, J.; Zhang, X.; Yonzon, C. R.; Haes, A. J.; Van Duyne, R. P., Localized surface plasmon resonance biosensors. *Nanomedicine* **2006**, *1* (2), 219-228.

107. Mayer, K. M.; Hafner, J. H., Localized surface plasmon resonance sensors. *Chemical Reviews* **2011,** *111* (6), 3828-3857.

108. Szunerits, S.; Boukherroub, R., Sensing using localised surface plasmon resonance sensors. *Chemical Communications* **2012,** *48* (72), 8999-9010.

109. Haes, A. J.; Chang, L.; Klein, W. L.; Van Duyne, R. P., Detection of a biomarker for Alzheimer's disease from synthetic and clinical samples using a nanoscale optical biosensor. *Journal of the American Chemical Society* **2005,** *127* (7), 2264-2271.

110. Hall, W. P.; Modica, J.; Anker, J.; Lin, Y.; Mrksich, M.; Van Duyne, R. P., A conformation-and ion-sensitive plasmonic biosensor. *Nano Letters* **2011,** *11* (3), 1098-1105.

111. Kneipp, K.; Wang, Y.; Kneipp, H.; Perelman, L. T.; Itzkan, I.; Dasari, R. R.; Feld, M. S., Single molecule detection using surface-enhanced Raman scattering

(SERS). *Physical Review Letters* **1997,** *78* (9), 1667.

112. Kneipp, J.; Kneipp, H.; Kneipp, K., SERS-a single-molecule and nanoscale tool for bioanalytics. *Chemical Society Reviews* **2008,** *37* (5), 1052-1060.

113. McNay, G.; Eustace, D.; Smith, W. E.; Faulds, K.; Graham, D., Surface-enhanced Raman scattering (SERS) and surface-enhanced resonance Raman scattering (SERRS): a review of applications. *Applied Spectroscopy* **2011,** *65* (8), 825-837.

114. Porter, M. D.; Lipert, R. J.; Siperko, L. M.; Wang, G.; Narayanan, R., SERS as a bioassay platform: fundamentals, design, and applications. *Chemical Society Reviews* **2008,** *37* (5), 1001-1011.

115. Campion, A.; Kambhampati, P., Surface-enhanced Raman scattering. *Chem. Soc. Rev.* **1998,** *27* (4), 241-250.

116. Kneipp, K.; Moskovits, M.; Kneipp, H., *Surface-enhanced Raman scattering: physics and applications*. Springer: 2006; Vol. 103.

117. Baia, M.; Astilean, S.; Iliescu, T., *Raman and SERS investigations of pharmaceuticals*. Springer: 2008.

118. Aroca, R., Surface-Enhanced Raman Scattering. *Surface-Enhanced Vibrational Spectroscopy* **2006**, 73-106.

119. Domke, K. F., Surface Enhanced Raman Spectroscopy. Analytical, Biophysical and Life Science Applications. Edited by Sebastian Schlücker. Wiley Online Library: 2011.

120. Cao, C.; Zhang, J.; Wen, X.; Dodson, S. L.; Dao, N. T.; Wong, L. M.; Wang, S.; Li, S.; Phan, A. T.; Xiong, Q., Metamaterials-Based Label-Free Nanosensor for Conformation and Affinity Biosensing. *ACS Nano* **2013,** *7* (9), 7583-7591.

Chapter 2 Bacterial bioluminescent assay for pesticides detection

Due to their high sensitivity and cost effectiveness, the luminescent bacterial biosensors or bioassays have been widely used in diverse fields like biotechnology,[1] environmental monitoring,[2] and ecotoxicology.[3] However, the majority of published works have studied the bacterial bioluminescent in a short period (around 30 min) and the bioluminescent tests have been conducted at room temperature.[4-7] In addition, a large amount of genetically engineered bacterial cells have been constructed and directly used for biochemical detection over the past decades,[8-12] but the essential details concerning the bioluminescent behavior of these bacterial cells are missing. For instance, the typical engineered luminescent *E. coli* bacterial cells exhibit considerable background bioluminescent signals after certain cultivation time even without exposure to any toxicants.[13] Thus the bacterial bioluminescence can be affected by their internal metabolic products which may result in ambiguous positive responses in bioassays.

In this chapter, two novel bioluminescent protocols have been developed for the purpose of increasing the sensitivity of pesticide detection using two genetically engineered bacterial cells (*E. coli* TV1061 and *E. coli* DPD2794). The first protocol is named as “fresh-overnight” two stages test,[14] while the second one is denoted as “incubation-centrifugation-washing” three steps test.[15] The primary idea behind these two protocols is the modulation of bacterial physiology and/or metabolism in order to decrease the background bioluminescence of bacterial cells, which will lead to the improvement of analytical performance of bioluminescent assay for toxicants detection. Various parameters (bacterial optical density, test temperature, bacterial/toxicant suspension mixing and incubation time, etc.) are optimized in order to achieve sensitive detection of pesticides (atrazine and carbofuran) toxicity.

2.1 Experimental Section

2.1.1 Materials

Kanamycin sulfate (K1377), LB-broth (L3032), atrazine (45530) and carbofuran (32056) were purchased from Sigma (Lyon, France). Deionized water was produced by Millipore Mill-Q water purification system (France) and sterilized prior to preparation of analyte stock solution. Bacteria strains of *E. coli* TV1061 and *E. coli* DPD2794 were provided by Prof. Shimshon Belkin from Hebrew University of Jerusalem in Israel. Bioluminescence measurements were performed within standard 96 wells Costar microtiter-plates (Corning Incorporated, USA).

2.1.2 Medium preparation

Luria Bertani (LB) medium was prepared by adding 2 g LB broth powder into 100 mL double distilled water in a 200 mL glass bottle, followed by sterilization in an autoclave-steam sterilizer (2540 ML-Tuttnauer, Netherlands) for 15 min at 121 °C. Fresh sterilized LB medium was used in preparation of pesticides dilutions.

2.1.3 Instrumentation

For the growth of *E. coli* TV1061 and *E. coli* DPD2794 bacteria strain, a water bath was purchased from Grant Instruments (Type VF, Cambridge Ltd, UK). A DR/ 2500 spectrophotometer (Odyssey, HACH Company, USA) was used for recording the bacteria optical density (OD) at the optimized wavelength of 600 nm, while the mixing between bacteria cultures and different dilutions of toxicant solutions were performed using a vortex mixer (G560E, Scientific Industries, Inc. USA). The qualification of various pesticide dilutions were conducted by using an Agilent 6460 triple quadrupole liquid chromatography/mass spectrometry (LC/MS) with a high energy dynode detector (CARSO, Lyon, France). Centrifugation and bioluminescent measurements were conducted by using a centrifuge (Universal 320R, Andreas Hettich GmbH, Germany) and a luminometer (Luminoskan Ascent, Thermo Fisher Scientific, USA), respectively. Luminescence values were presented in instrument's relative light units (RLU).

2.1.4 Bacteria growth conditions

The strain *E. coli* TV 1061 (*grpE*::*luxCDABE*) is sensitive to cellular metabolism changes, which is due to fact that the promoter *grpE* is one of about 20 promoters that are activated under conditions that the cells experience protein damage (e.g. upon addition of ethanol or phenol). Followed this activation, the reporter gene is therefore transcribed into necessary components that are responsible for light production.[16] The other strain *E. coli* DPD2794 is constructed by fusing the DNA-damage inducible promoter *recA* and reporter gene (*luxCDABE*), thus this strain is responsive to the genotoxical materials.[17] Cultivation of *E. coli* bacteria TV1061 and *E. coli* DPD2794 strains were performed in 10 mL fresh LB medium supplemented with 10 μL of 50 mg/mL kanamycin aqueous solution. The bacteria cells were grown overnight for 9 hr at 37 °C in a thermostated water bath, followed by vigorous vortexing (2000 rpm) of densely formed suspension of *E. coli* strains cultures. Then, 200 μL of bacterial suspension grown overnight was inoculated in 10 mL fresh LB medium without antibiotics and kept incubated at 37 °C for appropriate time to get desired bacteria optical density (OD).

2.1.5 96 wells microtiter plate preparation

For all the bacterial bioluminescent experiments, the standard 96 wells white plastic microtiter plates were used and the preparation is the same unless specially explained. Generally, 360 μL bacterial suspension with desired optical density (OD) was mixed with 40 μL toxicant dilution of different concentrations in a 1.5 mL eppendorf centrifuge tube, followed by vortex mixing for 1 min. Then the resulted bacterial/toxicant mixtures were subjected to different steps defined by the specific protocols used. Finally, 100 µL bacterial/toxicant suspension (volume ratio of 9:1) was transferred into each well of the microtiter plate, and 100 µL bacterial suspension without any toxicant was used as the control in all the measurement. There are three replicas for each toxicant dilutions and the average RLU value is reported hereafter. The specific bacterial OD value and concentration of toxicant stock solution are dependent on the bacteria cells and protocols used, thus all these details will be presented in the corresponding parts later.

2.2 Results and Discussion

2.2.1 The background bioluminescence of engineered *E. coli* bacteria

The general construction of engineered bacterial cells and the toxicant induced bioluminescence were illustrated in **Figure 2.1**. Firstly, the plasmid of the host bacterial cell is replaced by the genetically recombinant plasmid, where contains the gene sequences called promoter and reporter. Once the promoter genes are activated by the exogenous toxicants, the expression of reporter gene is triggered, leading to the production of luminescent enzyme (luciferase), substrate (luciferin) and cofactors *in vivo*. Finally, the bioluminescence is generated by bacterial cells *via* a cascade of biochemical reaction using the enzyme, substrate and other cofactors.

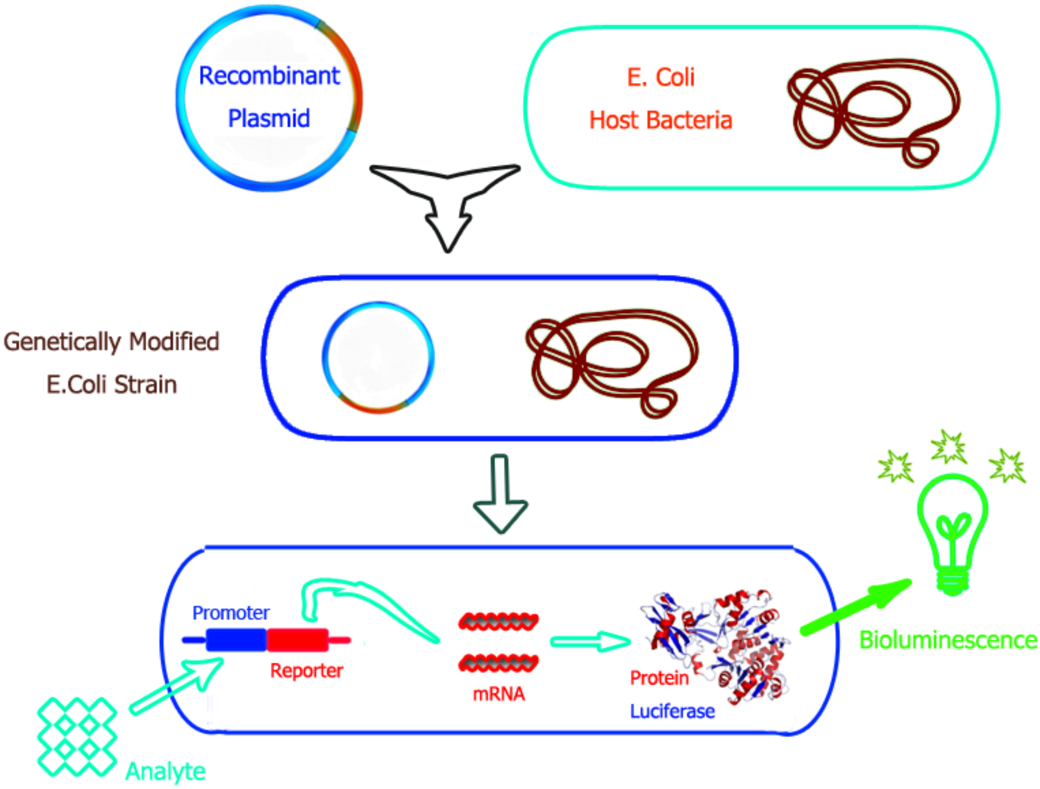

Figure 2.1 Schematic of genetic modification of regular *Escherichia coli* bacteria and specific mechanism of bioluminescence development induced by toxicant.

The principle of bioassay based on engineered luminescent bacteria is the toxicant induced bioluminescence changes. Thus ideally the background bioluminescence from intact bacterial cells should remain stable during the measurement in order to improve the signal-to-noise ratio (SNR) for toxicants detection. However, these engineered bacterial cells can emit lights without the presence of any toxicant and the background bioluminescence is strongly dependent on the bacterial optical density and test temperature.[13] Taking the *E. coli* TV1061 bacteria (protein damage sensitive strain) as an example, the significant background bioluminescent signals were recorded after 4 hr cultivation at room temperature and the bioluminescence is still detectable even after additional 9 hr incubation of bacterial cells at 4 °C. As shown in **Figure 2.2**, the background bioluminescent from *E. coli* TV1061 is highly dependent on the bacterial

OD value. Specially, the bioluminescence of bacterial cells with three different OD values (0.03, 0.08 and 0.12) was tested immediately after cultivation (named "fresh" mode) and after additional overnight incubation of "fresh" tested bacterial cells at 4 °C (named "overnight" mode). For the "fresh" mode (curves in right side, solid symbols), whichever the OD was (0.03, 0.08 or 0.12), two peaks were recorded, a major one followed by a minor one. When the OD was increased from 0.03 to 0.12, a shift of the peaks towards the lowest time from 265 minutes to 210 minutes was observed. The increase of the OD has also lead to an increase of the peak amplitude. For the "overnight" mode (curves in left side, open symbols), a more diffuse peak versus time has been observed at an earlier time (30 min) and the appearance time of the peak was OD independent. However, the intensity of this peak was obviously decreased compared to the one of the major peak obtained for the "fresh" mode. In addition, the increase of the OD has led to a decrease of the peak amplitude in the "overnight" mode.

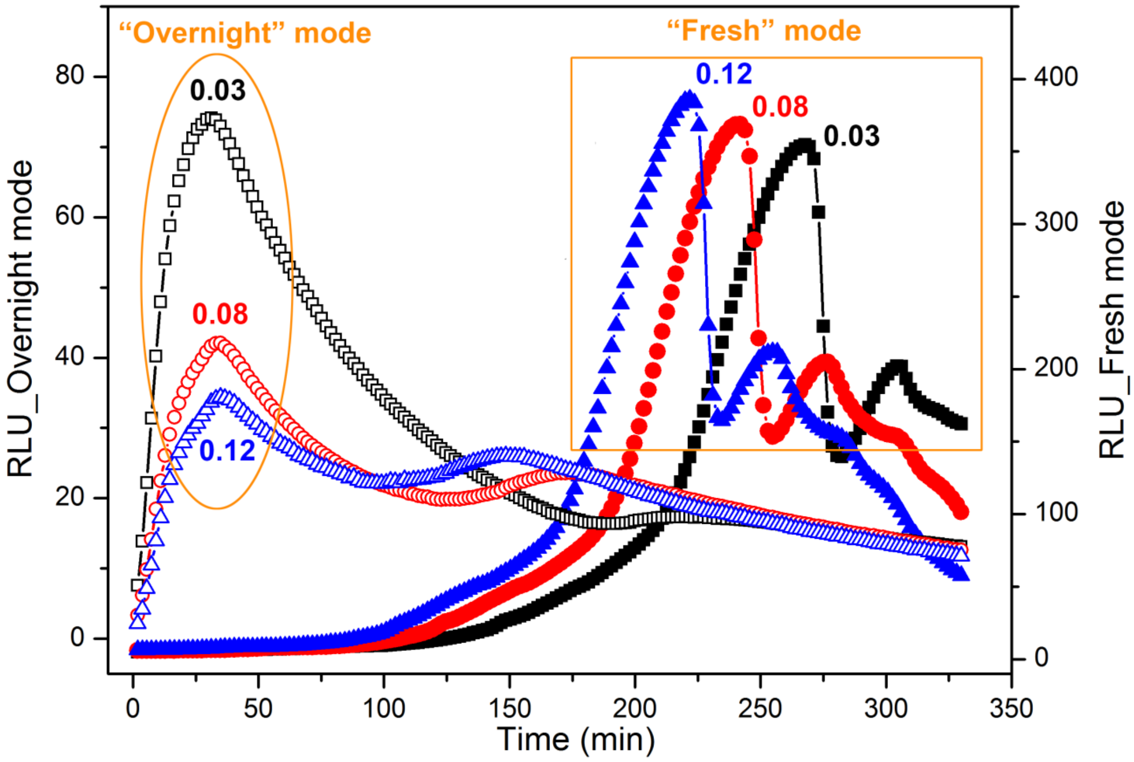

Figure 2.2 The time dependent background bioluminescence of *E. coli* TV1061 bacteria cells without exposure to any toxicants. Two modes were used in the bioluminescent measurement at room temperature: the "fresh" mode represents the immediate test after bacteria cultivation (right side curves, solid symbols), while the "overnight" mode (left side curves, open symbols) refers to test subject to additional 9 hr incubation at 4 °C after the initial "fresh" test. The optical density was measured with spectrometer at 600 nm, which is the optimized wavelength for bacterial cells.

The existence of bioluminescence peaks without the presence of pollutants must have been induced by a yet to be explained normative background metabolism, or a yet to be studied possible inducement from their own metabolic products, that may eventually be released by the bacteria into the medium or some other reason, causing the usually considered difficult to control "background" luminescence. From the above results, it clearly shows that the OD only affects the intensities and appearance time of the peaks, but not the whole shape of the spectra. The shift of the appearance time of the peaks versus OD still remains unclear.

The main difference between the two studied modes concerns the storage of the bacteria at low temperature (4 °C) during one night. The metabolism of bacteria clearly depends on the temperature and for this type of bacteria it is assumed that their metabolism is lowered when the temperature is decreased. Under this assumption, the decrease of the bioluminescent peak intensity versus OD can be explained in the following manner. Firstly, it's worthwhile to notice that prior to the overnight storage at 4 °C, the bacteria were growing during the bioluminescent measurement at 25 °C, constantly producing their own metabolic product. By storage at the lower temperature of 4 °C, the pollutant is able to be collected by the bacterium inside the cell, thus increasing "artificially" the concentration, while not being very active in the luminescence-related metabolism, and then when the bacteria do return to room temperature, the induction turns out to be enhanced. A similar explanation concerning the penetration into the *E. coli* DPD2794 bacteria cells of nonylphenol toxicant was reported as well.[18]

In addition, it should be noted that the bioluminescent peak was more diffuse in the "overnight" mode, and the appearance of the peak occurred very quickly (30 min) after the 4 °C storage and that it was OD independent. As discussed above this phenomenon could be explained by the fact the bacterial cells are continuously growing during the bioluminescence measurements at 25 °C, and therefore, are producing toxic compounds that could inhibit the bioluminescence signals. It is reasonable to assume that the more the bacteria are, the more the toxic compounds will be produced explaining why the RLU is lower for the higher optical density in the second "overnight" test.

Based on the above results, the engineered *E. coli* bacterial cells indeed produce considerable light in the absence of any toxicants and this consecutive self-emitting luminescence becomes more obvious in longer time. In order to use the engineered bacterial cells in bioluminescent assay for pesticides detection, the background bioluminescence from bacterial cells *per se* should be decreased. Therefore, two novel protocols have been created to increase the bioassay sensitivity for pesticides detection.

2.2.2 First protocol: "fresh - overnight" 2 stages test

The first protocol is named as "fresh-overnight" test, it's a 2-stage reading approach (both were required), including a first 5 hr reading of a freshly prepared bacterial suspension in the presence of the water insoluble atrazine toxicant, and a second reading after 9 hr "overnight" 4 °C incubation (see **Figure 2.3**). In both phases, the bioluminescence responses were acquired at 25 °C. The atrazine stock solution was prepared by dissolving 1 mg atrazine into 1 mL DMSO, then tenfold dilution from 0.1 mg/mL to 0.1 pg/mL were prepared by diluting stock solution using fresh LB medium. Since the toxicant solution was diluted another ten times in the 96 well microtiter plate (volume ratio of bacteria/toxicant is 9:1), the real tested atrazine concentration range should be 0.01 mg/mL to 0.01 pg/mL, all concentrations indicated in the later part were referred to the concentrations in the microtiter plate unless specially stated. Moreover, the optical density of bacterial cells has been optimized by using three different OD values of 0.03, 0.08 and 0.12, from which the 0.08 OD is the optimized one for atrazine detection. Initially, the “overnight” measurements were conducted after cold incubation for different times such as 3 hr, 6 hr, 9 hr and 12 hr, respectively. From the obtained results, the 9 hr cold incubation experiment exhibits the best sensitivity for atrazine detection.

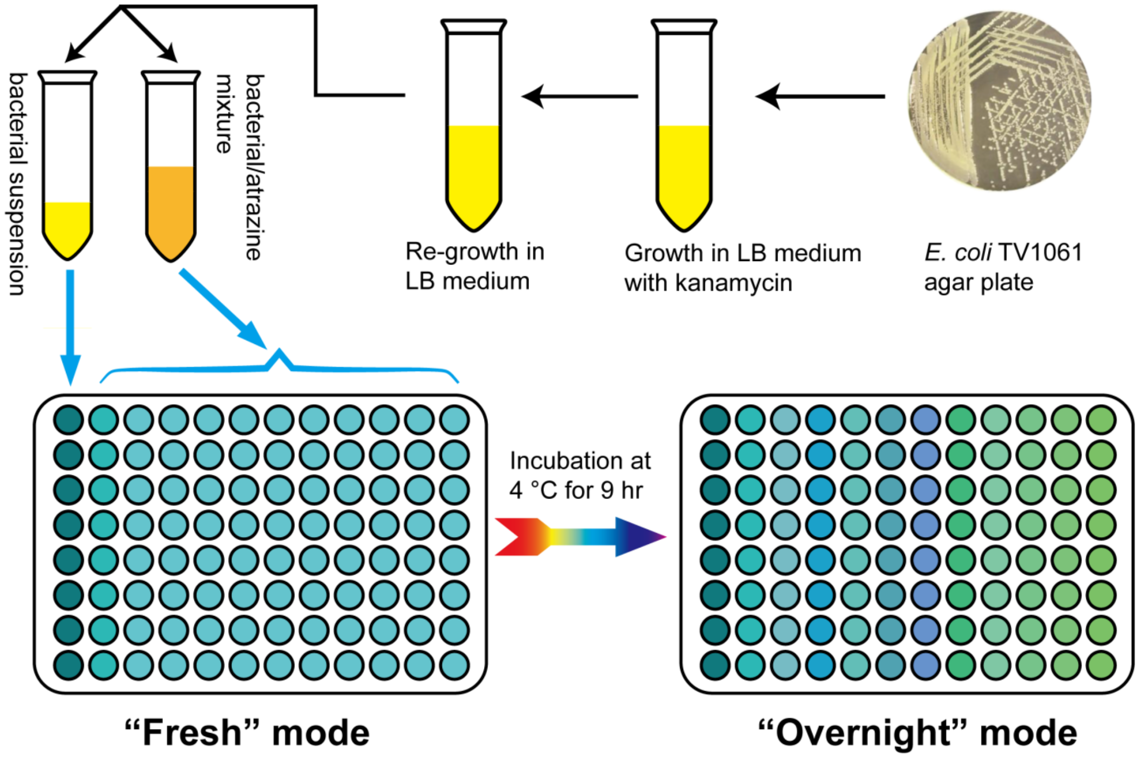

Figure 2.3 The schematic of 2 stage protocol including the “fresh” mode of immediate bioluminescent test of bacterial/toxicant solution and “overnight” mode of second test after incubation of the same microtiter plate at 4 °C for 9 hr. The bacterial cells alone were used as the control and the bioluminescent measurements were conducted at 25 °C.

2.2.2.1 Atrazine bioluminescent induction of E. coli TV1061 bacteria in "fresh" and "overnight" mode

The toxic effect of different atrazine concentrations on *E. coli* TV1061 bacteria was evaluated through the proposed "fresh" and "overnight" consecutive tests for an optical cell density (OD) equal to 0.08, since at this OD the bacteria cells have the best discrimination ability towards different concentrations of atrazine. **Figure 2.4** depicts the variation of the bioluminescence intensity versus time for no atrazine (condition A), lower atrazine concentration ranging from 0.01 pg/mL to 1 µg/mL (condition B) and high atrazine concentration of 10 µg/mL (condition C) under "fresh" conditions.

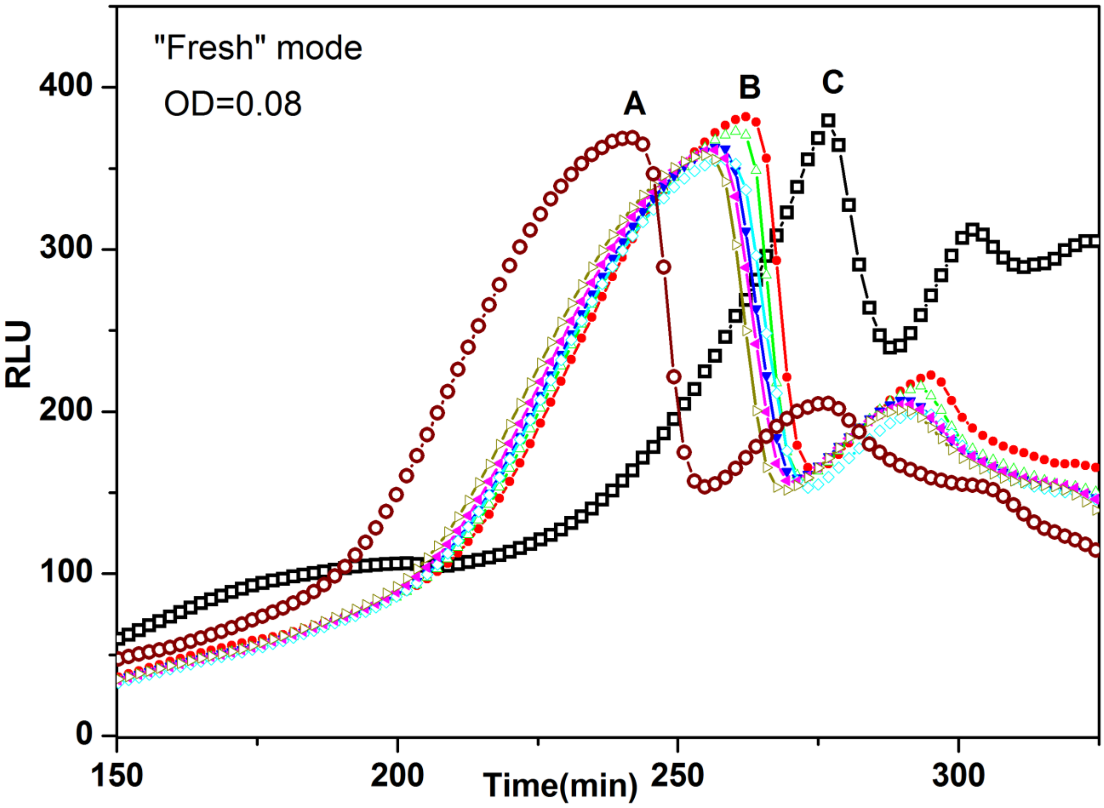

Figure 2.4 Luminescence behaviors of *E. coli* TV1061 bacteria (OD was 0.08) within the presence of different atrazine concentrations in the "fresh" mode. Luminescent measurements were recorded at 25 °C, (A-bacteria without toxicant; B-bacteria/toxicant from 0.01 pg/mL to 1 µg/mL; C- bacteria/toxicant 10 µg/mL).

Bioluminescent curves under conditions A and B exhibit very similar shapes. The first effect of the atrazine toxicant is a shift in the appearance time of the major peaks which may depend on the atrazine content. The second effect is a slight increase of the peak intensity for the two higher contents of the tested range, leading to a strenuous discrimination between atrazine contents using their peak amplitudes. The major peak of the curve under condition C is sharper than the major peaks observed on the other two conditions. The shift of this peak appearance versus time is also more pronounced. Thus, it is only possible to discriminate between the high and low atrazine toxicity at this “fresh” stage.

Figure 2.5 depicts the variation of the bioluminescence signal versus time for bacteria control and bacteria/atrazine suspension for the “overnight” mode. For a better visualization, the inset in **Figure 2.5** presents the bacterial bioluminescence details induced by a lower concentration of atrazine from 0.01 pg/mL to 1 μg/mL and the control. In contrast to the results in “fresh” mode, it is clear that all the bioluminescent curves exhibited a more diffuse peak in the “overnight” mode, which appeared very quickly after the beginning of the measurement process for all the tested atrazine content. The amplitude of the peak regularly increased with the atrazine content from 47 RLU for 0.01 pg/mL to 64 RLU for 1 μg/mL atrazine, except for the highest content (10 μg/mL) for which a strong bioluminescence increase was observed (150 RLU).

In the “overnight” mode, the use of the cold incubation seems to reduce the effect of the bacteria’s own metabolism or more likely may enable the accumulation of the toxicant inside the cell during a slowing of the overall metabolism, and consequently to enhance the capability of the bacteria to sense atrazine when the overnight mode is used. It is also worthwhile to note as the discrimination mode is of the “light on” type (increase of bioluminescence within the presence of the pollutant), the trace concentration of atrazine could be sensed as low as 0.01 pg/mL.

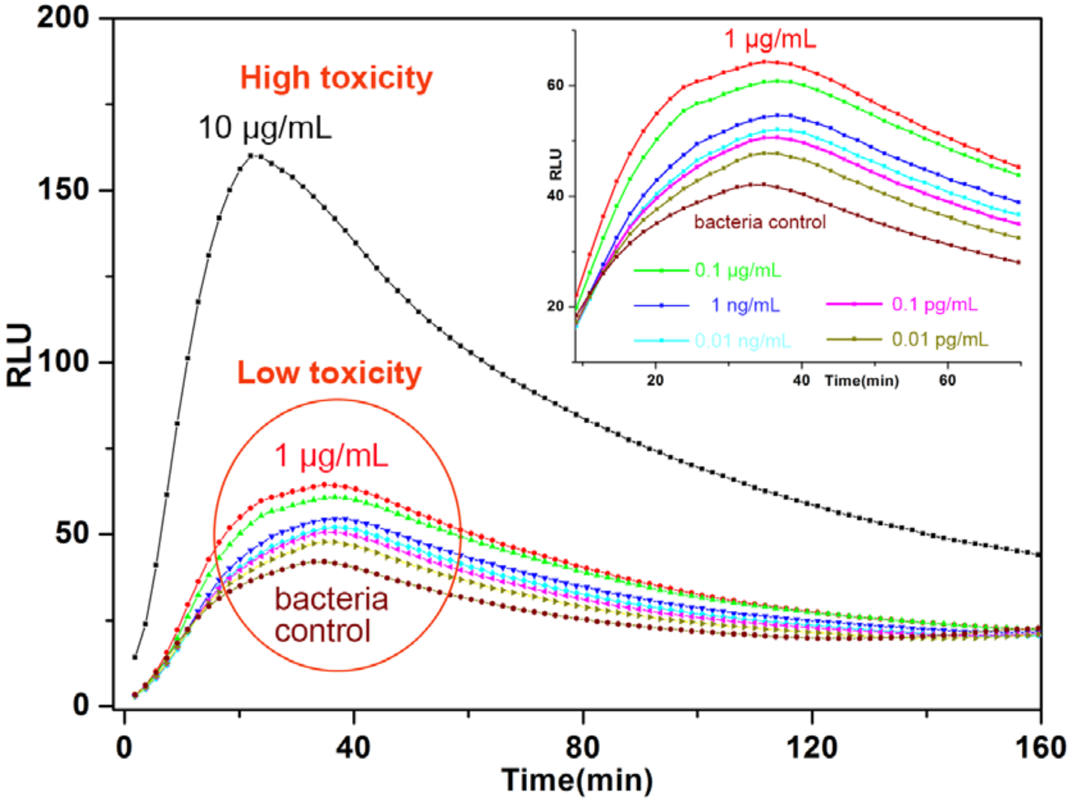

Figure 2.5 Bioluminescence behavior after overnight incubation of *E. coli* TV1061 at 4 °C (optical density: 0.08) with different atrazine concentrations. Shown inset is the luminescent signal of low concentrations of atrazine from 0.01 pg/mL to 1 µg/mL and the bacteria control. Luminescent measurements were recorded at 25 °C.

In addition, it can be noticed that the two modes (fresh and overnight) can also be used for the detection of the pollutant threshold which corresponds to the visible bioluminescent discrimination in the bacterial behavior from low to high toxicity level. Therefore, the strong shift between the “B”- peaks and “C”- peak over time (in the “fresh” mode) or the sudden increase of the bioluminescence intensity between the same peaks (in the “overnight” mode) were respectively observed. This particular bacteria evolution can be considered as a toxicity indicator between a low toxicity effect (for “B” peaks, 1 µg/mL to 0.01 pg/mL) and a high toxicity effect (for “C” 10 µg/mL).

2.2.2.2 Calibration curves for atrazine detection under "overnight" mode

From the recorded bioluminescence signals versus time, the relative area under the curve (AUC) is defined as the integration of experimental RLU values over a fixed range of time, which can be calculated using the build-in algorithm of Origin software. Thus, the bioluminescent results of the "overnight" mode were used to construct calibration curves by plotting the relative area under the curve (corrected from bacterial control) versus different atrazine concentrations for three bacteria optical densities (0.03, 0.08 and 0.12) (**Figure 2.6**). Generally, the curves displayed the same trends such as an increase of the relative areas for lower atrazine concentration, ranging from 0.01 pg/mL to 0.1 µg/mL Moreover, the highest responses to atrazine concentrations are observed for bacteria with an optical density of 0.08, which is corroborated with the results obtained from bioluminescent test.

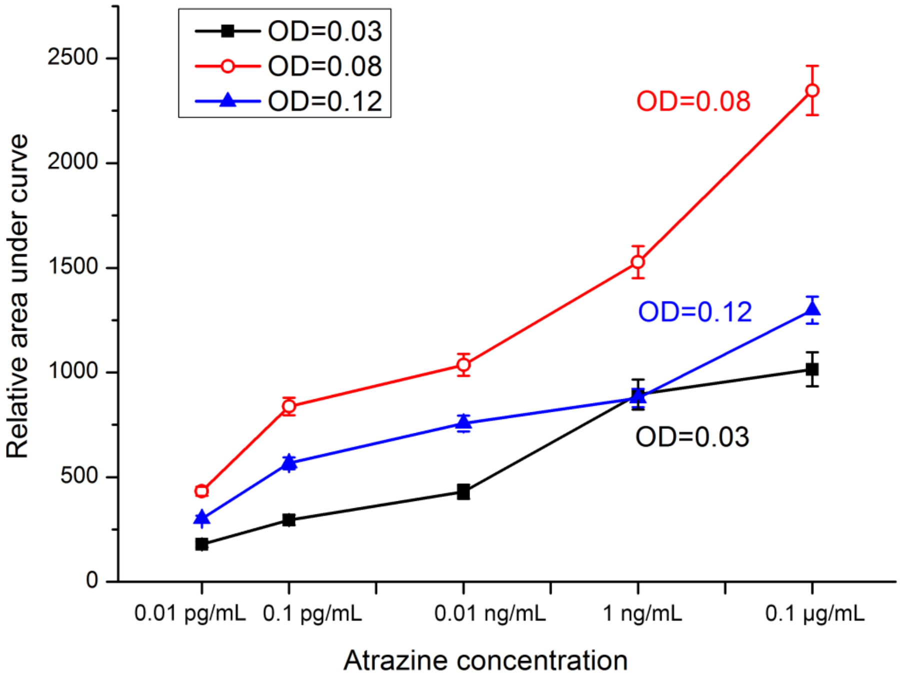

Figure 2.6 Bioluminescent calibration curves for atrazine detection using *E. coli* TV1061 bacteria of 3 optical densities (0.03; 0.08; 0.12) under "overnight" mode. The luminescent measurements were recorded at 25 °C.

Additionally, LC/MS analysis has been conducted to confirm the concentration of various tested atrazine dilutions, these results are summarized in **Table 2.1**, where the atrazine expected concentration (C_{exp}) and real concentration ($C_{LC/MS}$) are compared. The correction factor (the ratio of C_{exp} to $C_{LC/MS}$) was calculated for atrazine concentrations from 100 mg/L to 100 ng/L and was found in the range of 0.7 and 0.8. The low variation of this correction factor validates the used process to accurately prepare various atrazine solutions and the capability of the studied bioreporter to sense the prepared atrazine contents.

Table 2.1 LC/MS measurements for various atrazine prepared contents

Expected values of atrazine content (C_{exp})	HPLC measurements ($C_{LC/MS}$)	Ratio of C_{exp} to $C_{LC/MS}$
100 mg/L	81.1 mg/L	0.811
10 mg/L	7.92 mg/L	0.792
1 mg/L	0.776 mg/L	0.776
10 μg/L	7.79 μg/L	0.779
100 ng/L	71 ng/L	0.71

2.2.2.3 Specificity of pesticides detection

The idea of the first protocol was not to discuss the mechanism of the bacteria bioluminescence but to prove that, for a given toxicant concentration (even traces) the experimental conditions can greatly affect the bacteria behavior. Moreover, the purpose was to find out a protocol which leads to a linear response versus toxicant content. It is known that the heat shock genes/promoters usually respond to a wide array of stimuli and consequently the specificity of this bioreporter could be questionable.[16] As the very preliminary step, additional experiments within the presence of two more pollutants: carbofuran and nonylphenol were performed with the proposed protocol to evaluate the analytical selectivity of bioassay and the results were shown in **Figure 2.7**. It can be seen that in the case of carbofuran and nonylphenol, a more pronounced second peak is observed in comparison with the single peak from atrazine of same concentration (**Figure 2.7**A) in the "overnight" mode, it can be also seen that the bacteria are not very sensible to carbofuran and that the maximum RLU intensity of peak 1 depends on the type of pollutant as shown in **Figure 2.7**B. Even though the number of the tested toxicants is still low (only 3), it seems that the shape of the peaks and the maximum value of the peak intensity in the "overnight" mode can differ from one toxicant to another one. Consequently, comparison between reference spectra measured on various toxicant and experimental spectra could help to discriminate among various toxicants.

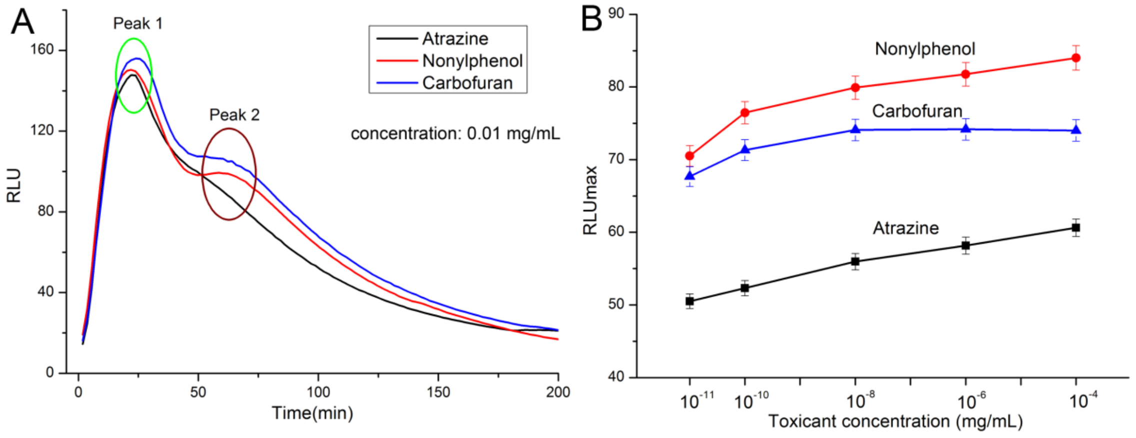

Figure 2.7 Bioluminescence curves of *E. coli* TV1061 versus three different pollutants (atrazine, nonylphenol and carbofuran) with same concentration of 0.01 mg/mL (A) and the maximum bioluminescent intensity RLU_{max} from peak 1 in function of the toxicant concentration ranging from 10^{-11} mg/mL to 10^{-4} mg/mL (B) after overnight "cold" incubation.

In conclusion, an improved protocol has been developed for the identification of the toxic effect of water insoluble pesticide atrazine using bioluminescent reporter bacteria through an overnight cold incubation at 4 °C. Bacteria can be affected in the "fresh" mode by 10 µg/mL atrazine in about 180-300 min at 25 °C in the first luminescence measurement, while for the visualizations of lower atrazine concentrations effects, bacteria do require additional overnight (9 hr) cold incubation at 4 °C prior to their second luminescence reading at 25 °C. These results demonstrate an alternative experimental methodology which enables a greater sensitivity identification of atrazine toxic effects down to 0.01 pg/mL.

2.2.3 Second protocol: “incubation-centrifuge-washing” 3 steps test

As mentioned above, the background bioluminescence from intact bacterial cells should be effectively decreased to improve the bioassay sensitivity. Besides of the first protocol using cold incubation, a second protocol contains three major steps of “incubation-centrifuge-washing” has been developed to decrease the bacterial background bioluminescent signals as well. In this protocol, the DNA damage sensitive bacteria strain of *E. coli* DPD2794 was used as the bioreporter cell and carbofuran pesticide was used as the model toxicant. The toxicant stock solution (0.05 mg/mL) was prepared by dissolving 1 mg carbofuran into 20 mL ddH$_2$O, and then various aliquots of 10^{-1}, 10^{-2}, 10^{-4}, 10^{-6} and 10^{-8} were prepared by diluting stock solutions with fresh LB medium. The validation of carbofuran dilution process down to 10^{-6} corresponded to an experimental concentration of 0.05 ng/mL was conducted using liquid chromatography/mass spectrometry (LC/MS) technique for three times.

For the bioluminescent measurements, 100 μL mixtures of bacterial suspension and toxicant dilution (volume ration of 9:1) were distributed into the 96-well white microtiter plate, while 100 μL of bacterial suspension was used as the control. All the bioluminescent measurements were conducted at 30 °C for 400 min. The novel bioluminescent protocol that enabled higher bioluminescence production contained three main steps.

Step I: *Incubation of bacterial suspension and toxicant dilutions*. Bacterial suspensions were incubated with various concentrations of toxicants at room temperature for different periods of time (2, 4, 6, 9, and 12 hr, respectively). The control experiment was conducted follow the same procedure but without using the incubation step (control 2 in **Figure 2.8**).

Step II: *Centrifugation and washing with fresh LB.* After the aforementioned incubation periods at room temperature, the bacterial/toxicant mixtures were centrifuged at 3000 rpm (856 g) for 15 min, where the resulting supernatant was discarded and replaced with fresh LB medium. The washing step was repeated twice. The control experiments were conducted by using “non-washed” bacterial cells under the same experimental conditions (control 1 in **Figure 2.8**).

Step III: *Bioluminescence measurement at 30 °C.* The bacterial/toxicant mixtures (volume ratio of 9:1) were distributed into the 96-well microtiter plates. Bioluminescence measurements were conducted at a favorable physiological higher temperature of 30 °C, so as to gain a faster bioluminescent response. In each bioluminescence measurement, the resulting signals obtained from the bioreporter cell that were not exposed to the toxicant (called not induced samples), were recorded as the third control in each measurement.

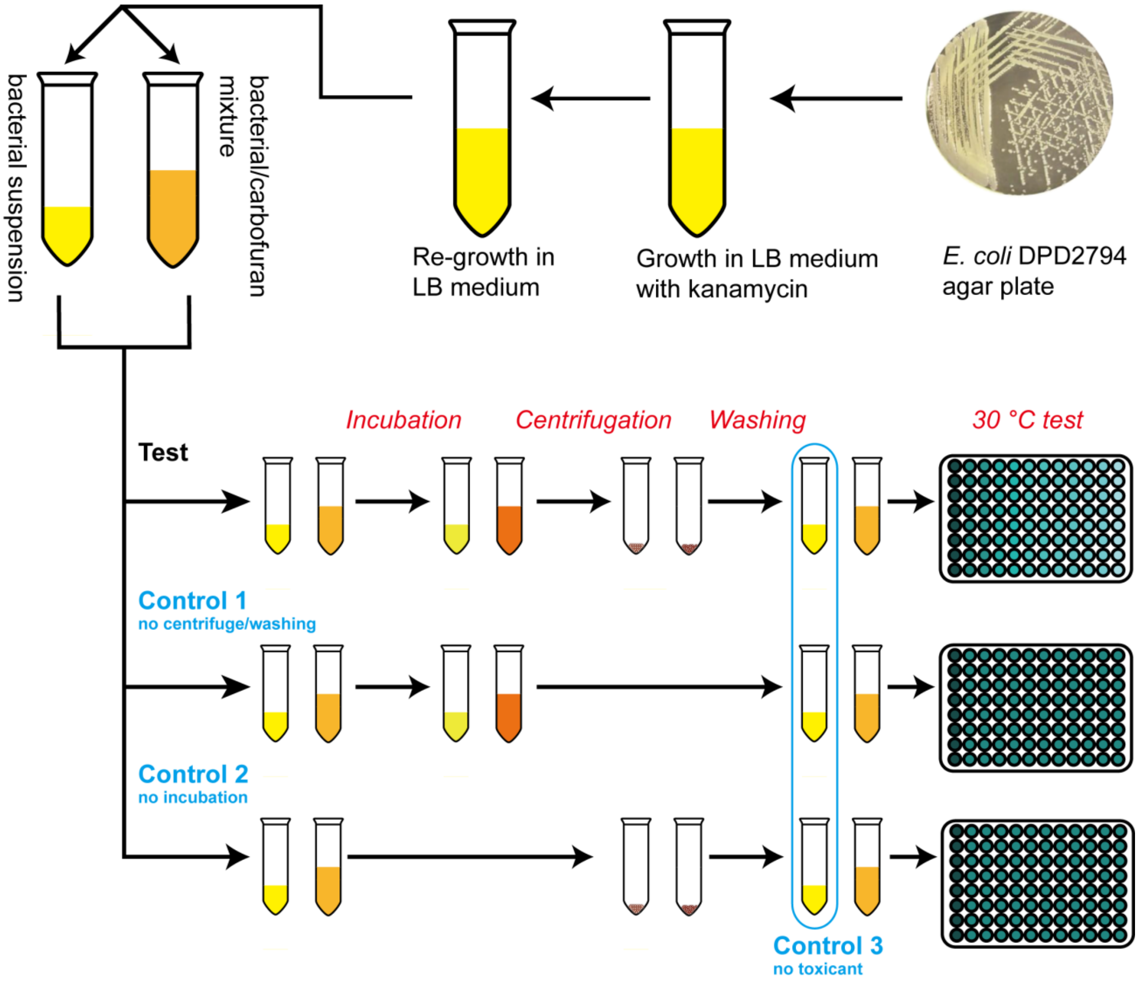

Figure 2.8 The second bioluminescence enhancement protocol contains three major steps: the incubation of bacterial suspension with carbofuran toxicant solution at room temperature for different periods of time; followed by centrifugation of the resulted bacterial/toxicant suspension and the replacement of aged supernatant with a fresh LB medium without any toxicants, finally the bacterial bioluminescence was recorded at 30 °C. There are three independent control experiments: the first control represents the same procedure except of centrifugation/washing step, while the same experiment without incubation step is considered as the second control, the third control denotes the bioluminescence from bacterial cells alone without exposure to any toxicants.

2.2.3.1 Temperature dependence of E. coli DPD2794 bioluminescence

In most of published work, the engineered *E. coli* bacterial bioluminescence is exclusively recorded at room temperature,[4-6] however we have found that the toxicant-induced bioluminescence of *E. coli* DPD2794 bacteria is highly dependent on test temperature. As an example, the *E. coli* DPD2794 bacterial cells were simply mixed with different concentration of carbofuran dilutions and the resulted bioluminescence was recorded at two different temperatures (room temperature and 30 °C). Interestingly, *E. coli* DPD2794 bacteria respond to the toxicant effect much faster at 30 °C, as major peaks appeared around 250 min as shown in **Figure 2.9**B, however the dominant bioluminescent peaks with similar intensities were detected after 350 min (**Figure 2.9**A) at 26 °C, therefore we have tested all the *E. coli* DPD2794 bacterial bioluminescence at the optimized temperature of 30 °C hereafter.

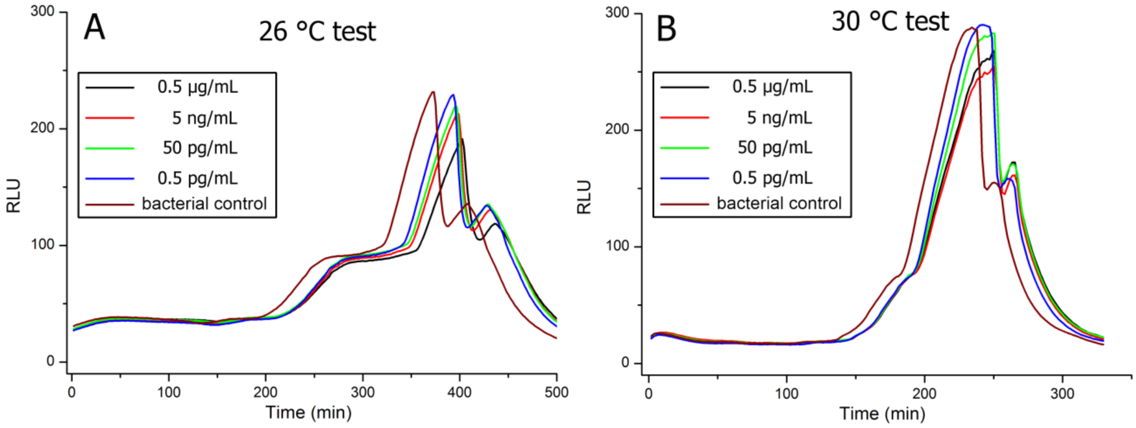

Figure 2.9 Bioluminescence signals of *E. coli* DPD2794 strain in the presence of different concentration of carbofuran recorded at different temperatures such as 26 °C (A) and 30 °C (B), respectively.

2.2.3.2 Indispensability of "centrifugation/washing" step

Although a higher test temperature does contribute to faster bacterial bioluminescent responses to targeted toxicant, the bioluminescence from bacterial control is still larger than that of toxicant/bacterial mixture ("light off" mode). Thus the signal-noise-ratio is deteriorated by this light off detection, which is the main reason for developing a more sensitive "light on" protocol. Actually, the incubation of bacterial cells with toxicant and the subsequent washing of these bacterial cells are extremely important steps in the reported new protocol. As an example to demonstrate the improvement, the bacterial bioluminescent spectra in the presence of carbofuran following the aforementioned protocol are shown in **Figure 2.10**. Moreover, results of the control experiments without washing steps are also presented with an exampled toxicant incubation time of 4 hr.

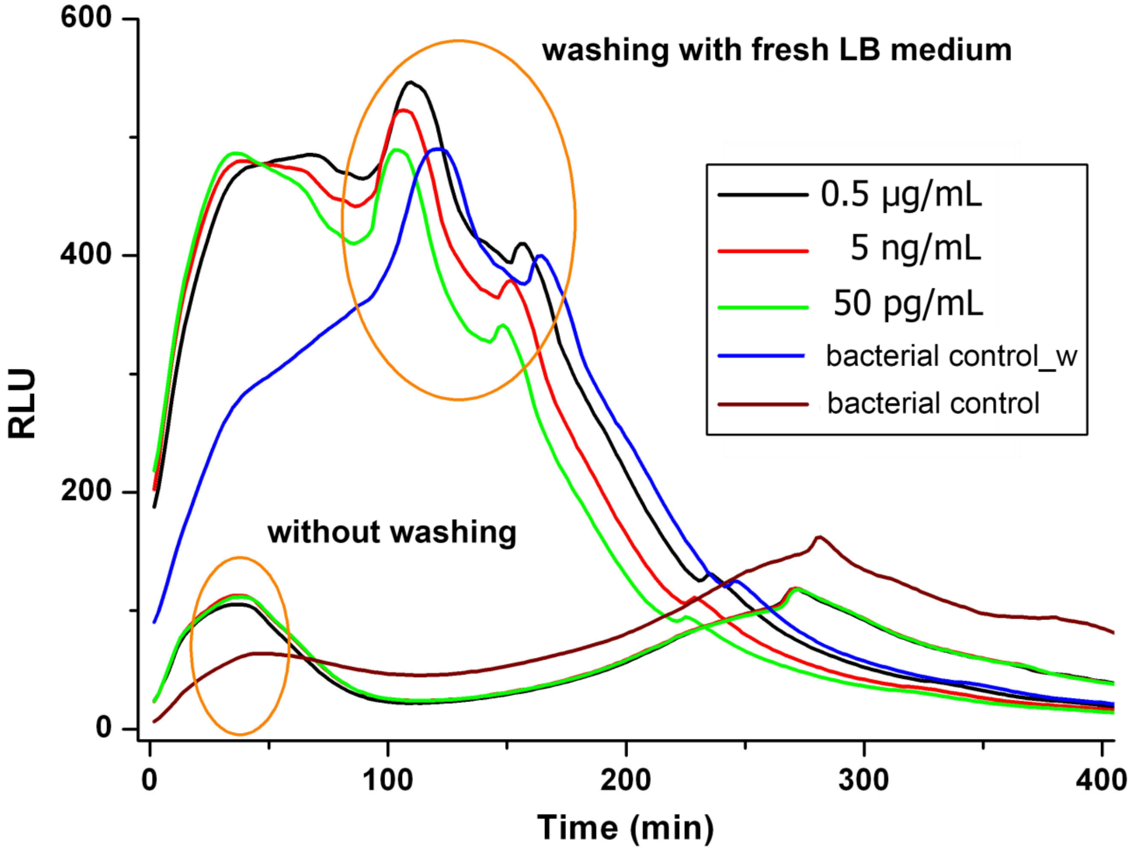

Figure 2.10 Bioluminescence of *E. coli* DPD2794 bacteria exposed to various concentration of carbofuran (0.5 μg/mL, 5 ng/mL, 50 pg/mL) with incubation at room temperature for 4 hr. The concentration of carbofuran stock solution was 0.05 mg/mL. Bioluminescence was recorded at 30 °C from washing (w) (top curves) and non-washing (bottom curves) experiments. The *E. coli* DPD2794 bacterial cells alone were used as the control in both cases.

Generally, the bioluminescence intensity was obviously enhanced due to the washing steps. Specifically, in the control experiments without any washing steps (bottom group of curves), two peaks with intensity around 100 RLU appeared at around 30 min and 270 min during the measurement, respectively. Although the bacterial bioluminescence in the presence of toxicant is totally different to that in the case of the bacterial control (higher RLU intensity for the first peak and lower RLU intensity for the second one), the bioluminescence curves corresponding to three different carbofuran contents are overlapped. At this stage, it is difficult to distinguish the bacterial cell responses for different toxicant concentrations.

When the bioluminescence was measured after the washing steps, two different luminescent peaks were observed in the case of the bacterial control (blue curve labeled with "control_w" in **Figure 2.10**). The two peaks were located closer with each other at around 120 min and 165 min of measurement with increases of RLU intensities to 490 RLU and 400 RLU, respectively. Interestingly, one additional luminescent peak was recorded for the bacteria exposed to carbofuran at the beginning (35 min) of the measurement using the washing procedure. The overall RLU intensity in the presence of carbofuran was generally larger than that of the bacterial control, and the different carbofuran contents can also be distinguished in terms of their different maximum RLU intensity.

It is assumed that without any washing steps, the bacterial metabolites and the presence of excess carbofuran toxicant may affect the overall bioluminescence signals by providing additional non-discriminatory stress to the whole bioreporter cell activities, thus leading to a complicated bioluminescence evolution and impossibility to discriminate between various carbofuran contents. Thus the "centrifugation-washing" step is indispensable as the potential background interference can be greatly reduced.

2.2.3.3 Optimization of bacterial/toxicant suspension incubation time

In order to optimize the incubation time, the background bioluminescence from bacterial cells have been tested after different periods of room temperature incubation and the results were shown in **Figure 2.11**. It was found that the bioluminescence of bacteria without any incubation, exhibited the highest RLU intensity, while the overall luminescent intensity was decreased for the bacterial cells involved in the incubation procedure. Moreover, the longer the incubation time, the lower the luminescence intensities were recorded. Based on these results, the incubation step indeed decreases the background bioluminescent signal from bacterial control, however the same experiments using carbofuran toxicant stressed bacterial cells should be conducted as well to finally optimize the incubation time.

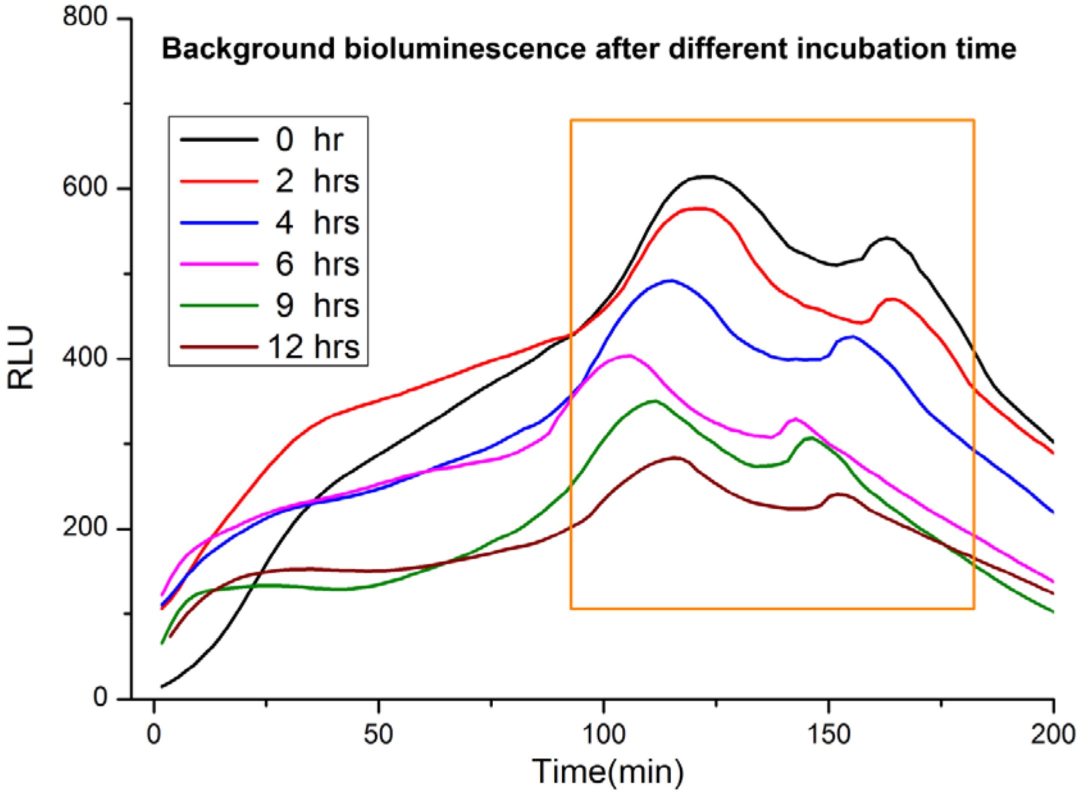

Figure 2.11 Background bioluminescence of *E. coli* DPD2794 bacteria cells without any incubation (0 hr) and after different incubation times (2-12 hr) prior to bioluminescent measurements at 30 °C.

In order to obtain the optimum incubation time to discriminate various concentrations of carbofuran, independent experiments with different incubation time of 0 hr (i.e. no incubation), 2hr, 4 hr, 6 hr, 9 hr and 12 hr at room temperature were conducted. From the results, the overall bioluminescence evolutions (curve shapes), were similar for various incubation times; however the recorded maximum luminescent intensity was dependent on incubation time. In order to highlight these differences, the relative maximum bioluminescence signal, defined as the peak difference (RLU_{max} - $RLU_{control}$) between toxicant induced luminescence RLU_{max} and control luminescent $RLU_{control}$, was calculated for different incubation time. It should be mentioned that only three carbofuran dilutions were shown in **Figure 2.12** for a better visualization.

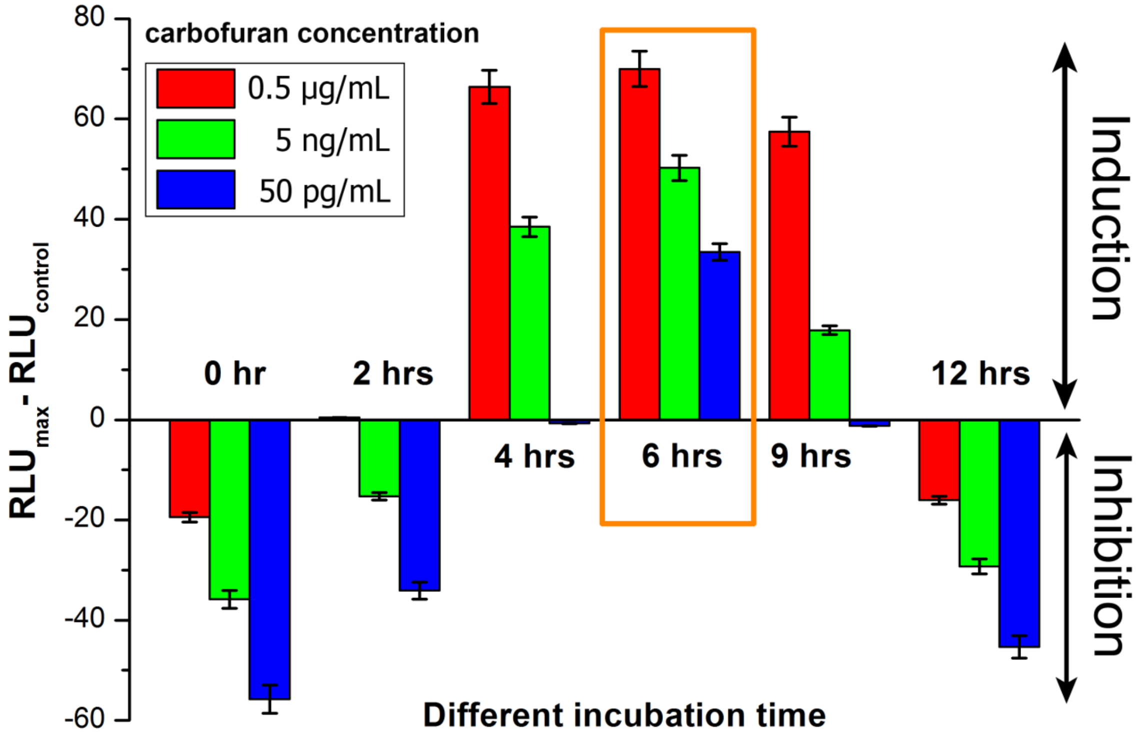

Figure 2.12 The relative maximum bacterial bioluminescent induced by various contents of carbofuran (0.5 μg/mL, 5 ng/mL, 50 pg/mL) for different incubation time experiments.

In all experiments using different incubation times, the bioluminescence maximum intensity was always proportional to the carbofuran concentration. However, the bacterial bioluminescence in the presence of toxicant was lower than that of bacterial control for 0 hr, 2 hr and 12 hr incubation experiments. The specific reason for the inhibition of bacterial bioluminescence in these cases is unclear, however it might be attributed to the competition between bacterial growth due to the transition to 30 °C and the increased sensitivity to the toxicant due to the higher temperature of exposure, which will be discussed in details later. For the experiments using 4 hr and 9 hr incubation time, the observed bacterial bioluminescence was enhanced by the presence of two higher carbofuran dilutions of 0.5 µg/mL and 5 ng/mL, while for the lowest 50 pg/mL dilution, the bacterial bioluminescence was not affected by the presence of toxicant given that the relative difference was almost zero. Interestingly, for the experiment using 6 hr of incubation, the bacterial bioluminescence signals were proportionally enhanced by all three tested toxicant concentrations. In this case, the "light ON" bioluminescence (RLU signal above the control bacteria) was observed. However at 0 hr, 2 hr and 12 hr or 4 hr and 9 hr partially positive or very low relative luminescence may be explained by the fact that the toxicant affects negatively the luciferase activity. Based on these results, the optimum room temperature incubation time for carbofuran detection using *E. coli* DPD2794 bacteria bioreporter cells was chosen as 6 hr, and the whole bioluminescent evolution in this optimized condition was shown in **Figure 2.13** where different concentration of carbofuran dilution can be readily detected by bacterial bioluminescence.

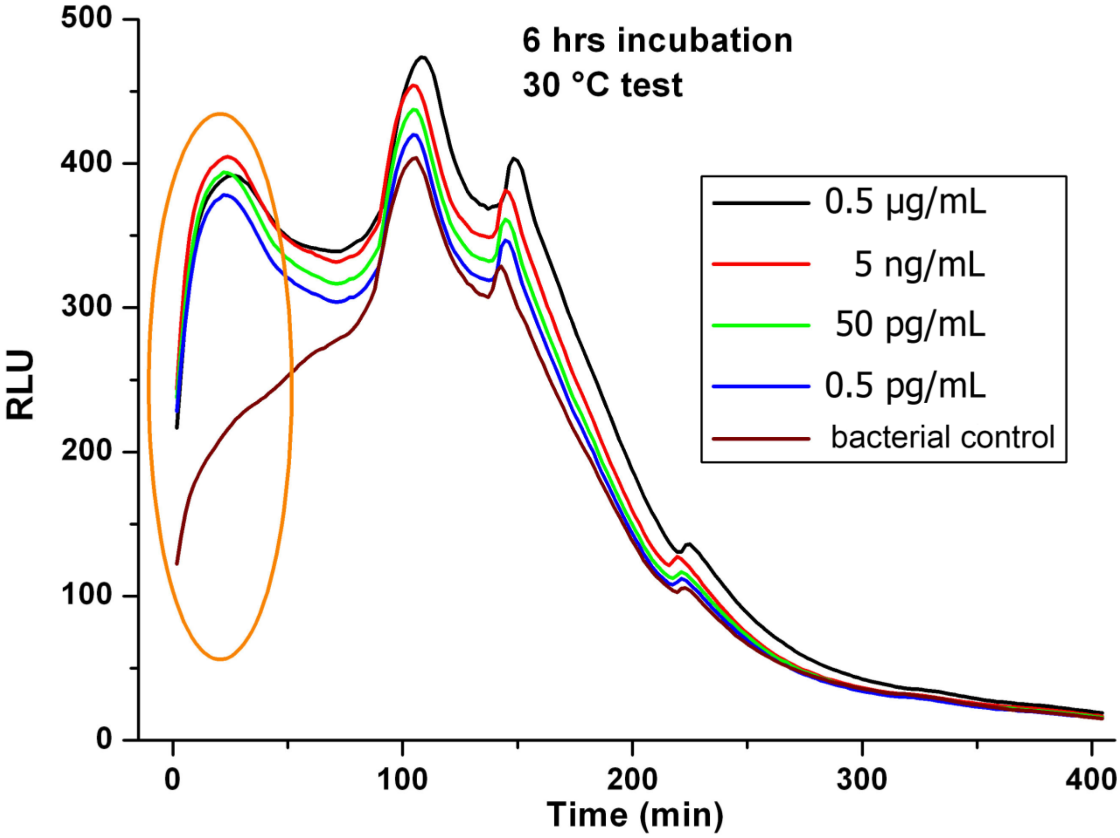

Figure 2.13 *E. coli* DPD2794 bioluminescence in the presence of different carbofuran contents (0.5 μg/mL, 5 ng/mL, 50 pg/mL, 0.5 pg/mL) with 6 hr incubation prior to measurements at 30 °C.

In the first 60 min of measurement, the bacteria exposed to carbofuran showed distinct bioluminescent evolutions when compared to those in the control. Specifically, the toxicant induced bacterial bioluminescence reached a maximum intensity around 378~404 RLU within around 20 min, while the control bioluminescence was gradually increased without any peaks observed in this period of 60 min. Considering that the incubation step is used in the proposed protocol, there should be some carbofuran molecules uptaken into bacterial cells prior to bioluminescent measurement, which could be main reason for this dramatically increased luminescence in the beginning of measurement. However, in the following measurement, two main luminescent peaks appeared at about 100 min and 145 min, and were recorded in all the curves. The bacterial bioluminescence in the presence of toxicant was generally larger than that of bacteria control, and the maximum intensity of these two peaks was proportional to the carbofuran concentration used.

Further, the physiological properties of bacterial cells are particularly important to the evolution of bacterial bioluminescence, and the temperature changing from room temperature of incubation stage to 30 °C of bioluminescence measurement stage could lead to significant influences to bacterial metabolism. Thus, the OD values changes of washed and non-washed bacterial cells with two typical carbofuran dilutions were monitored following the same conditions like bioluminescent test. Experimentally, 3 mL mixture of bacteria suspension (0.7 OD) and carbofuran toxicants (with volume ratio of bacteria: carbofuran =9:1) and 3 mL bacterial suspension was used as the control were investigated for an OD evolution. Moreover, the bacterial cells/carbofuran suspensions were incubated at room temperature for the first 6 hr and then incubated at 30 °C for the next 6 hr. To be consistent with the bioluminescence measurements, two sets of experiments at washing and non-washing conditions were conducted and the results were shown in **Figure 2.14**. For the non-washing experiments, the OD changes of bacterial cells are slightly affected by the presence of higher carbofuran concentration (0.5 µg/mL), while in the case of lower concentrations of carbofuran (50 pg/mL) an obvious increase of OD values occurs. In the washing experiments, the presence of carbofuran toxicant always inhibits the growth of bacterial cells. Interestingly, there are dramatic OD changes around 460 min, which coincides with the appearance time of bioluminescent peaks that could be used to discriminate different concentrations of carbofuran toxicants as shown in **Figure 2.13**. Based on these results, it is believed that refreshed bacterial cells populations can distinguish the different carbofuran concentrations around 100 min in the case of the washing experiments and test temperature switches to 30 °C.

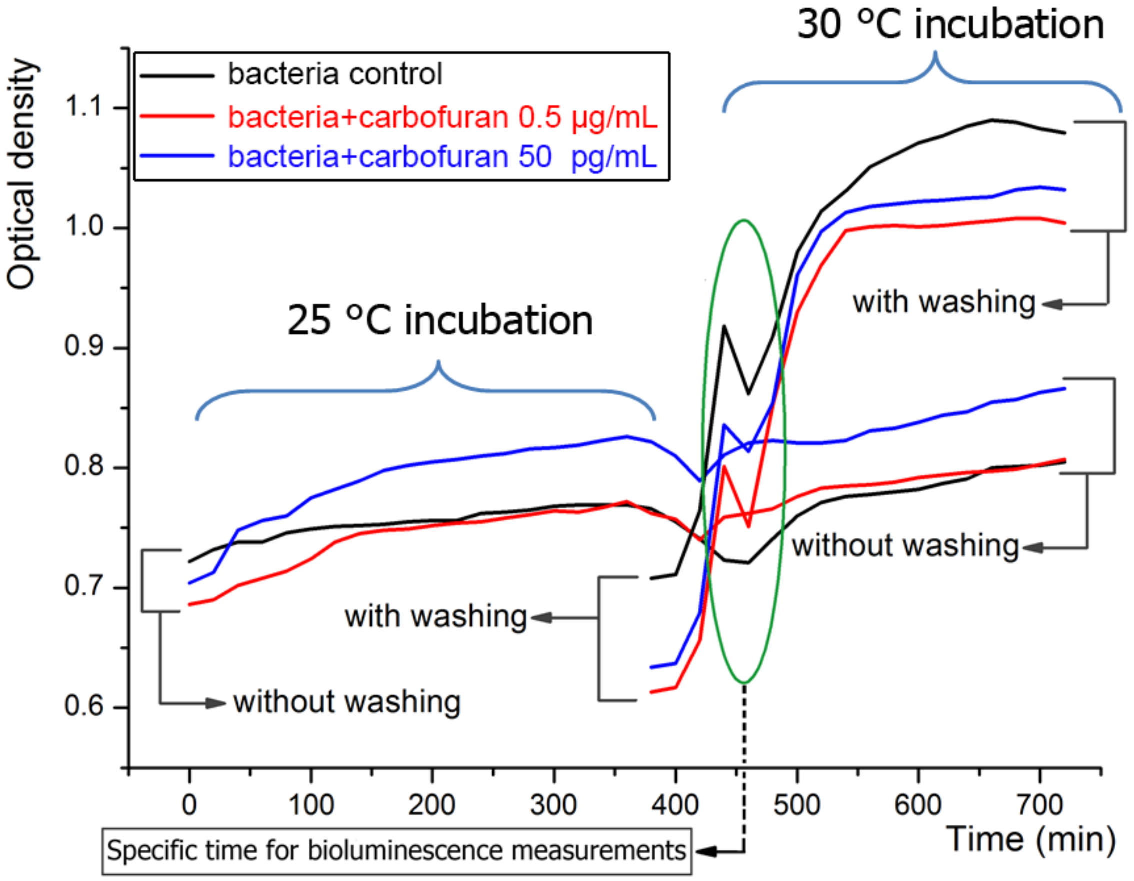

Figure 2.14 Continuous monitoring of the optical density (OD) evolution of "washing" and "non-washing" *E. coli* DPD2794 strain (0.7OD) over 12 hr in the presence of two different carbofuran concentrations (50 pg/mL and 0.5 μg/mL). To be consistent with bioluminescent test condition, in the first 6 hr the bacterial cells were incubated at room temperature (25 °C) immediately followed by their incubation at 30 °C for another 6 hr.

2.2.3.4 Calibration curve for carbofuran detection using E. coli DPD2794 bacteria

Since several luminescent peaks were recorded during the bioluminescent measurement, thus in order to better evaluate the carbofuran toxic effects to the bacterial cells, one must not only monitor the single maximum intensity value, but also the areas under the whole bioluminescence curves. Thus the area under curve value was calculated for each curve from **Figure 2.13** and these results along with traditional peak

RLU value were summarized in **Table 2.2**.

Table 2.2 The characteristic bioluminescent data for experiment with 6 hr incubation time

Concentration /Dilution	AUC[a]	(RLU_{max1})[b]	(RLU_{max2})[c]
0.5 μg/mL (10^{-2})	82966.1	473.7	403.6
5 ng/mL (10^{-4})	78702.8	453.9	381.4
50 pg/mL (10^{-6})	75137.7	437.2	361.2
0.5pg/mL (10^{-8})	71380.8	415.3	343.2
Bacteria control	62953.6	403.7	328.9

a: AUC is the area under curve, calculated by a build-in algorithm from the software Origin.

b: RLU_{max1} is the recorded maximum luminescent intensity for the first peak appeared at 100 min of measurement in Figure 2.13.

c: RLU_{max2} is the recorded maximum luminescent intensity for the second peak appeared at 145 min of measurement in Figure 2.13.

From the results shown in **Table 2.2**, both the calculated AUC value and recorded maximum intensities from the two main peaks were proportional to the carbofuran concentration. As discussed previously, one additional luminescence peak was observed (not found in the control curve) when the bacterial cells were exposed to the carbofuran toxicant (see **Figure 2.13**). This additional area was taken into account in the calculated areas under curves. Thus, instead of using luminescent peak intensity to construct the calibration curve, a more comprehensive calculation of the area under the curve (AUC) was plotted against carbofuran concentration as shown in **Figure 2.15**. It should also be noted that the relative values (ΔAUC) obtained by subtracting the background AUC value (62953.6) from the bacterial control was used. Additionally, the carbofuran dilution preparation was validated by standard LC/MS test and the data were illustrated in **Figure 2.15** as well.

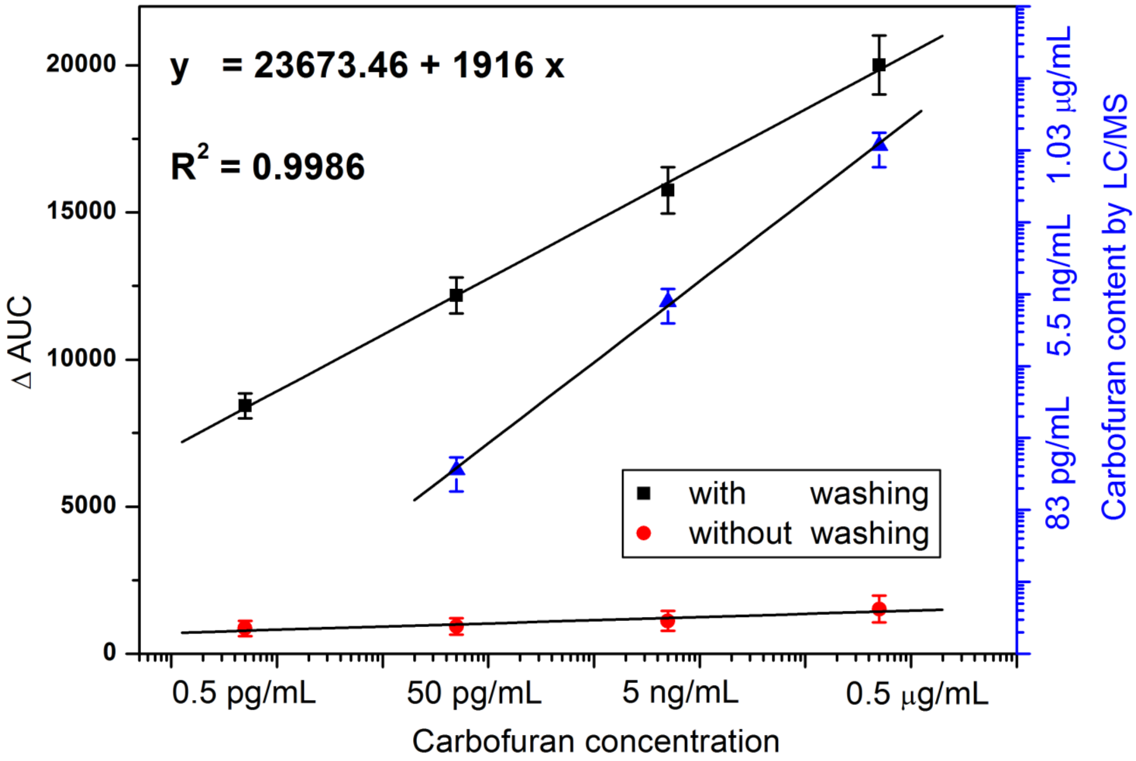

Figure 2.15 Calibration curve for carbofuran detection using the "washing" protocol under optimized conditions. LC/MS measurements are correlated with the expected carbofuran concentrations. AUC: area under the curve, LC/MS: liquid chromatography/mass spectrometry.

From the calibration curve, the induced bacterial bioluminescence response, based on calculated relative AUC value, was highly dependent on carbofuran concentration. The linear response to various carbofuran concentrations was observed from 0.5 pg/mL to 0.5 µg/mL, with a linear regression equation of y = 23673.46 + 1916 x (y is the relative AUC value, x is the log concentration factor of carbofuran dilutions) and a correlation coefficient of 0.9986. Additionally, the expected 10^{-6} dilution would represent 0.05 ng/mL given that the stock solution concentration is 50000 ng/mL. The LC/MS measurements were repeated thrice and an average value of 0.067 ng/mL for this dilution was obtained, validating the dilution process used in the experiment. From these results, the trace concentration of carbofuran as low as 0.5 pg/mL can be detected using bacteria *E. coli* DPD2794 strain via the new protocol.

In summary, since the generation of bioluminescence implies complex biochemical reactions in living cells, metabolism active bacterial cells are required in the analytical investigations of the toxicant.[19] It is convinced that the exogenous analyte is not the only factor to induce the bacteria bioluminescence changes. In this sense, modulating cellular metabolic changes in bacterial cells, during a longer monitoring period, will contribute to decreased background noises in the measured bioluminescence. Therefore, the bacterial bioluminescence response to the target analyte could be optimized by fine tuning of bacterial cellular metabolism, which is expected to be a cost-effective way to increase sensitivity of the bioassay.

2.3 Conclusions and Perspectives

In this work, instead of constructing new bacterial strains, the basic bioluminescent assay protocols of engineered *E. coli* bacterial cells have been refined to improve the sensitivity for pesticides detection. Using the protein damage sensitive bacteria strain of *E. coli* TV1061, the first protocol was developed for the identification of the toxic effect of water insoluble pesticide atrazine through an overnight “cold incubation” at 4 °C. Bacteria can be affected in the “fresh” mode by 10 μg/mL atrazine in about 180-300 min at 25 °C in the first luminescence measurement, while for the visualizations of lower atrazine concentrations effects, bacteria do require an overnight cold incubation at 4 °C prior to their second luminescence reading at 25 °C. This study demonstrates an alternative experimental methodology, not known to be used so far in the literature that enables a greater sensitivity identification of atrazine down to 0.01 pg/mL. Moreover, using the DNA damage responsive bacteria strain of *E. coli* DPD2794, the second protocol containing three major steps of “incubation/centrifugation/washing” is devised to modulate the physiology of the bacterial cells whilst being exposed to a toxicant carbofuran. This new protocol enables an improved sensitivity meanwhile providing an interesting set of peaks, which surely contain useful information. By applying a simple incubation/washing step, it is able to obtain a low detection limit of the toxic effect of carbofuran down to 0.5 pg/mL.

Although the bioluminescence bioassays for toxicant detection based on genetically engineered bacterial cells have been studied for over 20 years since the first report published,[20] there is still long way for their real application in different scenarios. The most challenging task is how to obtain applicable selectivity towards specific target pollutants, given the fact that the promoter gene used in most of engineered bacteria normally is responsive to many toxicants. The increasing advancement of microbiology and molecular biology would provide more detailed information about the bacteria cellular interaction with exogenous toxicants, thus would eventually leading to new engineered strains that are more specific to target compounds. Alternatively, the fine tuning of the physiology or metabolism of bacterial cells via modulating various experimental parameters is already proven to be a more economical option to enhance the analytical performance of bioassays based on our work, thus more detailed study on the bacterial metabolism should be conducted and particularly it is expect that much more interesting information will be deduced from single bacterial cell study.

References:

1. Yagi, K., Applications of whole-cell bacterial sensors in biotechnology and environmental science. *Applied Microbiology and Biotechnology* **2007,** *73* (6), 1251-1258.

2. Girotti, S.; Ferri, E. N.; Fumo, M. G.; Maiolini, E., Monitoring of environmental pollutants by bioluminescent bacteria. *Analytica Chimica Acta* **2008,** *608* (1), 2-29.

3. Kahru, A.; Dubourguier, H.-C.; Blinova, I.; Ivask, A.; Kasemets, K., Biotests and biosensors for ecotoxicology of metal oxide nanoparticles: a minireview. *Sensors* **2008,** *8* (8), 5153-5170.

4. Belkin, S.; Smulski, D. R.; Dadon, S.; Vollmer, A. C.; Van Dyk, T. K.; Larossa, R. A., A panel of stress-responsive luminous bacteria for the detection of selected classes of toxicants. *Water Research* **1997,** *31* (12), 3009-3016.

5. Gu, M.; Choi, S., Monitoring and classification of toxicity using recombinant bioluminescent bacteria. *Water Science and Technology* **2001,** *43* (2), 147-154.

6. Rajan Premkumar, J.; Rosen, R.; Belkin, S.; Lev, O., Sol–gel luminescence biosensors: Encapsulation of recombinant *E. coli* reporters in thick silicate films. *Analytica Chimica Acta* **2002,** *462* (1), 11-23.

7. Vollmer, A. C.; Belkin, S.; Smulski, D. R.; Van Dyk, T. K.; LaRossa, R. A., Detection of DNA damage by use of Escherichia coli carrying recA':: lux, uvrA':: lux, or alkA':: lux reporter plasmids. *Applied and Environmental Microbiology* **1997,** *63* (7), 2566-2571.

8. D'souza, S., Microbial biosensors. *Biosensors and Bioelectronics* **2001,** *16* (6), 337-353.

9. Lei, Y.; Chen, W.; Mulchandani, A., Microbial biosensors. *Analytica Chimica Acta* **2006,** *568* (1), 200-210.

10. Robbens, J.; Dardenne, F.; Devriese, L.; De Coen, W.; Blust, R., Escherichia coli as a bioreporter in ecotoxicology. *Applied Microbiology and Biotechnology* **2010,** *88* (5), 1007-1025.

11. Su, L.; Jia, W.; Hou, C.; Lei, Y., Microbial biosensors: a review. *Biosensors and Bioelectronics* **2011,** *26* (5), 1788-1799.

12. Woutersen, M.; Belkin, S.; Brouwer, B.; van Wezel, A. P.; Heringa, M. B., Are luminescent bacteria suitable for online detection and monitoring of toxic compounds in drinking water and its sources? *Analytical and Bioanalytical Chemistry* **2011,** *400* (4), 915-929.

13. Bechor, O.; Smulski, D. R.; Van Dyk, T. K.; LaRossa, R. A.; Belkin, S., Recombinant microorganisms as environmental biosensors: pollutants detection by *Escherichia coli* bearing *fabA*':: *lux* fusions. *Journal of Biotechnology* **2002,** *94* (1),

125-132.

14. Jia, K.; Eltzov, E.; Toury, T.; Marks, R. S.; Ionescu, R. E., A lower limit of detection for atrazine was obtained using bioluminescent reporter bacteria via a lower incubation temperature. *Ecotoxicology and Environmental Safety* **2012,** *84*, 221-226.

15. Jia, K.; Eltzov, E.; Marks, R. S.; Ionescu, R. E., Bioluminescence enhancement through an added washing protocol enabling a greater sensitivity to carbofuran toxicity. *Ecotoxicology and Environmental Safety* **2013,** *96*, 61-66.

16. Van Dyk, T. K.; Majarian, W. R.; Konstantinov, K. B.; Young, R. M.; Dhurjati, P. S.; Larossa, R. A., Rapid and sensitive pollutant detection by induction of heat shock gene-bioluminescence gene fusions. *Applied and Environmental Microbiology* **1994,** *60* (5), 1414-1420.

17. Rosen, R.; Davidov, Y.; LaRossa, R. A.; Belkin, S., Microbial sensors of ultraviolet radiation based on recA'::lux fusions. *Applied Biochemistry and Biotechnology* **2000,** *89* (2-3), 151-160.

18. Gu, M. B.; Min, J.; Kim, E. J., Toxicity monitoring and classification of endocrine disrupting chemicals (EDCs) using recombinant bioluminescent bacteria. *Chemosphere* **2002,** *46* (2), 289-294.

19. Der Meer, V.; Roelof, J.; Tropel, D.; Jaspers, M., Illuminating the detection chain of bacterial bioreporters. *Environmental Microbiology* **2004,** *6* (10), 1005-1020.

20. King, J.; DiGrazia, P.; Applegate, B.; Burlage, R.; Sanseverino, J.; Dunbar, P.; Larimer, F.; Sayler, G. a., Rapid, sensitive bioluminescent reporter technology for naphthalene exposure and biodegradation. *Science* **1990,** *249* (4970), 778-781.

Chapter 3 Localized surface plasmon resonance (LSPR) biosensor for (bio)molecules detection

The analytical sensitivity and selectivity are two important parameters in the typical optical biosensor applications. The bacterial bioluminescent bioassays discussed in previous chapter provide competitive analytical sensitivity towards pesticides detection, however the detection specificity remains a major challenge for these whole-cell based assays, although the *E. coli* TV1061 bacteria show somewhat different bioluminescent responses to various pesticides in the "fresh-overnight" two stages test (see section 2.2.2.3, **Figure 2.7** in Chapter 2). In order to guarantee the analytical specificity, a wide range of biomolecular interactions, such as enzyme-substrate,[1] antibody-antigen,[2] complementary oligonucleotides,[3] sugar-lectin,[4] have been explored in the biointerfaces. Among these specific biomolecular recognitions, the antibody-antigen immunological interaction is the most frequently used one due to its excellent specificity, thus tremendous immunosensors combined with different optical signal readouts have been developed for sensitive and specific detection of biomolecules.[5-7] With respect to the various optical detection methods (fluorescent, chemiluminescence, phosphorescence, surface plasmon resonance, etc.), the localized surface plasmon resonance (LSPR) based on noble metal nanoparticles witnesses increasing popularity, mainly due to the lively interplay between traditional bioanalysis and rapidly growing nanophotonics during last decades.[8]

In this chapter, a robust LSPR biosensing technique has been developed for sensitive, specific and multiplexing biomolecules detection. The comprehensive studies including nanostructures fabrication, morphology optimization, surface biomodification and strategies to improve the analytical performance have been conducted. Specifically, the gold evaporation followed by high temperature annealing is used to obtain extremely stable gold nanostructures on glass substrate as the first step. Secondly, two independent protocols have been created to fabricate various gold nanostructures on single glass substrate, which are further transformed into well-organized gold micro/nano-structures that facilitate the biosensor applications. The third part deals with the surface biomodification of plasmonic nanostructures, i.e., immobilization of antibody biomolecules on gold nanoparticles. This thiol mediated surface biomodification has been verified by a complementary mass sensitive technique based on quartz crystal microbalance (QCM) as well. The sensitive and specific detection of (bio)molecules targets (such as atrazine, bovine serum albumin) have been well corroborated by the combinational results from LSPR and QCM biosensing experiments. Finally, the sensitivity of LSPR biosensor has been improved by two different ways: using gold-silver bimetallic nanostructures to increase the plasmonic quality factor and poly-dopamine based functional coatings to ameliorate the interfacial biomodification efficiency, respectively.

3.1 Experimental Section

3.1.1 Materials and instruments

All the materials used in this chapter are listed in **Table 3.1**. All the chemical compounds are used as received without further treatment unless specially mentioned.

Table 3.1 The compounds and materials used in different stages of LSPR biosensor experiment.

materials	abbreviation	company	function
11-mercaptoundecanoic acid	MUA	Sigma	gold biomodification
1-ethyl-3-[3-dimethylaminopropyl] carbodiimide hydrochloride	EDC	Sigma	gold biomodification
N-Hydroxysuccinimide	NHS	Sigma	gold biomodification
dopamine	-	Sigma	Au NPs and surface biomodification
monoclonal anti-atrazine antibody	anti-atrazine	Antibodies-online	antibody for biosensor
monoclonal anti-BSA antibody	anti-BSA	Sigma	antibody for biosensor
polyclonal anti-human IgG	anti-human	Sigma	control antibody for biosensor
bovine serum albumin	BSA	Sigma	analyte for biosensor
atrazine	-	Fluka	analyte for biosensor
trizma hydrochloride	Tris-HCl	Sigma	buffer preparation
sodium hydroxide	NaOH	Fluka	buffer pH adjusting
hydrochloric acid	HCl	Fluka	buffer pH adjusting
sodium chloride	NaCl	Sigma	PBS buffer preparation
sodium phosphate dibasic	Na_2HPO_4	Sigma	PBS buffer preparation
sodium phosphate monobasic	NaH_2PO_4	Sigma	PBS buffer preparation
deionized water	ddH_2O	Millipore	PBS buffer preparation
ethanol	-	Fluka	sample washing
acetone	-	Fluka	sample washing
decon90	-	Decon Laboratories	detergent for sample washing
microscope glass slide	glass	Carl Roth	glass substrate
transmission electron microscope sample grid	TEM grid	TED Pella	gold evaporation mask
aluminum staples	staples	Leitz	gold evaporation mask
scotch tape	scotch	Elami	gold evaporation mask

For the instruments, an ultrasonic water bath (Elmasonic S30H) was used for sample cleaning, the vacuum evaporator (MEB 400, Playssys, France) and the high temperature oven (Nabertherm, Germany) were used for metal evaporation and subsequent sample annealing, respectively. The optical microscope (Nikon, Eclipse LV100), the conventional scanning electron microscope (SEM, Hitachi S3500N) and field emission scanning electron microscope (FESEM, Raith, FEG eLine) were used for substrate characterization of obtained micro-/nano plasmonic structures. A home built confocal extinction measurement system was used to record the LSPR spectra from different zones of biochips in the UV-Vis-NIR range from 200 nm to 1100 nm. The optical setup contained a white light source (DH-2000-BAC, Ocean Optics), two optical fibers (one for illumination, Φ600 µm and other for collection, Φ150 µm), a portable phtotospectrometer (QE65000, Ocean Optics, wavelength sensitivity of 1 nm) and adjustable sample holder. It should be noted that due to the optical fibers and lens combinations used in the confocal setup, the incident beam with a spatial resolution of 10 µm was focused perpendicularly onto the patterned glass during all the measurements. A quartz crystal microbalance (QCM200, Stanford Research Systems, California, US) with a crystal oscillator (QCM25) was used to monitor the frequency and motional resistance changes in real time during modification of crystal and the immunoreactions between antibody and antigen.

3.1.2 Fabrication of plasmonic nanostructures

Gold evaporation followed by high temperature annealing. Classical microscope glass slides were cut around 25 × 8 mm and subsequently used as substrates for gold film deposition. Prior to gold evaporation, all the glass substrates were placed in a plastic sample holder and washed in the mixture of detergent (decon90) and deionized water (2:8, v/v ratio) in an ultrasonication water bath at 50 °C for 15 min. Further, the resulted samples were rinsed with excess amount of deionized water, drying under a N_2

stream and subjected to another ultrasonication washing in deionized water at 50 °C for 5 min. Finally, the glass substrates were rinsed three times with deionized water, dried in an oven at 100 °C for 10 min, and ready to be used as substrate for gold thin film evaporation. For the evaporation step, the dried clean glass substrates were placed on a circular evaporation plate with a diameter of 200 mm. The metal evaporation was conducted in the evaporator using the electron beam evaporation mode at ambient temperature under a high vacuum (pressure was around 1.0×10^{-6} Torr). The evaporating rate was adjusted around 0.08 nm/s by slowly changing the current intensity. The film thickness was monitored by a build-in quartz crystal sensor. Three groups of samples with three different nominated gold film thicknesses (2 nm, 5 nm and 8 nm, respectively) were fabricated. After evaporation, the modified glass samples were transferred in a high temperature oven with accessible temperature range from 30 °C to 3000 °C to conduct the annealing procedure in the presence of oxygen. Three different annealing temperatures (in the vicinity of glass transition temperature of glass substrate) of 500 °C, 550 °C and 600 °C were studied in our work. In addition, it was also studied the thermal history influence prior exposure to the desire annealing temperature of as-evaporated gold samples. Experimentally, all the samples of 2 nm film thicknesses were annealed at the same temperature of 550 °C for 8 hr, but subject to different initial thermal history (e.g. the increasing rate used to get 550 °C from room temperature was 5, 10, 15 and 20 °C/min, respectively).

Multiplexing gold nanostructures on single glass substrate. In order to prepare different gold nanostructures on single glass substrate, two different masks were used during the gold evaporation. Specifically, in the first protocol, the gold evaporation cycle (2 nm thickness) was repeated different times at different predefined areas onto the glass slide (scotch tape mask was used to separate different areas), thus multiple areas with known evaporation thickness were created on single glass substrate. In the second protocol, aluminum staples were fixed on top of glass substrate to create gold-glass interfacial areas where the gold evaporation process was modulated because of the "shadowing effects" of staples, leading to gradually changed gold film evaporation thickness in this specific interfacial areas. After evaporation, the modified glass samples were transferred into a high temperature oven to conduct the thermal annealing in the presence of oxygen at 550 °C for 8 hr, allows generation of different morphology nanostructures on single substrate.

Well-organized gold micro/nano-structures on single glass substrate. The classical microscopy glass slide was cut, washed and dried in a same way as reported above, then a commercial TEM copper grid (200 mesh, diameter of 3.05 mm) was integrated onto the clean glass substrates as a mask, from which the gold evaporation procedure was conducted. After the gold evaporation, the TEM grid mask were carefully removed and the patterned glass substrate was transferred into a high temperature oven to conduct the thermal annealing at 500 °C for 8 hr in the oxygen atmosphere, after which the grids micro-patterns were converted into well-organized gold nanoparticles.

Preparation of Au/Ag bi-metallic NPs. A clean glass fixed with TEM grid on top was used as the substrate. For the metal evaporation, the optimized combination for LSPR biosensor application is one gold layer (4 nm) followed by another silver layer (2 nm), they were successively evaporated on the glass substrate through the TEM grid mask. Moreover, other configurations with equivalent thickness (such as Au 4nm, Au 6nm, Ag 4nm, Ag 6nm, Ag 2nm followed by Au 4 nm and Ag 4nm followed by Au 2nm) were prepared as well. After the evaporation step, the grid mask was carefully removed, and the metal modified glass substrates were transferred into a high temperature oven to be annealed at 500 °C for 8 hr. Finally, the well-organized Au/Ag bi-metallic nanostructures were created on the glass substrate.

3.1.3 Surface biomodification

Surface biomodification in LSPR biosensor experiment. For the gold nanoparticles to be used in LSPR biosensors, the immobilization of antibody biomolecules on surface of gold nanostructures is realized through thiol chemistry. Specifically, the annealed samples were firstly washed with ethanol/acetone mixture (volume ratio of 1:1) in an ultrasonic bath at room temperature for 30 min to clean and stabilize the nanostructures. After drying under a N_2 stream, the samples were immersed in 11-mercaptoundecanoic acid ethanolic solution (MUA, 1 mM in 10 mL ethanol) for 12 hr at room temperature. The gold nanoparticles (NPs) modified with MUA were extensively rinsed with ethanol to remove the excess thiol and dried with N_2. Further, the terminal carboxyl groups of thiolated surface were activated with mixed EDC/NHS (0.4 mM/0.1 mM) aqueous solution at room temperature for 50 min. Next, the antibodies dilutions in PBS buffer (100 µg/mL) were incubated with the activated gold nanostructures at 4 °C for 5 hr. After PBS rinsing, various antigen dilutions with different concentrations diluted in PBS were incubated with antibodies modified nanoparticles for 3 hr at 4 °C to complete the antibody-antigen immunoreactions. Different (bio)molecules targets such as atrazine pesticide and BSA proteins have been detected in this work, thus the specific antibody and antigen concentrations used will be presented in the following sections in details. The LSPR responses were recorded after each (bio)functionalization step. It should be noted that for the steps involving PBS buffer, a rinsing step with ddH_2O before spectroscopy measurements was necessary, otherwise the salt crystals from buffer were deposited on the substrate surface, which could produce interferences in the LSPR measurements.

Surface biomodification in QCM biosensor experiment. Firstly, the quartz crystal was washed in a mixed solvent solution of ethanol/acetone (10 mL, 1:1 v/v volume ratio) for 12 hr at room temperature. Secondly, a commercial TEM grid was fixed on the center of a gold crystal surface as a mask. Next, a gold evaporation process (thickness of 5 nm) was conducted through the grid mask, while the rest of quartz crystal surface was covered with a scotch tape to avoid the gold deposition over the entire crystal. The resulted micro-patterned crystal was immersed into the 11-mercaptoundecanoic acid (MUA) ethanolic solution (1 mM, 10 mL) for 12 hr at room temperature, followed by washing with ethanol and ddH$_2$O solutions. The resulted thiolated crystal was further activated with a mixed solution of EDC/NHS (0.2 mM/0.05mM). After activation step ends, tiny amount of atrazine and carbofuran antibodies (0.6 µL, 0.1 mg/mL) were immobilized onto two different patterns of crystal at 4 °C over 5 hr. The quartz crystal with antibody drops was placed in a sealed humid petri-dish to avoid fast liquid evaporation. After washing and drying steps, the antibody-modified crystal was mounted in the QCM200 system and used for the specific and non-specific analyte acoustic investigations.

3.2 Results and Discussion

3.2.1 Fabrication of ultra-stable gold nanostructures

The requirement of stable gold nanostructures with large plasmonic tunability and high plasmonic sensitivity are the prerequisites in constructing robust LSPR biosensors. In addition, the surface bound gold nanostructures are of special interests in the LSPR biosensor application, because the gold nanoparticles patterned solid surface can be easily regenerated to be reusable and easier to be combined with different microfluidic devices, from which the multiplexing and high throughput detection can be realized. Among the various protocols to fabricate plasmonic nanostructures on solid substrates, the evaporation of thin film followed by thermal annealing would be more competitive due to the relatively low cost and potential large-scale fabrication ability. Moreover, for the transmission mode LSPR configuration, glass is the mostly desirable substrate due to its transparent color and inexpensiveness.

However, there is a major obstacle for the use of regular glass for deposing thin metal film due to the instability of the noble metal to the bare glass substrate upon exposing to aqueous solutions, solvents and buffers, which are the common places in real biosensor applications.[9] For instance, the instability of Au film deposited on glass substrate has been well documented in literatures, and this instability is due to the poor adhesive ability of gold towards glass.[10] Moreover, the morphology of gold thin film deposited on glass surface was reported to be seriously changed due to immersion in solvents,[11] which could lead to the suspicious random LSPR resonant-peak changes and thus deteriorating the measurement reproducibility.

There are several published work dedicated to overcome the inherent instability of noble metal nanoparticles to glass substrate. For example, an intermediate metal layer (Cr, Ni, Ti) can significantly strength the gold adhesion on glass, but the plasmon damping effects derived from this additional metal layer also decrease the plasmon quality of resulted sample. As the competitive alternatives, Israel Rubinstein and co-authors have recently developed some protocols to stabilize the gold thin film binding on glass surface, including pre-modification of glass using silane molecule together with post-depositing a very thin layer of silica[12] and one-step partial embedding of Au NPs in glass substrate through intensive thermal annealing.[13] On the other hand, the Sabine Szunerits group has also improved the metal nanoparticle binding ability to glass substrates from different ways. Basically, their works focus on the protection of plasmonic structures by various oxide-based overlayers, such as tin-doped indium oxide (ITO), SiO_x, diamond as well as amorphous carbonated silicon thin films.[14]

In this first part, gold nano-structures exhibiting strong LSPR properties have been fabricated by electron beam evaporating of thin gold film on commercial glass followed by thermal annealing at high temperature close to the glass transition temperature of substrate. The morphology and the spectroscopy of obtained LSPR surface were systematically studied under various experimental conditions, such as different film thickness and annealing temperature.

3.2.1.1 Influence of gold evaporation thickness onto the morphology and LSPR spectroscopy of annealed gold nanoparticles

In the metal evaporation-annealing protocol, the gold film evaporation thickness and annealing temperature are two important parameters to determine the morphology of resulted gold nanostructures. Therefore, the gold film with different thicknesses of 2 nm, 5 nm and 8 nm were evaporated on glass substrate and annealed at three different temperatures of 500 °C, 550 °C and 600 °C. The photograph of obtained samples with different parameters is shown in **Figure 3.1**. The prepared gold films exhibit different colors changing from light blue for 2 nm to light green for 5 nm and to golden color for

8 nm thicknesses. These colors change significantly after the gold samples are annealed at different temperatures for 8 hr. Experimentally, the high temperature annealing leads to a violet color for the thinnest gold evaporated layer (2 nm), while for the intermediate thickness (5 nm) and thickest deposited film (8 nm) the color emerge from dark blue to orange pink, respectively. Therefore, the higher annealing temperature was used, the darker colors were observed.

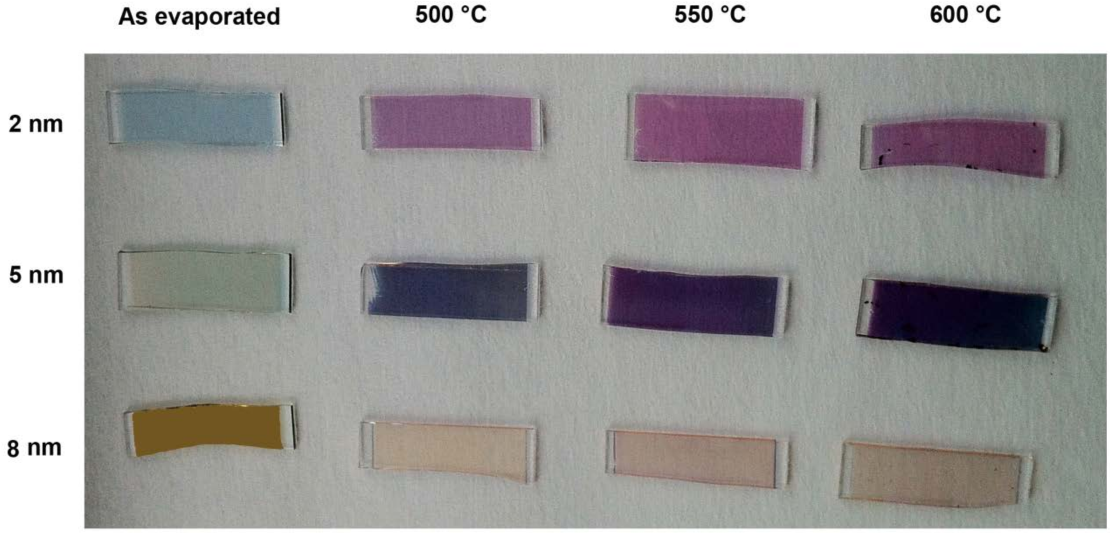

Figure 3.1 Photograph of prepared samples with different nominative gold evaporation thicknesses (2 nm, 5 nm and 8 nm) and annealed at different temperature (500 °C, 550 °C and 600 °C) for 8 hr.

The evaporated film thickness was already reported to play a decisive role in the determination of LSPR properties of gold nano-structures.[15] The LSPR spectra for gold-evaporated sample with three different nominative film thicknesses (2 nm, 5 nm and 8 nm, respectively) were showed in **Figure 3.2**, where a wide extinction peak located at 642 nm with optical density (OD) of 0.2 was observed for the thinnest film of 2 nm. For the other two gold films, the extinction peaks shared the similar features, that contain a minimum OD of 0.17 around 520 nm followed by a large plateau in NIR wavelength range, combined with a slight increase of OD value for 8 nm sample. The wide extinction peak for 2 nm gold sample was attributed to the formation of discrete nanostructures in the very thin evaporated film, while the features of 5 nm and 8 nm sample were considered as typical plasmonic properties of (semi-) continuous film.[16]

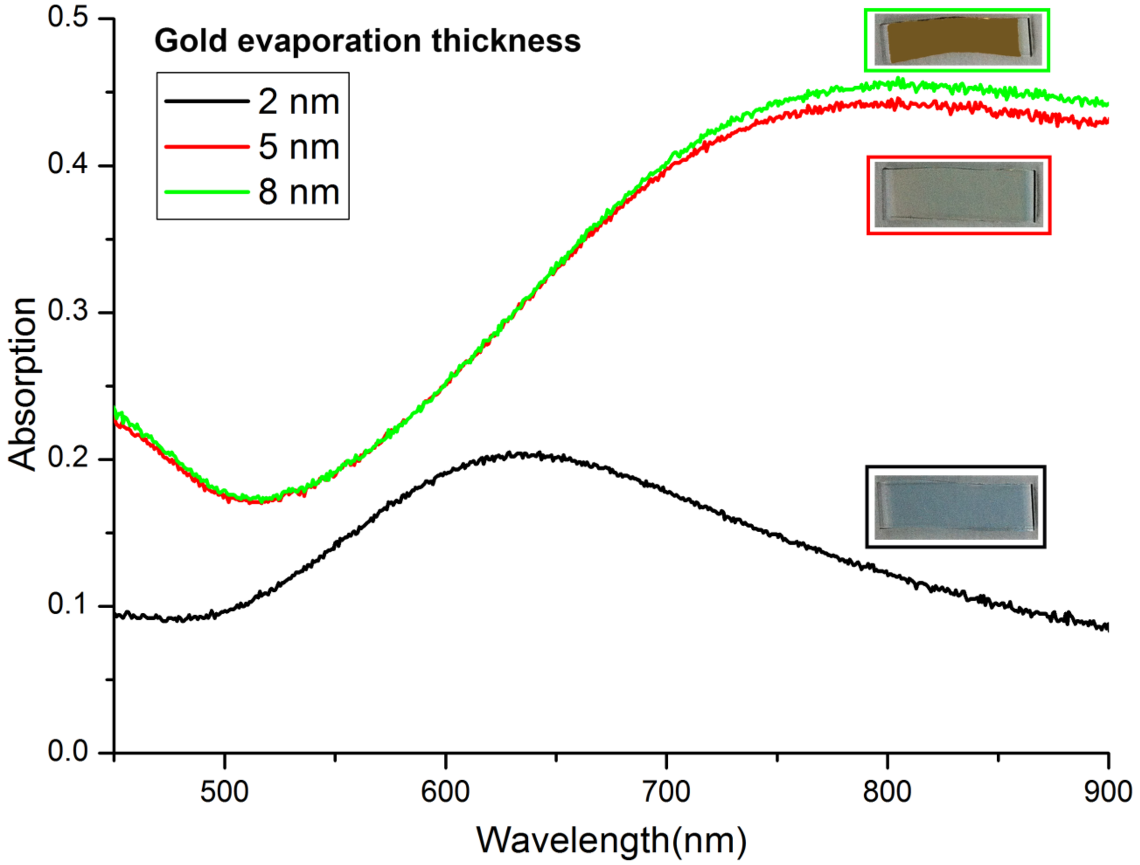

Figure 3.2 LSPR spectra of gold evaporated sample with different nominative film thicknesses of 2 nm, 5 nm and 8 nm. The images of samples were shown next to their corresponding spectra.

Although the glass substrate modified with very thin gold films (2 nm) exhibits an obvious plasmonic resonant peak according to results in **Figure 3.2**, the gold nano-structures were not very stable because of the weak affinity between gold and glass in this case. To prepare well defined Au NPs with reproducible optical characteristics, a high temperature annealing (close to the glass transition temperature) was conducted in the presence of oxygen. As shown in **Figure 3.3**A, the LSPR spectra of the three types of samples with different gold thicknesses changed significantly after annealing at 550 °C for 8 hr. Interestingly, all these annealed samples have well-defined plasmonic peaks. Moreover, by increasing the gold thicknesses, it was noticed that the maximum resonant wavelength was recorded at 553 nm for 2 nm, at 579 nm for 5 nm and at 712 nm for 8 nm sample. Also, it can be remarked that LSPR-peaks became wider with the increasing of gold-evaporated film thickness. There is a maximum plasmonic intensity which was measured for a thickness of 5 nm. This thickness corresponds to nanoparticles sizes (see **Figure 3.3**C) which give an optimal extinction coefficient where radiation losses are not too important.

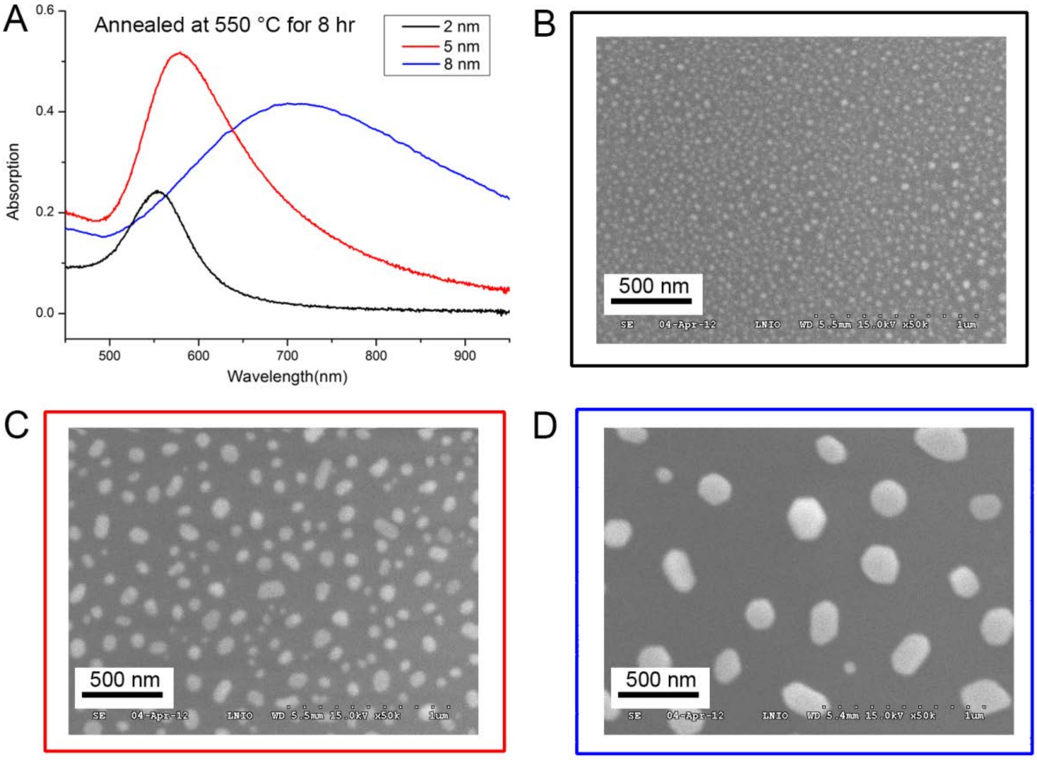

Figure 3.3 LSPR spectra (A) of high temperature annealed samples with different initial nominative evaporation thickness and their corresponding SEM images for 2 nm (B), 5 nm (C) and 8 nm (D), the annealing was conducted in the presence of oxygen at 550 °C for 8 hr. The microscope images (B-D) were captured using conventional SEM (Hitachi, S3500N) and were in the same scale bar of 500 nm.

Annealed gold nano-structures were also characterized by SEM microscopy that allows better understand their morphologies at various temperatures. **Figure 3.3**A shows LSPR spectra while the SEM images of three gold annealed samples with thicknesses of

2 nm, 5 nm and 8 nm at 550 °C for 8 hr are presented in **Figure 3.3**B, **Figure 3.3**C, and **Figure 3.3**D, respectively. It was noticed that the size of gold nanoparticles increased from 10 nm (**Figure 3.3**B) for thinnest sample to about 200 nm for thickest sample (**Figure 3.3**D). Moreover, the interparticle distance also increased as the raising of initial nominated film thickness, e.g. the sample with thicker evaporated film always has less particle density after exposure at high annealing temperature. It is well known that the maximum LSPR-extinction peak is red-shifted as the nano-particle's sizes increasing,[17] which is consistent with the obtained results shown in **Figure 3.3**. Moreover, the shapes of the extinction peaks and their OD values were assumed to be determined by the interplay among particle size, shape and interparticle distance.

3.2.1.2 Influence of annealing temperature onto the morphology and plasmonic spectroscopy of gold nanoparticles

Besides the evaporation of various gold thicknesses onto glass substrates, the other investigated parameter important for the construction of sensitive LSPR measurements was the annealing temperature. Recently, it has been reported that by thermal annealing at a temperature close to the transition temperature of the glass substrate would improve the stability of created gold nanostructures.[18] Therefore, the systematic studies about the influence of different evaporated thicknesses combined with that of different annealing temperatures have been conducted. The results are shown in **Figure 3.4.**

Samples with smaller initial film thickness of 2 nm and 5 nm, shared plasmonic peaks with similar evolution as following: at higher annealing temperature, the plasmonic peak was sharper, blue shifted in its resonant wavelength with larger OD value. Specifically, as the annealing temperature increased from 500 °C to 600 °C, the extinction peak was slightly blue shifted from 554 nm to 546 nm with a concomitant amplitude increases of 0.07 OD for thinner gold film (2 nm). In the case of the sample with 5 nm thicknesses (**Figure 3.4**B), although the LSPR peaks became wider than that sample with 2 nm (**Figure 3.4**A), its amplitude increased (0.06 OD) with a concomitant larger blue shift (27 nm) was observed when the annealing temperature was raised. It should be noted that a different plasmonic peak evolution was noticed for the annealed 8 nm sample when compared with those of 2 nm and 5 nm samples (**Figure 3.4**D). Thus, higher annealing temperatures lead to large red-shift plasmonic resonances around 126 nm (from 654 nm at 500 °C to 780 nm at 600 °C annealing) with decreasing of OD value as 0.04 (**Figure 3.4**C). In addition, no matter what annealing temperature was used, the extinction LSPR-peak always becomes wider as the nominative thicknesses were increased.

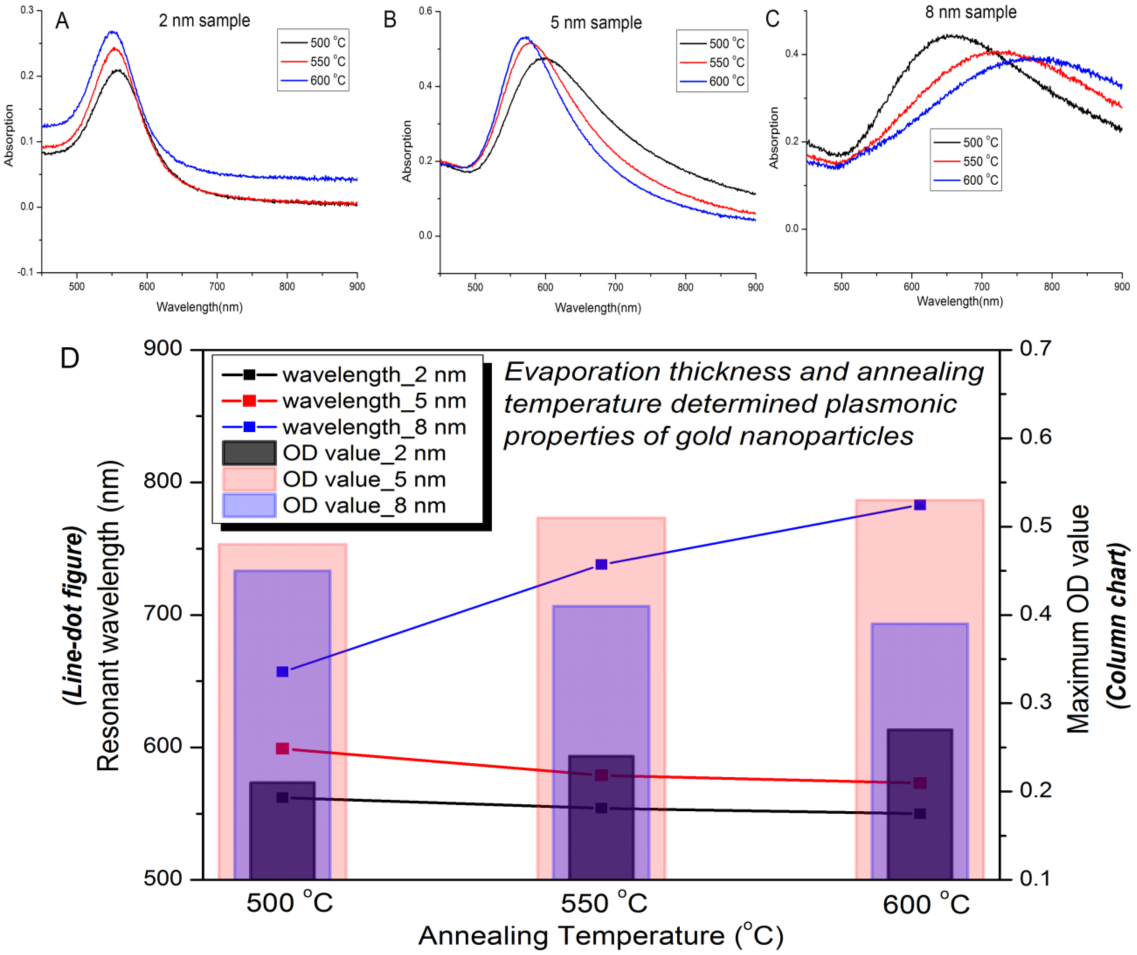

Figure 3.4 The LSPR spectra for samples annealed at three different temperatures (500 °C, 550 °C and

600 °C) with nominative evaporation film thickness of 2 nm (A), 5 nm (B) and 8 nm (C), respectively. The characteristic plasmonic properties from each spectrum were plotted in function of annealing temperature and evaporation thickness, the resonant wavelength was shown as the line-dot figure, while the maximum OD value was displayed as the column chart in panel D.

As mentioned, the thermal annealing of metal films promotes an interparticle separation in order to decrease the surface tension energy between Au NPs and substrate,[19] which in turn enhances the affinity between gold nanoparticles and glass substrate. Additionally, the gold NPs obtained at higher annealing temperatures will become more homogeneous than those obtained at lower annealing temperature, where uniform NPs have sharper LSPR spectra than inhomogeneous ones.[20] Such NPs characteristics are in agreement with our results for the 2 nm and 5 nm gold thicknesses. As clearly shown in **Figure 3.5**, the freshly-evaporated sample (**Figure 3.5**A) with 5 nm nominative thicknesses has the feature morphology of continuous film containing many tiny grooves, which are consistent with its typical continuous film LSPR spectra in **Figure 3.2**. All the annealed samples have developed large area of well distributed gold nanoparticles with a logical size evolution once the annealing temperature was increased. Round NPs were dominantly formed at 600 °C when compared with those obtained at 500 °C and 550 °C, where the particles of various shapes were obtained (**Figure 3.5** B-D for the three annealing temperatures). These results can be interpreted by a better homogeneity of Au NPs shapes after higher temperature annealing.

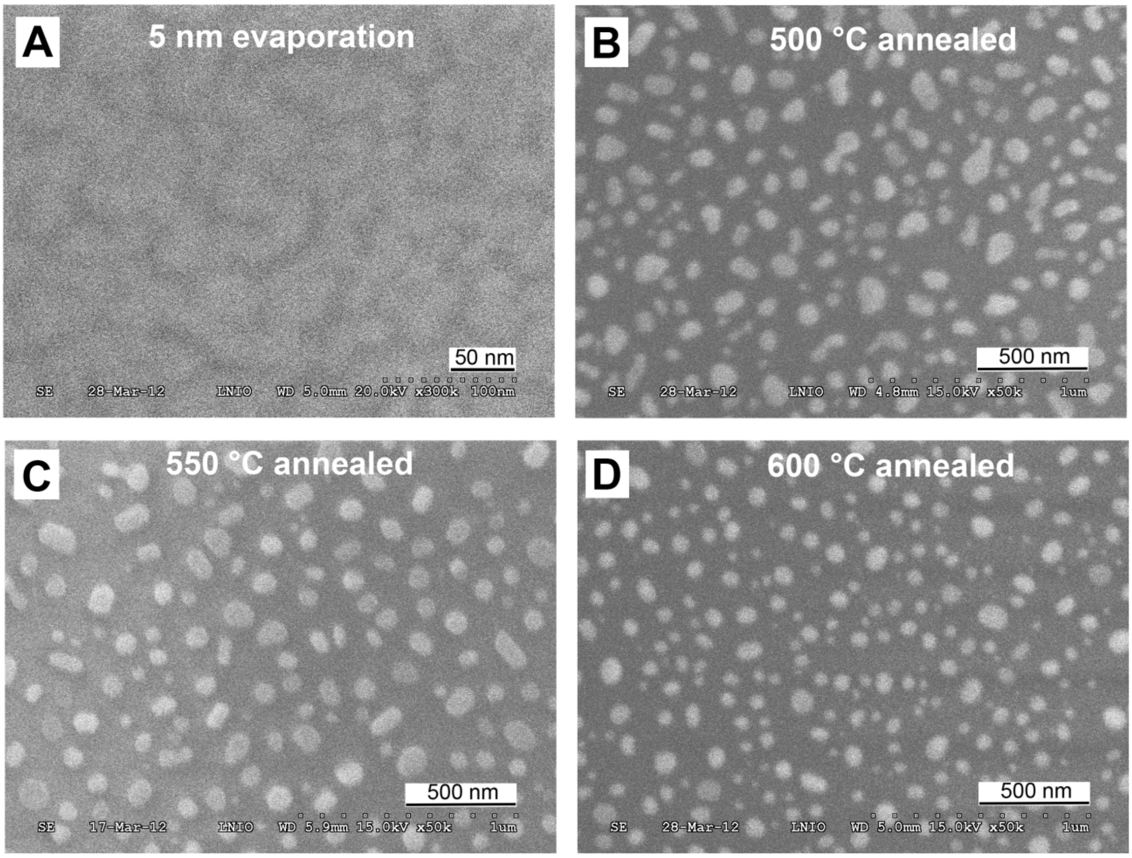

Figure 3.5 The SEM imaging for samples with nominative thickness of 5 nm under different conditions: as evaporated (A), annealing at 500 °C (B), 550 °C (C) and 600 °C (D) for 8 hr. The images are captured by Hitachi S3500N SEM and scale bar is 50 nm for (A) and 500 nm for (B-D) respectively.

Since the LSPR spectra of 8 nm thickness sample has totally different characteristics at a given annealing temperature, when compared with those of 2 nm and 5 nm thicknesses sample (**Figure 3.4D**), the SEM morphology characterization was employed and the results were shown in **Figure 3.6**. For 8 nm "almost" continue evaporated gold film, similar groove-like structures as in case of 5 nm thicknesses were observed (**Figure 3.6**A). These results are corroborated with the previous results shown in **Figure 3.2**. However, for the annealed surface, the size of nanoparticles was evidently increased after annealing at higher temperature, which would be the reason for the red-shift of resonant wavelength at higher annealing temperature.

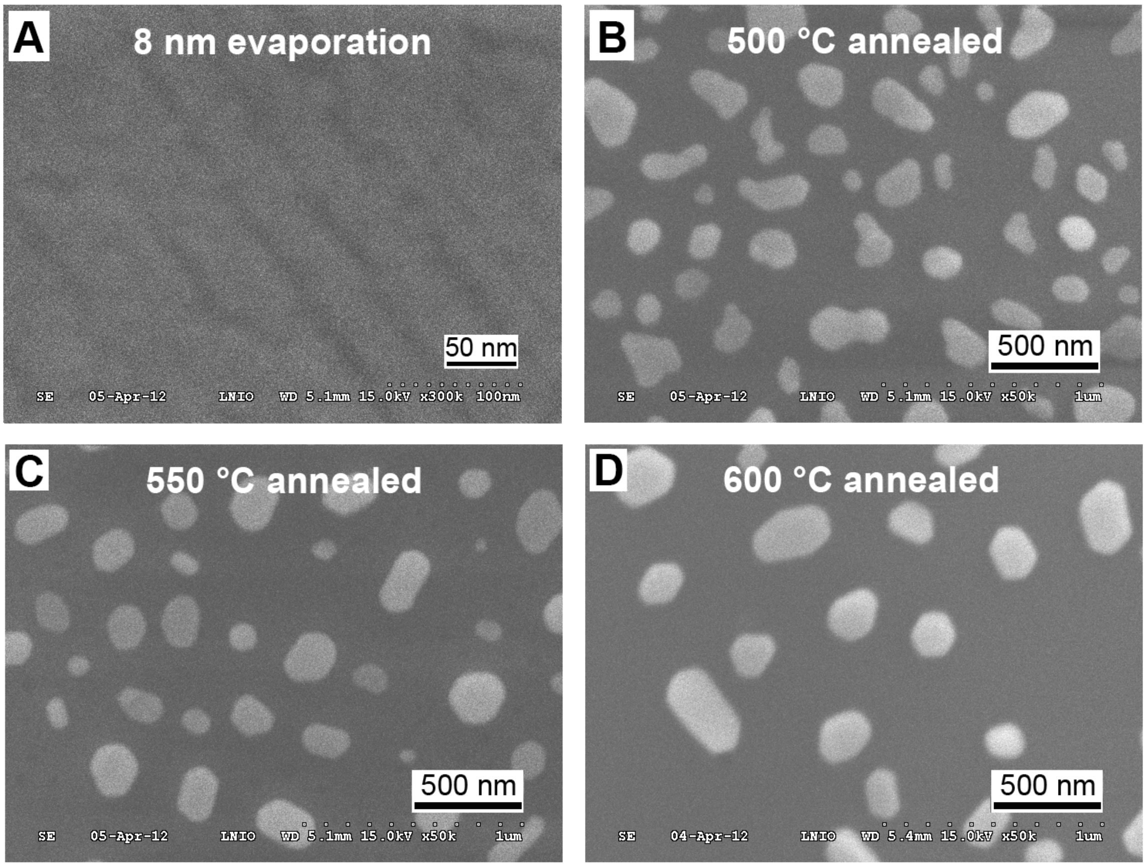

Figure 3.6 The SEM imaging for samples with nominative thickness of 8 nm under different conditions: as evaporated (A), annealing at 500 °C (B), 550 °C (C) and 600 °C (D) for 8 hr. The images are captured by Hitachi S3500N SEM and scale bar is 50 nm for (A) and 500 nm for (B-D) respectively.

In short, the annealing temperature has more complicated influence onto the plasmonic extinction peak evolution when compared with the use of various gold film thicknesses. Considering the fact that as increasing of annealing temperature, the totally different plasmonic peak evolutions (wavelength shift, intensity and shape changes) were recorded, it can be induced that there would be a critical film thickness, where maybe different mechanisms are responsible for distinct annealing temperature dependent plasmonic tunability.

3.2.1.3 Reproducibility of plasmonic spectra

Since the metal evaporation followed by high temperature annealing is intended to fabricate stable gold nanoparticle on glass in large scale, the reproducibility of this protocol should be evaluated. Firstly, the plasmonic properties of obtained Au NPs are studied in terms of thermal annealing history. While there are some reports pointed out the stability of gold nanostructure on glass substrate is formulated in the beginning of thermal annealing (around 15 min), the longer periods of times may contribute to the sinking of gold nanoparticles partially inside glass.[17] Based on these assumptions, thermal pre-incubation studies before achieving the desired the high annealing temperature have been conducted. Experimentally, it was studied the LSPR properties of 2 nm sample subject to different temperature increases rate from room temperature up to 550 °C. As shown in **Figure 3.7**A, after annealing at 550 °C for 8 hr, the plasmon peak amplitude and resonant wavelength are independent of thermal history prior to high temperature annealing. Thus, the LSPR spectra were only dependent of film thickness and annealing temperature in this protocol. Additionally, several batches of samples were measured and very reproducible LSPR spectra were recorded in a relative large test area (about 1 cm^2) (**Figure 3.7**B). Thus, the obtained Au NPs show excellent reproducible plasmonic spectra.

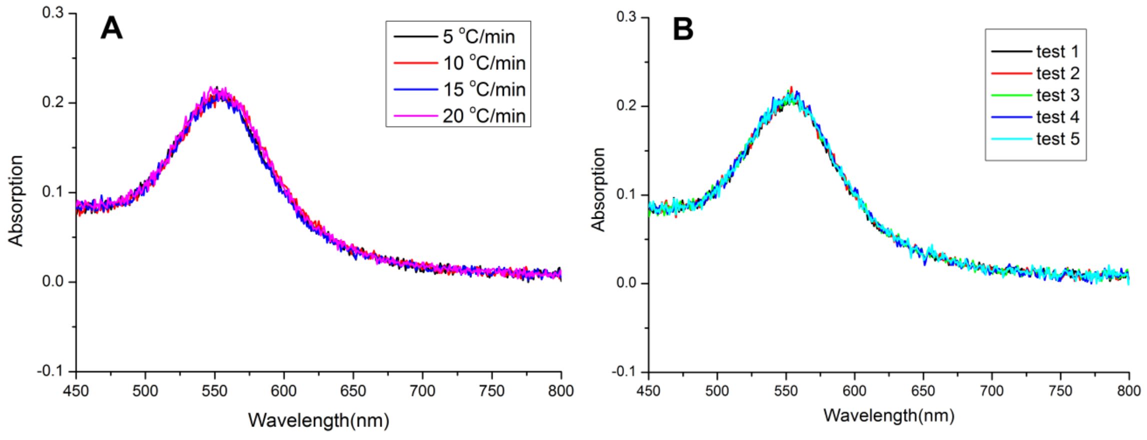

Figure 3.7 The LSPR spectra for annealed sample with different initial thermal history (A) and reproducible optical response of homogenous surface (B), test 1 to test 5 represent the different points measured around 1 cm^2 area on gold nano-structured surface.

In conclusion, crystalline gold nano-structures were prepared by electron beam evaporation approach followed by the high annealing temperature procedure in this part. The influence of different gold evaporated thicknesses (2 nm, 5 nm and 8 nm) and annealing temperatures (500 °C, 550 °C and 600 °C) through the LSPR spectra were investigated. For samples with smaller nominative thicknesses (2 nm and 5 nm), the isotropic effects due to higher temperature annealing was responsible for blue-shifted and sharper plasmonic peaks, while for the sample with larger film thicknesses (8 nm), the size increasing effect contributed to the plasmonic peak evolution. Based on these results, the protocol of evaporation followed by annealing near glass transition temperature of substrate was considered as an effective and robust methodology to obtain stable LSPR nanostructure with great plasmonic tunability, which should open the possibility to large scale fabrication of LSPR structures on glass substrate.

3.2.2 Multiplexing nanostructures on single glass substrate

The extremely stable Au nanoparticles have been created on glass substrate via the robust protocol of evaporation followed by high temperature annealing from previous part **3.2.1**, however the disadvantage is that Au nanoparticles of only one specific size is obtained from single experiment. Thus, a lot of samples with different sizes are required in the LSPR biosensor applications where the optimization of nanoparticles size normally is the prerequisite. Therefore, the protocols capable of fabricating multiplexing gold nanostructures on single substrate are highly demanded.

In this part, two new protocols are reported to obtain different zones of localized surface plasmon resonance (LSPR) gold nanostructures on single glass substrate by using very simple materials like staples and scotch tapes, respectively. The first protocol enables the preparation of “barcode-like” sample from which the systematic correlation between evaporation thickness and size of obtained Au NPs is constructed, thereby allowing the fast selection of optimized nanoparticle size for biosensor applications. The second protocol is designed to continuously modify the gold nanoparticles sizes in a specific area on glass substrate. There are pros and cons for these two independent protocols. A precise “calibration-curve” between nanoparticle size and evaporation thickness from first protocol allows reproducible fabrication of optimized Au nanoparticles, but this protocol is a slow process and needs more gold compared to the second one. On the contrary, the second protocol is time-efficient in terms of nanoparticle size optimization; while it is quite challenge to provide the corresponding experimental conditions (evaporation thickness) to reproduce the same nanoparticles.

3.2.2.1 Independent preparation of various zones of gold nanoparticles on single glass substrate – two protocols

It has been reported that the nominative thickness of evaporated film plays a decisive role in the final morphology of gold nanoparticles after annealing, which in turn determines their plasmonic properties.[18] Most of published works have evaporated one fixed thickness of gold film on single substrate, thus a specific plasmon resonance has been developed for each annealed sample.

In the present work, it is able to fabricate different zones of nanoparticles on single glass substrate, which has remarkable advantages in the multiplexing LSPR nanosensor applications. Given the importance of evaporated film thickness as mentioned above, the two proposed protocols both focus on the modulation of evaporated gold film thickness in a controlled manner before annealing.

3.2.2.2 First protocol: repeated gold evaporations on single glass substrate

This protocol is based on 4 cycles of gold evaporation (2 nm film for each cycle). The scotch tape was used as mask to prevent certain glass areas from gold deposition. Consequently, “barcode like” substrates containing four different nominative thicknesses (2 nm, 4 nm, 6 nm and 8 nm) of gold film were prepared. Thus, different nanoparticles sizes and shapes (i.e. different colors) on single substrate were developed after high temperature annealing step at 550 °C, a schematic illustration for this repeated gold evaporation cycles on predefined glass was shown in **Figure 3.8**.

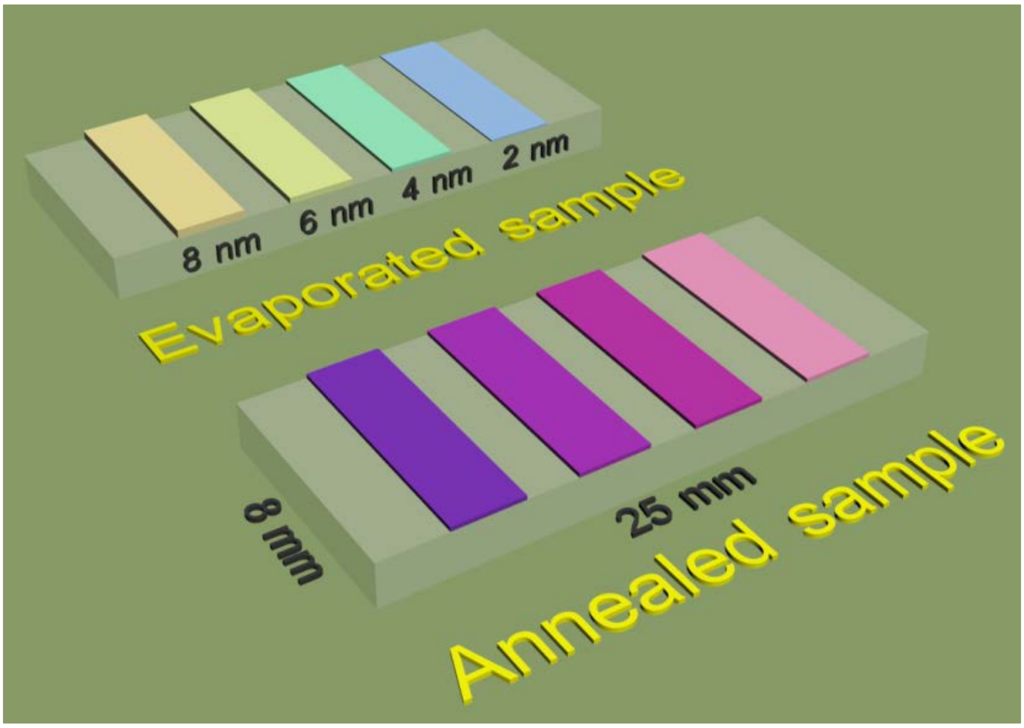

Figure 3.8 The illustration of "barcode" like samples prepared from first protocol of repeated gold evaporation onto predefined areas of glass substrate. The gold evaporation thicknesses and sample dimensions are shown in figure, it should be noted that these numbers are not in real scale and only used for description.

3.2.2.3 LSPR spectra and SEM morphology characterization of Au NPs obtained from first protocol

The LSPR spectra and corresponding nanostructures morphology are characterized using extinction measuring and field emission scanning electron microscopy (FESEM) imaging, respectively. For the sample obtained with the first protocol, the measured LSPR spectra for four independent zones were correlated with their initial evaporated film thicknesses (**Figure 3.9**A). It should be noted that in the beginning, as the nominative gold film increasing, the peak amplitude is obviously increased while the resonant wavelength is slightly shifted. However, the wavelength shift becomes dominant as further increasing of film thickness. For example, when the nominative evaporated film thickness increased from 2 nm to 4 nm, the maximum optical density was increased from 0.23 to 0.45 while the resonant wavelength only slightly red shifted from 561 nm to 566 nm. However, when the evaporated film thickness further increased from 4 nm to 6 nm, a relative large red-shift of resonant wavelength (25 nm) was observed, while the maximum optical density was only increased 0.08. Finally, when the film thickness further increased to 8 nm, a large wavelength red-shift to 742 nm was observed, and a much wider peak with maximum optical density declined to 0.4 was recorded. Extinction of smaller particles is dominated by absorption and thus there is a small size induced red shift. For bigger particles when extinction is dominated by scattering a strong red shift is observed.

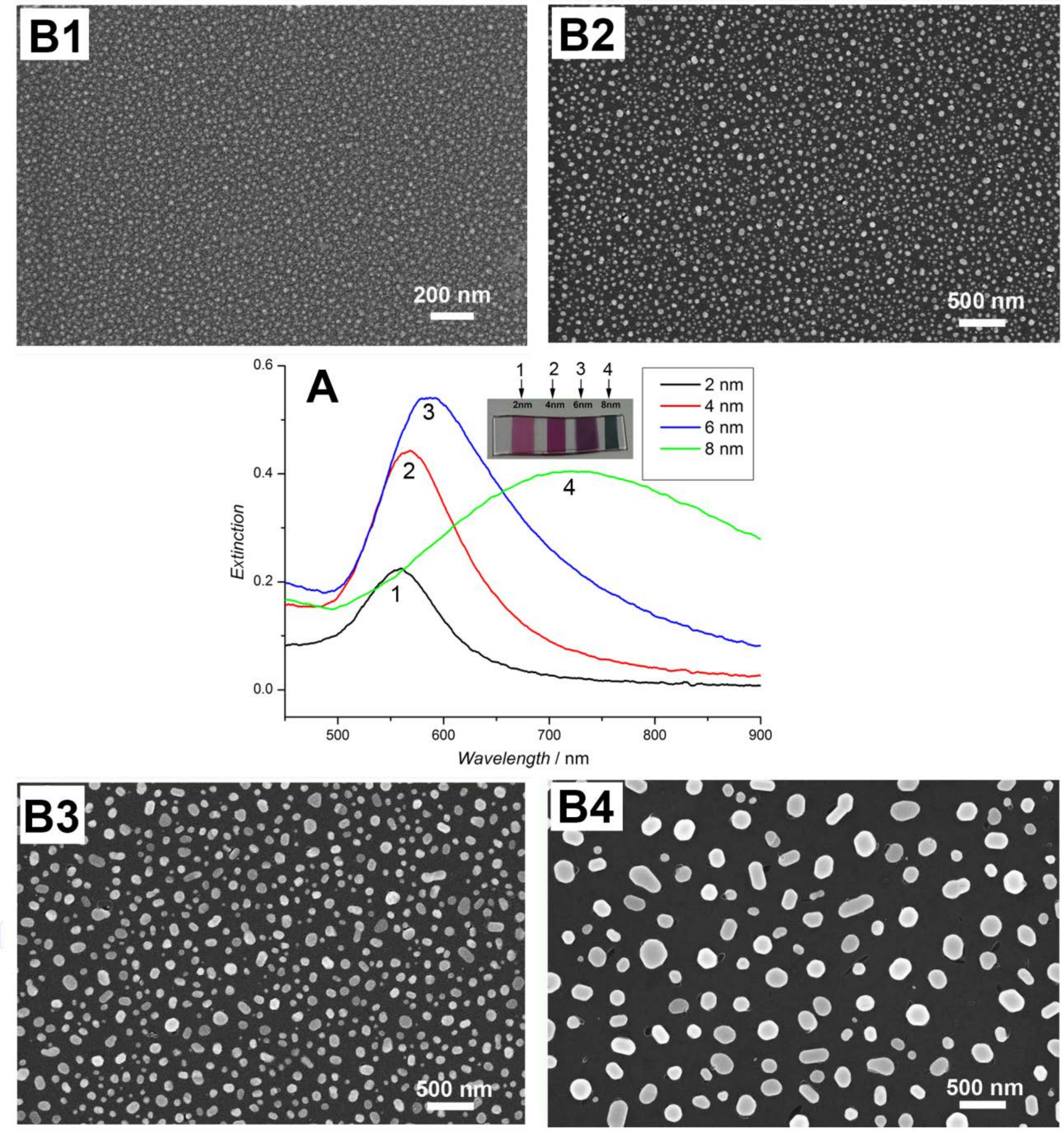

Figure 3.9 LSPR spectra (A) and corresponding SEM morphology of gold nanoparticles (B) for 550 °C annealed samples with nominative evaporated film thickness of 2 nm (B1), 4 nm (B2), 6 nm (B3) and 8 nm (B4), the number 1, 2, 3, 4 are corresponding to the different evaporated thickness of 2 nm, 4 nm, 6 nm and 8 nm before high temperature annealing, respectively.

From the corresponding SEM images shown in **Figure 3.9**B1-B4 and the size distribution histogram in **Figure 3.10**, as the nominative evaporated film thickness increased, the interparticle distance was increased, which can imply a blue shift of resonant peak; however, if interparticle gaps are larger than particles diameters this effect will be negligible. Size increasing becomes the dominant factor for the thicker film. It should be noted that the size distribution for 8 nm film sample (**Figure 3.10**) was less uniform than that of sample with lower film thicknesses, which is partly responsible for the observed spectra broadening effects in this case. Additionally, the broadening effect is attributed to radiation damping induced by the nanoparticles size increases.

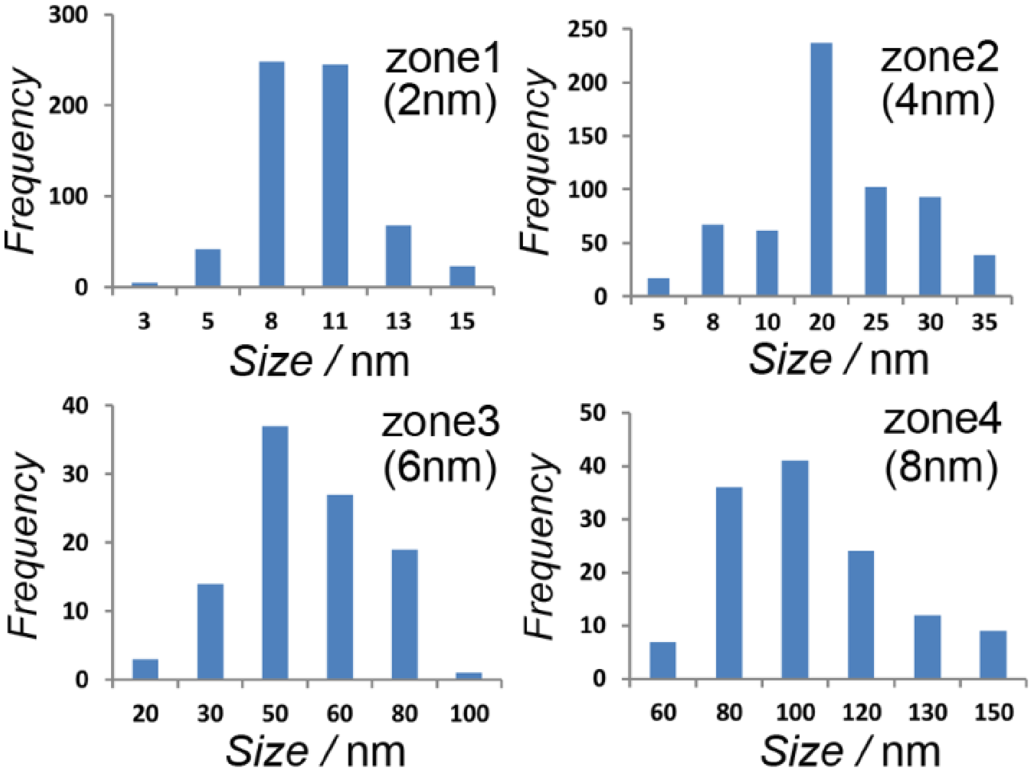

Figure 3.10 Gold nanoparticle size distribution histograms for annealed sample (550 °C, 8 hr) with different initial film thickness of 2 nm (zone1), 4 nm (zone2), 6nm(zone3) and 8 nm (zone4).

It is well known that the plasmonic properties (resonant wavelength, peak width and amplitude) are determined by the morphological features of gold nanoparticles, which can be readily modulated by using different nominative evaporated film thicknesses after annealing. Using the first protocol to fabricate samples with different evaporation thicknesses on single glass substrate, it is able to construct a correlation between initial film thickness and plasmonic properties, which is plotted in **Figure 3.11**. Interestingly, the most intense plasmonic peaks are obtained for particles with an average size of 57.5 nm, which is in agreement with Mie theory calculations.[21]

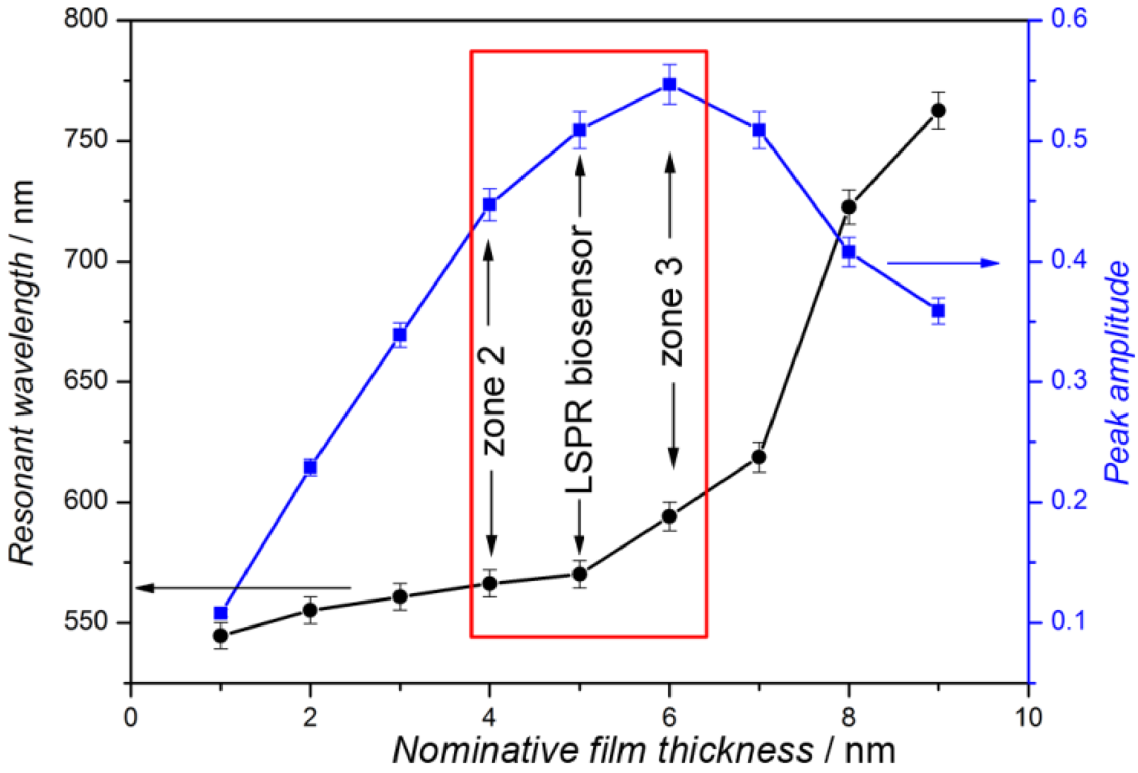

Figure 3.11 Correlation between evaporated film thickness before annealing and its plasmonic features of resonant wavelength and maximum extinction after annealing at 550 °C for 8 hr.

It can be seen that the most intensive plasmonic peaks are observed between zone 2 (4 nm gold evaporation) and zone 3 (6 nm gold evaporation) after annealing at 550 °C for 8 hr. This specific range is thus considered as the “LSPR biosensor window”, which should contain the optimized plasmonic structures for biosensing experiment. The detailed physical dimensions information and optical spectra data (including resonant wavelength and maximum OD value) were summarized in **Table 3.2**.

Table 3.2 Physical dimensions of obtained gold nanoparticles and corresponding LSPR features for samples with different initial evaporated film thickness from 1 to 8 nm. All the samples were annealed at 550 °C for 8 hr.

Evaporated film thickness [nm]	Physical dimensions		Optical spectra	
	Average Size [nm]	Aspect ratio	Peak wavelength [nm]	Maximum extinction
1	8.2 ± 2.4	1.12 ± 0.06	544.65	0.108
2	10.2 ± 2.8	1.14 ± 0.08	555.15	0.229
3	17.5 ± 3.9	1.08 ± 0.09	560.82	0.339
4	21.6 ± 5.4	1.13 ± 0.11	566.34	0.447
5	42.8 ± 8.3	1.06 ± 0.08	570.11	0.509
6	57.5 ± 10.8	1.11 ± 0.07	594.14	0.547
7	75.4 ± 15.3	1.23 ± 0.12	618.76	0.509
8	110.4 ± 23.7	1.35 ± 0.16	722.53	0.408

3.2.2.4 Second protocol: morphology gradually modulated Au NPs on single substrate

In this protocol, metal staples were fixed on the top of a glass substrate, leaving a gap between the mask (staples) and the substrate (glass). Due to the “shadowing effects” of used staples, an artificial gold-glass interfacial area was created, where the thickness of evaporated gold film in transversal directions was gradually modulated, leading to different sized gold nanoparticles after high temperature annealing (550 °C) step. A schematic illustration for the samples obtained from this protocol was shown in **Figure 3.12**, two transition zones located exactly at the gold-glass interface (e.g. area underneath the staples) were observed for the annealed sample. When these special areas were projected using conventional optical microscope, a multicolor transition zones were recorded (see inset microscope image), and the color changed from violet (glass side) to blue (gold nanoparticle side). According to a systematic study of thermal annealed gold nanostructures, the sample with varying evaporated film thickness exhibited different colors after annealing. Thus, a violet color corresponds to thinner evaporated film while the blue color is attributed to the thicker film, which corroborates the assumption of “shadowing effect” provided by metal staples mask.

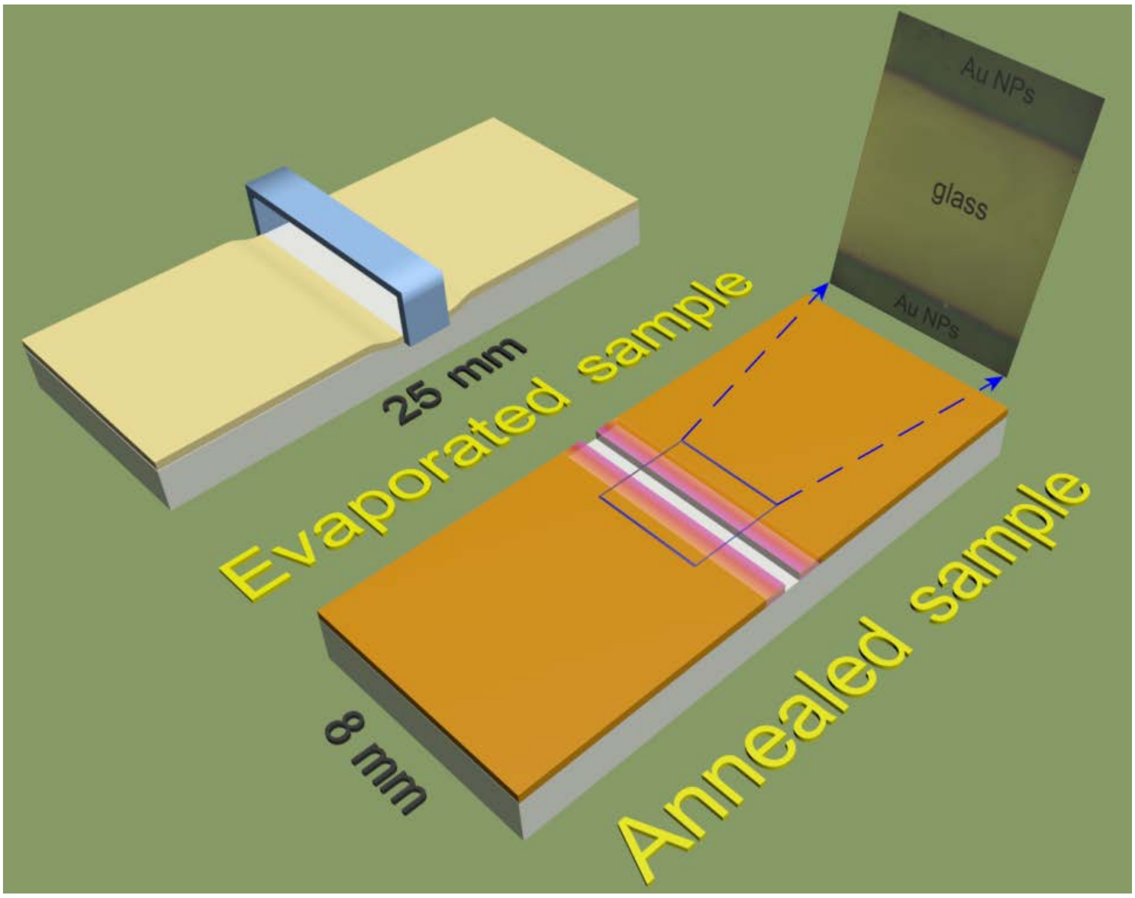

Figure 3.12 The illustration of samples prepared from second protocol using metal staples as the mask to gradually modulate the gold evaporation thickness on specific area of glass substrate. A typical optical microscope image of the “shadowed” areas (highlight by blue rectangle) is shown in the inset.

3.2.2.5 LSPR spectra and SEM morphology characterization of Au NPs obtained from second protocol

For the samples prepared with the second protocol, we have focused on the gold-glass interfacial area. In order to better understand the plasmonic spectra and SEM morphology, different gold nanoparticles in the vicinity of the gold-glass interfacial area were numbered from 1 to 4, corresponding to position moving from glass side to gold side, as indicated with a black arrow in the **Figure 3.13**A. The LSPR spectra for the 4 different zones were recorded, while the SEM images corresponding to different zones of gold nanoparticles were illustrated in **Figure 3.13**B1-B4. Experimentally, when moving from area 1 to area 4 within the interfacial zones, the maximum extinction wavelength red-shifted from 568 nm for curve 1 to 677 nm for curve 4, with a concomitant increasing of peak amplitude from 0.2 to 0.475, respectively.

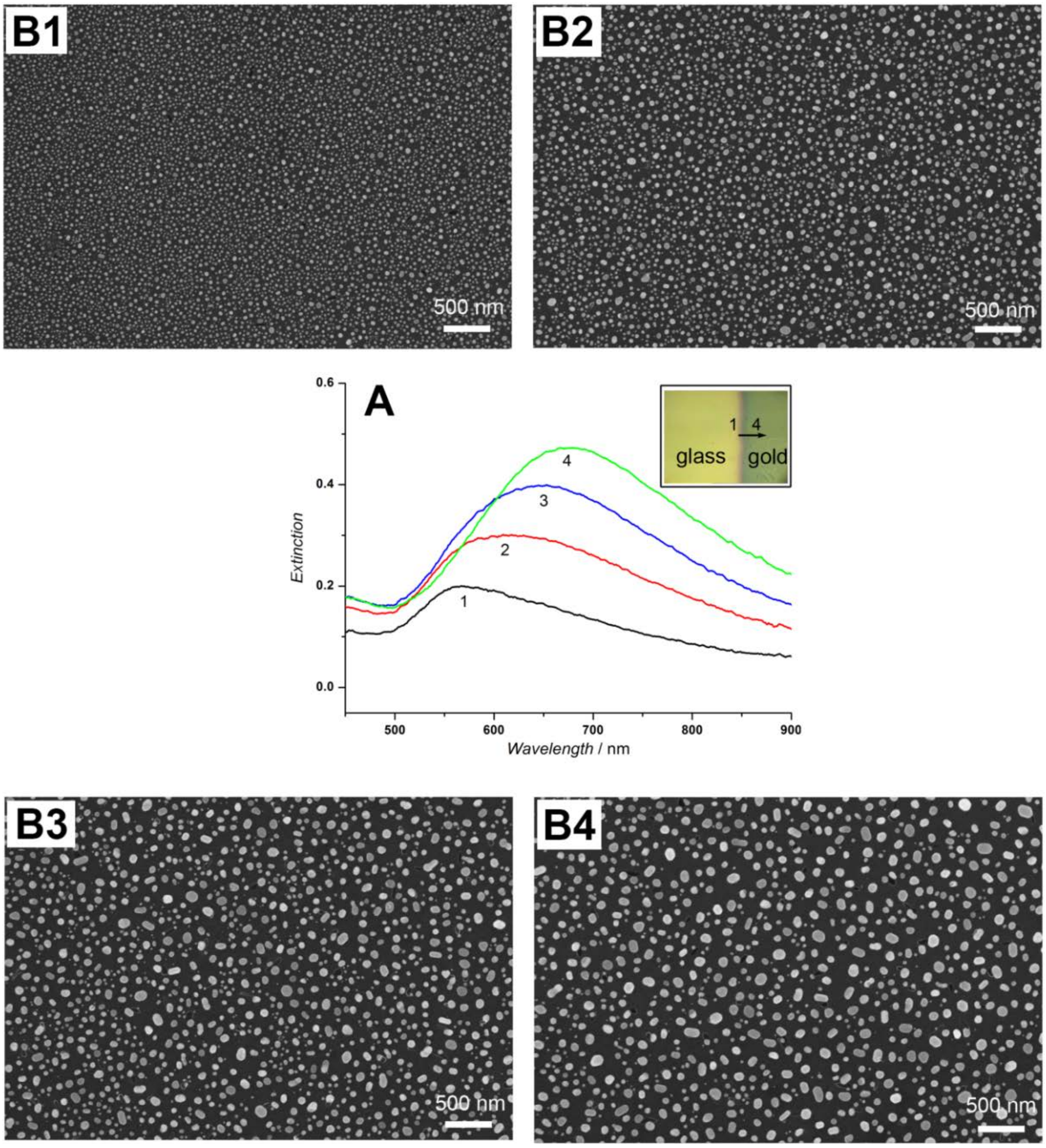

Figure 3.13 LSPR spectra (A) of different zones of gold nanoparticles in the glass-gold transitions (1 to 4) and their corresponding SEM morphology (B1-B4), number B1 to B4 denotes the nanoparticle zones moving from glass side to gold side, respectively.

The Au nanoparticle size distribution was analyzed by ImageJ software for each zone and these results were shown in **Figure 3.14**. It is obvious that the average size of gold nanoparticle was increasing from 15 nm for zone 1 to 45 nm for zone 4. Thus, the red-shift of resonant extinction wavelength and increasing of optical density recorded in **Figure 3.13**A were mainly attributed to the increasing of nanoparticle size.

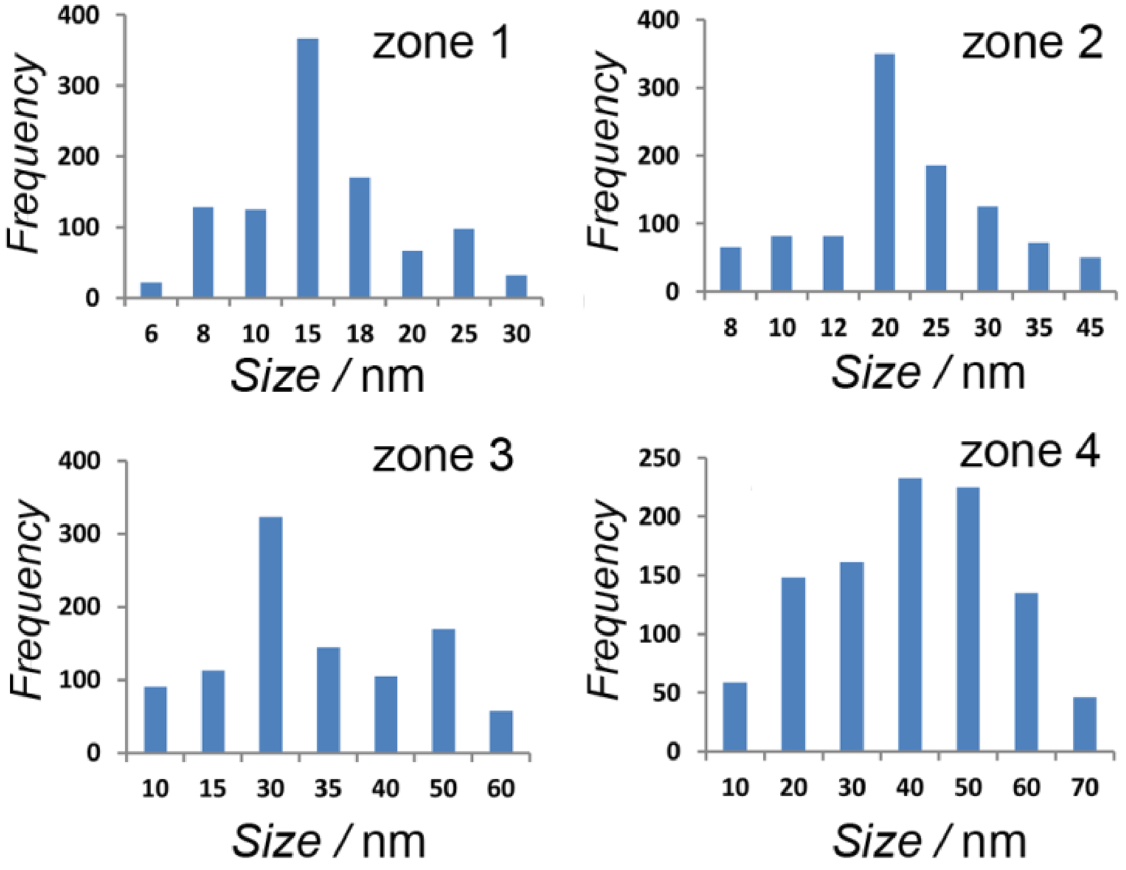

Figure 3.14 Gold nanoparticle size distribution histograms for different zones within the glass-gold interfacial area of sample obtained from second protocol.

In summary, the reported two protocols both stem from the idea to modulate gold evaporated film thickness at predefined area on the same glass slide, thus allowing fabrication of multiplexing gold nanostructures with different morphology on single glass substrate. By comparing the spectroscopic data with the nanoparticles morphology obtained from the two protocols, the plasmonic peaks for the sample of second protocol were generally wider than those recorded for the sample of first protocol. Indeed, a narrower size distribution was observed for the sample obtained by repeated evaporation protocol (see **Figure 3.9** and **Figure 3.10**), which explains the sharper peaks observed with first protocol. More homogenous nanoparticles generally lead to sharper plasmonic extinction peak.[20] The optimization of Au NPs morphology, i.e. size, shape and interparticle distance, is especially important for LSPR biosensors application and normally is a time consuming procedure given the diversity of nanoparticle morphology. Fortunately, the two protocols developed in this work provide effective plasmonic substrate to quickly select the optimized Au NPs among many possible candidates. The second protocol to created morphology gradually modulated Au NPs on single substrate seems particularly interesting; however there is an obvious disadvantage from this protocol, the different sized Au nanoparticles are continuously located in very limited areas, thus it is quite challenge to precisely record the LSPR spectra and the corresponding SEM morphology for one specific nanostructure. In fact, this disadvantage serves as the drive force for the following work to prepare well organized plasmonic micro/nano-structures.

3.2.3 Well-organized gold micro/nano-structures on glass substrate

In the first two parts, some basic requirements for the plasmonic substrates to be used in LSPR biosensor have been systematically addressed. For instance, the first part **3.2.1** mainly introduces the robust protocol of metal evaporation followed by high temperature annealing to fabricate ultra-stable Au nanostructures on glass substrate. The second part of **3.2.2** deals with the preparation of multiplexing gold particles with different sizes on single glass substrate, which facilitates the experimental screening the optimized plasmonic structure for intended LSPR biosensor application. However, there is still one essential aspect missing: the possibility to use one single glass substrate for several biomolecules dilutions detection. In this part, the commercial transmission electron microscope (TEM) sample holder, micro-structured cooper grid is used as the mask during the metal evaporation to create well-organized gold micro/nano-structures after high temperature annealing.

3.2.3.1 TEM grid mask: to prepare well-organized gold micro/nano-structures

A schematic illustration describing the preparation of gold micro/nano structure on glass substrate is shown in **Figure 3.15**. Experimentally, a TEM cooper grid (200 mesh, diameter of 3.05 mm) was fixed onto the clean glass substrate as a mask in the metal evaporation of gold thin film (4 nm), after a high temperature annealing at 500 °C for 8 hr, the gold micro/nano plasmonic structures were created.

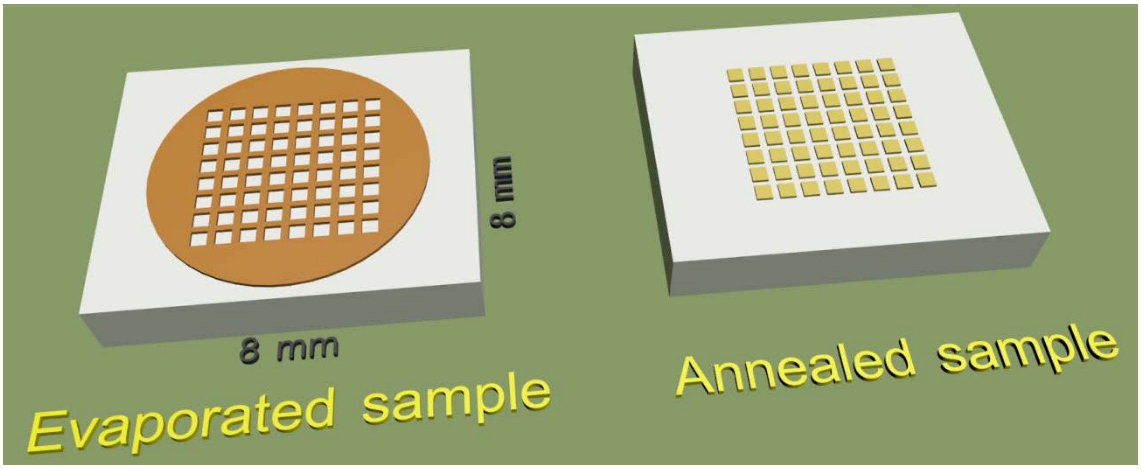

Figure 3.15 The illustration of TEM grid used as the mask to fabricate the well-organized gold micro/nano-structures on glass substrate. The dimensions of glass substrate are in 8 mm × 8 mm.

Thanks to the patterned TEM grid onto the glass substrate, well-defined zones of thin layer of gold (4 nm) are obtained after evaporation, which further are converted into stable gold nanoparticles inside patterns once the annealing procedure is performed (**Figure 3.16**). The experimental results show that if the TEM grid is carefully removed after the gold evaporation step, then the integrity of the deposited gold patterns isn't destroyed and consequently larger areas of well-organized gold micropattetns are created in a millimetre scale (diameter of grid is 3 mm). Interestingly, the micro/nano structures remain unchangeable after high temperature annealing procedure, except for their color that is changing from light blue for the gold evaporated sample to light violet for the annealed sample. Moreover, the annealed patterns consisting of gold nanoparticles are extremely stable in various solvents and biological buffers, which is due to the partial embedding of nanoparticles inside glass derived from the high temperature annealing procedure.

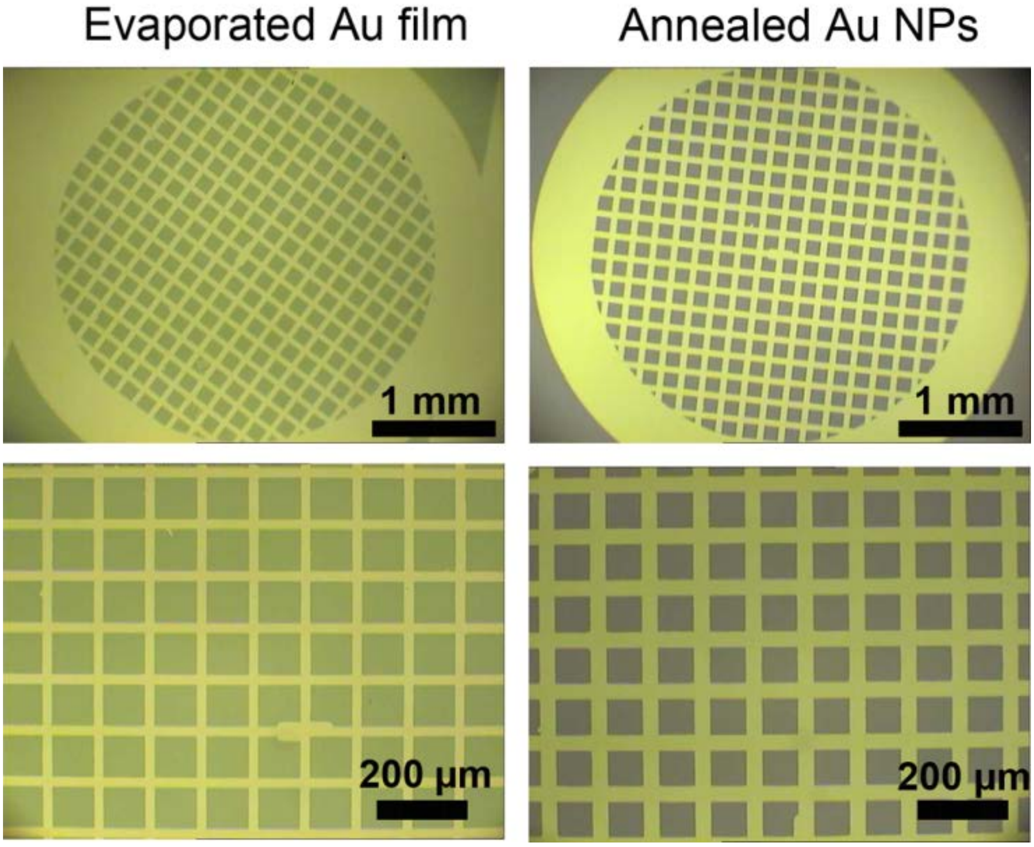

Figure 3.16 Optical microscopy images of patterned gold micro/nano-structures onto a glass substrate by using different magnifications (top: objective 4x; bottom: objective 10x) before annealing (left) and after annealing (right).

3.2.3.2 LSPR spectra and SEM morphology characterization of well-organized Au NPs obtained from TEM grid mask

It should be mentioned that the LSPR extinction spectra were measured by a home-built confocal transmission UV-Vis-NIR optical setup. Because of the optical fibers and lens combination used in the measurement setup, the incident beam with spatial resolution of 10 µm was focused perpendicularly to the nanosensor chip. Since the size of single grid’s pattern is about 100 µm, at least 5 different areas inside one tested pattern were investigated, compared and averaged in the final LSPR spectra. The statistical analysis of LSPR properties of obtained Au nanostructures were conducted by recording extinction spectra from 8 independent samples and the results were summarized in **Table 3.3**. It should be noted that for each sample, three different patterns were chosen and 5 different points inside one pattern were tested. From these statistical data, for a sample with 4 nm initial evaporated gold film thickness and annealed at 500 °C for 8 hr, the average plasmonic resonant wavelength located at 566.7 ± 1.5 nm, and the maximum optical density was recorded as 0.27 ± 0.03. The relative standard derivation (RSD) value for resonant wavelength and maximum optical density is lower than 0.3 % and 5.5 %, respectively, which indicates a good reproducibility of LSPR properties of obtained Au nanostructures.

Table 3.3 LSPR data including resonant wavelength and maximum extinction of annealed Au NPs obtained from three different patterns of 8 independent samples. The data shown represent the average of 5 LSPR measurements inside one pattern. One pattern corresponds to one square of a TEM-grid pattern.

	λ: resonant wavelength (nm), OD: maximum extinction			Average λ, OD	RSD	
Sample	Pattern 1	Pattern 2	Pattern 3		λ	OD
No 1	566.8, 0.31	567.9, 0.29	567.1, 0.30	567.3, 0.3	0.1%	3.3%
No 2	564.8, 0.26	563.1, 0.25	563.7, 0.26	563.9, 0.26	0.15%	2.25%
No 3	566.2, 0.30	567.8, 0.29	568.5, 0.32	567.5, 0.3	0.21%	5.04%
No 4	566.1, 0.27	564.9, 0.26	565.1, 0.25	565.4, 0.26	0.12%	3.85%
No 5	566.2, 0.28	565.9, 0.29	567.8, 0.31	566.6, 0.29	0.18%	5.21%
No 6	566.8, 0.27	568.4, 0.28	567.9, 0.3	567.7, 0.28	0.14%	5.39%
No 7	565.8, 0.26	566.1, 0.26	567.2, 0.25	566.4, 0.26	0.26%	2.25%
No 8	565.3, 0.31	566.7, 0.3	567.9, 0.32	566.6, 0.31	0.23%	3.23%

A single gold micro-pattern annealed at 500 °C for 8 hr is characterized by using the field emission scanning electron microscopy (FESEM, Raith). Prior to imaging, the sample was sputter coated with a thin layer (about 2 nm) of palladium to suppress the charging effects. **Figure 3.17**A shows a gold pattern measured as 91 μm × 91 μm, which is very close to the copper grid mesh size (90 μm). In addition, under higher SEM magnification (**Figure 3.17**B), the individual gold nanoparticles with smooth surfaces are clearly observed thanks to their good dispersion onto the glass substrate. The sizes of gold nanoparticles are analyzed by using the public domain software ImageJ developed by National Institutes of Health, and the obtained histogram is shown as an inset (**Figure 3.17**B). Based on the histogram results, after the sample is annealed at high temperature of 500 °C, stable and homogenous gold nanoparticles with average size of 22.4 ± 2.8 nm are created on the individually organized micrometre scale patterns.

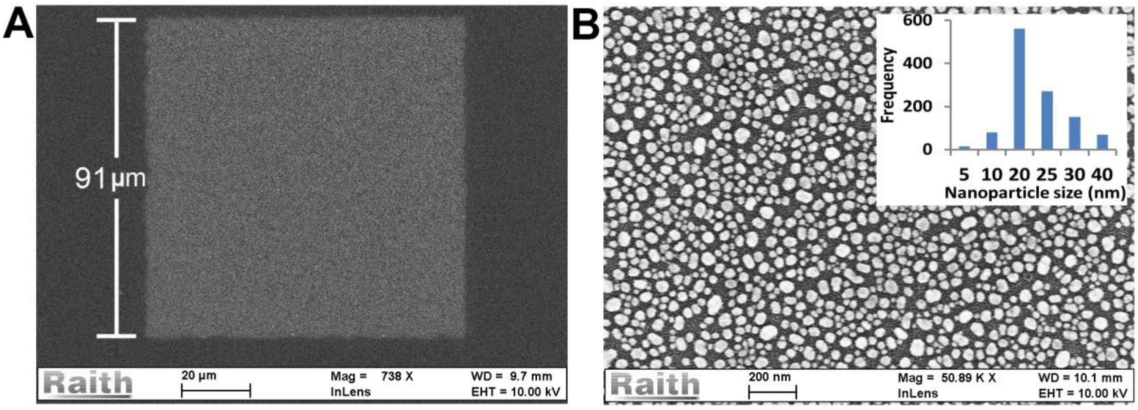

Figure 3.17 SEM characterization of a single TEM-grid pattern (A) and gold nanoparticles inside the same pattern (B). The patterned grid is annealed at 500°C for 8 hr. The inset shows a size distribution histogram of obtained gold nanoparticles.

In summary, the systematic studies concerning the preparation of extremely stable Au NPs are presented in this chapter of **3.2**, where also includes several independent protocols to fabricate multiplexing and well-organized gold nanostructures on single glass substrate. Using these innovative protocols, a wide range of Au NPs with controlled modulating morphology can be readily fabricated in large scale.

3.2.4 Biomodification of Au nanostructures and specific biomolecules detection

In a typical LSPR biosensor application, a sensing element (antibody, enzyme, or nucleic acid) is modified on the surface of nanoparticles to specifically recognize its target, and this biochemical reaction will be converted to the quantifiable optical signals via the transducer, in this case is the metal nanoparticles.[22] The optical responses of LSPR biosensors are highly dependent on the local electromagnetic field distribution in the surroundings of nanoparticles. Considering the exponentially decay of an evanescent plasmon field away from nanoparticle surface, the distance dependent optical response of LSPR biosensor upon the formation of a functional layer at the metal surface can be described according to Campbell and co-workers:[23]

$$R= m(\eta_a-\eta_s)\exp(-2d_i/L_d)[1- \exp(-2d_a/L_d)] \qquad (1)$$

where d_i and d_a are the thickness of recognition interface layer and adsorbed layer, respectively, assuming both layers have same refractive index η_a. According to the Equation 1, in order to obtain the best sensitivity of LSPR biosensor, attention should be dedicated: (i) to increase the refractive sensitivity (m) of nanoparticles, (ii) to optimize the balance between decay length (L_d) and the biorecognition interface layer thickness (d_i and d_a). Therefore, by using nanoparticles of different shapes, sizes and compositions, it is possible to maximize the refractive index sensitivity (m). If the recognition biomolecules are located outside the sensing ranging of nanoparticles ($d_i>L_d$), the following binding events could not be detected anymore; on the other hand, if the decay length is much larger compared to size of biomolecules ($L_d>> d_i$), the biorecognition events would occupy limited fraction of the sensing range of nanoparticles. In both cases a poor sensitivity of LSPR biosensor will be obtained.[24-25]

As the first step, the samples prepared from the staples mask protocol have been used to quickly screen the optimized Au nanostructures for biosensor application, proved by sensitive detection of atrazine, then the TEM grid based protocol was explored to fabricate the well-organized micropatterns containing the specifically optimized gold nanostructure. Further, the optimized gold micro/nano-structures were functionalized as the high throughput biochip for multiplexing detection of BSA. Finally, the antibody biomodification on gold procedure was studied in an alternative surface sensitive technique based on quartz crystal microbalance (QCM) as well. Based on these results, the biomodification protocol used in this work guarantees the reliable immobilization of biorecognition molecules onto gold nanoparticles, leading to the sensitive and specific detection of biomolecules targets in a high throughput manner.

3.2.4.1 The screening of optimized gold nanostructures using samples obtained from staples masks protocol

In order to select the optimized gold nanostructures for LSPR biosensor application, a wide range of gold nanoparticles with different morphology (size, shape, interparticle distance, etc.) were subjected to various biomodification steps and their corresponding LSPR spectra were recorded and compared. Generally, this optimization is a time consuming process, and the efficiency is even worse when the samples used contain only one sized nanoparticles. Fortunately, it is able to speed up this nanoparticles size optimization using one substrate containing a range of sized Au NPs.[26] Therefore, the sample prepared based on “shadowing” effects protocol is firstly used to screen the optimized gold nanostructures. The LSPR spectra of annealed Au NPs and Au NPs successively modified with MUA self-assemble monolayer (SAM) and anti-human antibody are shown in **Figure 3.18**.

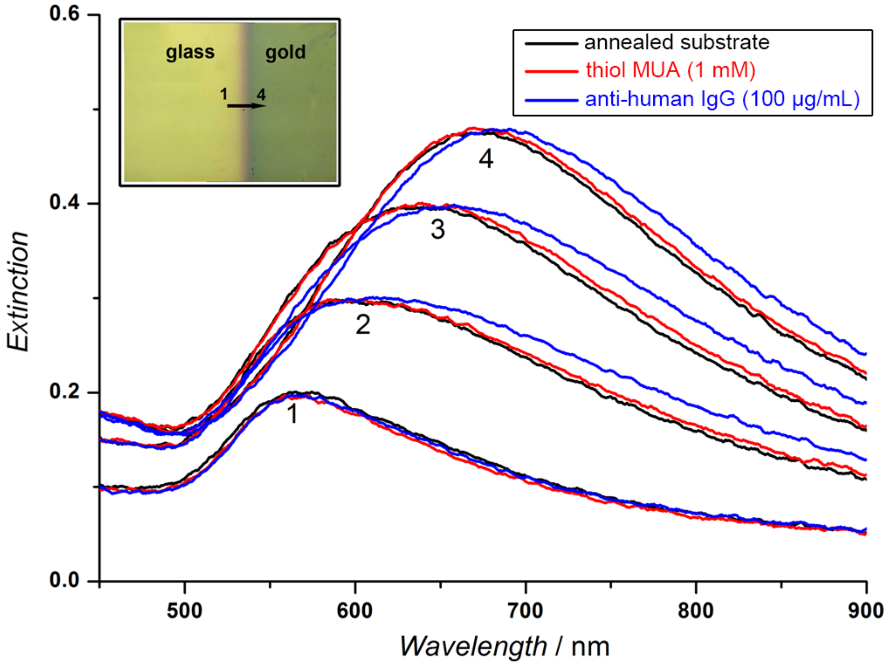

Figure 3.18 LSPR responses for different areas upon simultaneous biomodification of gold nanoparticles within the gold-glass interfacial zone. The sample is prepared by using the staples mask protocol described in **Figure 3.12** and a microscope image of this sample is shown in inset.

It is noticed that after the MUA functionalization step, the resonant wavelength was slightly red-shifted. Further, when the larger biomolecules (anti-human antibody) were immobilized in these interfacial areas, more obvious wavelength shifts were observed. Specifically, after binding of 100 µg/mL anti-human IgG antibody on gold nanoparticles, a 25 nm and 15 nm red shifts of resonant wavelength were measured for curve 4 and curve 3, respectively. However, only 6 nm of shift was observed for curve 2 and no obvious plasmonic responses were recorded for area 1. In short, the LSPR sensitivity was increased when the nanoparticle size increases from zone 1 to zone 4 within the gold-glass interfacial areas. Moreover, according to work of Chilkoti and co-authors,[27] the sensitivity of the LSPR nanosensor using larger gold nanoparticle (39 nm) was much better than that of smaller nanoparticles (13 nm). Interestingly, the average gold nanoparticles size corresponding to the most sensitive LSPR area in our work was also around 40~50 nm (**Figure 3.14**). Based on these results, the different LSPR sensitivity observed for different gold nanoparticle zones (**Figure 3.18**) could be attributed to a better match between the nanoparticle decay length and physical dimension of absorbed biomolecules.

On the basis of results in **Figure 3.18** and **Table 3.2**, gold nanoparticles with average size of 42.8 nm could be obtained by annealing the sample with 5 nm evaporated gold film thickness at 550 °C for 8 hr. Taking into consideration these parameters, the Au NPs with the optimized size was fabricated and used for atrazine detection. The LSPR spectra corresponding to different biomodification steps and atrazine dilutions are shown in **Figure 3.19**.

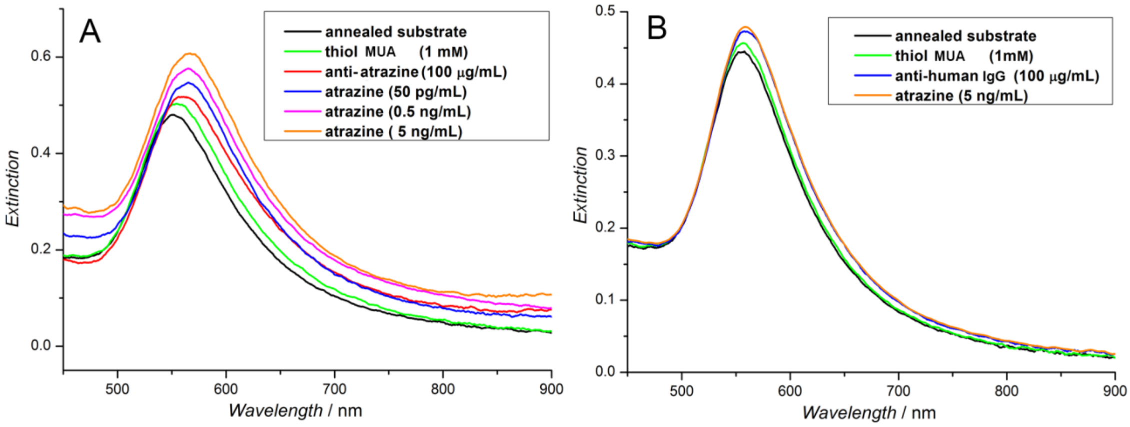

Figure 3.19 LSPR biosensor for specific detection of atrazine (A) and experimental control using atrazine non-specific anti-human IgG antibody under the same conditions (B). The initial evaporated film thickness was 5 nm followed by thermal annealing at 550 °C for 8 hr.

It is clear that the immobilization of MUA alkanethiol layer and anti-atrazine antibodies leads to a wavelength red-shift of 4 nm and 13 nm, respectively (**Figure 3.19**A). Next, after binding of antigen (atrazine), the wavelength shift was rather small as 5 nm for highest content atrazine. Instead, the peak intensity modulations become more important. Besides, the shift is independent of the concentration of the atrazine antigen. Specifically, the optical density increased from 0.547 for binding of 50 pg/mL dilution to 0.576 for 0.5 ng/mL dilution, which was further increased to 0.608 after binding of higher atrazine content of 5 ng/mL. From the obtained results, where the small molecules of atrazine (about 220 Da) were specifically detected through an LSPR immunosensor configuration, the main plasmonic response was firstly considered as wavelength shift due to large antibody immobilization, after which the optical intensity changes became predominant once the different antigen concentrations have been tested. In a control experiment using atrazine non-specific anti-human IgG modified Au NPs (**Figure 3.19**B), plasmonic wavelength is red-shifted after modification of thiol and anti-human IgG antibody. However, after exposure to 5 ng/mL atrazine, no plasmonic shifts were observed. Therefore, the LSPR responses shown in **Figure 3.19**A do correspond to the specific binding of atrazine to its antibody.

3.2.4.2 High throughput detection of BSA

Followed successful selecting of optimized Au NPs size, the plasmonic substrate was constructed as a biochip for large protein molecule (BSA) detection. Therefore, the plasmonic biochip was fabricated by using TEM grid protocol,[28] and then the overall biochip was functionalized by anti-BSA IgG antibody to demonstrate the possibility of detecting three different concentrations of antigen on single substrate.

The LSPR spectra corresponding to different biomodification steps involved in BSA immunosensor constructions are recorded in **Figure 3.20**A. As expected, due to the well-organized micrometric patterns on glass substrate and the precise control of incident beam position, the same patterns are followed during all these plasmonic measurements. Indeed, the TEM-approach highly facilitates the identification of one particular nano-structured micropattern at any time during experiments, therefore reducing drastically the usual area-to-area differences resulted from random LSPR investigations of gold nanoparticles after their formation at 500 °C. It is found that the bare gold nanoparticles inside the pattern exhibit obvious plasmonic peak at 567 nm with optical density of 0.3, after the thiol (MUA) surface modification of the gold nanoparticles, the resonant wavelength red-shifted to 570 nm with concomitant peak intensity increased to 0.33. Further, when the bigger anti-IgG BSA antibody is immobilized to the thiolated-substrate, a larger red-shift of wavelength of 7 nm is recorded, and the optical intensity is also increased to 0.37. Finally, after immobilization of antigen BSA (0.01 mg/mL), the LSPR peak is further red-shifted to 584 nm with optical density of 0.4.

On the other hand, the control experiment is also conducted by immobilizing a BSA non-specific antibody (anti-atrazine IgG) on the gold nanoparticles, the LSPR spectra corresponding to stepwise biomodification are described in **Figure 3.20**B. As can be seen, there are observed well-defined plasmonic wavelength shifts and increases of optical densities as the nanostructures are modified by the thiol and anti-atrazine IgG antibody. These results confirm the robustness of the surface biomodification based on high temperature annealed gold substrates. However, when the high concentration of BSA (0.01 mg/mL) is deposited on the non-specific antibody modified substrate, no wavelength shift combined with a slightly variance of the maximum optical density are observed. These experiments confirm the non-specific interaction of BSA with the anti-atrazine IgG antibody modified surfaces.

Moreover, the morphology of gold nanoparticles before and after BSA immobilizations is also characterized using FESEM. As shown in **Figure 3.20**C, a relative smooth surface is observed for the pure gold nanoparticles, and the bare gold nanoparticles are individually separated with each other. However, after the antigen BSA protein modification, a relative rough surface morphology of gold nanoparticles is observed where the protein modified nanoparticles tended to be connected together, especially in the area highlighted with the red rectangle.

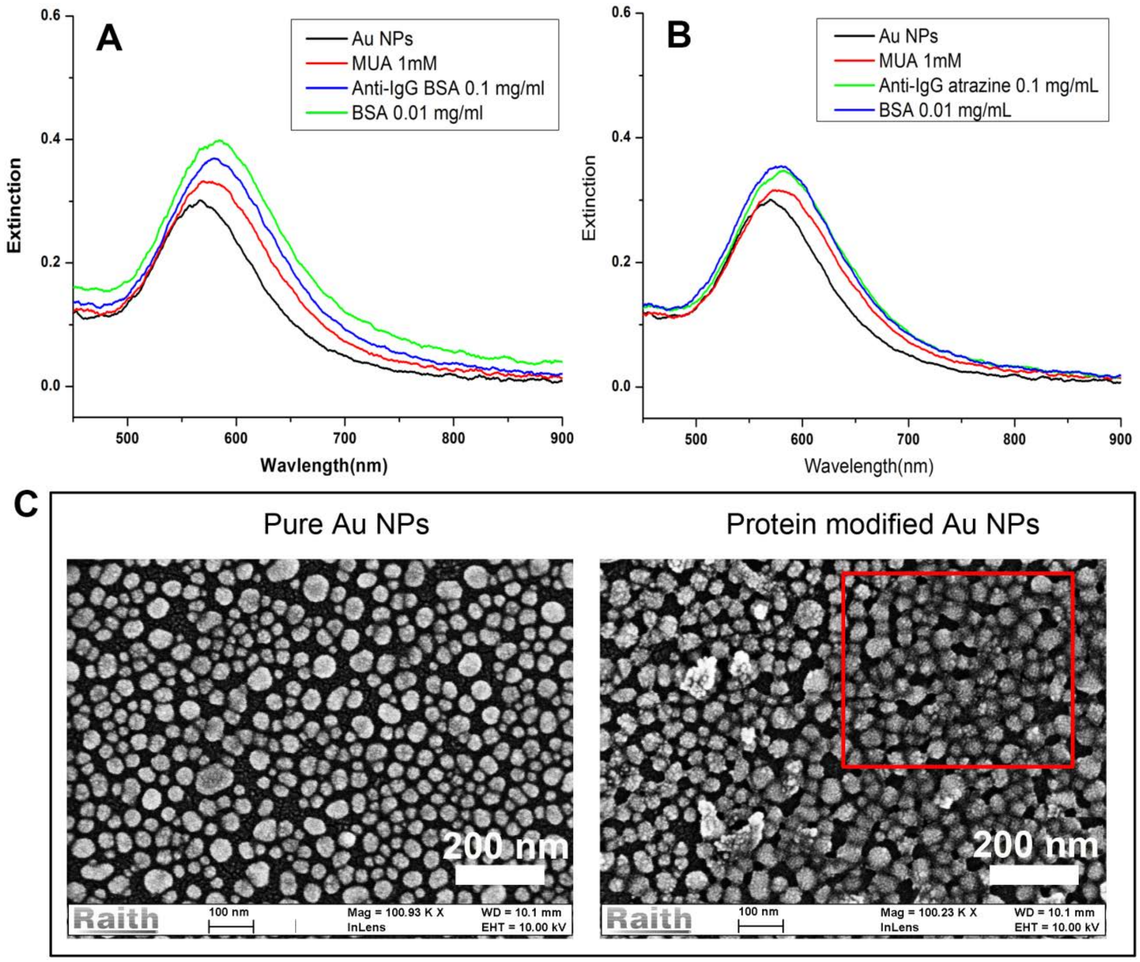

Figure 3.20 LSPR spectra of single gold micro-pattern after each biomodification step for specific BSA detection (A), control experiments using BSA non-specific antibody (anti-atrazine IgG) modified Au NPs (B), the same concentration of antigen (0.01 mg/mL BSA) was used in two experiments, and gold nanoparticles morphology before (left) and after (right) biomodification with 0.01 mg/mL BSA (C).

Finally, the gold micro/nano structured home-made chip is used to detect albumin protein in a high throughput manner. Specifically, three drops of varying concentrations of BSA dilution are deposited onto different zones of the LSPR chip, a cartoon and optical microscopy imaging showing this drop deposition were illustrated in **Figure 3.21** A, B panels. It should be noted that the volume of each BSA drop is only 0.2 μL, thus the LSPR chip is placed at 4 °C for 3 hr in a humid petri-dish sealed strictly with parafilm to avoid fast liquid evaporation. From the LSPR spectra shown in **Figure 3.21**C, different concentrations of BSA can be obviously distinguished based on the red-shift of resonant wavelength and concurrent increased of optical density. For example, as the increasing of antigen concentration from 1 ng/mL to 0.01 mg/mL the plasmonic peak is steadily red-shifted from 567 nm to 580 nm with a concurrent optical density increased from 0.33 to 0.38. On the contrary, in the control experiments using a BSA non-specific antibody (anti-atrazine IgG), the LSPR spectra corresponding to three different concentrations of BSA-antigen are overlapped and cannot be differentiated as shown in **Figure 3.21**D, primarily due to the random non-specific interaction between BSA molecule and Au NPs modified with atrazine antibody.

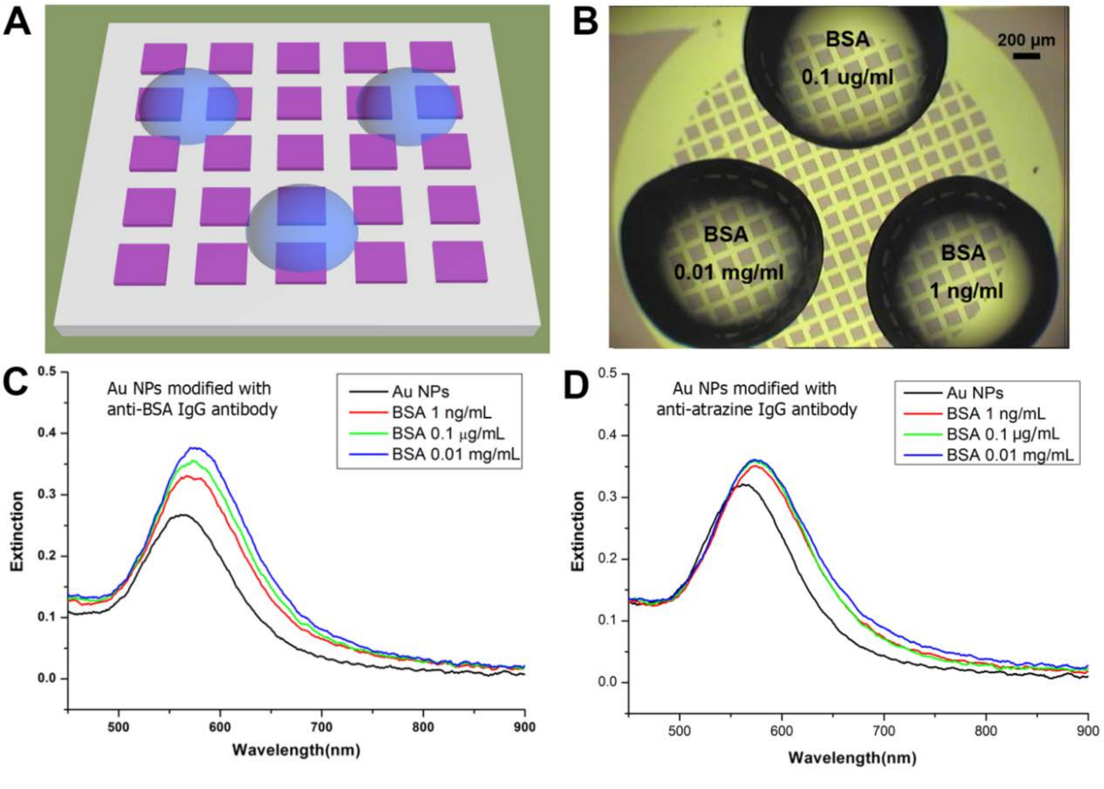

Figure 3.21 The illustration (A) and optical microscopy imaging (B) of three BSA drops of different concentration deposited onto different areas of plasmonic biochip, the specific (C) and nonspecific (D) specific plasmonic detection of various BSA concentrations were realized using specific anti-BSA antibody and a non-specific anti-atrazine antibody, respectively.

Finally, the reproducibility of the surface bio-modifications is also confirmed by measuring the LSPR spectra among different spots for two different samples as shown by the RSD statistic results in **Table 3.4**. Again, the LSPR measurements corresponding to each biomodification step are recorded from three different patterns for each sample and 5 different spots in each pattern are tested.

Table 3.4 Plasmonic properties (resonant wavelength and maximum extinction) of stepwise preparation of LSPR biosensors (sample 1) and high throughput specific detection of three different concentrations of BSA in a single experiment (sample 2).

		λ: resonant wavelength (nm), ODmax: maximum extinction			**Mean λ, ODmax**	**RSD**	
		P1	**P2**	**P3**		**λ**	**ODmax**
Sample 1	NPs	566.8, 0.31	567.9, 0.29	566.2, 0.30	566.9, 0.3	0.15%	3.3%
	MUA 1mM	571.2, 0.32	570.1, 0.33	572.1, 0.34	571.1, 0.33	0.18%	3.03%
	Ab 0.1 mg/mL	579.5, 0.36	576.8, 0.35	576.8, 0.38	577.7, 0.36	0.27%	4.2%
	BSA 0.01 mg/mL	584.9, 0.38	582.6, 0.42	582.8, 0.39	583.4, 0.4	0.33%	5.25%
Sample 2	NPs	564.8, 0.26	563.1, 0.25	563.7, 0.26	563.9, 0.26	0.15%	2.25%
	BSA 1 ng/mL	567.8, 0.33	566.2, 0.33	568.9, 0.35	567.6, 0.34	0.24%	3.43%
	BSA 0.1 µg/mL	571.5, 0.34	574.1, 0.36	572.8, 0.35	572.8, 0.35	0.23%	2.86%
	BSA 0.01 mg/mL	578.5, 0.39	581.8, 0.38	582.1, 0.41	580.8, 0.39	0.34%	5.13%

Inter-assay RSD of BSA 0.01 mg/mL between sample1 and sample 2:
For wavelength: 0.36% ; for extinction: 4.16%

It is found that for these two samples, the maximum RSD between different positions inside one sample is around 0.34% for the resonant wavelength and 5.25% for the optical density. In addition, when compared with the LSPR results of spots modified by the same concentrations of BSA (0.01 mg/mL) from these two different samples, a small interassay RSD is obtained as 0.36 % and 4.16 % for wavelength and optical density, respectively, which confirms the reproducibility of surface biomodification.

3.2.4.3 The QCM technique to confirm the surface biomodification

The sensitive, specific and multiplexing detection of biomolecules have been realized by the label-free LSPR biosensors so far. A robust gold surface biomodification is indispensable to obtain the convincible results. Especially, the immunoreactions between surface grafted antibody and exogenous added antigen is the key step during the overall biomodification procedure. However, the LSPR biosensors discussed above only provide the indirect and end-point information concerning the antibody-antigen interactions. As one promising alternative, the surface mass sensitive acoustic biosensor based on quartz crystal microbalance (QCM) is able to probe the interfacial antibody-antigen interaction in a real-time way, thus it is expected that the QCM experiments will provide complementary information (such as kinetics data) for the biorecognition elements used in the previous LSPR biosensors.

The quartz crystal microbalance (QCM) is widely used as the transducer for the acoustic biosensor, mainly because of its excellent sensitive piezoelectric properties.[29] Thanks to the pioneering work of Sauerbrey in 1959 to derive the relationship between resonant frequency and mass deposited on crystal surface,[30] the QCM devices have found widespread applications in gas phase detection[31] and thin film characterization.[32] However, the Sauerbrey equation is only valid for the rigid, thin and homogenous film deposition on crystal, which hinders its applications on soft and solvated interfaces involved in liquid phase.[33] Fortunately, a new model for QCM operation in liquid was proposed by Kanazawa and Gordon.[34] According to the published work, if only one side of crystal is exposing to liquids, the frequency shift (ΔF) due to the liquid deposition on crystal surface can be described as:

$$\Delta \mathrm{F} = -\left(\frac{F_0^{\frac{3}{2}}}{\sqrt{\pi \mu_q \rho_q}}\right)\sqrt{\rho_L \eta_L} \qquad (2)$$

where F_0, μ_q and ρ_q are the characteristic resonant frequency, shear modulus (2.947×10^{11} g cm^{-1} s^{-2}) and density (2.648 g cm^{-3}) of the quartz crystal, respectively, while the ρ_L and η_L are the density and viscosity of the bulk liquid. In terms of experimental development, there are different ways to perform QCM measurements in liquid phase, either by using impedance analysis or QCM with dissipation and with oscillator circuits.[35] In this work, the simple and effective drop deposition onto a QCM electrode was explored to detect varying concentrations of antigens,[36-37] the schematic illustration for the QCM experiment of drop mode is shown in **Figure 3.22**.

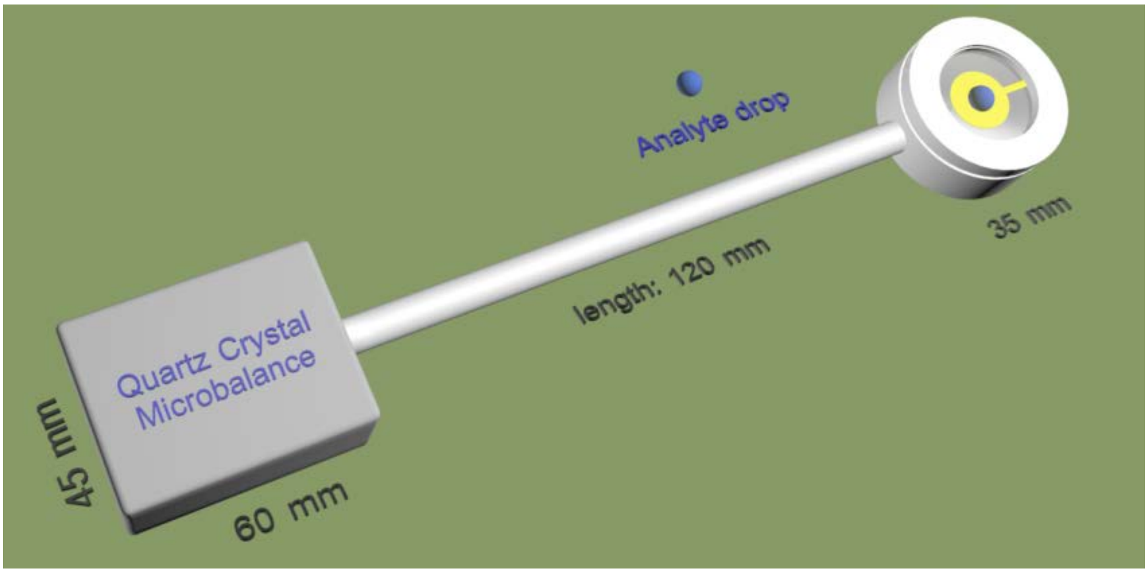

Figure 3.22 The schematic of analyte drop (blue sphere) deposition method used in QCM experiment. The basic dimensions of QCM instrument were shown in the figure.

In this part, a QCM quartz crystal was gold micro-structured with a help of a commercial TEM-grid via a well-controlled vacuum evaporation technique. The resulted micro-structured QCM crystal was further used as the platform for sensitive and specific acoustic immunosensing of different (bio)molecules. One of the major ideas for this QCM experiment is to provide complementary results to antibody-antigen interaction for previous optical biosensors, thus the same gold surface biomodification protocols used in LSPR biosensors experiments have been utilized on gold electrode of crystal. Specifically, a successful immobilization of different antibodies (anti-atrazine IgG and anti-carbofuran IgG) onto different QCM patterns to sequentially detect two antigens (atrazine and carbofuran) in a sequential acoustic measurement is reported.

The stepwise preparations of acoustic immunosensors are described in **Figure 3.23**A, while the photos of TEM-modified gold QCM crystals and their SEM images are shown in **Figure 3.23**B.

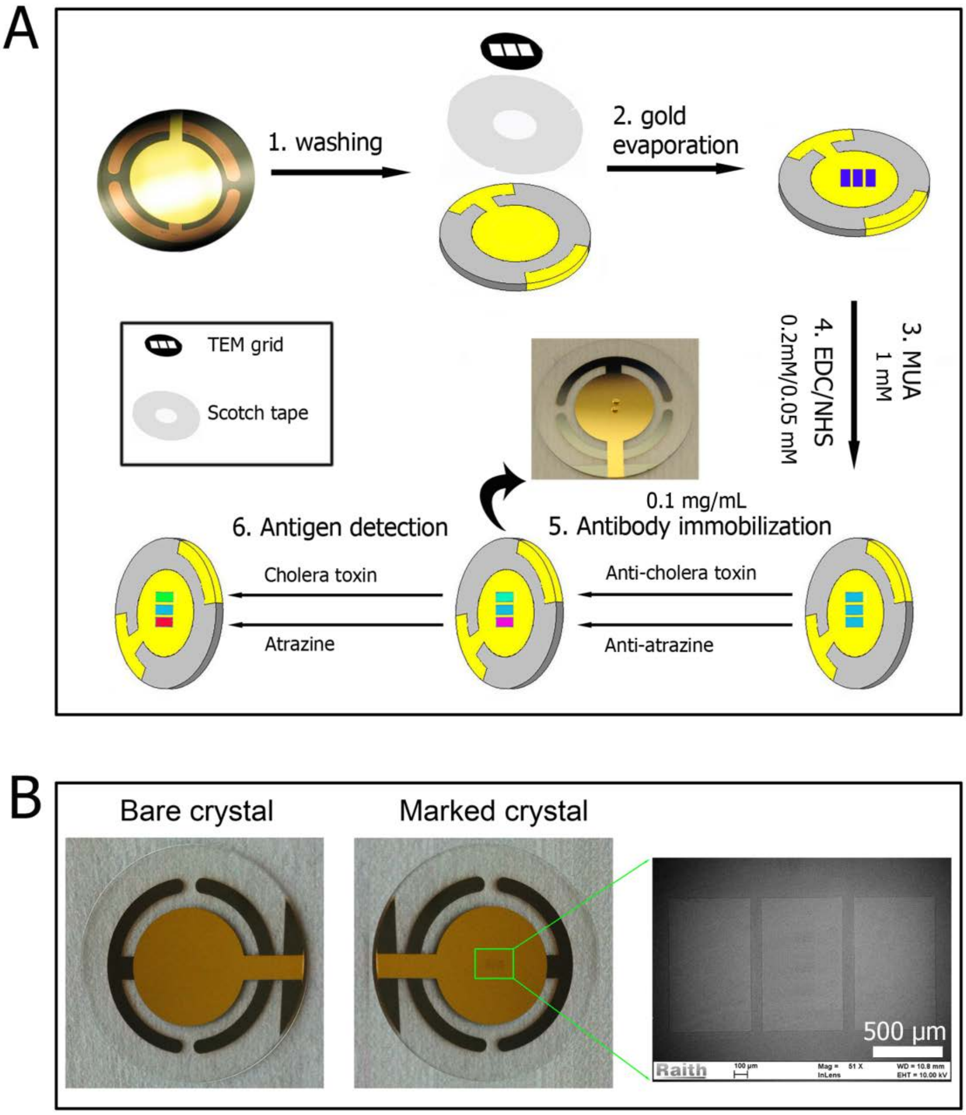

Figure 3.23 Stepwise fabrication of acoustic sensors used for sequential detection of carbofuran and atrazine using a single QCM-crystal (A). Photo of gold micro-patterned QCM-crystal and its SEM-image characterization (B).

In the present work, a thin layer of gold (5 nm) was evaporated onto the crystal surface through a TEM-grid mask and consequently, a well-organized marker containing three independent slots was obtained. After carefully grid removing, the size of one pattern was measured as 0.6 mm × 1 mm which was very close to the grid pattern. Moreover, the thin deposed gold film has negligible influences onto the surface morphology of commercial QCM-crystal gold electrode, as indicated in the SEM images in **Figure 3.24**. The reproducibility of the drop-deposition measurements is highly improved, as individual drops can be precisely deposited onto the same position due to the presence of a visible TEM-grid marker on the crystal surface.

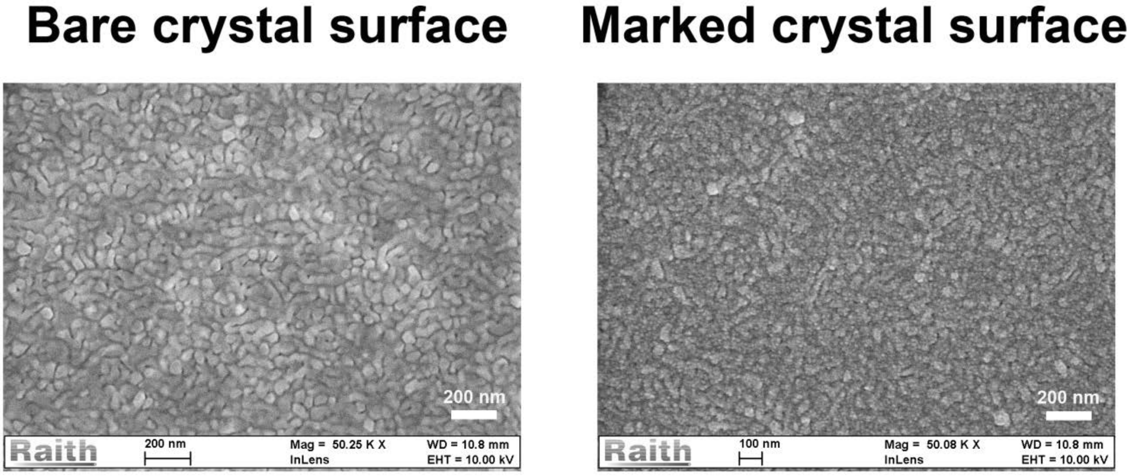

Figure 3.24 The surface micromorphology of bare crystal and nanoscale marker modified crystal characterized by FESEM. The nearly identical morphology was displayed for two crystals.

Since there are three gold TEM-patterns on the surface of a QCM-crystal, their frequency responses due to the successively deposition of 0.3 μL water drops onto each pattern were monitored (**Figure 3.25**). It was found that the frequency response for the first (zone 1) and the third (zone 3) patterns are identical, providing the basis of using these two patterns to detect different targets.

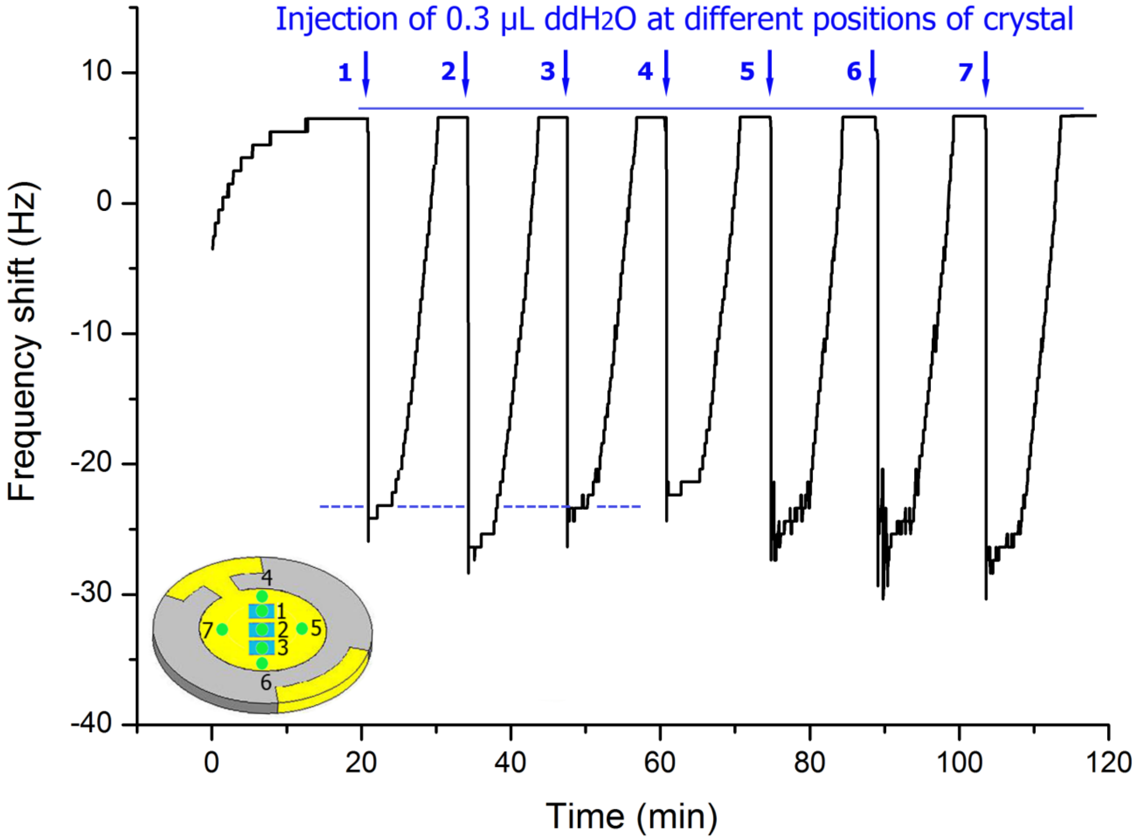

Figure 3.25 The frequency responses upon sequential deposition of water drops (0.3 µL) onto the micro-structured areas (zone 1, 2 and 3) and onto the non-structured areas (crystal borders, zone 4, 5, 6 and 7). It is clear that the frequency responses of the two structured patterns (zone 1 and 3) have similar acoustic behaviour, while from the middle pattern, a larger frequency shift is recorded after the injection of ddH_2O drop. The area 1 and 3 are used in the present work for pollutants detection.

Further, these two micro-patterns were biofunctionalized with two different types of antibodies. The middle pattern was not modified with any antibodies and used to separate the two target sideways patterns in the presented acoustic experiments. Moreover, the resonant frequency shifts (**Figure 3.26**) upon deposition of different concentrations of atrazine and carbofuran antigens were recorded at room temperature. The differences of resonant frequency for the initial dried crystal before and after antigen binding (shown as the vertical red and blue dashed lines for carbofuran and atrazine, respectively) were used as the analytical signals in this work.

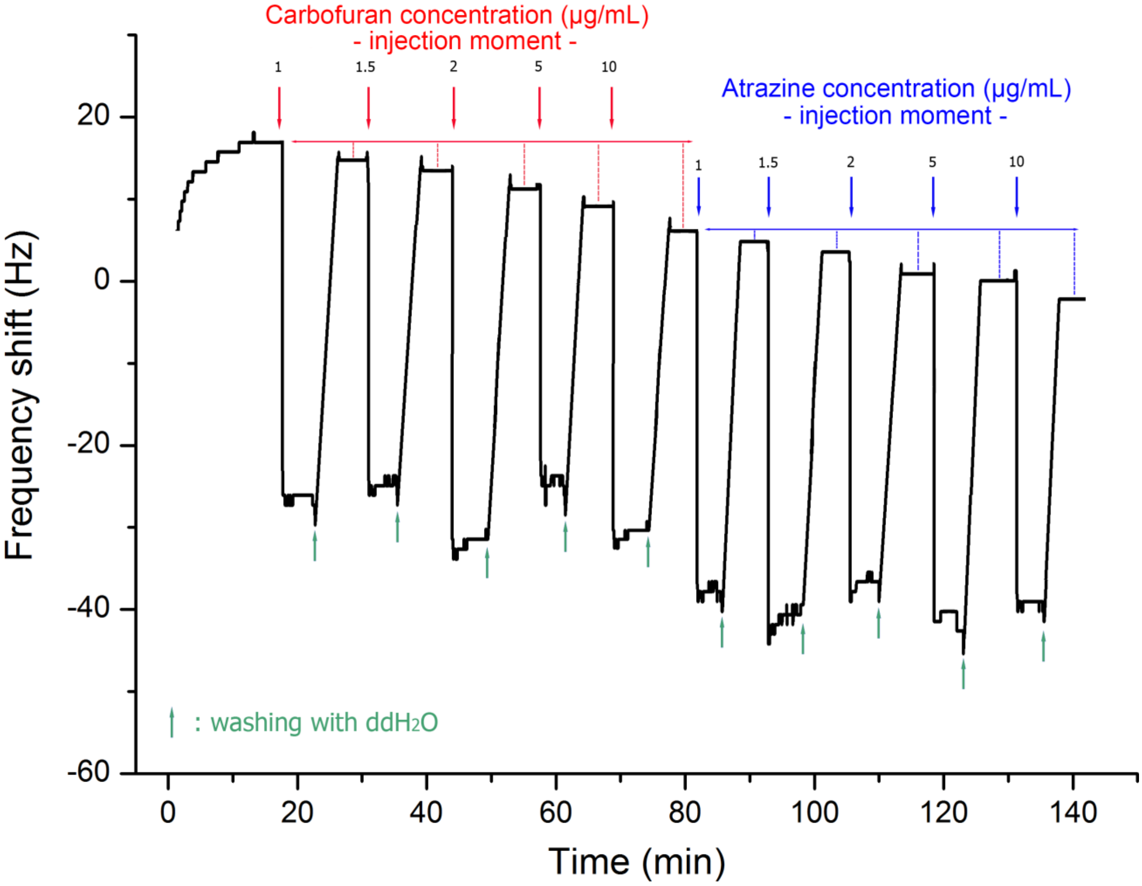

Figure 3.26 The sensorgram of acoustic detection of carbofuran and atrazine within a drop-deposition procedure correlated with the resonant frequency shifts upon the injection of different concentrations of the analytes. The red and blue arrows are indicating the injection of different concentrations (1 µg/mL, 1.5 µg/mL, 2 µg/mL, 5 µg/mL and 10 µg/mL) of carbofuran and atrazine onto their specific IgG antibody modified microspot-pattern. The green arrows under the curves represent the ddH$_2$O washing step after each antigen concentration immobilization step onto the quartz crystal is finished (10 min). The acoustic signal is calculated as the difference between the resonant frequency of a dried crystal before and after antigen binding (red for carbofuran and blue for atrazine). The drop volume of each antigen concentration was 0.3 µL and the QCM measurements were conducted at room temperature.

Generally, the frequency shifts are proportional to the antigen concentration, where binding of carbofuran always contributed to a slightly larger frequency shifts when compared with binding of atrazine of the same concentration. For instance, the specific recognition of 10 µg/mL atrazine induce frequency shift of only 12 Hz, while upon immobilization of the same concentration of carbofuran, a slightly larger frequency shift (16 Hz) was recorded. This different frequency response between carbofuran and atrazine should be due to the minute differences of their molecular weight (216 g/mol for atrazine and 221 g/mol for carbofuran) and the possible different kinetics and equilibrium constants of their immunoreactions. In addition, the pesticide pool of atrazine and carbofuran were prepared by mixing equal volume of atrazine and carbofuran dilutions and were tested on the anti-atrazine IgG modified microspot, where the frequency responses for the atrazine/carbofuran mixture are lower than those of atrazine alone under the same concentrations (**Figure 3.27**).

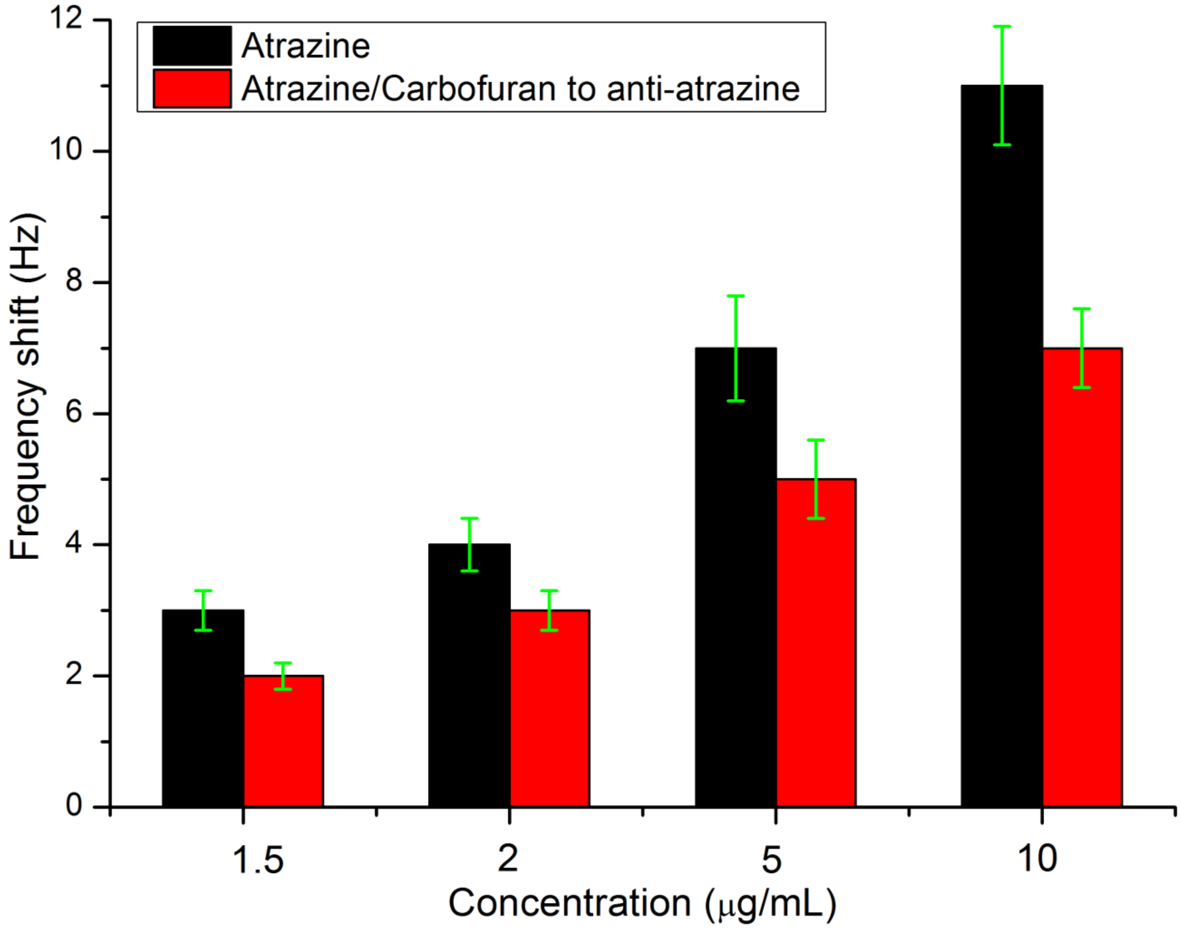

Figure 3.27 The frequency shift upon deposition of the atrazine/carbofuran pesticide pool (atrazine: carbofuran volume ratio = 1:1) onto the anti-atrazine antibody modified microspots. For comparison, the frequency shifts characteristic for the atrazine alone is also shown in the figure.

The calibration curves for the specific recognition of antigens and two sets of control experiments are shown in **Figure 3.28**. Thus, although the frequency is still slightly shifted in the two control experiments when antigen binds either to non-specific antibody or to thiolated crystal, the frequency shifts corresponding to the specific antibody-antigen interactions are highly representative. For the carbofuran specific detection, a linear frequency shift response was observed for antigen concentration ranging from 1 µg/mL to 10 µg/mL with a regression equation of $y=1.25x+3.92$, $R^2=0.97$ and standard error of 1.08. For the detection of smaller molecule such as atrazine, the frequency shift is smaller than that obtained for carbofuran detection while a linear frequency shift versus antigen concentration ($y = 0.96x+ 1.64$) was also obtained in the concentration range of 1~10 µg/mL with a coefficient of 0.98 and standard error of 0.83. Since the dispensed volume of each antigen dilution is only 0.3 µL, the lower limit detection for carbofuran and atrazine is 1 µg/mL.

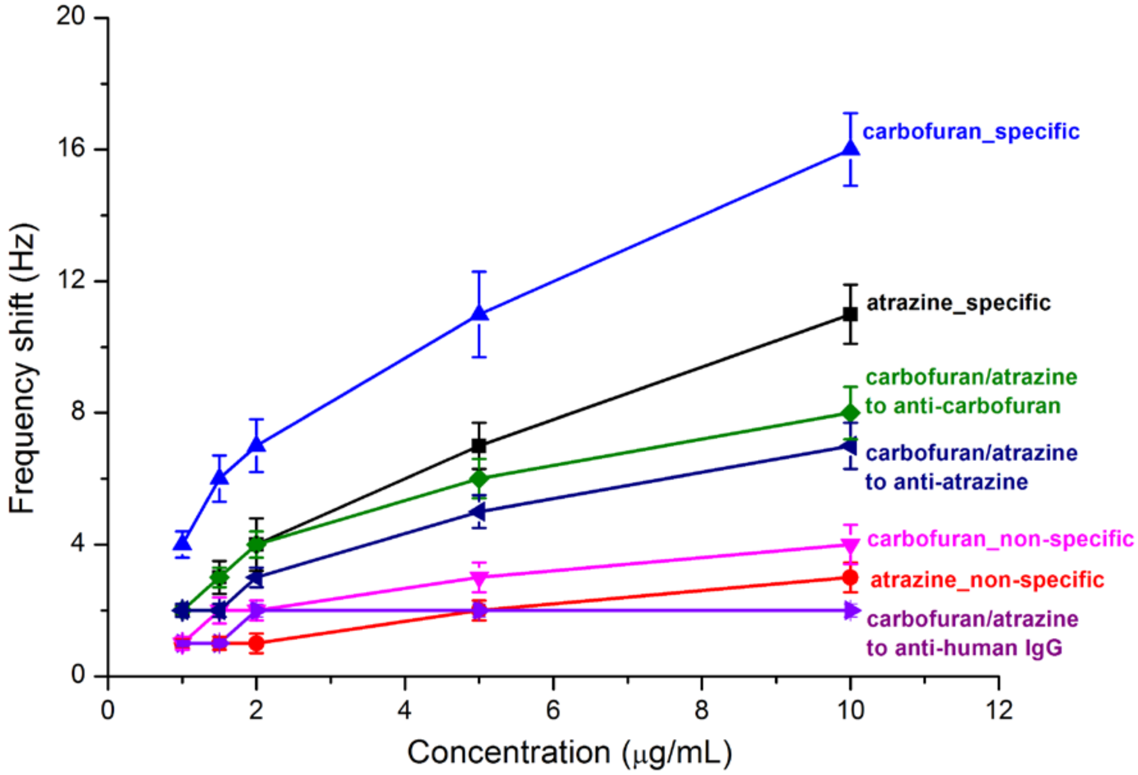

Figure 3.28 Calibration curve for acoustic detection of different concentrations of carbofuran and atrazine antigen ranging from 1 μg/mL to 10 μg/mL. Two targets (carbofuran and atrazine) are detected on their corresponding antibody modified microspot in the specific case, while in the non-specific case, carbofuran is detected on non-specific anti-atrazine modified microspot and vice versa for atrazine. For the control experiment of direct deposition of antigens drops onto thiolated modified gold electrodes without any antibodies, the frequency shift is less than 2 Hz for all the tested concentration and thus are not shown in above figure.

In summary, a cost-effective protocol to fabricate acoustic immunosensors based on a quartz crystal microbalance (QCM) is designed to provide additional information for the antibody-antigen interaction on gold surface. Based on the previous experience to construct high throughput LSPR biochip,[28] the patterned quartz crystal is prepared via an electron beam evaporation of gold through a commercial transmission electron microscope (TEM) grid as a mask.[36] Two different patterned zones on the crystal electrode surface were functionalized either with the monoclonal anti-carbofuran or with anti-atrazine IgG antibody by using thiol chemistry. Different concentrations of antigens (carbofuran or atrazine) were deposited onto their corresponding antibody modified zones monitoring *in-situ* the specific interaction between antibody and its antigen from both resonant frequency changes versus time. Two sets of controls experiments, including antigen interactions with non-specific antibody and simple antigen deposition onto thiolated-QCM quartz crystal were also investigated. It was found that the proposed methodology allows sequential specific detection of 4.5 μM carbofuran and 4.6 μM atrazine, respectively. These QCM results are well corroborated with the previous data obtained from LSPR biosensor experiments, which indicates the gold surface biomodification protocol used in the work is robust and efficient.

3.2.5 Improvement of LSPR biosensor sensitivity

Based on the previous parts, the gold evaporation followed by high temperature annealing is able to provide ultra-stable gold nanostructures on glass substrate, and this fundamental protocol can be readily adapted with different masks to ultimately enable the specific and multiplexing detection of several biomolecules using single LSPR biochip. However, there are two disadvantageous in this basic evaporation/annealing protocol. Firstly, the Au nanoparticles obtained from this protocol show considerable inhomogeneity of nanoparticle shape, in other word, a range of different shaped Au nanoparticles are obtained, which will result to inhomogeneous broadening of plasmonic resonant peak. Secondly, the Au nanoparticles resulted from high temperature annealing are believed to be embedded inside the underline glass substrate, which will significantly decrease the effective gold nanoparticle surface area that can be modified by the biorecognition element (i.e. antibody). Due to these two shortcomings, the obtained monometallic Au NPs show less sensitivity in LSPR biosensor applications. Therefore, in this final part, two independent protocols have been proposed to improve the overall sensitivity of LSPR biosensor. Specially, the first protocol is used to increase the intrinsic plasmonic sensitivity of nanoparticles transducer by employing more sensitive Au/Ag bi-metallic NPs, while the second protocol is based on the spontaneous polymerization of dopamine molecule in base solution, which consequently serves as the versatile functional coatings to improve the interface biomodification, more specifically to increase the content of immobilized antibody onto bi-metallic NPs.

3.2.5.1 Preparation of Au/Ag bi-metallic NPs and their plasmonic spectra

Thanks to the commercial TEM copper grid used as mask during the evaporation process, extremely well-organized and large scale micropatterns of Au/Ag bi-metallic NPs were developed after 8 hr at 500 °C (**Figure 3.29**A). From the optical microscope image shown in **Figure 3.29**B, the gold/silver patterns were obtained after the careful removing of TEM grid mask and sample annealing. One square of pattern measures (91 µm × 91 µm)^2, which is very close to the mesh size of copper grid (90 µm× 90 µm)^2.

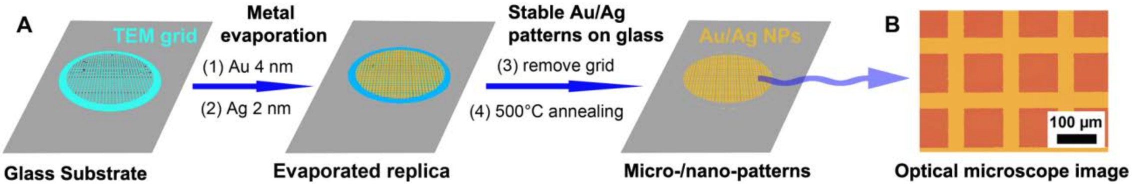

Figure 3.29 Fabrication steps of Au/Ag bi-metallic NPs (A) and an optical microscope image of gold TEM grid patterned onto glass substrate (B).The orange squares contain Au/Ag bi-metallic NPs.

Based on the previous results,[18] the LSPR properties evolutions of monometallic Au NPs are mainly determined by the gold evaporation thickness before annealing. Since the plasmon resonant wavelength is always red-shifted and broaden as the increasing of gold evaporation thickness, the well-known interparticle coupling effects resulted from the Bragg diffraction of ordered arrays of metal nanostructures[38] are not observed in these experiments, which could be attributed to the random distribution of obtained metallic NPs. In addition, the optimized monometallic Au NPs for biosensor applications correspond to a gold evaporation thickness of 4 to 6 nm.[26] Herein, we have chosen to further enhance the plasmonic sensitivity by incorporating of more sensitive silver into the previously optimized monometallic Au NPs with gold evaporation thickness of 4 nm.

The LSPR spectra of Au NPs and Au/Ag bi-metallic NPs obtained by using different evaporation combinations are investigated. Thus, a wider plasmonic peak is observed at 572 nm with a maximum optical density value of 0.29 for Au NPs (**Figure 3.30**). After evaporation of silver (2 nm) onto the gold (4 nm) modified glass and annealing at 500 °C, a sharper plasmonic peak is recorded at 529 nm with an optical density value of 0.23 for Au/Ag bi-metallic NPs.

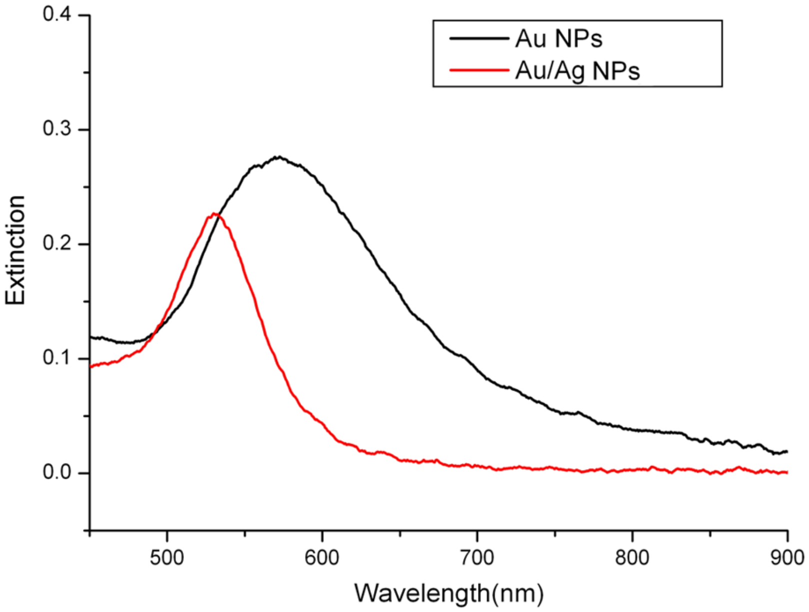

Figure 3.30 LSPR spectra of Au NPs (4 nm) and Au (4 nm)/Ag (2 nm) bi-metallic NPs. (Au – gold; Ag – silver). Both nanoparticles were annealed at 500 °C for 8 hr.

The LSPR spectra were also recorded for other nanoparticles obtained using different evaporation combinations. The samples with evaporated silver alone (4 nm or 6 nm) are not stable after annealing at 500 °C for 8 hr (**Figure 3.31**A, B). Moreover the samples with first evaporation of Ag (4 nm) followed by Au evaporation (2 nm) or samples with Ag (2 nm) and Au (4 nm) show less intense plasmonic peaks (**Figure 3.31**C, D) that lower the signal-to-noise ratio for biosensing applications. Based on the obtained results, the optimized bi-metallic configuration is considered as Au (4 nm) followed by Ag (2 nm) evaporation. Moreover, the high sensitive plasmonic material (Ag) is the top layer in the optimized biosensor configuration, which can directly contribute to an improved LSPR sensitivity.

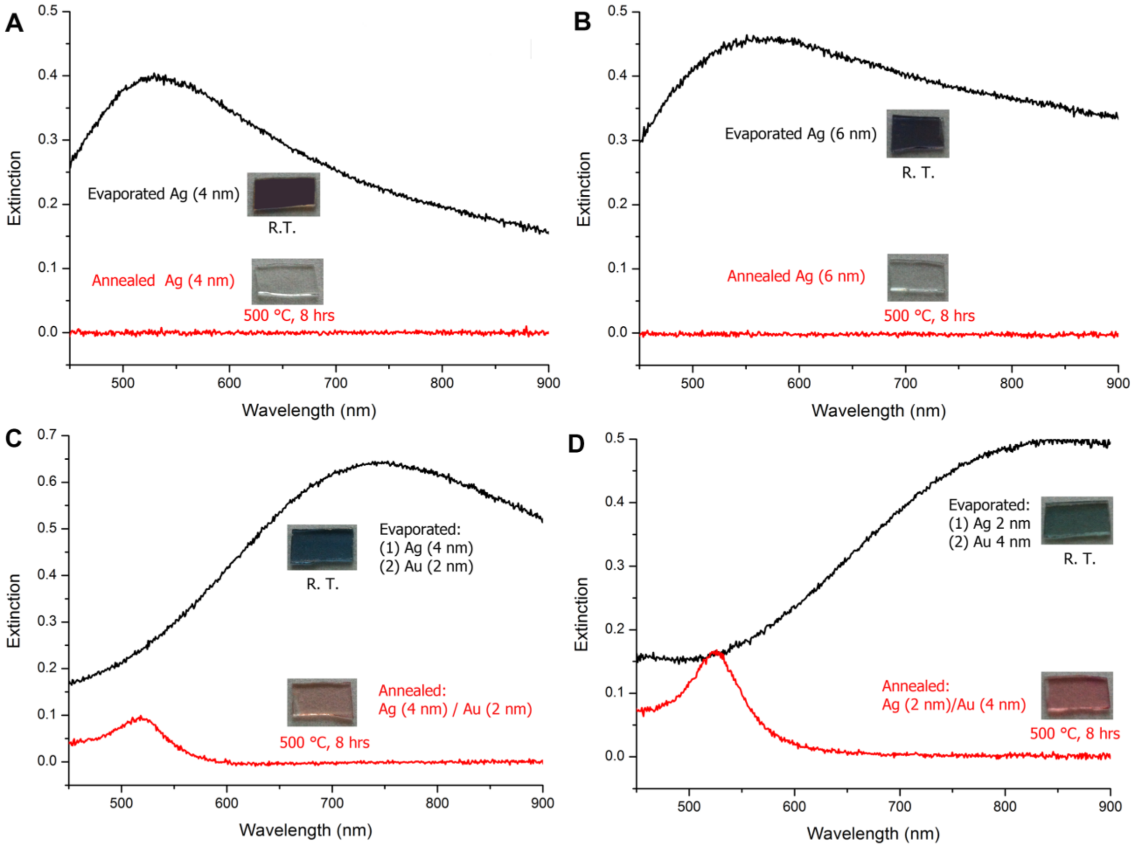

Figure 3.31 LSPR spectra of glass samples modified with evaporated silver of different thickness of 4 nm (A), 6 nm (B) and with two successive evaporated bi-metallic layers of Ag (4 nm)/ Au (2 nm) (C) or Ag (2 nm)/Au (4 nm) (D) The photos of samples before and after annealing treatment are included in each panel. Interestingly, the silver-modified glasses expose unstable NPs after annealing at 500 °C for 8 hr.

The SEM images of Au NPs and Au/Ag bi-metallic NPs are illustrated in **Figure 3.32** A, B, respectively. The nanoparticle size distribution is obtained by using the public software ImageJ developed at National Institutes of Health. Although extremely well-dispersed nanoparticles are obtained in both cases, the Au/Ag bi-metallic NPs exhibited more uniform size and shape distribution when compared to Au NPs. Specifically, spherical and rod-like Au NPs with average size of 23.1 nm (**Figure 3.32** C) coexist while a dominant spherical Au/Ag NPs with average size of 36.6 nm (**Figure 3.32** D) annealed at same temperature are identified.

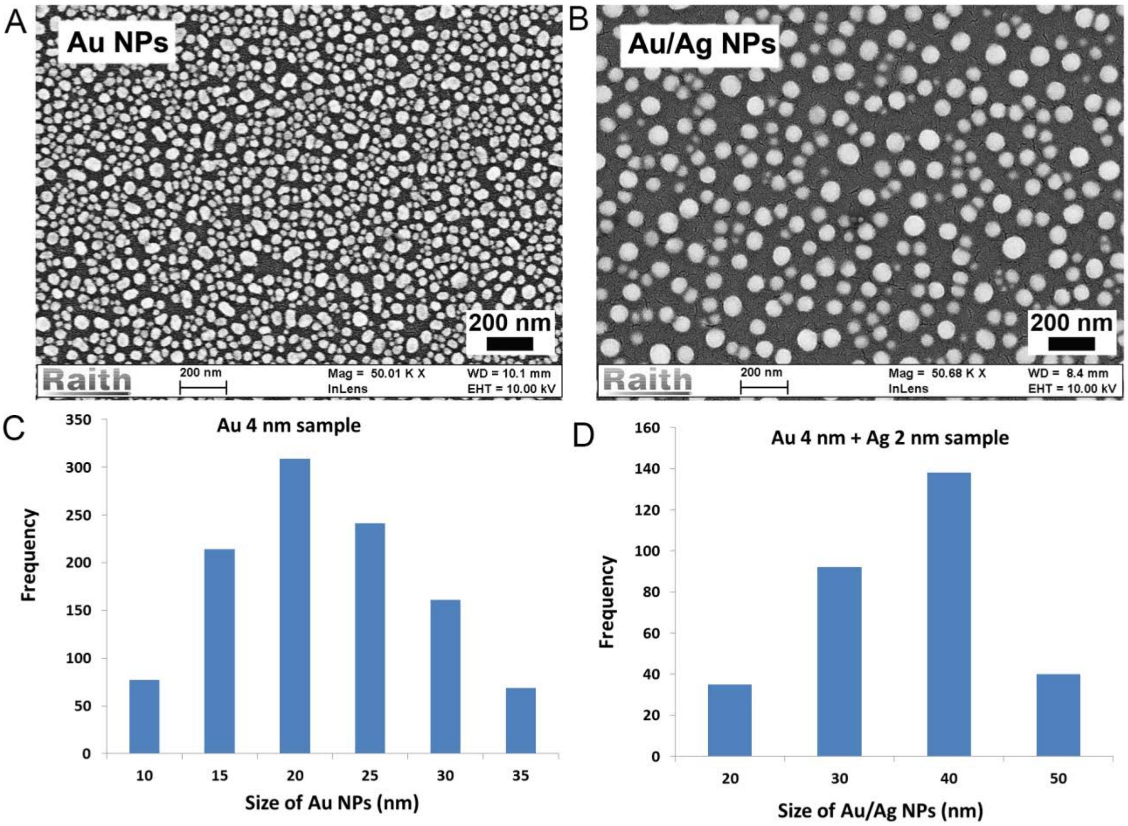

Figure 3.32 The SEM image (A) and corresponding size distribution (C) of monometallic Au NPs obtained by annealing 4 nm gold evaporated sample at 500 °C for 8 hr, the SEM image (B) and size distribution (D) of optimized Au/Ag bi-metallic NPs obtained by annealing the Au (4 nm)/Ag (2 nm) sample at same temperature.

3.2.5.2 Enhanced plasmonic behavior of Au/Ag bi-metallic NPs

It has been reported that the plasmonic responses of silver nanoparticles are more sensitive than those of gold nanoparticles with same geometrical properties.[39] It is well known that bi-metallic materials combine desirable properties that are not possessed by single component (metal) alone.[40] On the other hand, inspired from the mussel's strong adhesive ability to almost any types of organic and inorganic surfaces, a quite cost-effective, very efficient and robust surface modification protocol, based on the spontaneous polymerization of chemical compound dopamine in base solution, has been developed by Phillip B. Messersmith and co-workers.[41] It has been found that a thin film of poly-dopamine can be deposited on almost any surface just by dipping the sample into a base solution of dopamine, and more interestingly, the thickness of the resulted polymer film could be adjusted easily by controlling the dipping time. Since the plasmonic properties of noble metal nanoparticles show strong distance dependence (the characteristic decay length up to few tens of nanometers are reported), the dopamine based surface modification protocol is applied for the first time for Au and Au/Ag bi-metallic NPs.

For biological diagnostic using plasmonic sensitivity, the Au and Au/Ag bi-metallic NPs samples are immersed in 10 mM dopamine solution (1 mL) of Tri-HCl buffer (pH=8.5) for different periods of time (**Figure 3.33**). It is noticed that with the increasing of reaction time, the steady red-shift of resonant wavelength and increased maximum peak intensity are recorded for both Au NPs and Au/Ag bi-metallic NPs.

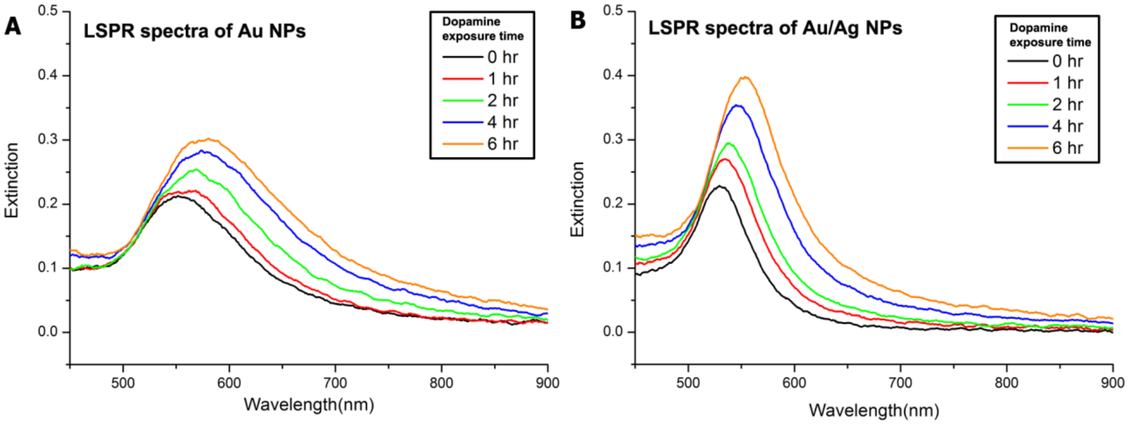

Figure 3.33 LSPR spectra of Au NPs (4 nm) (A) and Au (4 nm) /Ag (2 nm) bi-metallic NPs (B) exposed to dopamine solution (10 mM) for different periods of time. The dopamine solution is prepared with Tris-HCl buffer (pH=8.5) and stored in a sealed plastic tube at room temperature.

Variation of the resonant wavelength length, the maximum optical density (OD), full width at half maximum (FWHM), Q factor and a modified figure of merit (FoM) values as a function of the dopamine incubation time are reported in **Table 3.5**. Thus, in the case of Au NPs, after 6 hr treatments with dopamine, a 30 nm red-shift of resonant wavelength and 0.09 increase of maximum OD value are noticed. Interestingly, the Au/Ag bi-metallic NPs, although presented a similar red-shift of wavelength (29 nm), a much larger maximum OD value increases of 0.17 is obtained, which is almost twice enhanced when compared to Au NPs. In both cases, as the dopamine coating time arising from 1 hr to 6 hr, the FWHM is increased from 82.1 nm to 111.1 nm for Au NPs and from 45.9 nm to 62.1 nm for Au/Ag bi-metallic NPs. On the contrary, the Q factor is decreased from 6.72 to 5.23 for Au NPs and from 11.54 to 8.59 to Au/Ag NPs, respectively. For the modified figure of merit (FoM) defined as ratio between the maximum resonant wavelength shift (the 0 hr dopamine coating time used as the reference) and the FWHM, a significant increase value for Au/Ag bi-metallic NPs (0.45) is remarked when compared to that of Au NPs (0.27) exposed to dopamine solution for 6 hr.

Table 3.5 LSPR analytical performances of Au NPs and Au/Ag bi-metallic NPs independently exposed to dopamine solution (1mM) for different periods of time at room temperature.

Sample	Parameters	0 hr	1 hr	2 hr	4 hr	6 hr
Au NPs	Wavelength (nm)	551.6	561.7	569.4	573.3	581.1
	Optical density (OD)	0.21	0.22	0.25	0.28	0.3
	FWHM (nm)	82.1	91.3	97.4	104.2	111.1
	Q factor[1]	6.72	6.15	5.85	5.5	5.23
	Figure of Merit (FoM)[2]	---	0.11	0.18	0.21	0.27
Au/Ag NPs	Wavelength (nm)	529.1	535.3	538.4	544.7	556.3
	Optical density (OD)	0.23	0.27	0.3	0.35	0.4
	FWHM (nm)	45.9	51.3	53.6	59.7	62.1
	Q factor	11.54	10.45	10.05	9.12	8.98
	Figure of Merit (FoM)	---	0.12	0.19	0.26	0.45

1: Q factor =λmax/FWHM, λmax is the maximum resonant wavelength.

2: Figure of Merit (FoM) = Δ λmax/FWHM, Δ λmax is the shift of maximum resonant wavelength using the resonant wavelength at 0 hr coating time as the references (551.6 nm for Au NPs and 529.1 nm for Au/Ag bi-metallic NPs).

Based on the above reported results, the authors unambiguously demonstrated that plasmonic sensitivity of Au/Ag bi-metallic NPs is clearly enhanced when compared to Au NPs, especially for the increase of maximum optical density upon different biofunctionalization of bi-metallic particles. Although the exact mechanisms responsible for the improvement of plasmonic responses in the presence of dopamine are yet to be explored, the introduction of more sensitive plasmonic material such as silver in the fabrication of bi-metallic materials could normally induce better LSPR properties than those of a single metal.[39]

3.2.5.3 High throughput LPSR detection of BSA using (bio)functionalized Au/Ag bi-metallic nanoparticles

Since the Au/Ag bi-metallic NPs have exhibited more sensitive plasmonic responses than Au NPs, they can be used as substrates for the construction of immunosensors for sensitive detection of albumin. Due to the TEM grid mask, the large scale (in millimeter range) of micro-/nano- plasmonic structures is easily prepared. In addition, the incident beam can be launched precisely to different zones of NPs with the spatial resolution of 10 μm assured by the home-build confocal measurement setup. Therefore, the extremely well organized micro-/nano-structures are used as high throughput biochips to sequentially detect several chemical compounds. Experimentally, different concentrations of BSA antigen (0.3 μL) are deposited onto the different areas of the antibody modified NPs-biochip. The plasmonic responses corresponding to different concentration of BSA ranging from 0.01 ng/mL to 10 μg/mL are shown in **Figure 3.34**.

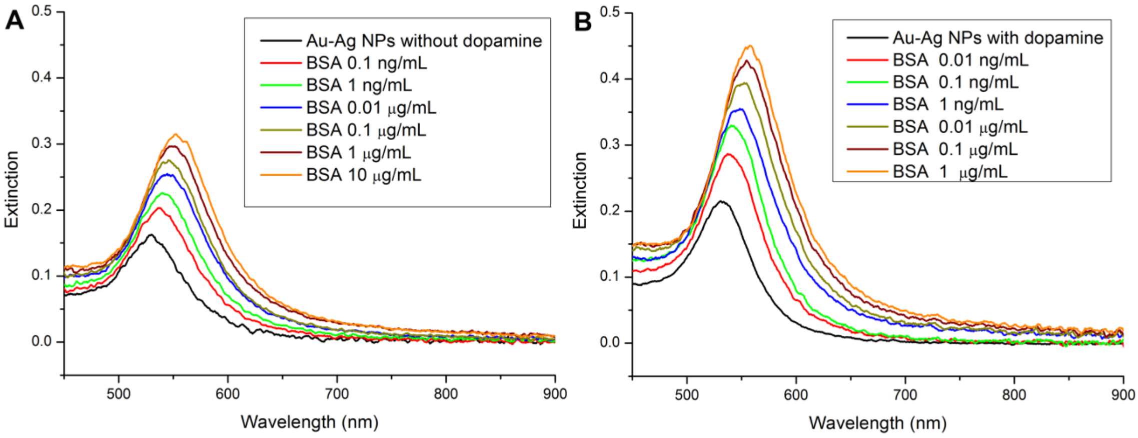

Figure 3.34 LSPR spectra of Au/Ag bi-metallic NPs without (A) and with (B) dopamine coating film to detect different BSA concentrations starting from 0.01 ng/mL up to 10 μg/mL. For each TEM grid patterned chip, up to three drops of different BSA concentrations are deposited using a micropipette for LSPR detection.

It is found that the LSPR biosensor based on Au-Ag bi-metallic NPs are able to discriminate different concentrations of BSA antigen (see **Figure 3.34** A). Specifically, as the BSA concentration increases from 0.1 ng/mL to 10 μg/mL, a red-shifted of resonant wavelength (from 535.9 nm to 554.6 nm) and an increase of OD (from 0.2 to 0.32) were observed, respectively. Experimentally it was found that the annealed Au/Ag bi-metallic NPs were quite stable in liquid phase during extensive biofunctionalization steps, mainly due to their partial embedding inside the glass after 8 h at 500 °C. However, the effective surface area of metal nanoparticles is expected to decline affecting the binding quantity of antibody molecules, which finally may result to a less sensitive response to antigen molecules recognition.

In order to further increase the plasmonic sensitivity of high temperature annealed NPs on glass substrate, the universal dopamine surface modification is used in this work. Since the spontaneous dopamine polymerization in base solution can occur at almost any surface, it is expected that both the Au/Ag bi-metallic NPs and the interstitial spaces between NPs can be modified with a uniform layer of poly-dopamine. Even more interestingly, the dopamine modified surface can be used to bind thiol via the Michael addition between catechol and thiol groups.[42] Since the localized surface plasmon resonance is rapidly damping away from nanoparticles, the thickness of poly-dopamine layer should be carefully controlled to make sure that the biomolecule binding is in the plasmonic sensing volume. Therefore, the annealed Au/Ag bi-metallic NPs subject to 1 hr dopamine treatment prior to thiol modification is used to improve the LSPR sensitivity. Moreover, the surface modification with poly-dopamine also improves the biocompatibility and oxidation resistance of top silver layer for the obtained Au-Ag bi-metallic NPs.

Indeed, from the plasmonic spectra recorded from Ag/Au bi-metallic NPs modified with dopamine (**Figure 3.34** B), a larger shift of resonant wavelength and increasing of optical density are recorded when exposed to the BSA antigen. Specifically, a plasmonic peak red-shifted from 536.9 nm to 561.4 nm, and a larger OD increasing of 0.17 are obtained upon specific binding of different BSA concentrations from 0.01 ng/mL to 1 µg/mL. The plasmonic responses are saturated for the higher BSA concentration (10 µg/mL). The control experiment using the same Au-Ag-dopamine NPs modified with a BSA non-specific antibody was also conducted, where the different concentrations of BSA cannot be detected (**Figure 3.35**). These results confirm that the specific plasmonic changes reported in **Figure 3.34** B are resulted from specific antibody-antigen interaction.

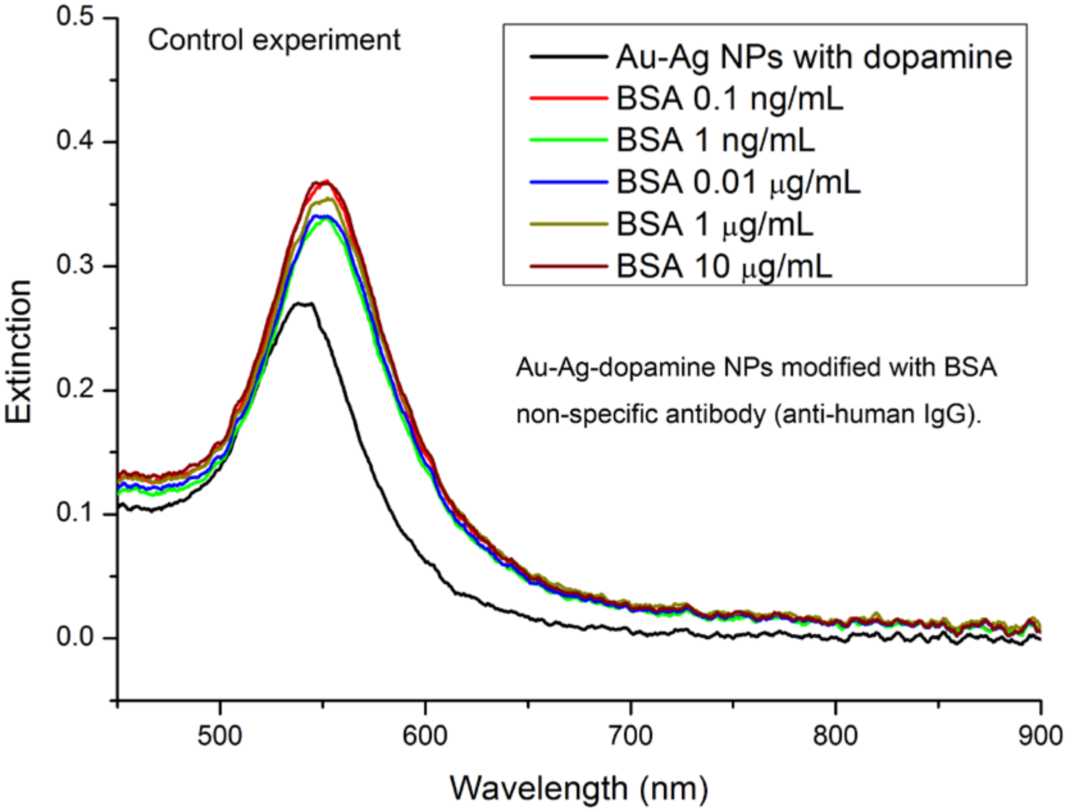

Figure 3.35 LSPR spectra recorded in the control experiments using Au-Ag-dopamine NPs modified with BSA non-specific antibody (anti-human IgG). Clearly, the different concentrations of BSA (from 0.1 ng/mL up to 10 µg/mL) cannot be detected from such control experiments.

The calibration curves for detection of different concentrations of BSA using Au-

Ag bi-metallic NPs without and with dopamine modification are depicted in **Figure 3.36**. Moreover, the results from the mono-metallic Au NPs are included as well. In terms of lower limit of detection, while 1 ng/mL of BSA is detectable using mono-metallic Au NPs, the lower concentration of 0.1 ng/mL BSA can be readily determined by using Au-Ag bi-metallic NPs. The sensitivity is further increased to 0.01 ng/mL for Au-Ag bi-metallic NPs modified with poly-dopamine, which is lower than the analytical sensitivity (0.5 ng/mL) of a recently published BSA biosensor study.[58] Moreover, a much larger linear detection range of 0.01 ng/mL to 100 ng/mL is obtained under the optimized conditions. Thus, the obtained TEM grid-marker LSPR biosensor chip can be used for the high throughout detection, which can be time efficient and cost-effective in many application scenarios.

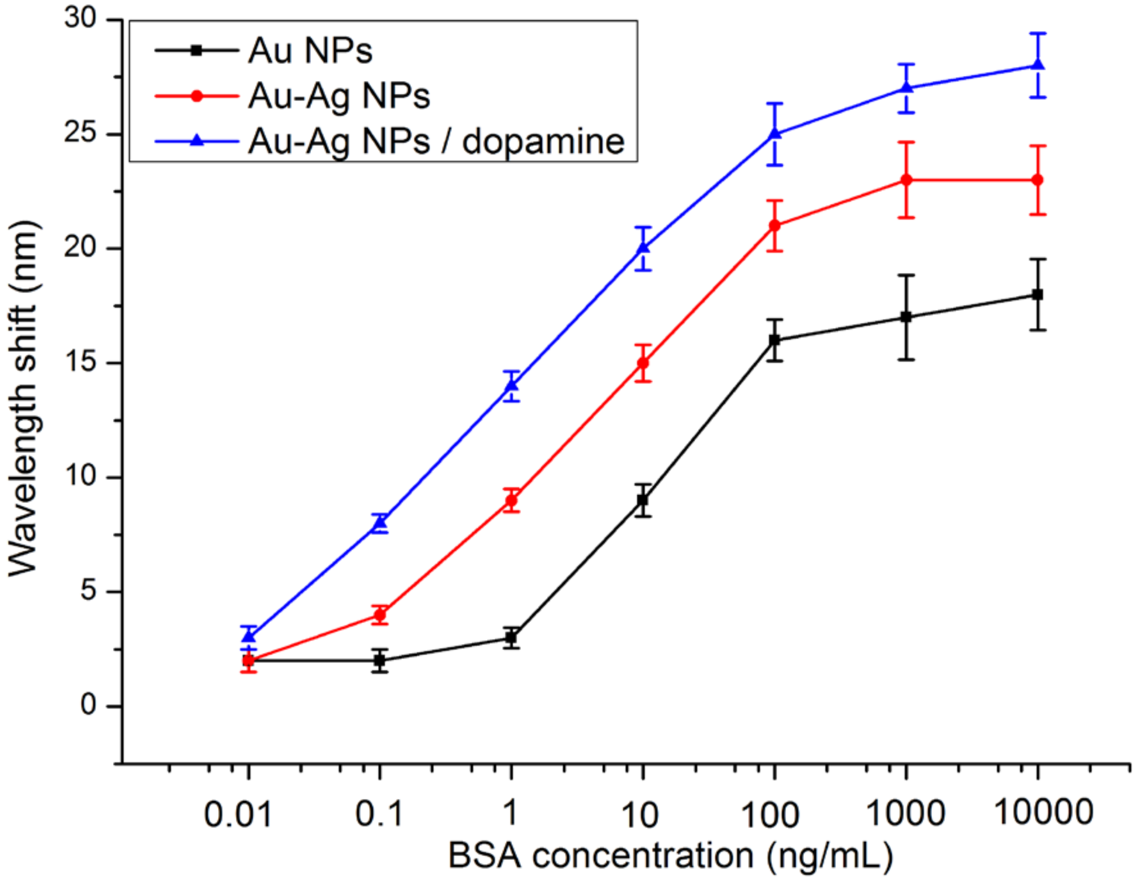

Figure 3.36 Calibration curves for BSA detection using different substrates of mono-metallic Au NPs

(black curve), bi-metallic Au-Ag NPs (red curve) and dopamine modified Au-Ag bi-metallic NPs (blue curve). The evaporation thicknesses of Au and Ag are 4 nm and 2 nm, respectively. All samples were annealed at 500 °C for 8 hr. Three experiments were conducted for each substrate and the average results are shown in the above figure.

Since the plasmonic responses are saturated at highest BSA concentration of 10 µg/mL, the surface morphology of Au/Ag bi-metallic NPs modified with this concentration of BSA is characterized with scanning electron microscope (SEM). For the Au/Ag bi-metallic NPs without dopamine treatment (**Figure 3.37**A), a rough surface morphology is observed as albumin aggregates are formed, indicating thus a successfully biofunctionalization step. Interestingly, the BSA coating layer is mainly found around or near the metal nanoparticles while for the interstitial spaces between NPs, no obvious protein depositions are observed. However, for the Au/Ag bi-metallic NPs with dopamine treatment (**Figure 3.37**B), the entire sample surface was modified with albumin molecules. Moreover, structures like "core-shell" are clearly visible for bigger NPs on glass substrate (**Figure 3.37**B).

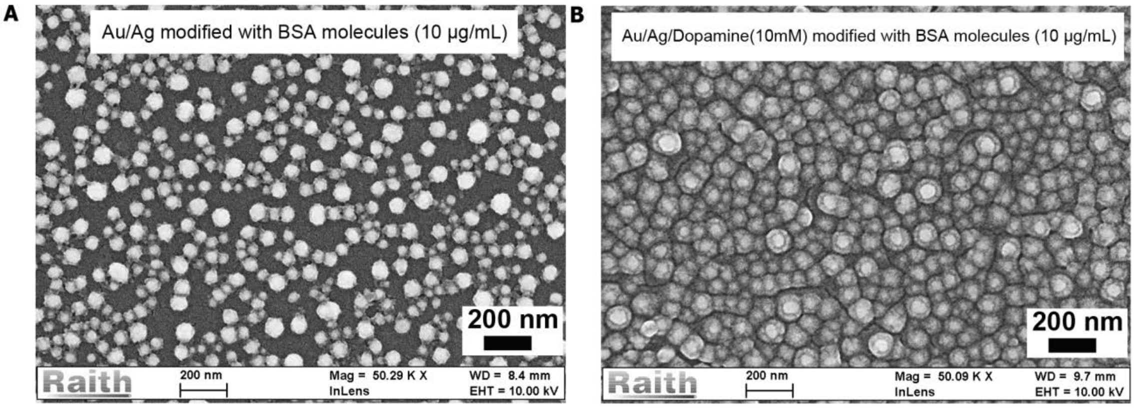

Figure 3.37 SEM images of Au/Ag bi-metallic NPs without (A) and with (B) dopamine treatment after BSA antigen (10 µg/mL) immunoreactions with anti-BSA antibody (0.1 mg/mL).

Although, it is difficult to probe the exact composition of glass surface modified with Au/Ag/dopamine/antibody/BSA antigen films, the authors emphasize that such

NPs functionalization steps are observed over several repeated experiments when the samples have been exhaustively rinsed with ddH_2O and ethanol to remove any possible impurities prior to the SEM imaging characterization. Based on the above surface protocol treatment, the observed SEM morphology could be attributed mainly to the specific presence of BSA molecules and poly-dopamine films.

In short, extremely well-organized and stable Au/Ag bi-metallic NPs are fabricated on glass after 8 hr annealing at high temperature (500 °C) in this part. It was found that fabricated Au/Ag bi-metallic NPs have sharper plasmonic peak in the visible spectrum range with plasmonic response more sensitive than those of monometallic Au NPs. To increase the sensitivity of the LSPR immunosensor, a surface modification strategy based on the multifunctional poly-dopamine layer coating Au/Ag bi-metallic NPs is explored to increase the immobilization quantity of antibody. Thus, as low as 0.01 ng/mL of BSA can be detected under the optimized conditions. The proposed nanoparticle treatment contributes to the development of sensitive LSPR biochips able to detect different concentrations of protein in a simple and high throughput manner.

3.3 Conclusions and Perspectives

In this chapter, the comprehensive studies concerning every essential aspect of label-free LSPR biosensors have been conducted. Generally, the overall work can be divided into five successive parts with each one focuses on one specific challenge for developing the robust label-free LSPR biosensors. In the beginning, the fundamental protocol to prepare ultra-stable gold nanoparticles for reliable biosensors applications has been introduced and the gold nanoparticles morphology dependence on the key experimental parameters such as evaporation thickness and annealing temperature are well documented. The next step involves the preparation of multiple gold nanostructures with different morphology on single glass substrate, which is made possible by exploring two independent protocols: the repeated gold evaporation cycles on predefined areas on single substrate and the using of staples as mask during metal evaporation. The gold evaporation thickness can be readily modulated via these two protocols, which finally leads to the different sized Au nanoparticles on single substrate after annealing at high temperature. The third part deals with the possibility of making multiplexing plasmonic measurement on single substrate. The innovative idea of using commercial TEM grid as the mask allows fabrication of well-organized gold micro/nano-structures on glass substrate. The fourth part focuses on the gold surface biomodification and subsequent specific detection of biomolecules using the optimized Au nanoparticles. In order to verify the surface biomodification protocol used in LSPR biosensors experiments and provide additional information concerning the interaction between antibody and antigen, the complementary technique based on acoustic QCM biosensors have been constructed and used for sequential detection of two different pesticides on single quartz crystal in real-time. Although the gold nanoparticles preparation, surface biomodification and subsequent specific biosensors have been well demonstrated in the first four parts, the LSPR biosensor sensitivity can be further improved as shown in the final part. Two independent ideas of using Au/Ag bi-metallic NPs and dopamine-based functional coatings are proposed to further increasing the lower limit detection of LSPR biosensor towards BSA to 0.01 ng/mL.

Based on these results, the label-free LSPR biosensors can be used to sensitively and specifically detect biomolecules targets in a high throughput manner. Thanks to the large tunability of plasmonic properties from noble metal nanostructures, the LSPR biosensor is increasingly accepted as the one of most competitive optical biosensing technique. Along with the continuous developments made in this field during recently years, the LSPR technique is now expanding its traditional biomolecular detection regime into emerging new frontiers such as alternative energy, photonics mediated catalysis and biomedicine research. Although the LSPR biosensors exhibit so many fantastic advantages as mentioned above, the biorecognition element, i.e. antibody, is still required for analytical specificity and it is unable to probe the chemical structures information of biomolecules targets by conventional transmission LSPR biosensors. In order to really “see” the biomolecules, another promising plasmonic based technique of SERS, namely surface enhanced Raman spectroscopy, allows simultaneous probing the concentration and chemical structures information of the biomolecules target. Inspired by the previous work of bioluminescent bacteria and LSPR biosensors, an innovative SERS biochip has been developed, which will be discussed in details in next chapter.

References:

1. Yemini, M.; Reches, M.; Gazit, E.; Rishpon, J., Peptide nanotube-modified electrodes for enzyme-biosensor applications. *Analytical Chemistry* **2005,** *77* (16), 5155-5159.

2. Rowe, C. A.; Scruggs, S. B.; Feldstein, M. J.; Golden, J. P.; Ligler, F. S., An array immunosensor for simultaneous detection of clinical analytes. *Analytical Chemistry* **1999,** *71* (2), 433-439.

3. Li, J.; Lu, Y., A highly sensitive and selective catalytic DNA biosensor for lead ions. *Journal of the American Chemical Society* **2000,** *122* (42), 10466-10467.

4. Yang, S.; Chen, Z.; Jin, X.; Lin, X., HRP biosensor based on sugar-lectin biospecific interactions for the determination of phenolic compounds. *Electrochimica Acta* **2006,** *52* (1), 200-205.

5. Mauriz, E.; Calle, A.; Montoya, A.; Lechuga, L. M., Determination of environmental organic pollutants with a portable optical immunosensor. *Talanta* **2006,** *69* (2), 359-364.

6. Cui, R.; Pan, H.-C.; Zhu, J.-J.; Chen, H.-Y., Versatile immunosensor using CdTe quantum dots as electrochemical and fluorescent labels. *Analytical Chemistry* **2007,** *79* (22), 8494-8501.

7. Sakai, G.; Nakata, S.; Uda, T.; Miura, N.; Yamazoe, N., Highly selective and sensitive SPR immunosensor for detection of methamphetamine. *Electrochimica Acta* **1999,** *44* (21), 3849-3854.

8. Sepúlveda, B.; Angelomé, P. C.; Lechuga, L. M.; Liz-Marzán, L. M., LSPR-based nanobiosensors. *Nano Today* **2009,** *4* (3), 244-251.

9. Gluodenis, M.; Manley, C.; Foss, C. A., In situ monitoring of the change in extinction of stabilized nanoscopic gold particles in contact with aqueous phenol solutions. *Analytical Chemistry* **1999,** *71* (20), 4554-4558.

10. Grabar, K. C.; Freeman, R. G.; Hommer, M. B.; Natan, M. J., Preparation and characterization of Au colloid monolayers. *Analytical Chemistry* **1995,** *67* (4), 735-743.

11. Ye, J.; Bonroy, K.; Nelis, D.; Frederix, F.; D’Haen, J.; Maes, G.; Borghs, G., Enhanced localized surface plasmon resonance sensing on three-dimensional gold nanoparticles assemblies. *Colloids and Surfaces A: Physicochemical and Engineering Aspects* **2008,** *321* (1), 313-317.

12. Ruach-Nir, I.; Bendikov, T. A.; Doron-Mor, I.; Barkay, Z.; Vaskevich, A.; Rubinstein, I., Silica-stabilized gold island films for transmission localized surface plasmon sensing. *Journal of the American Chemical Society* **2007,** *129* (1), 84-92.

13. Karakouz, T.; Tesler, A. B.; Bendikov, T. A.; Vaskevich, A.; Rubinstein, I., Highly stable localized plasmon transducers obtained by thermal embedding of gold island films on glass. *Advanced Materials* **2008,** *20* (20), 3893-3899.

14. Szunerits, S.; Praig, V. G.; Manesse, M.; Boukherroub, R., Gold island films on indium tin oxide for localized surface plasmon sensing. *Nanotechnology* **2008,** *19* (19), 195712.

15. Karakouz, T.; Holder, D.; Goomanovsky, M.; Vaskevich, A.; Rubinstein, I., Morphology and refractive index sensitivity of gold island films. *Chemistry of Materials* **2009,** *21* (24), 5875-5885.

16. Karakouz, T.; Maoz, B. M.; Lando, G.; Vaskevich, A.; Rubinstein, I., Stabilization of gold nanoparticle films on glass by thermal embedding. *ACS Applied Materials & Interfaces* **2011,** *3* (4), 978-987.

17. Tesler, A. B.; Chuntonov, L.; Karakouz, T.; Bendikov, T. A.; Haran, G.; Vaskevich, A.; Rubinstein, I., Tunable localized plasmon transducers prepared by thermal dewetting of percolated evaporated gold films. *The Journal of Physical Chemistry C* **2011,** *115* (50), 24642-24652.

18. Jia, K.; Bijeon, J.-L.; Adam, P.-M.; Ionescu, R. E., Large scale fabrication of gold nano-structured substrates via high temperature annealing and their direct use for the lspr detection of atrazine. *Plasmonics* **2013**, *8*, 143-151.

19. Yan, C.; Chen, Y.; Jin, A.; Wang, M.; Kong, X.; Zhang, X.; Ju, Y.; Han, L., Molecule oxygen-driven shaping of gold islands under thermal annealing. *Applied Surface Science* **2011,** *258* (1), 377-381.

20. Zhang, X.; Zhang, J.; Wang, H.; Hao, Y.; Zhang, X.; Wang, T.; Wang, Y.; Zhao, R.; Zhang, H.; Yang, B., Thermal-induced surface plasmon band shift of gold nanoparticle monolayer: morphology and refractive index sensitivity. *Nanotechnology* **2010,** *21* (46), 465702.

21. Jain, P. K.; Lee, K. S.; El-Sayed, I. H.; El-Sayed, M. A., Calculated absorption and scattering properties of gold nanoparticles of different size, shape, and composition: applications in biological imaging and biomedicine. *The Journal of Physical Chemistry B* **2006,** *110* (14), 7238-7248.

22. Zhao, J.; Zhang, X.; Yonzon, C. R.; Haes, A. J.; Van Duyne, R. P., Localized surface plasmon resonance biosensors. *Nanomedicine* **2006**, *1* (2), 219-228.

23. Jung, L. S.; Campbell, C. T.; Chinowsky, T. M.; Mar, M. N.; Yee, S. S., Quantitative interpretation of the response of surface plasmon resonance sensors to adsorbed films. *Langmuir* **1998,** *14* (19), 5636-5648.

24. Bendikov, T. A.; Rabinkov, A.; Karakouz, T.; Vaskevich, A.; Rubinstein, I., Biological sensing and interface design in gold island film based localized plasmon transducers. *Analytical Chemistry* **2008,** *80* (19), 7487-7498.

25. Nusz, G. J.; Marinakos, S. M.; Curry, A. C.; Dahlin, A.; Hook, F.; Wax, A.; Chilkoti, A., Label-free plasmonic detection of biomolecular binding by a single gold nanorod. *Analytical Chemistry* **2008,** *80* (4), 984-989.

26. Jia, K.; Bijeon, J. L.; Adam, P. M.; Ionescu, R. E., Sensitive localized surface

plasmon resonance multiplexing protocols. *Analytical Chemistry* **2012,** *84* (18), 8020-8027.

27. Nath, N.; Chilkoti, A., Label-free biosensing by surface plasmon resonance of nanoparticles on glass: optimization of nanoparticle size. *Analytical Chemistry* **2004,** *76* (18), 5370-5378.

28. Jia, K.; Bijeon, J. L.; Adam, P. M.; Ionescu, R. E., A facile and cost-effective TEM grid approach to design gold nano-structured substrates for high throughput plasmonic sensitive detection of biomolecules. *Analyst* **2013,** *138* (4), 1015-1019.

29. Marx, K. A., Quartz crystal microbalance: a useful tool for studying thin polymer films and complex biomolecular systems at the solution-surface interface. *Biomacromolecules* **2003,** *4* (5), 1099-1120.

30. Sauerbrey, G., Verwendung von schwingquarzen zur wagung dunner schichten und zur mikrowagung. *Zeitschrift fur Physik* **1959**, *155*, 206-222.

31. Ding, B.; Yamazaki, M.; Shiratori, S., Electrospun fibrous polyacrylic acid membrane-based gas sensors. *Sensors and Actuators B: Chemical* **2005,** *106* (1), 477-483.

32. Hinsberg, W.; Willson, C.; Kanazawa, K., Measurement of thin‐film dissolution kinetics using a quartz crystal microbalance. *Journal of the Electrochemical Society* **1986,** *133* (7), 1448-1451.

33. Rickert, J.; Brecht, A.; Göpel, W., QCM operation in liquids: constant sensitivity during formation of extended protein multilayers by affinity. *Analytical Chemistry* **1997,** *69* (7), 1441-1448.

34. Keiji Kanazawa, K.; Gordon II, J. G., The oscillation frequency of a quartz resonator in contact with liquid. *Analytica Chimica Acta* **1985,** *175*, 99-105.

35. Reviakine, I.; Johannsmann, D.; Richter, R. P., Hearing what you cannot see and visualizing what you hear: interpreting quartz crystal microbalance data from solvated interfaces. *Analytical Chemistry* **2011,** *83* (23), 8838-8848.

36. Jia, K.; Adam, P.-M.; Ionescu, R. E., Sequential acoustic detection of atrazine herbicide and carbofuran insecticide using a single micro-structured gold quartz crystal microbalance. *Sensors and Actuators B: Chemical* **2013**, 188, 400-404.

37. Jia, K.; Toury, T.; Ionescu, R. E., Fabrication of an atrazine acoustic immunosensor based on a drop-deposition procedure. *IEEE Transactions on Ultrasonics, Ferroelectrics and Frequency Control* **2012,** *59* (9), 2015-2021.

38. Kravets, V.; Schedin, F.; Grigorenko, A., Extremely narrow plasmon resonances based on diffraction coupling of localized plasmons in arrays of metallic nanoparticles. *Physical Review Letters* **2008,** *101* (8), 087403.

39. Jiang, R.; Chen, H.; Shao, L.; Li, Q.; Wang, J., Unraveling the Evolution and Nature of the Plasmons in (Au Core) - (Ag Shell) Nanorods. *Advanced Materials* **2012,** *24* (35), OP200-OP207.

40. Cortie, M. B.; McDonagh, A. M., Synthesis and optical properties of hybrid and alloy plasmonic nanoparticles. *Chemical Reviews* **2011,** *111* (6), 3713-3735.

41. Lee, H.; Dellatore, S. M.; Miller, W. M.; Messersmith, P. B., Mussel-inspired surface chemistry for multifunctional coatings. *Science* **2007,** *318* (5849), 426-430.

42. Lee, Y.; Chung, H. J.; Yeo, S.; Ahn, C.-H.; Lee, H.; Messersmith, P. B.; Park, T. G., Thermo-sensitive, injectable, and tissue adhesive sol-gel transition hyaluronic acid/pluronic composite hydrogels prepared from bio-inspired catechol-thiol reaction. *Soft Matter* **2010,** *6* (5), 977-983.

Chapter 4 SERS substrates based on well-organized gold nanostructures grown on *Escherichia coli* cell templates

The LSPR biosensors reported in previous chapter are able to specifically and sensitively detect biomolecules, however the expensive antibody is indispensable and no chemical structures information can be deduced from the label-free LSPR biosensors. On the contrary, Raman spectroscopy is considered as an important analytical tool thanks to the fact that it provides molecular fingerprint identification.[1-3] However, analyte Raman intensity is very low, which limits the widespread use of conventional Raman spectroscopy in ultrasensitive detection. Fortunately, Raman sensitivity can be dramatically enhanced by virtue of surface enhanced Raman scattering (SERS) effects which were firstly observed by Fleischman et al.[4] in 1974 and independently discovered by Van Duyne[5] and Creighton[6] in 1977. Even though there is still theoretical argumentation towards the origin of SERS, localized surface plasmon resonance (LSPR) of noble metal nanoparticles has been widely considered as the main driving force for the remarkable improvement in SERS sensitivity.[7-9] Therefore, the efficiency of the SERS substrate is highly dependent on the plasmonic properties of its metal nanoparticles that would need to be finely tuned by adjusting their size, shape, and composition.[10] In addition, interparticle spacing is especially important in SERS activity, because the strong plasmonic coupling occurring in the sub-10 nm gap contributes to the generation of so-called “hot spots”, where a local electromagnetic field is prominently enhanced.[11-13] Thus, one can obtain up to 10^{10} and 10^{9} Raman signal enhancement respectively for Ag and Au NPs, which enables single molecule detection.[14-15] Thus, building on its unique features such as high sensitivity, fingerprint specificity, rapidity and ease of operation, SERS has been intensively studied in medical,[16] environmental,[17] biosensor[18-19] and material research [20]during recent years.

A sensitive SERS substrate is the primary prerequisite for any SERS nanosensor applications. A wide range of strategies have been developed in the fabrication of active SERS substrates, so as to control the aggregation and surface roughness of plasmonic nanostructures either by physical manipulation or by chemical transformation.[21] Top-down physical methods (nano-lithography) [22-25] are able to precisely control the size, shape, distance, placement and morphology of metal nanostructures, which ensures good reproducibility of SERS substrates, while there are some inherent disadvantages, including high cost, time consuming fabrication and requirement of specialized personnel. Indeed, it is quite a challenge to prepare plasmonic nanostructures with interparticle distance of sub-10 nm with top-down protocol,[26] where SERS efficiency is enormously improved due to strong plasmon coupling effects. Alternatively, different geometric nanostructures (like nanorods, nanoflowers and controlled nanoclusters, etc.) with a gap distance in sub-10 nm range can be easily obtained by bottom up chemical protocols,[27-30] which results in a random arrangement and aggregation of individual nanoparticles providing irreproducible SERS properties.[31] In order to create closely spaced plasmonic nanostructures in a controlled manner, the template based protocols have received increasing research interests during recent years.[32] For instance, closely spaced arrays of metal nanodisk dimers have been prepared via; 1., electrodeposition using porous anodized aluminum oxide (AAO) membranes as templates;[33] or 2., a nanostructured metal film over a closely-packed colloid template (Ag FON, film over nanoparticle) as an effective SERS substrates,[34] which was later developed as a glucose SERS biosensor,[35] and now incorporated into an implantable glucose detection platform to monitor the concentration of glucose *in vivo*.[36] Biological templates such as DNA,[37] proteins,[38] virus[39] and even butterfly wings[40] have also been explored as versatile templates to fabricate highly sensitive and reproducible SERS active substrates.

In this chapter, the samples used in the previous LSPR biosensors have been firstly tested in the SERS experiment. However, due to the fact that both the size and interparticle distance of these Au NPs increase at the same time as the evaporation film thickness increases, the overall SERS efficiency is compromised. Indeed, it has already been reported that larger Au NPs size (≥ 40 nm) with smaller gap distances are two important factors for a highly efficient SERS substrate.[41] In this context, based on the previous research experiences in bacterial cells (**Chapter 2**) and gold nanoparticles (**Chapter 3**), an interesting protocol is created to fabricate a highly sensitive SERS substrate by using *E. coli* bacterial cells as templates to finely control the creation of stable Au NPs, through high temperature annealing. Thus, the bacterial cell templated Au nanostructures show considerably enhanced SERS intensity when comparing to freely annealed Au NPs made without bacterial templates.

4.1 Experimental Section

4.1.1 Cultivation and fixation of *E. coli* bacterial cells

Fresh LB medium was prepared by dissolving 2 g LB broth powder (L320, Sigma) into 100 mL ddH$_2$O followed by autoclave at 121 °C for 15 min and was used as bacterial cell culture solution. Then, a drop of *E. coli* bacteria stock was inoculated into 10 mL fresh LB medium containing 10 µL kanamycin solution (50 mg/mL) and cultivated at 37 °C for 12 hr in a water bath to obtain an optical density of 0.7. Furthermore, 1 mL of the resulting bacterial cells suspension was centrifuged at 10,000 rpm for 10 min followed by two fresh PBS buffer washes. Next, the obtained bacterial cells pellet was fixed in 500 µL glutaraldehyde (G7651, Sigma) aqueous solution of 2.5 wt % at 4 °C for 4 hr. After fixation, the bacterial suspension was centrifuged (10,000 rpm, 5 min) and washed twice with ddH$_2$O, followed by a stepwise dehydration using graded ethanol aqueous solutions of 30 %, 50 %, 70 % and 100 %, respectively. Each step was conducted for 15 min at 4 °C followed by centrifugation (10,000 rpm, 5 min) and washing with ddH$_2$O. Finally, the bacterial cells were dispersed in 1 mL absolute ethanol and ready to be used as SERS templates.

4.1.2 Fabrication of *E. coli* bacterial cells templates containing plasmonic gold nanostructures

A classical microscopy slide was cut into pieces (25 mm × 8 mm)^2 and used in the preparation of SERS substrates. The glass substrate was exposed to a 2:8 (detergent Deco 90-ddH$_2$O) solution in an ultrasonic water bath at 50 °C for 15 min. After drying with a N$_2$ flow, 20 µL of a previously obtained bacterial cell suspension (0.7 OD) in absolute ethanol was deposited onto the clean glass substrate and dried freely in air. Furthermore, a TEM copper grid (PELCO, 200 mesh, diameter of 3.05 mm) was fixed onto the bacteria modified glass and used as a mask through a thin gold film evaporation process (thickness from 2 nm to 6 nm) in a vacuum metal evaporator (Plassys MEB 400) by using the electron beam mode. Finally, after carefully removing the TEM grid, the gold evaporated glass sample was transferred into a high temperature oven (Nabertherm) to conduct the thermal annealing at 550 °C for 8 hr in an oxygen atmosphere.

4.1.3 Optical measurement and morphology characterization

The LSPR extinction measurements were conducted by using a home built confocal UV-Vis-NIR system in the transmission mode. The SERS performance of the obtained substrates was evaluated using a typical non-resonant Raman label of trans-1, 2-bis(4-pyridyl)ethylene (BPE). The SERS measurements were conducted by using a Jobin Yvon LabRam microscope system equipped with a red laser of 633 nm and 11 mW working in the back reflection mode. One drop (10 µL) of BPE solution with different concentrations ranging from 10^{-5} to 10^{-12} M was deposited onto the gold-bacteria template substrate, the SERS results were recorded using a 10× objective directly in air. The morphology of fixed bacterial cells and SERS substrates were characterized using a field emission scanning electron microscope (FEG eLine, Raith). Prior to SEM imaging, all the samples were sputter coated with a thin layer of palladium to suppress the charging effects.

4.2 Results and Discussion

4.2.1 The SERS experiments on freely annealed Au NPs

For the samples obtained after high temperature annealing, Au nanoparticles were well dispersed and extremely stable on the glass substrate, and the morphology of these nanostructures (size, shape and interparticle spacing) can be readily modified by experimental parameters, such as with gold film evaporation thickness,[42] which in turn determines the final LSPR properties that strongly affect the SERS efficiency of the obtained substrates. In terms of Au NPs size, it has already been reported that the larger size of Au NPs (≥ 40 nm) normally show excellent SERS intensity when they are closely spaced with each other.[41] However, for the typical Au nanostructures obtained by evaporation followed by high temperature annealing protocol, the Au NPs size and interparticle distance both increased at same time with increased thickness of the evaporation gold film. Therefore, different samples with gold evaporation thickness of 2 nm, 4 nm and 6 nm were prepared to optimize the SERS intensity. The samples used in these experiments were prepared according to the multi-cycle evaporation protocol that has been reported previously (see **Figure 3.8**).[43] The LSPR extinction spectra were recorded in transmission extinction measurement (**Figure 4.1**A) and their corresponding SERS properties were evaluated by recording the Raman spectra after deposition of 10 µL BPE solution (10^{-5} M) onto different zones of Au nanoparticles (**Figure 4.1**B) as illustrated in inset of figures.

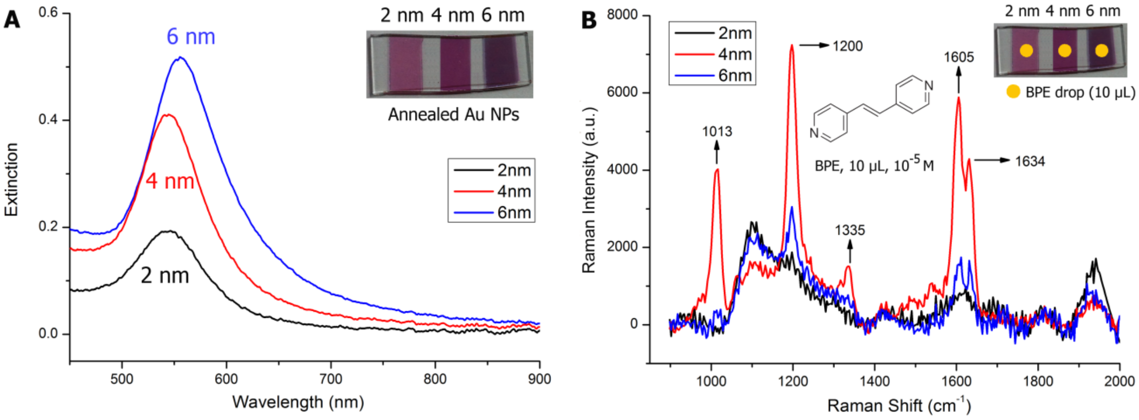

Figure 4.1 The LSPR spectra (A) of different gold nanostructures with initial gold film evaporation thickness of 2 nm, 4 nm, 6 nm and their SERS spectra (B) upon deposition of 10 µL 10^{-5} M BPE solution on the surface, the yellow circle represents one drop of BPE solution. The “barcode” like sample was prepared according to the previously reported protocol[43] and was shown in inset of figures.

The LSPR results in **Figure 4.1**A, show that the plasmon resonant wavelength is slightly red shifted, while the maximum optical density dramatically increases with an increased thickness of gold evaporation. Specifically, large increases of the maximum optical density from 0.19 to 0.52 with a slight red-shift of the resonant wavelength (10 nm) were observed as the evaporation thickness increased from 2 nm to 6 nm. When these samples were used as substrates for SERS measurements, the Au NP zones with an intermediate gold evaporation thickness of 4 nm presented the largest SERS intensity for a same BPE drop (**Figure 4.1**B) when compared to the other thicknesses. When the evaporated gold thickness was 4 nm, the major Raman peaks of BPE molecule were clearly observed and these Raman shifts can be identified based on some published work as follows: the peak at 1200 cm^{-1} is attributed to the ring breathing mode of pyridine including the vibrational movement of the pyridyl nitrogen atom, while the two peaks at 1605 cm^{-1} and 1634 cm^{-1} represent the C-N stretching mode in both the pyridyl ring and BPE vinyl group vibration, respectively.[44-45] The peak located at 1013 cm^{-1} should be attributed to the chemical absorption of BPE onto Au nanoparticles.[46] Additionally, the Raman intensity of the three characteristic peaks of the BPE molecule at 1200 cm^{-1}, 1605 cm^{-1} and 1634 cm^{-1} were measured as 7240, 5887 and 4288 a.u. respectively. The intensity of the same peaks declined to 3050, 1743 and 1659 a.u. respectively for the Au NP zones with a gold evaporation thickness of 6 nm, while these peaks become almost undetectable at a thinner gold film of 2 nm. Based on the Au NPs morphology study in the previous chapter (**Figure 3.9**, **Figure 3.10**), it is assumed that their size and interparticle distance are perfect for an intermediate evaporation thickness (4 nm), which will contribute to an optimal SERS intensity.

4.2.2 The SERS experiments on bacterial cells-templated Au NPs

From part **4.2.1**, it was demonstrated that SERS efficiency of freely annealed Au nanostructures can be enhanced by optimizing the thickness of evaporated gold film, however the overall Raman intensity is still quite limited. Inspired by their micrometer scale rod-like structures and fine membrane morphological features in nanoscale,[47] bacterial cells were used as putative templates to control the assembly of Au nanoparticles during high temperature annealing. When comparing to freely annealed Au nanoparticles, bacterial cell templated Au nanostructures after high temperature annealing present extraordinary enhancement of Raman intensity, such as in the case of an evaporated 4 nm gold film (**Figure 4.2**). Specifically, the intensity of three characteristic Raman peaks at 1200 cm^{-1}, 1605 cm^{-1} and 1634 cm^{-1} are measured as 26850, 42670 and 28669 a.u. respectively, which is up to 8 times enhancement compared to the freely annealed Au NPs without bacterial cells templates. Moreover, there are several additional Raman peaks of BPE molecule such as 1337 cm^{-1}, 1425 cm^{-1}, 1490 cm^{-1} and 1540 cm^{-1} that only appeared in the case of bacterial cell templated Au NPs, which are not presented for the freely annealed Au NPs case, also confirming the excellent SERS enhancement from bacterial cell templated Au NPs.

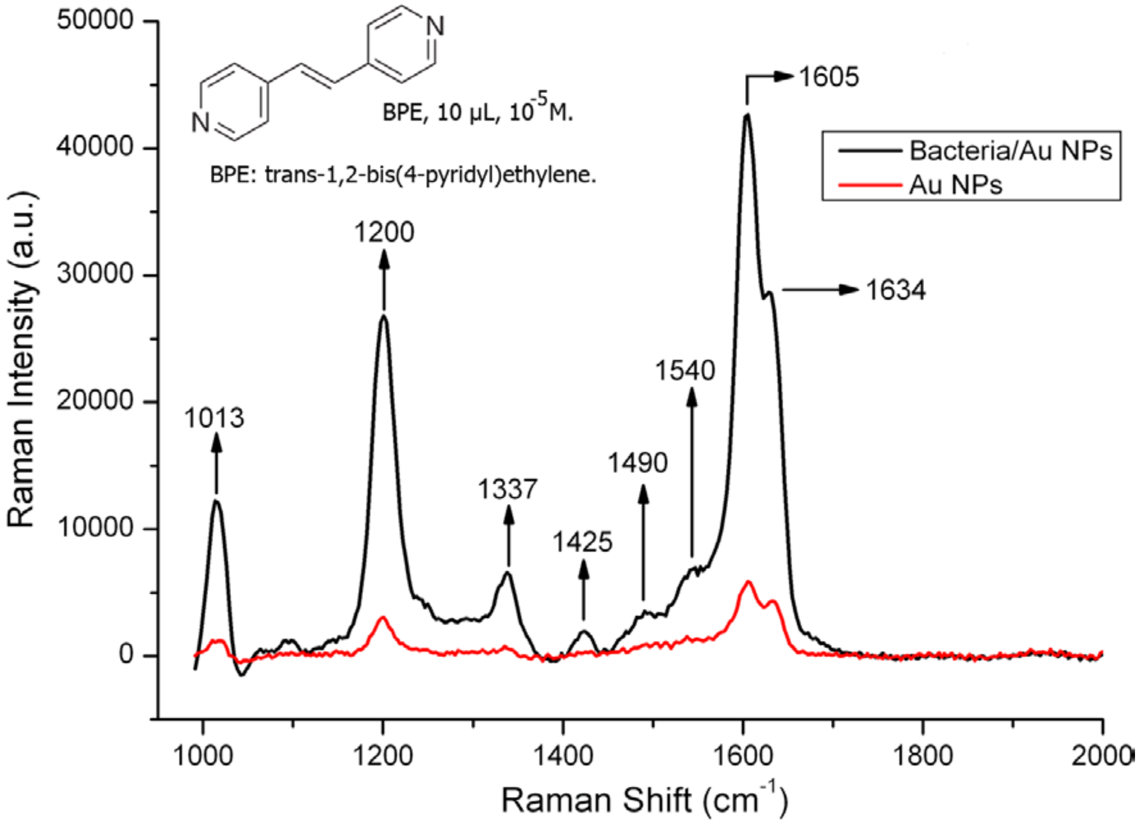

Figure 4.2 The SERS enhancement of bacterial cells templated Au nanostructures upon deposition of 10 μL BPE solution (10^{-5} M) compared to the freely annealed Au nanoparticles without using bacterial cells templates. These two samples have the same evaporation gold film thickness of 4 nm and both are annealed at 550 °C for 8 hr, the accumulation time of SERS measurement is 5 s.

In the case of the other gold evaporation thicknesses (2 nm and 6 nm), the employment of bacterial cell templates also contributed to a dramatically increased SERS intensity under same conditions (**Figure 4.3**). Specifically, for a 2 nm evaporation sample, there are no obvious characteristic BPE Raman peaks detected when freely annealed Au NPs are used, while the three mains peaks at 1013, 1200 and 1605 cm^{-1} show obviously increased Raman intensity (up to 18.7 times increase for 1605 cm^{-1} peak) on bacteria-templated Au NPs. When compared to the SERS results from three bacterial cell templated Au nanostructures, the optimized gold film evaporation thickness is found again at a thickness of 4 nm.

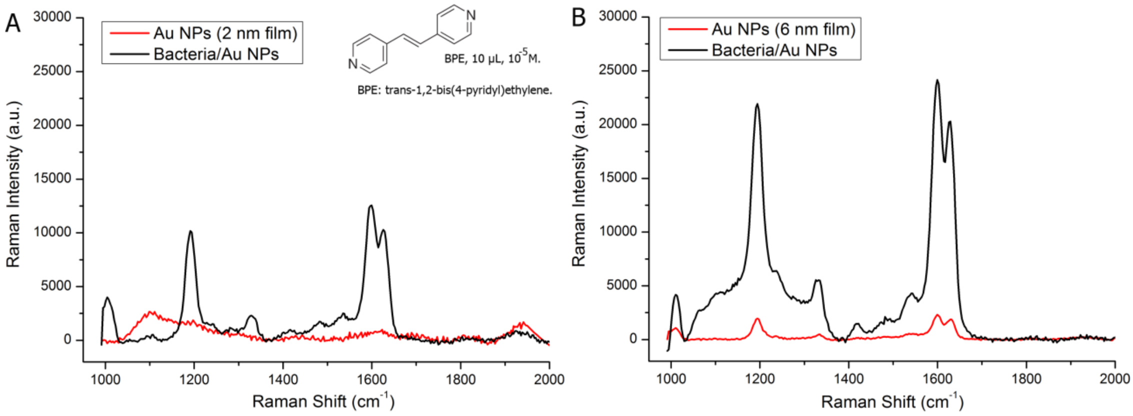

Figure 4.3 The SERS spectra upon deposition of 10 μL BPE (10^{-5} M) onto bacterial templated Au NPs with initial gold evaporation thickness of 2 nm (A) and 6 nm (B). The accumulation time is 10 s.

In order to better understand the reasons for the obviously enhanced SERS signal from bacterial cell templated Au NPs, FE-SEM was used to characterize the morphology-topography of the process steps used in this study. A typical surface morphology of bacterial cells is seen (**Figure 4.4**A), after fixation with glutaraldehyde, the individual *E. coli* bacterial cell is clearly observed with the typical length of 1~2 μm and width around 600 nm, the nanoscale roughness of bacterial cell membrane and the fine features of peritrichous bacterial flagella are clearly observed as well. The freely annealed Au NPs with an initial evaporated gold film thickness of 4 nm show Au NPs that are well dispersed on the glass surface, the average Au nanoparticle size in this case is found to be around 20 nm (**Figure 4.4**B). When the *E. coli* bacterial cells are used as templates, one gets Au NPs aggregates confined to bacterial cells, leading to a higher density of Au NPs inside bacteria templates, and to less dense Au NPs freely annealed outside of the templates (**Figure 4.4**C). The larger Au NPs are generated in the centre of bacterial cell, while large amounts of smaller Au NPs were densely organized along the envelop of cell templates, where much smaller gap distance were readily observed. In addition, the glass surface morphology is obviously modified by the bacteria cells after the high temperature annealing process (**Figure 4.4**D). Based on these morphological characterizations, the high density of plasmonic hot spots especially located along the outer membrane of bacterial cell templates, is likely responsible for the excellent SERS properties brought about by bacteria cell templated Au nanostructures, although the exact mechanism for this excellent SERS enhancement is still yet unclear.

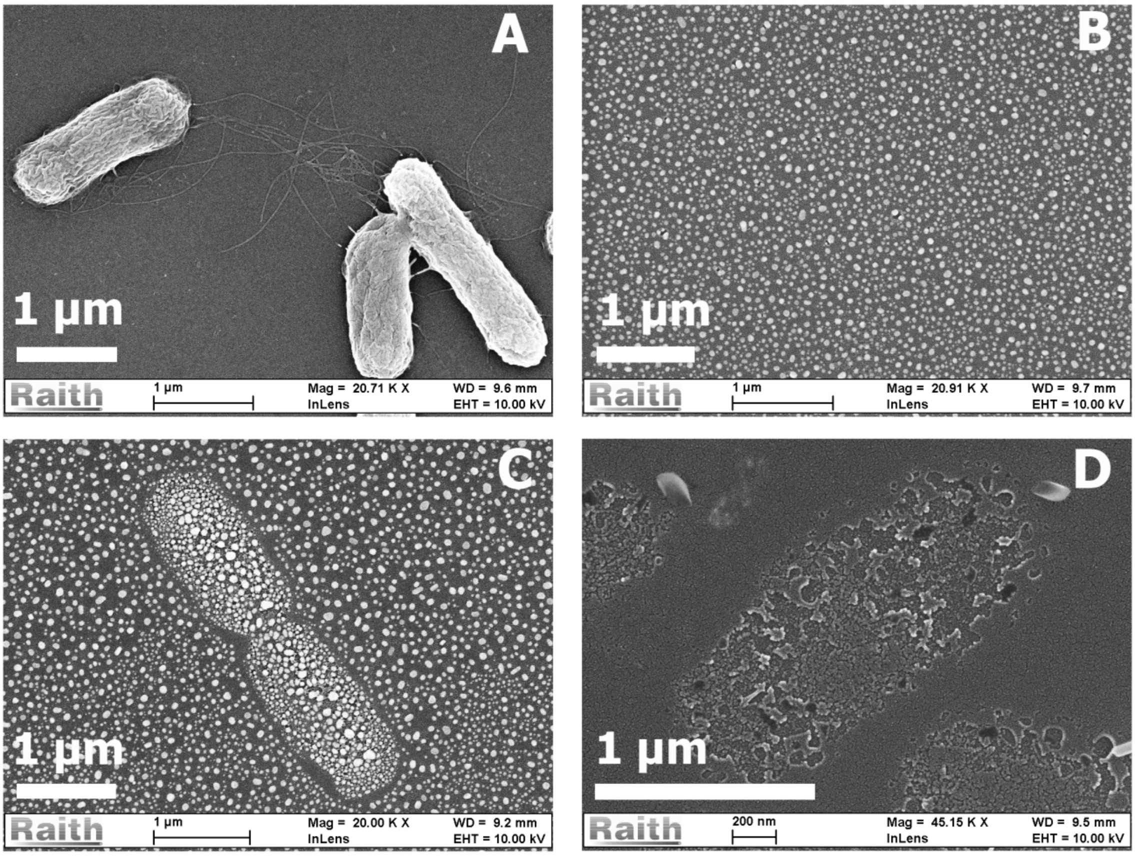

Figure 4.4 The morphology of *E. coli* bacteria after fixation with 2.5 wt % glutaraldehyde solution (A), gold nanoparticles obtained by annealing substrate of 4 nm evaporated film at 550 °C for 8 hr (B), the *E. coli* bacterial cells templated gold micro/nanostructures (C) obtained at same conditions (4 nm evaporation film thickness and annealing at 550 °C for 8 hr) and surface morphology of bacteria cells modified glass substrate after annealing (D).

Furthermore, the size distribution of Au NPs inside and outside the single bacterial cell shown in **Figure 4.4**C was analyzed using the public domain software ImageJ developed by National Institutes of Health and the results were described in **Figure 4.5**. It should be noted that the Au NP zones with the same area size were analyzed. In addition, given the complex and random structures of Au NPs involved, the Au NPs surface area coverage that is negatively correlated with interparticle distance is calculated instead of direct analysis of particle spacing. For the Au NPs located inside the bacterial cell template, a wider size distribution was observed and ranging from 5 nm to 30 nm, with a majority of NPs sized in the 10 nm to 20 nm range (**Figure 4.5**A), while a much narrower size distribution of Au NPs outside the bacterial cell template was recorded with a majority averaging a size of 20 nm (**Figure 4.5**B). However, the surface coverage of Au NPs inside the template (44.2 %) is two times larger than that of Au NPs outside template (20.4 %). Given these analyzed zones, with a same total surface area, a denser surface coverage should correspond to a smaller interparticle distance, which may corroborate with the fact that an obviously enhanced SERS intensity was recorded for the bacterial cell templated Au nanostructures.

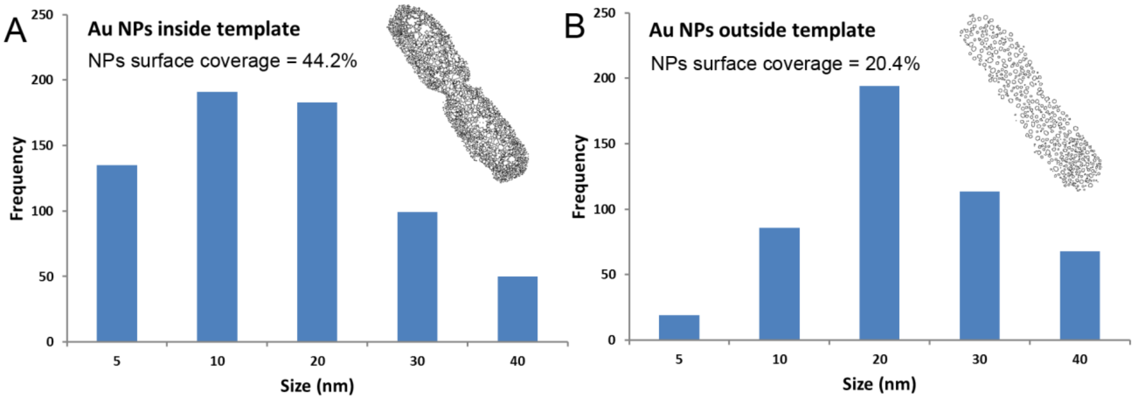

Figure 4.5 Au nanoparticles size distribution inside (A) and outside (B) of single bacterial cell template for the annealed sample with initial gold film thickness of 4 nm. It should be noted that the Au NPs zones analyzed in two cases having the same total areas, which are also illustrated in inset of figures, the Au NPs surface coverage rate is thus calculated from these specifically analyzed zones.

The same quantitative analysis of Au nanoparticle size distribution and surface coverage were also conducted for the other two gold evaporation thicknesses of 2 nm and 6 nm. When the initial gold evaporation thickness is 2 nm, the obtained Au NPs are much smaller than those obtained with 4 nm gold evaporation, and the Au NPs inside the bacterial cell template are again slightly larger than those outside the template (**Figure 4.6** A, B). Quantitatively, the Au NPs inside the template show the size distribution ranging from 5 nm to 20 nm and Au NPs surface coverage of 32.7 % (**Figure 4.6** C), while for the Au NPs outside the template, the majority of the NPs are more uniform in size (8 nm) but the overall Au NPs surface coverage (17.4 %) is almost two times lower than its counterparts inside the template (**Figure 4.6** D).

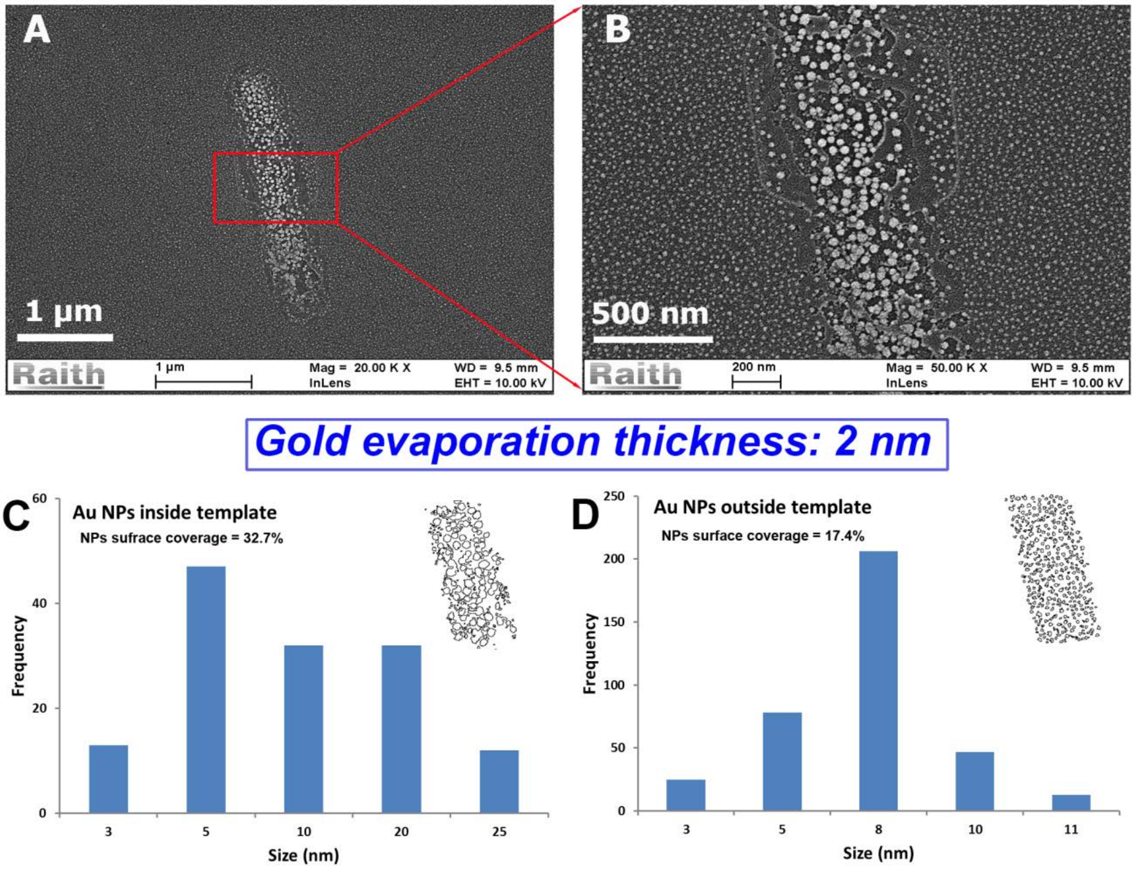

Figure 4.6 The SEM morphology of *E. coli* bacteria templated Au NPs with initial gold film thickness of 2 nm (A) and magnified image (B) showing the detailed Au NPs inside bacterial cell template. Size distribution corresponding to the Au NPs shown in magnified SEM image (B), including the Au NPs

inside the bacteria cell template (C) and freely annealed outside of template (D). The Au NPs zones analyzed in two cases have the same total areas, which are also illustrated in inset of figure. The Au NPs surface coverage rate is calculated from the above analyzed zones.

The same analyses have been conducted for the other sample with 6 nm initial gold evaporation thickness. Although the overall Au NP size for this sample is the largest from all the samples (**Figure 4.7** A, B), quantitative analysis of size distribution and Au NPs surface coverage show similarity with both 2 nm and 4 nm samples (5 nm to 40 nm) which is much wider than that of Au NPs outside the template (40 nm), while the surface coverage is again almost twice larger (33.7 %) when compared to the Au NPs (18.2 %) outside the template (**Figure 4.7** C, D).

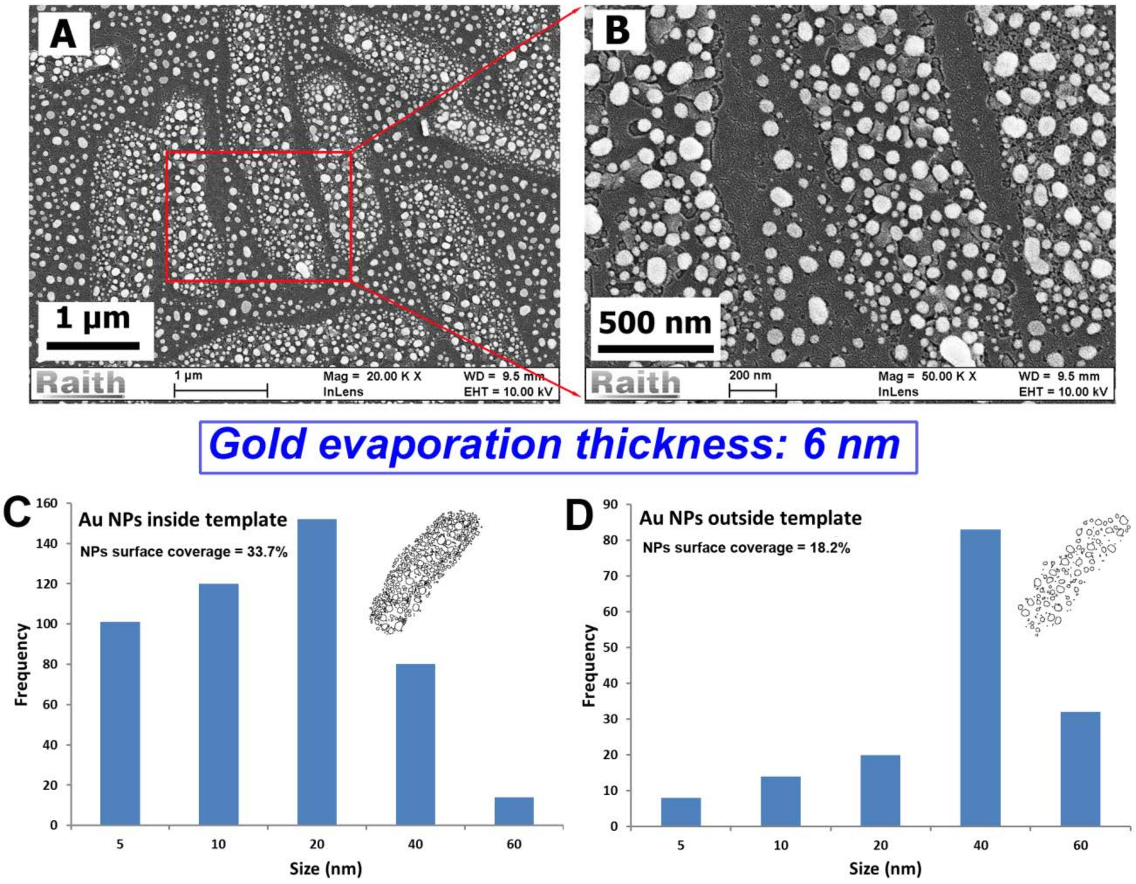

Figure 4.7 The SEM morphology of *E. coli* bacteria templated Au NPs with initial gold film thickness of 6 nm (A) and magnified image (B) showing the detailed Au NPs inside bacterial cell template. Size

distribution corresponding to the Au NPs shown in magnified SEM image (B), including the Au NPs inside the bacteria cell template (C) and freely annealed outside of template (D). The Au NPs zones analyzed in two cases have the same total areas, which are also illustrated in inset of figure. The Au NPs surface coverage rate is calculated from the above analyzed zones.

Finally, it should be noted that these statistical analyses have been conducted using several bacterial cells templated Au NPs zones for all three gold evaporation thicknesses and similar trends were obtained. All these statistical analysis data of Au NPs size range and surface density are summarized in **Table 4.1**.

Table 4.1 The Au NPs average size range and surface coverage inside and outside of the bacterial cells templates for the samples with initial gold film evaporation thickness of 2 nm, 4 nm and 6 nm.

Gold film evaporation thickness [nm]	Inside the bacteria cell template		Outside the bacteria cell template	
	Size range [nm]	Surface coverage [a]	Size range [nm]	Surface coverage
2	5 ~ 20	32.7 %	8 ~ 10	17.4 %
4	5 ~ 30	44.2 %	20 ~ 25	20.4 %
6	5 ~ 40	33.7 %	40 ~ 50	18.2 %

[a] The surface coverage is calculated from Au NPs zones with same total surface area, thus is negatively correlated to the interparticle distances.

4.2.3 SERS detection of BPE

Followed by optimization of Au NPs morphology, the SERS substrate was used for BPE detection. SERS responses for a 10 µL BPE solution at different concentrations ranging from 10^{-12} to 10^{-5} M were recorded using bacterial cell templated Au NPs with an optimized initial gold evaporation thickness of 4 nm, with the control experiment conducted by depositing 10 µL of ddH_2O onto the same sample surface and the SERS spectra thus recorded (**Figure 4.8**).

The intensity of three characteristic Raman peaks of BPE molecule at 1200 cm^{-1}, 1605 cm^{-1} and 1634 cm^{-1} was generally proportionally increased with increasing of BPE concentration. There are additional small Raman peaks at 1337 cm^{-1}, 1425 cm^{-1}, 1490 cm^{-1} and 1540 cm^{-1} as well, however the intensities of these peaks are not well correlated with the BPE concentration. It is observed that the peak at 1634 cm^{-1} gets wider with a BPE concentration lower than 10^{-9} M and finally diminishes with the lowest concentration tested of 10^{-12} M, while the other two peaks at 1200 cm^{-1} and 1605 cm^{-1} are clearly seen for all the BPE concentrations tested, especially for the peak corresponding to pyridyl ring C-N stretching vibration at 1605 cm^{-1}. Therefore, the relationship between Raman intensity of 1605 cm^{-1} peak and various BPE concentrations is used to further evaluate the SERS efficiency of samples with different initial gold film evaporation thicknesses.

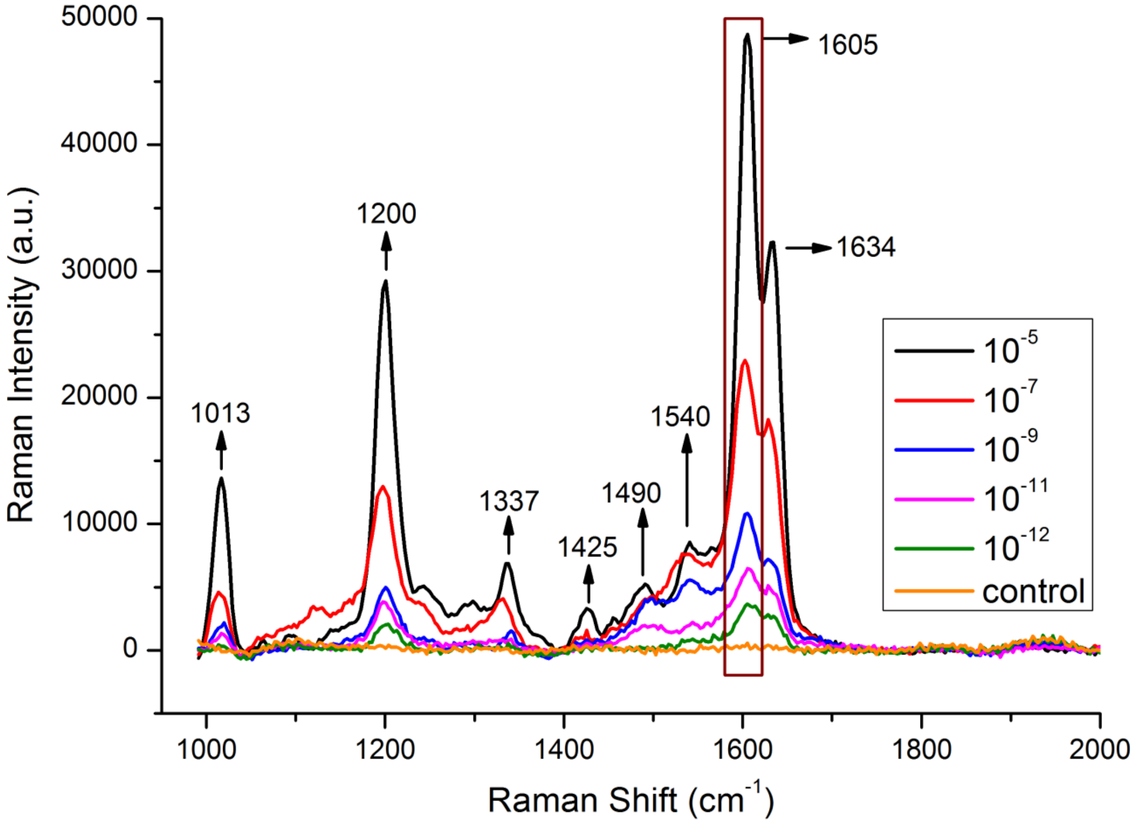

Figure 4.8 The SERS spectra of bacterial templated Au nanostructures upon deposition of 10 μL BPE solution with different concentrations. 10 μL ddH$_2$O is deposited to the same Au nanostructures and used as control. The initial evaporated film thickness is 4 nm, the accumulation time of SERS measurement is

5 s for highest BPE concentration 10^{-5} M and 10 s for other concentrations.

When the Raman intensity of 1605 cm^{-1} peak is plotted versus different concentrations of BPE solutions for the sample with different initial evaporation film thicknesses (**Figure 4.9**), the lowest limit of detection is again obtained at 4 nm sample. Specifically, a BPE concentration as low as 10^{-12} M can be detected from an initial 4 nm film and a wider linear detection range from 10^{-7} M to 10^{-12} M (R^2=0.9647) is recorded as well, while the lower limit of detection of BPE for 2 nm and 6 nm evaporation film sample was found at 10^{-9} M and 10^{-11} M, respectively.

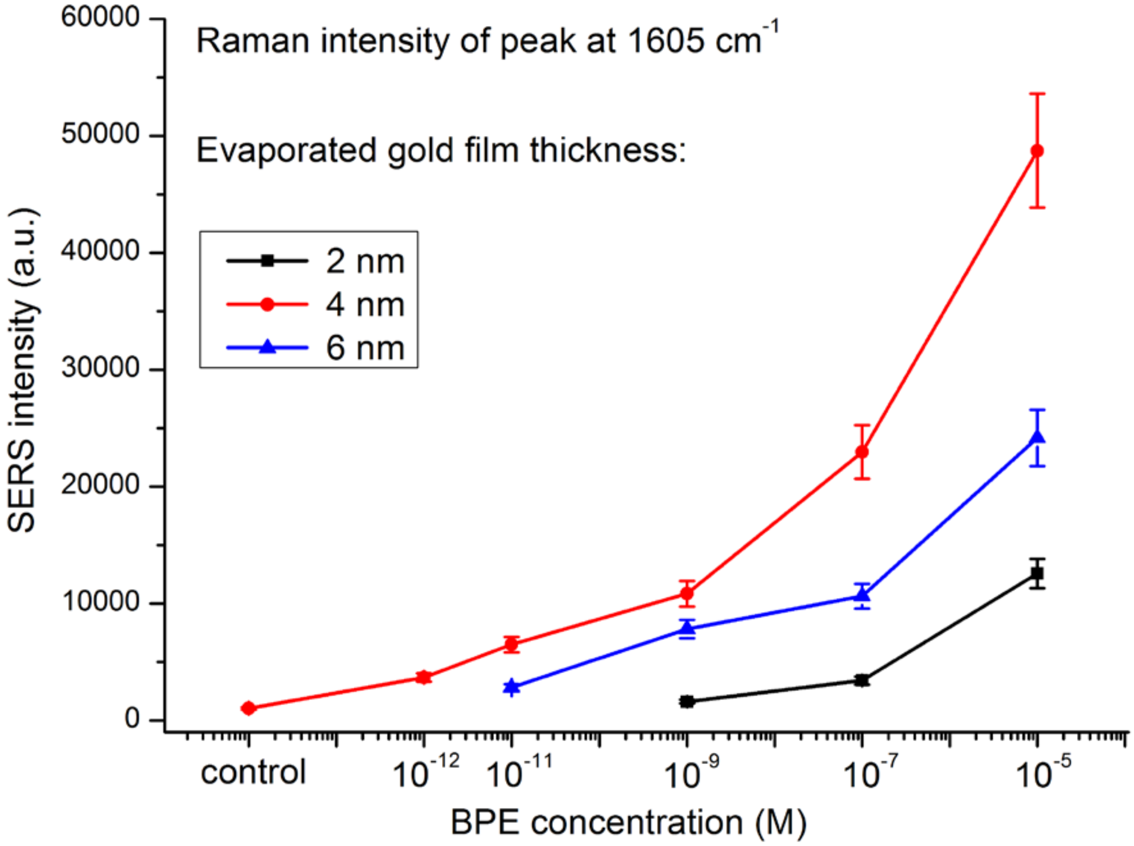

Figure 4.9 The Raman intensity of peak at 1605 cm^{-1} corresponding to different BPE concentrations ranging from 10^{-12} to 10^{-5} M using samples with different initial gold evaporation thicknesses of 2 nm, 4 nm and 6 nm, and same amount of ddH_2O is used as control.

4.3 Conclusions and Perspectives

In this report, a highly sensitive SERS substrate fabrication protocol is reported. The basic idea is to realize the controlled aggregation of plasmonic gold nanostructures by using bacterial cells as the templates. Due to the bacterial cell templating effects, the Au NPs are confined inside the cells and thus closely organized alongside the bacterial cell membrane during high temperature annealing, which lead to a much smaller interparticle distance compared to the Au NPs freely annealed in the absence of bacterial cell templates. As a consequence, the enhanced SERS signals are recorded for the Au nanostructures prepared via bacterial cell templates. The initial gold evaporation thickness is found to play an important role in the SERS performance of the final substrates, and the optimized gold film evaporation thickness was found to be 4 nm. Under the optimized experimental conditions, an extremely low concentration (10^{-12} M) of BPE solution can be readily detected from this novel active SERS substrate and the linear SERS detection was recorded for the BPE concentration range from 10^{-7} to 10^{-12} M. Therefore, it is believed that this presented protocol exploring bacterial cells templates will open new avenues to fabricate sensitive SERS substrates at a large scale.

Although the reported protocol is cost-effective and shows competitive SERS sensitivity for BPE molecules, there are still some important questions need to be solved. For instance, the homogeneity of the SERS intensity over a larger substrate surface should be further optimized, given that the structure complexity of bacterial cell templates will bring additional inhomogeneous effects to the randomly distributed Au NPs. On the other hand, the direct detection of atrazine is conducted by using the optimized SERS substrate, unfortunately there are no obvious atrazine Raman signals detected at this stage. The possible reasons could be the weak absorption of atrazine onto gold nanostructures and the sensitivity of gold-based SERS substrate. Therefore, in order to directly “see” these small molecules like pesticide of small scattering cross section with SERS technique, the more sensitive silver-based SERS substrate should be used and the additional surface modification would be required to facilitate the interfacial adsorption of target molecules onto plasmonic nanoparticles. All in all, the use of bacterial templates opens new avenues in the fabrication of SERS active substrates in a cost effective manner and the burgeoning advancement in this field will continuously expand the regime of SERS nanosensor.

References:

1. Lyon, L. A.; Keating, C. D.; Fox, A. P.; Baker, B. E.; He, L.; Nicewarner, S. R.; Mulvaney, S. P.; Natan, M. J., Raman spectroscopy. *Analytical Chemistry* **1998,** *70* (12), 341-362.

2. Mulvaney, S. P.; Keating, C. D., Raman spectroscopy. *Analytical Chemistry* **2000,** *72* (12), 145-158.

3. Kendall, C.; Isabelle, M.; Bazant-Hegemark, F.; Hutchings, J.; Orr, L.; Babrah, J.; Baker, R.; Stone, N., Vibrational spectroscopy: a clinical tool for cancer diagnostics. *Analyst* **2009,** *134* (6), 1029-1045.

4. Fleischmann, M.; Hendra, P.; McQuillan, A., Raman spectra of pyridine adsorbed at a silver electrode. *Chemical Physics Letters* **1974,** *26* (2), 163-166.

5. Jeanmaire, D. L.; Van Duyne, R. P., Surface Raman spectroelectrochemistry: Part I. Heterocyclic, aromatic, and aliphatic amines adsorbed on the anodized silver electrode. *Journal of Electroanalytical Chemistry and Interfacial Electrochemistry* **1977,** *84* (1), 1-20.

6. Albrecht, M. G.; Creighton, J. A., Anomalously intense Raman spectra of pyridine at a silver electrode. *Journal of the American Chemical Society* **1977,** *99* (15), 5215-5217.

7. Moskovits, M., Surface-enhanced spectroscopy. *Reviews of Modern Physics* **1985,** *57* (3), 783.

8. Campion, A.; Kambhampati, P., Surface-enhanced raman scattering. *Chemical Society Review* **1998,** *27* (4), 241-250.

9. Vo-Dinh, T., Surface-enhanced Raman spectroscopy using metallic nanostructures. *Trends in Analytical Chemistry* **1998,** *17* (8), 557-582.

10. Kelly, K. L.; Coronado, E.; Zhao, L. L.; Schatz, G. C., The optical properties of metal nanoparticles: the influence of size, shape, and dielectric environment. *The Journal of Physical Chemistry B* **2003,** *107* (3), 668-677.

11. Camden, J. P.; Dieringer, J. A.; Wang, Y.; Masiello, D. J.; Marks, L. D.; Schatz, G. C.; Van Duyne, R. P., Probing the structure of single-molecule surface-enhanced Raman scattering hot spots. *Journal of the American Chemical Society* **2008,** *130* (38), 12616-12617.

12. Li, W.; Camargo, P. H.; Lu, X.; Xia, Y., Dimers of silver nanospheres: facile synthesis and their use as hot spots for surface-enhanced Raman scattering. *Nano Letters* **2009,** *9* (1), 485-490.

13. Wustholz, K. L.; Henry, A.-I.; McMahon, J. M.; Freeman, R. G.; Valley, N.; Piotti, M. E.; Natan, M. J.; Schatz, G. C.; Duyne, R. P. V., Structure-activity relationships in gold nanoparticle dimers and trimers for surface-enhanced raman

spectroscopy. *Journal of the American Chemical Society* **2010,** *132* (31), 10903-10910.

14. Emory, S. R.; Haskins, W. E.; Nie, S., Direct observation of size-dependent optical enhancement in single metal nanoparticles. *Journal of the American Chemical Society* **1998,** *120* (31), 8009-8010.

15. Krug, J. T.; Wang, G. D.; Emory, S. R.; Nie, S., Efficient Raman enhancement and intermittent light emission observed in single gold nanocrystals. *Journal of the American Chemical Society* **1999,** *121* (39), 9208-9214.

16. Vo‐Dinh, T.; Yan, F.; Wabuyele, M. B., Surface‐enhanced Raman scattering for medical diagnostics and biological imaging. *Journal of Raman Spectroscopy* **2005,** *36* (6‐7), 640-647.

17. Halvorson, R. A.; Vikesland, P. J., Surface-enhanced Raman spectroscopy (SERS) for environmental analyses. *Environmental Science & Technology* **2010,** *44* (20), 7749-7755.

18. Pekdemir, M. E.; Ertürkan, D.; Külah, H.; Boyacı, İ. H.; Özgen, C.; Tamer, U., Ultrasensitive and selective homogeneous sandwich immunoassay detection by Surface Enhanced Raman Scattering (SERS). *Analyst* **2012,** *137* (20), 4834-4840.

19. Wang, Y.; Zhang, C.-H.; Tang, L.-J.; Jiang, J.-H., Enzymatic control of plasmonic coupling and surface enhanced Raman scattering transduction for sensitive detection of dna demethylation. *Analytical Chemistry* **2012,** *84* (20), 8602-8606.

20. Huang, D.; Bai, X.; Zheng, L., Ultrafast preparation of three-dimensional dendritic gold nanostructures in aqueous solution and their applications in catalysis and SERS. *The Journal of Physical Chemistry C* **2011,** *115* (30), 14641-14647.

21. Gong, X.; Bao, Y.; Qiu, C.; Jiang, C., Individual nanostructured materials: fabrication and surface-enhanced Raman scattering. *Chemical Communications* **2012,** *48* (56), 7003-7018.

22. Coluccio, M. L.; Das, G.; Mecarini, F.; Gentile, F.; Pujia, A.; Bava, L.; Tallerico, R.; Candeloro, P.; Liberale, C.; De Angelis, F.; Di Fabrizio, E., Silver-based surface enhanced Raman scattering (SERS) substrate fabrication using nanolithography and site selective electroless deposition. *Microelectronic Engineering* **2009,** *86* (4–6), 1085-1088.

23. Grand, J.; de La Chapelle, M. L.; Bijeon, J.-L.; Adam, P.-M.; Vial, A.; Royer, P., Role of localized surface plasmons in surface-enhanced Raman scattering of shape-controlled metallic particles in regular arrays. *Physical Review B* **2005,** *72* (3), 033407.

24. Schmucker, A. L.; Barin, G.; Brown, K. A.; Rycenga, M.; Coskun, A.; Buyukcakir, O.; Osberg, K. D.; Stoddart, J. F.; Mirkin, C. A., Electronic and optical vibrational spectroscopy of molecular transport junctions created by on-wire lithography. *Small* **2013,** *9* (11), 1900-1903.

25. Yu, Q.; Guan, P.; Qin, D.; Golden, G.; Wallace, P. M., Inverted size-dependence of surface-enhanced Raman scattering on gold nanohole and nanodisk arrays. *Nano*

Letters **2008,** *8* (7), 1923-1928.

26. Akil-Jradi, S.; Jradi, S.; Plain, J.; Adam, P.-M.; Bijeon, J.-L.; Royer, P.; Bachelot, R., Micro/nanoporous polymer chips as templates for highly sensitive SERS sensors. *RSC Advances* **2012,** *2* (20), 7837-7842.

27. Kim, J.-H.; Kang, T.; Yoo, S. M.; Lee, S. Y.; Kim, B.; Choi, Y.-K., A well-ordered flower-like gold nanostructure for integrated sensors via surface-enhanced Raman scattering. *Nanotechnology* **2009,** *20* (23), 235302.

28. Lee, C. H.; Hankus, M. E.; Tian, L.; Pellegrino, P. M.; Singamaneni, S., Highly sensitive surface enhanced Raman scattering substrates based on filter paper loaded with plasmonic nanostructures. *Analytical Chemistry* **2011,** *83* (23), 8953-8958.

29. Liang, H.; Li, Z.; Wang, Z.; Wang, W.; Rosei, F.; Ma, D.; Xu, H., Enormous surface-enhanced Raman scattering from dimers of flower-like silver mesoparticles. *Small* **2012,** *8* (22), 3400-3405.

30. Yap, F. L.; Thoniyot, P.; Krishnan, S.; Krishnamoorthy, S., Nanoparticle cluster arrays for high-performance SERS through directed self-assembly on flat substrates and on optical fibers. *ACS Nano* **2012,** *6* (3), 2056-2070.

31. Cheng, C.; Yan, B.; Wong, S. M.; Li, X.; Zhou, W.; Yu, T.; Shen, Z.; Yu, H.; Fan, H. J., Fabrication and SERS performance of silver-nanoparticle-decorated Si/ZnO nanotrees in ordered arrays. *ACS Applied Materials & Interfaces* **2010,** *2* (7), 1824-1828.

32. Jones, M. R.; Osberg, K. D.; Macfarlane, R. J.; Langille, M. R.; Mirkin, C. A., Templated techniques for the synthesis and assembly of plasmonic nanostructures. *Chemical Reviews* **2011,** *111* (6), 3736-3827.

33. Qin, L.; Zou, S.; Xue, C.; Atkinson, A.; Schatz, G. C.; Mirkin, C. A., Designing, fabricating, and imaging Raman hot spots. *Proceedings of the National Academy of Sciences* **2006,** *103* (36), 13300-13303.

34. Dick, L. A.; McFarland, A. D.; Haynes, C. L.; Van Duyne, R. P., Metal film over nanosphere (MFON) electrodes for surface-enhanced Raman spectroscopy (SERS): Improvements in surface nanostructure stability and suppression of irreversible loss. *The Journal of Physical Chemistry B* **2002,** *106* (4), 853-860.

35. Shafer-Peltier, K. E.; Haynes, C. L.; Glucksberg, M. R.; Van Duyne, R. P., Toward a glucose biosensor based on surface-enhanced Raman scattering. *Journal of the American Chemical Society* **2003,** *125* (2), 588-593.

36. Yuen, J. M.; Shah, N. C.; Walsh Jr, J. T.; Glucksberg, M. R.; Van Duyne, R. P., Transcutaneous glucose sensing by surface-enhanced spatially offset Raman spectroscopy in a rat model. *Analytical Chemistry* **2010,** *82* (20), 8382-8385.

37. Wilner, O. I.; Willner, I., Functionalized DNA nanostructures. *Chemical Reviews* **2012,** *112* (4), 2528-2556.

38. Uchida, M.; Klem, M. T.; Allen, M.; Suci, P.; Flenniken, M.; Gillitzer, E.;

Varpness, Z.; Liepold, L. O.; Young, M.; Douglas, T., Biological containers: protein cages as multifunctional nanoplatforms. *Advanced Materials* **2007,** *19* (8), 1025-1042.

39. Balci, S.; Noda, K.; Bittner, A. M.; Kadri, A.; Wege, C.; Jeske, H.; Kern, K., Self-assembly of metal-virus nanodumbbells. *Angewandte Chemie International Edition* **2007,** *46* (17), 3149-3151.

40. Tan, Y.; Gu, J.; Xu, L.; Zang, X.; Liu, D.; Zhang, W.; Liu, Q.; Zhu, S.; Su, H.; Feng, C., High density hotspots engineered by naturally piled-up subwavelength structures in three-dimensional copper butterfly wing scales for surface‐enhanced raman scattering detection. *Advanced Functional Materials* **2012,** *22* (8), 1578-1585.

41. Chen, G.; Wang, Y.; Yang, M.; Xu, J.; Goh, S. J.; Pan, M.; Chen, H., Measuring ensemble-averaged surface-enhanced Raman scattering in the hotspots of colloidal nanoparticle dimers and trimers. *Journal of the American Chemical Society* **2010,** *132* (11), 3644-3645.

42. Jia, K.; Bijeon, J.-L.; Adam, P.-M.; Ionescu, R. E., Large scale fabrication of gold nano-structured substrates via high temperature annealing and their direct use for the lspr detection of atrazine. *Plasmonics* **2013**, *8*, 143-151.

43. Jia, K.; Bijeon, J. L.; Adam, P. M.; Ionescu, R. E., Sensitive Localized Surface Plasmon Resonance Multiplexing Protocols. *Analytical Chemistry* **2012,** *84* (18), 8020-8027.

44. Blackie, E. J.; Ru, E. C. L.; Etchegoin, P. G., Single-molecule surface-enhanced Raman spectroscopy of nonresonant molecules. *Journal of the American Chemical Society* **2009,** *131* (40), 14466-14472.

45. Hatab, N. A.; Hsueh, C.-H.; Gaddis, A. L.; Retterer, S. T.; Li, J.-H.; Eres, G.; Zhang, Z.; Gu, B., Free-standing optical gold bowtie nanoantenna with variable gap size for enhanced raman spectroscopy. *Nano Letters* **2010,** *10* (12), 4952-4955.

46. Wells, S. M.; Retterer, S. D.; Oran, J. M.; Sepaniak, M. J., Controllable nanofabrication of aggregate-like nanoparticle substrates and evaluation for surface-enhanced Raman spectroscopy. *ACS Nano* **2009,** *3* (12), 3845-3853.

47. Sondi, I.; Salopek-Sondi, B., Silver nanoparticles as antimicrobial agent: a case study on *E. coli* as a model for Gram-negative bacteria. *Journal of Colloid and Interface Science* **2004,** *275* (1), 177-182.

Conclusion

Biosensors have witnessed unprecedented developments during recent decades, mainly due to the increasing demands of the sensitive, cost-effective and applicable analytical platforms from a wide range of fields such as medicine, biomedical research, drug discovery, the environment, food, process industries, homeland security and bioterrorism defense. Along with these diverse applications, a plenty of different biosensors have been constructed and some are commercialized and all these different biosensors have their specific pros and cons. While the topic of this thesis is confined to the optical biosensor or bioassay, which is a highly interdisciplinary subject requires knowledge from biotechnology, optical physics and materials chemistry.

In the beginning, the fundamentals of optical biosensors have been introduced in order to explain the main principles behind various optical biosensors, thereby enables a classification of catalytic and affinity based biosensors. Afterwards, the bioassay based on engineered bacteria bioluminescence and plasmonic mediated biosensors have been used as the representative examples, the essential aspects from both bioassays and biosensors are discussed, followed by summarizing the recent applications of these biosensors and explaining some highlight case studies.

Next, the experimental work concerning the whole-cell based *E. coli* bacterial bioluminescent assays have been presented in Chapter 2. In this part, instead of constructing new strains, we have basically developed two novel protocols that are able to sense the toxic effects of pesticides by modulation of bacterial metabolisms. The first protocol is a “fresh” and “overnight” two stage test, including a 9 hr cold incubation between two consecutive tests, finally allows a more sensitive distinguish atrazine toxic effects towards protein damage responsive engineered *E. coli* TV1061 bacteria. The second protocol consists of three major steps of incubation, centrifugation and washing, where the potential interference from bacterial metabolites is significantly reduced, which in turn enables a more sensitive detection of carbofuran toxicity using *E. coli* DPD2794 bacteria response to DNA damage. These two protocols used the existed engineered bacteria strains, the sensitivity improvement is obtained only by refining the experimental parameters, thus it is assumed these protocols are advantageous in terms of cost-effectiveness and these methods can be further extended into other engineered bacterial strains. The bacterial bioluminescent assays show competitive sensitivity, while their poor analytical specificity still needs to be greatly improved.

Further, the Chapter 3 focuses on the affinity-based optical biosensors, where the immunosensors on the basis of specific antibody-antigen interaction are the dominant workhorses. Although the immunoreactions can be transduced by various different optical methods, the experiments in this thesis are confined to the plasmonic mediated optical biosensors. In this part, the systematic studies including 5 inter-connected sections have been conducted. The first section introduces the fabrication of ultra-stable plasmonic substrate via gold evaporation followed by high temperature annealing as well as the modulation of Au nanoparticles morphology by evaporation thickness and annealing temperature, while the next parts deal with the preparation of multiplexing and well-organized plasmonic nanostructures using extremely simple masks (like scotch tape, staples and TEM grid). The following section involves selection of optimized Au NPs and subsequent nanostructures biomodification for specific biomolecules detection, the biomodification protocol used is also validated independently by the complementary QCM technique. The final part presents the enhancement of overall plasmonic biosensor sensitivity via Au/Ag bi-metallic NPs and dopamine functional coatings.

Finally, an interesting SERS active substrate has been fabricated based on the previous research experience from bacterial cells and gold nanoparticles. It is the first time of using bacterial cells as templates to create controlled Au nanostructures for such SERS applications. Thanks to the bacterial cells template effects, the Au NPs are organized into controlled micro/nano-structures containing high density of plasmonic hotspots, which finally leads to significantly enhanced Raman intensity. The feasibility of this substrate is exemplified by the ultrasensitive detection of BPE at 10^{-12} M after optimization of gold evaporation thickness.

Although the metabolism of the bacterial cells is already proved to exert significant influences onto the overall analytical performance of bioluminescent assays, the detailed knowledge concerning the bacterial metabolism and its physiology behaviors are highly demanded for the future study. Moreover, the optical bioassay based on bacterial bioluminescence is able to provide competitive sensitivity, however it is quite a challenge to obtain plausible analytical specificity. The analytical specificity can be guaranteed in the LPSR biosensors due to the interaction between antibody and antigen, and a reasonable sensitivity in ng/mL can be obtained after appropriate experimental optimization. However, these biosensors fail to provide the fingerprint structure information of analyte. Driven by this challenge, we created the active SERS substrate thanks to the effective integration of bacterial cells and Au NPs, and the preliminary results indeed proves the feasibility of this SERS substrate. The ultimate challenge is the reliable and reproducible determination, in other words, the homogeneity of SERS measurement should be carefully evaluated prior to the real application of these SERS active substrates. In additional, the biochemical information obtained from single analytical platform is limited, in this sense, the combination of two or several analytical techniques will ensure the more comprehensive understanding the biomolecules interactions. Although the QCM technique is used to validate the biomodification protocols involved in the LSPR biosensors, they are still independent experiments at present; more research efforts to seamlessly integrate the different optical detection platforms should be made. In additional, while the analytes are detected in the standard aliquots solutions in the present work, the following experiments should evaluate the analytical performance of these optical biosensors using the real world samples such as industrial waste water, blood and serum samples. With these challenges in mind, the research interests in the label-free optical detection will continuously grow and definitely expand their existing regime in the near future.

Chapter 5 French summary

5.1 Introduction

Avec la présence croissante de différents composés toxiques dans l'environnement et les préoccupations croissantes de leurs effets délétères sur la santé humaine, il est impératif de développer les méthodes d'analyse bas coût, rapides et faciles de mise en œuvre qui restent sensibles et spécifiques. Afin de détecter ces composés toxiques et les effets associés, les méthodes d'analyse disponibles peuvent être divisées en deux groupes différents: les analyses physico-chimiques classiques ou les biocapteurs et des essais biologiques. Le premier, illustré par la chromatographie en phase liquide couplée à la spectrométrie de masse (LC/MS), est capable de fournir une haute sensibilité et spécificité, mais les instruments complexes et coûteux sont difficilement accessibles pour de nombreux laboratoires, ce qui entrave l'utilisation plus large de ces méthodes. Au contraire, les biocapteurs ou les essais biologiques sont rapides et capables de fournir les informations sur la présence de polluants dans l'environnement et sur leurs effets sur la vie des biosystèmes. Les biocapteurs sont définis comme des dispositifs d'analyse incorporant un matériau biologique (par exemple des tissus, des micro-organismes, des organites, des récepteurs cellulaires, des enzymes, des anticorps, des acides nucléiques, des produits naturels, etc.), intimement associé ou intégré dans un transducteur physico-chimique ou microsystème de transduction, qui peut être optique, électrochimique, thermométrique, piézo-électrique, magnétique ou micromécanique. Même si de nombreux types de biocapteurs existent, cette thèse se concentre sur les biocapteurs et les systèmes où l'information est recueillie par la mesure des photons, en d'autres termes des biocapteurs optiques.

Les biocapteurs optiques constituent une classe de systèmes analytiques particulièrement performants et très largement utilisée. Généralement, il existe deux protocoles de détection qui peuvent être mises en œuvre dans les biocapteurs optiques: détection basée sur la fluorescence et détection sans étiquette. Même si la détection basée sur la fluorescence est encore largement utilisée, la détection sans étiquette apparaît comme une configuration très prometteuse dans les biocapteurs optiques, puisque les molécules cibles ne sont pas marquées ou altérés, et sont détectées sous leur forme naturelle. Ce type de détection est relativement facile à réaliser et peu cher. Il permet une mesure quantitative et cinétique de l'interaction moléculaire.

En se basant sur le principe de détection, les biocapteurs optiques sans étiquette dans cette thèse sont classés en deux groupes indépendants: les biocapteurs optiques catalytiques et ceux basés sur l'affinité. Dans le premier, les biocomposants sont utilisés pour reconnaître les espèces biochimiques et les transformer en un produit par une réaction biochimique. Dans le second, le principe est de détecter la liaison spécifique de l'analyte à un élément de bioreconnaissance. Le premier est illustré par la bioluminescence basée sur des cellules bactériennes génétiquement modifiées pour produire des signaux luminescents lorsqu'elles sont exposées à des substances toxiques. De nombreux biocapteurs d'affinité ont été développés à l’aide de différentes biomolécules et de méthodes de lecture optiques adaptées. Dans cette thèse, les immunocapteurs plasmoniques sont présentés comme l'exemple typique de biocapteur d’affinité.

5.2 Bioluminescence bactérienne pour la détection des pesticides

5.2.1 Fondements de bioluminescence bactérienne

La bioluminescence est le processus de production de la lumière à l'intérieur des organismes vivants, et existe chez de nombreuses créatures marines et certains invertébrés terrestres aussi. Bien que la bioluminescence puisse s’exprimer dans divers organismes, la bioluminescence bactérienne est naturelle pour 11 espèces bactériennes de quatre genres (*Vibrio*, *Photobactérie*, *Shewanella* et *Photorhabdus*), et est particulièrement importante en raison de l'omniprésence et la simplicité des cellules bactériennes. Initié il y a environ 20 ans, le capteur à bactéries bioluminescentes, qui se compose d'un microorganisme vivant génétiquement modifié pour émettre de la lumière en fonction du taux de toxiques présent dans son environnement et du stress occasionné, offre une alternative intéressante pour les applications de surveillance de l'environnement. La construction générale de cellules bactériennes génétiquement modifiées et le mécanisme de la bioluminescence induite par la substance toxique ont été illustrés par la **Figure 5.1**.

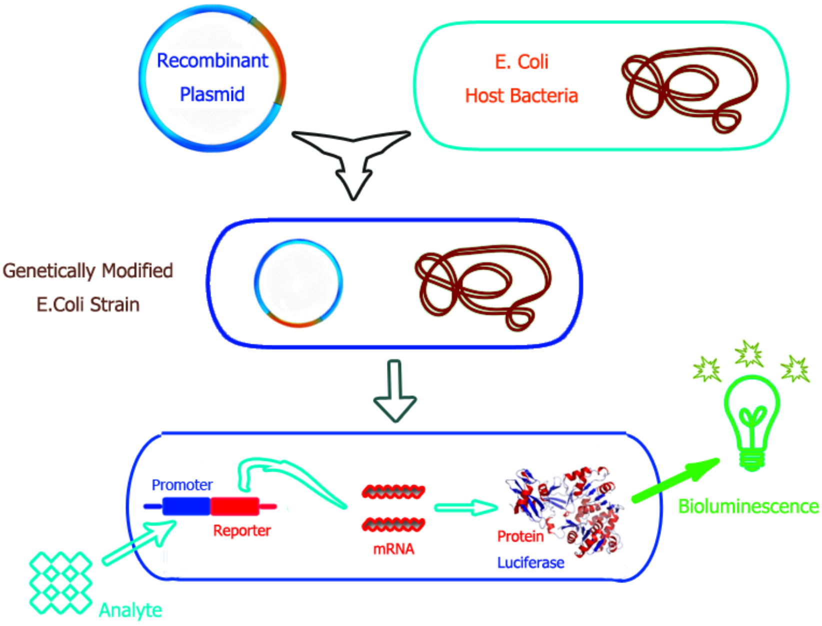

Figure 5.1 Schéma de la modification génétique des bactéries *Escherichia coli* régulières et le mécanisme

spécifique de développement de bioluminescence induite par toxique.

En raison de la diversité des parties de détection (gène promoteur) et des éléments de reportant (protéine fluorescente ou la luciférase), ainsi que les propriétés intrinsèques des cellules vivantes, les essais biologiques sur les cellules bactériennes sont capables de détecter les effets de la seule partie biodisponible de toxique et peut aussi quantifier la toxicité totale de plusieurs mélanges de substances toxiques pour les cellules vivantes. En outre, la bioluminescence bactérienne, permise par les gènes lux, est un type spécial de chimiluminescence produite dans les cellules microbiennes vivantes sans obligation d'excitation optique externe. Les biocapteurs ou les bioessais à base de bactéries luminescentes ont été largement utilisés dans divers domaines comme la biotechnologie, la surveillance environnementale et l’écotoxicologie. Cependant, la majorité des travaux publiés ont étudié la bioluminescence bactérienne dans une courte période (30 min) et les tests bioluminescents ont été réalisés à température ambiante.

Dans cette thèse, deux nouveaux protocoles bioluminescentes ont été développés dans le but d'augmenter la sensibilité de détection des pesticides en utilisant deux cellules bactériennes génétiquement modifiées (*E. coli* TV1061 et *E. coli* DPD2794). Le premier protocole consiste à mesurer l’activité des bactéries en présence de pesticides après une nuit d’incubation à 4°C. Le second consiste à remplacer à l’aide d’une centrifugeuse le milieu de culture après un temps optimisé d’incubation avec le pesticide. L'idée principale de ces deux protocoles est de contrôler le métabolisme des bactéries afin de diminuer la bioluminescence propre aux bactéries indépendante de la présence ou non de pesticides, ce qui conduira à l'amélioration des performances analytiques du système puisque le signal de bioluminescence est alors directement proportionnel à la quantité de pesticides. Différents paramètres (densité optique bactérienne, la température d'essai, et le temps d'incubation) sont optimisés de manière à obtenir une détection sensible de la toxicité des pesticides.

5.2.2 Premier protocole: description et résultats obtenus

La Figure 5.2 présente une vue d'ensemble de ce protocole, qui inclut une première lecture pendant 5h de la bioluminescence d'une suspension bactérienne fraîchement préparé en présence de l'atrazine, et une deuxième lecture après un temps d'incubation à 4 °C. Dans les deux cas, les mesures de bioluminescence ont été acquises à 25 °C. Les paramètres importants tels que la densité optique bactérienne et le temps d'incubation à 4 °C ont été optimisés et il a été montré que les deux valeurs optimales sont respectivement de 0,08 et de 9 h.

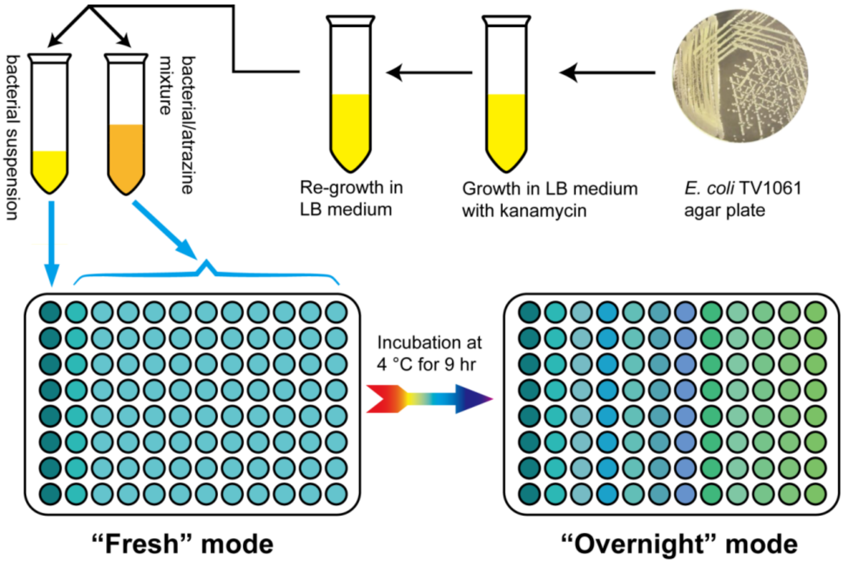

Figure 5.2 Schéma du protocole montrant la première étape avec une mesure de bioluminescence immédiatement après le mélange bactéries/toxique (« Fresh » mode) et la seconde étape après incubation de la même plaque de microtitrage à 4 °C pendant 9 h (« Overnight mode »). Des cellules bactériennes seules ont été utilisées comme contrôle et la mesure de bioluminescence a été effectuée à 25 °C, pour les deux étapes.

Ce protocole en deux étapes est donc utilisé pour détecter les effets toxiques de l'atrazine sur des cellules bactériennes *E. coli*. Dans le mode dit "fresh" (voir **Figure 5.3**), l'évolution temporelle de l'intensité de la bioluminescence bactérienne est enregistrée sous trois conditions: A, cellules bactériennes sans atrazine, B, cellules bactériennes avec des concentrations d'atrazine comprises entre 0,01 pg/mL à 1 µg/mL et C: cellules bactériennes des concentrations d'atrazine supérieures à 10 µg/mL.

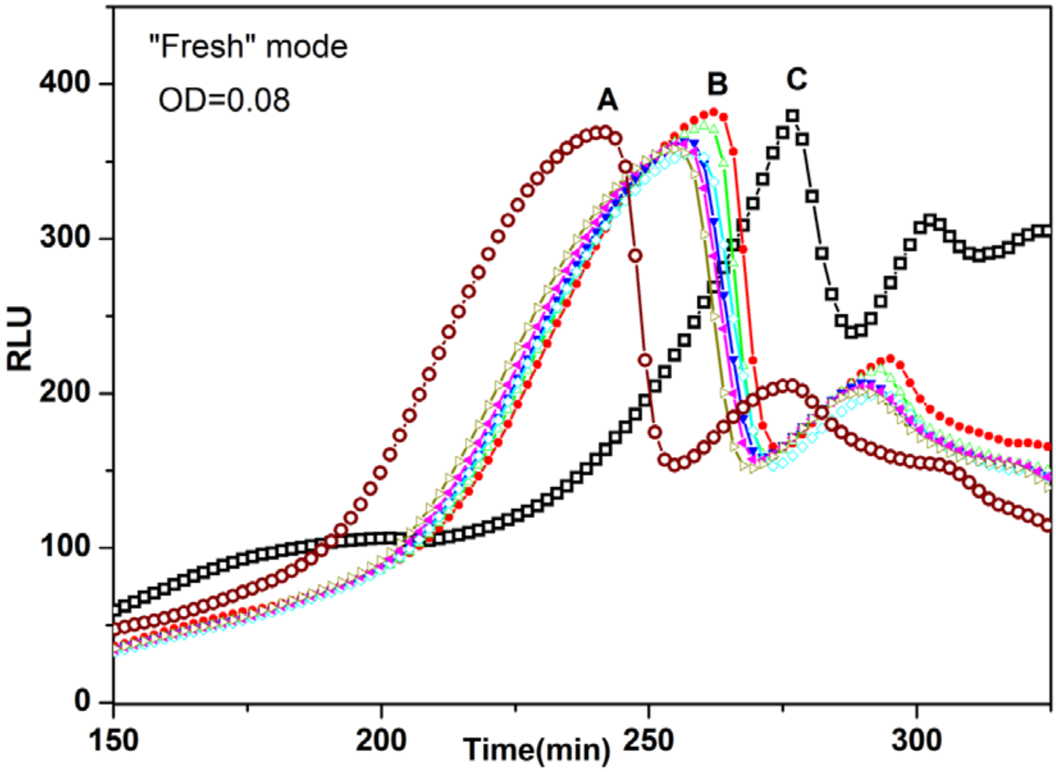

Figure 5.3 Evolution de la bioluminescence de bactéries *E. coli* TV1061 (0,08OD) en présence de différentes concentrations d’atrazine dans le mode dit "fresh". Les mesures ont été enregistrées à 25 °C, (A-bactéries, sans atrazine; B-bactéries en présence d’atrazine pour des concentrations comprises entre 0,01 pg/mL et 1 µg/mL, C-bactéries en présence d’atrazine de concentration 10 µg/mL).

Les courbes de bioluminescences dans les conditions A et B présentent des formes très similaires. La présence d'atrazine augmente le temps d’apparition des pics de bioluminescence. On observe une forte augmentation du temps d’apparition du pic principal lorsque la concentration en atrazine est fixée à 10 µg/mL et une modification de la forme du pic qui devient plus étroit que ceux observés pour des concentrations plus faibles. Le mode dit « fresh » permet seulement à partir du temps d’apparition du pic de confirmer la présence d’atrazine dans le milieu et de distinguer entre deux gammes de concentrations.

Par comparaison avec les résultats obtenu avec le mode dit « fresh », le mode dit « overnight » permet de discriminer entre les différentes concentrations d'atrazine comme le montre la **Figure 5.4**. Toutes les courbes de mesure de la bioluminescence présentent un pic qui est plus diffus pour ce mode, mais qui apparaît très rapidement après le début du processus de mesure. L'amplitude du pic augmente régulièrement de 47 RLU pour 10 fg/mL atrazine à 64 RLU pour 1 µg/mL atrazine, puis brutalement pour la concentration la plus élevée (10 µg/mL), où une valeur élevée de la bioluminescence a été observée (150 RLU). Pour une meilleure visualisation, l'encart dans la **Figure 5.4** présente les détails de la mesure de la bioluminescence bactérienne induite par les concentrations d'atrazine comprises entre 0,01 pg /mL et 1 µg/mL ainsi que le contrôle.

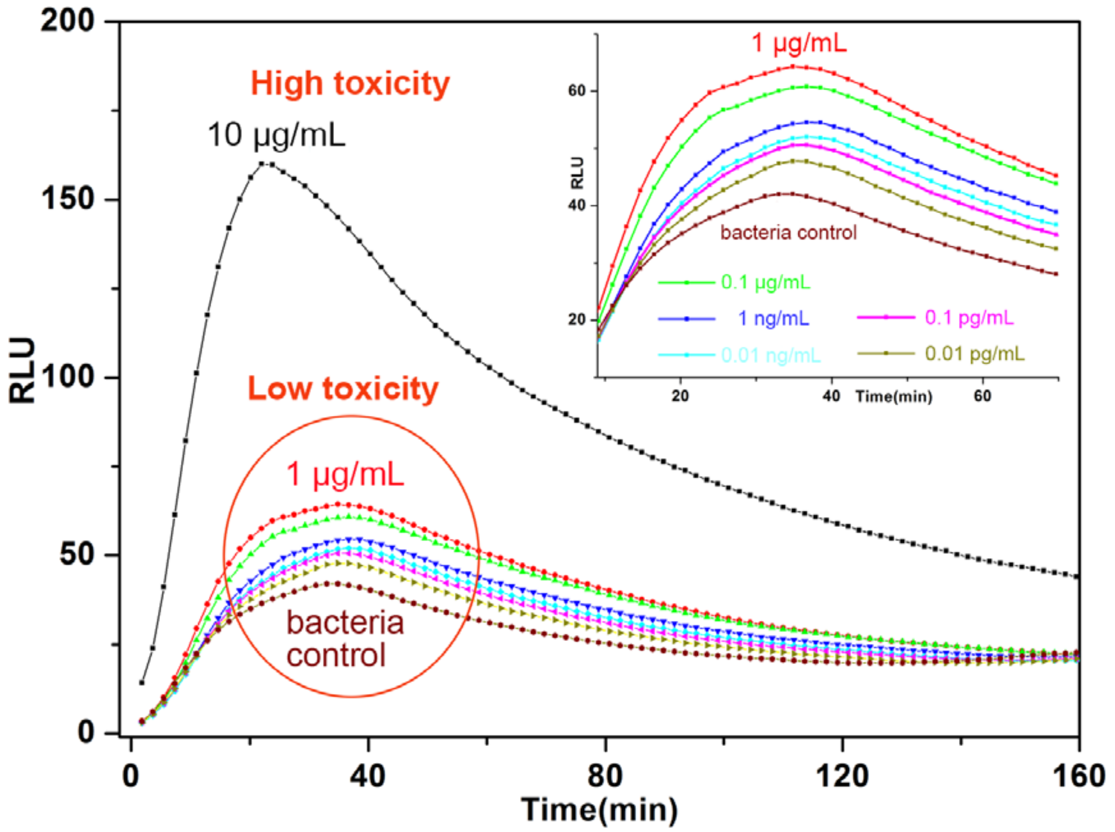

Figure 5.4 Evolution de la bioluminescence après incubation d'une nuit de *E. coli* TV1061 à 4 °C (densité optique: 0,08) avec différentes concentrations en atrazine. L’encart présent le signal mesuré d pour des concentrations d'atrazine entre 0,01 pg/mL et 1 µg/mL ainsi que le contrôle (signal sans atrazine). Les

mesures ont été enregistrées à 25 ° C.

5.2.3 Deuxième protocole: description et résultats obtenus

Le deuxième protocole est conçu pour réduire les interférences entre la bioluminescence propre aux bactéries et liée à leur métabolisme et celle due à la présence de produit toxique. Une représentation schématique de ce protocole est illustrée par la **Figure 5.5**.

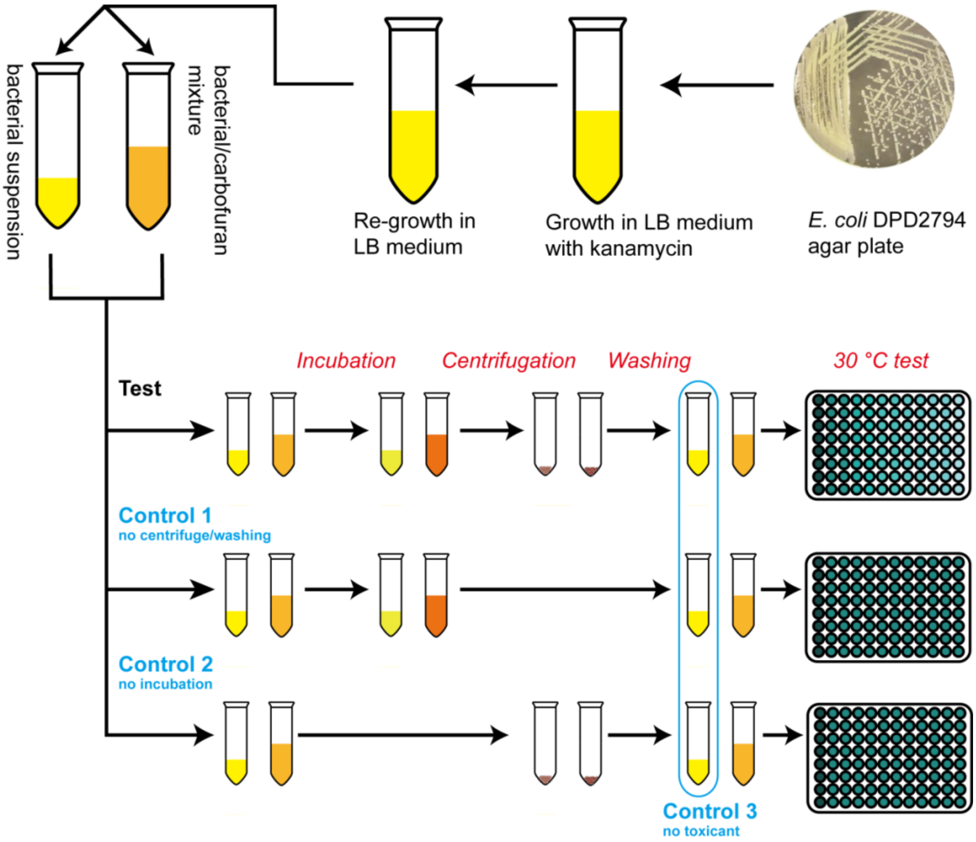

Figure 5.5 Le deuxième protocole comporte trois grandes étapes: **Incubation de la suspension bactérienne** avec une solution toxique de carbofuran à température ambiante pendant différentes périodes de temps, suivie d'une **centrifugation de la suspension bactérienne/solution toxique de carbofuran** et **du remplacement du surnageant** avec du milieu de culture (LB) frais, puis **mesure de du signal de la bioluminescence bactérienne** à 30 °C. Il existe trois expériences indépendantes de contrôles: la première suit le même mode opératoire à l'exception de l'étape de centrifugation/lavage, la seconde n’inclut pas l’étape d’incubation, la troisième consiste à mesurer la bioluminescence des bactéries sans

exposition au produit toxique.

L'incubation des cellules bactériennes avec les produits toxiques et l'étape de centrifugation/lavage pour remplacer le surnageant par du milieu neuf de culture constituent les étapes clefs de ce protocole. La **Figure 5.6** présente les spectres de bioluminescence bactérienne obtenue en suivant l'intégralité du protocole décrit ci-dessus. Les résultats des expériences de contrôle sans étape de lavage sont également présentés avec un temps d'incubation en toxique de 4 h.

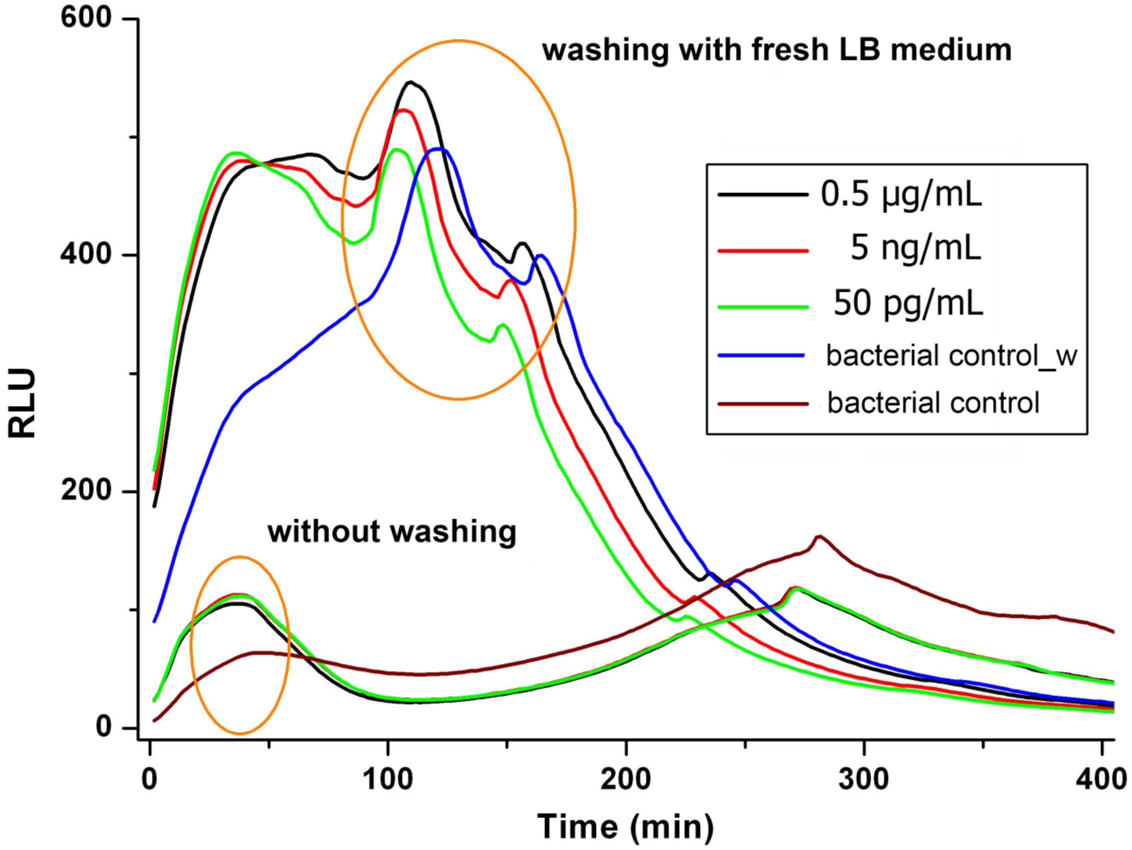

Figure 5.6 Bioluminescence de la bactérie *E. coli* DPD2794. Les bactéries sont exposées à différentes concentrations de carbofuran (0,5 µg/mL, 5 ng/mL, 50 pg/mL) avec incubation à la température ambiante pendant 4 h. La concentration de la solution mère de carbofuran était de 0,05 mg/mL. Le signal de bioluminescence a été enregistré à 30 °C avec étape de lavage (w) (courbes du haut) et sans étape de lavage (courbes du bas). Des bactéries DPD2794 seules ont été utilisées comme contrôle.

Pour les temps de mesure inférieurs à 200 minutes, l'intensité du signal de bioluminescence a été renforcée par le lavage. Lorsque le signal de bioluminescence est enregistré pour des expériences réalisées sans lavage (courbes du bas de la figure), on constate l’apparition de deux pics, un vers 30 minutes et l’autre vers 270 minutes avec une intensité voisine de 100 RLU. Il est très difficile de distinguer entre les courbes mesurées à différentes concentrations de polluant car les courbes se chevauchent.

Lorsque le signal de bioluminescence est enregistré pour des expériences réalisées avec lavage (courbes du haut de la figure), on observe une évolution plus riche en pics et d’intensités plus élevées. On remarque en particulier autour de 35 minutes, une augmentation de l’intensité du pic en présence de produit toxique par rapport à la solution bactérienne seule. L’intensité de ce pic diminue régulièrement avec la concentration en produit toxique. Par contre, autour de 100 minutes, le pic voit son intensité augmenter régulièrement quand la concentration en produit toxique augmente.

Même si les mécanismes ne sont pas complétement élucidés, il est clair que le lavage a permis de distinguer les effets des différentes concentrations sur au moins deux pics: décroissance régulière observable de l’intensité émise sur le premier pic apparu et augmentation régulière observable de l’intensité émise sur le second pic. Ceci permet donc de suivre la concentration en produit toxique dans le milieu en se basant sur l’évolution de l’intensité lumineuse émise par les bactéries.

L'autre paramètre important qui contrôle la réponse des bactéries est le temps d'incubation des bactéries avec le produit toxique. Celui-ci a été optimisé en menant plusieurs séries d’expériences pour différents temps d'incubation (2 h, 4 h, 6 h, 9 h et 12 h). A partir des résultats de ces expériences, le temps d'incubation optimisé a été fixé à 6 h, car cela correspond à la plus grande excursion sur l’intensité émise en fonction de la concentration en produit toxique et à des valeurs d’intensité supérieures à celles obtenues avec des bactéries en l’absence de produits toxiques (induction). L'évolution temporelle de bioluminescence sous cette condition optimisée est illustrée avec la **Figure 5.7**.

Dans les 60 premières minutes, la substance toxique induit la bioluminescence bactérienne qui atteint une intensité maximale autour de 378~404 RLU vers 20 min. Pendant cette même période de temps, pour les bactéries en l'absence de produits toxiques voient une augmentation progressive du signal de bioluminescence sans pics décelables.

Par la suite, 3 séries de pics sont observables que la bactérie soit mise en présence de produit toxique ou non. Il est remarquable de noter que les intensités des pics en présence de produits toxiques sont toujours supérieures à celles obtenues en leur absence et que ces intensités augmentent régulièrement avec la concentration.

Comme dit précédemment, ceci permet donc de suivre la concentration en produit toxique dans le milieu en se basant sur l'évolution de l'intensité lumineuse émise par les bactéries, mais avec une sensibilité optimisée.

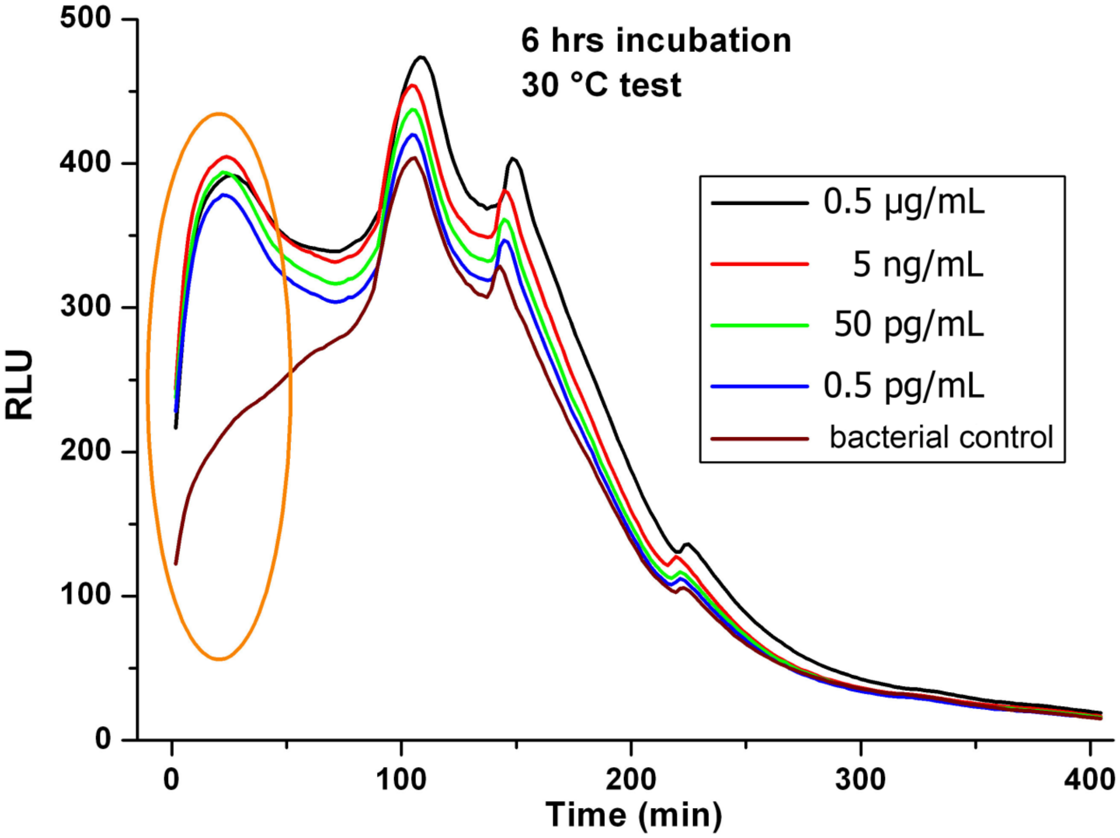

Figure 5.7 Signal de la bioluminescence de *E. coli* DPD2794 en présence de différents contenus de carbofuran (0,5 µg/mL, 5 ng/mL, 50 pg/mL, 0,5 pg/mL) pour 6 h d'incubation avant les mesures à 30 °C.

En conclusion, les deux protocoles développés pour la mesure de la bioluminescence de cellules de type *E. coli*, en présence de pesticides ont permis d'améliorer la sensibilité de détection en contrôlant le métabolisme des bactéries et en réduisant les interactions entre les signaux de bioluminescence induit par les toxiques et ceux provoqués par le métabolisme de la bactérie ou d'autres origines de stress. L'intensité du signal de bioluminescence a été ainsi rendu proportionnelle à la concentration de produit toxique.

En utilisant des bactéries *E. coli* TV1061, le premier protocole a été utilisé pour l'identification de l'effet toxique de l'atrazine grâce à une incubation pendant une nuit à 4 °C et a permis d'obtenir une limite de détection très compétitive de 10 fg/mL. En utilisant des bactéries *E. coli* DPD2794, le deuxième protocole est basé sur l'élimination des produits issus du métabolisme de la bactérie par une étape de centrifugation/lavage pour exalter l'effet unique du produit toxique. Ce nouveau protocole a permis d'obtenir avec une technique simple de bonnes sensibilités et d'obtenir une limite de détection basse de l'effet toxique du carbofuran à 0,5 pg / mL.

5.3 Biocapteurs utilisant la résonance des plasmons de surface localisés (LSPR)

La spécificité analytique est tout un défi pour les biorécepteurs bioluminescents bactériens, alors que ce problème peut être facilement résolu en utilisant des immunocapteurs. Le choix de travailler avec des plasmons de surface est dicté par la volonté d'avoir aussi des systèmes à forte sensibilité et capables de détecter sur un même échantillon plusieurs cibles.

Les études approfondies nécessaires à la mise au point de ce type de biocapteurs ont été conduites dans le cadre de cette thèse et incluent des travaux sur le développement de surfaces nano-structurées actives en plasmonique, sur la biofonctionnalisation des surfaces et sur des stratégies destinées à améliorer les performances analytiques.

5.3.1 Fabrication de substrat plasmonique

L'exigence de nanostructures d'or stables avec une grande accordabilité de la résonance des plasmons et une sensibilité plasmonique élevée sont les conditions préalables à la construction de biocapteurs LSPR. En outre, l'utilisation d'une surface modifiée par des nanostructures d'or présente deux intérêts majeurs dans les applications utilisant un biocapteur LSPR, le premier venant du fait que la surface peut être facilement régénérée pour être réutilisable et le second que ce type de surface est facile à coupler avec différents dispositifs microfluidiques, à partir de laquelle la multidétection peut être réalisée. Parmi les différents protocoles pour fabriquer des nanostructures plasmoniques sur des substrats, l'évaporation d’un film mince métallique suivie d'un recuit thermique serait plus compétitive en raison de son coût faible et de la possibilité de fabriquer ce type de surface à grande échelle. Parmi différents types de substrat, le verre est particulièrement attractif à cause de sa transparence et de son faible prix.

Par conséquent, tous les substrats plasmoniques utilisés dans cette thèse ont été réalisés évaporant le métal sur le verre puis en le recuisant à haute température. L'épaisseur du film d'or évaporé et la température de recuit sont deux paramètres importants pour déterminer la morphologie des nanostructures d'or. La photographie d'échantillons obtenus avec différentes épaisseurs d'évaporation d'or (2 nm, 5 nm, 8 nm) et la température de recuit (500 °C, 550 °C et 600 °C) est présentée sur la **Figure 5.8**.

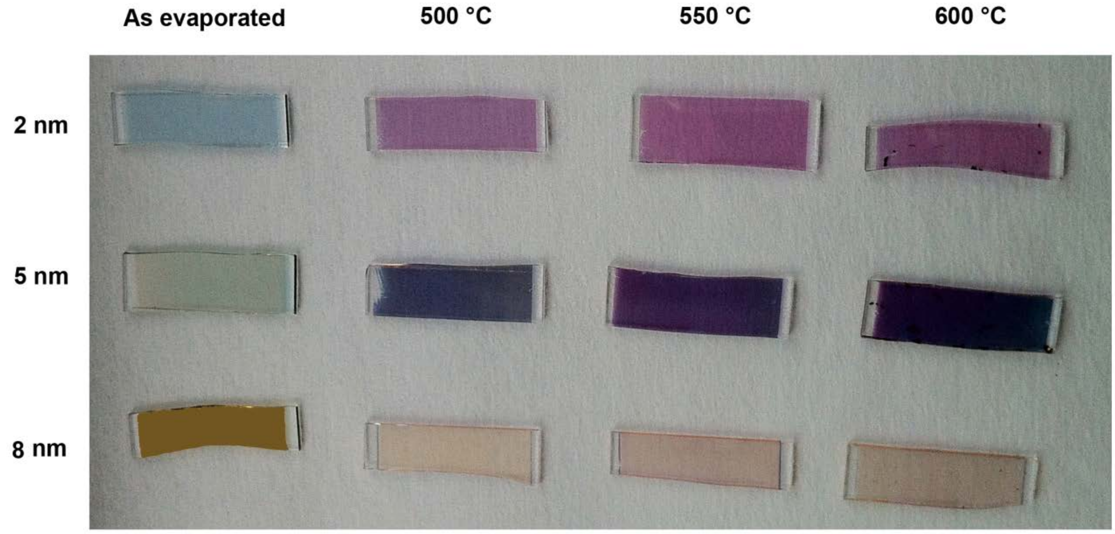

Figure 5.8 Photographie d'échantillons préparés avec différentes épaisseurs d'or évaporé (2 nm, 5 nm et 8 nm) et de recuit à différentes températures (500 °C, 550 °C et 600 °C) pendant 8 h.

L'influence de l’épaisseur d'or évaporé sur les spectres plasmoniques et sur la morphologie est présentée sur la **Figure 5.9**, les trois échantillons obtenus à partir d’or évaporé et recuit à 550 °C pendant 8 h présentent un pic de résonance plasmonique bien défini. L'augmentation de l’épaisseur d’or évaporé induit une augmentation de la longueur d'onde de résonance enregistrée à 553 nm pour 2 nm, à 579 nm pour 5 nm, et à 712 nm pour 8 nm. Le pic d’absorption présente 'une intensité maximale mesurée pour une épaisseur d’or évaporé de 5 nm. A partir des images MEB, il a été constaté que la taille moyenne des nanoparticules d'or passe de 10 nm (**Figure 5.9**B) pour l’échantillon le plus mince à environ 200 nm pour l’échantillon le plus épais (**Figure 5.9**D). En outre, la distance entre les particules augmente avec l’épaisseur d’or évaporé, l'échantillon obtenu à partir d’un film évaporé épais a toujours la densité de particules la plus faible. Ainsi, le décalage vers le rouge du pic plasmonique est lié à la taille des nanoparticules et à la distance inter-particules.

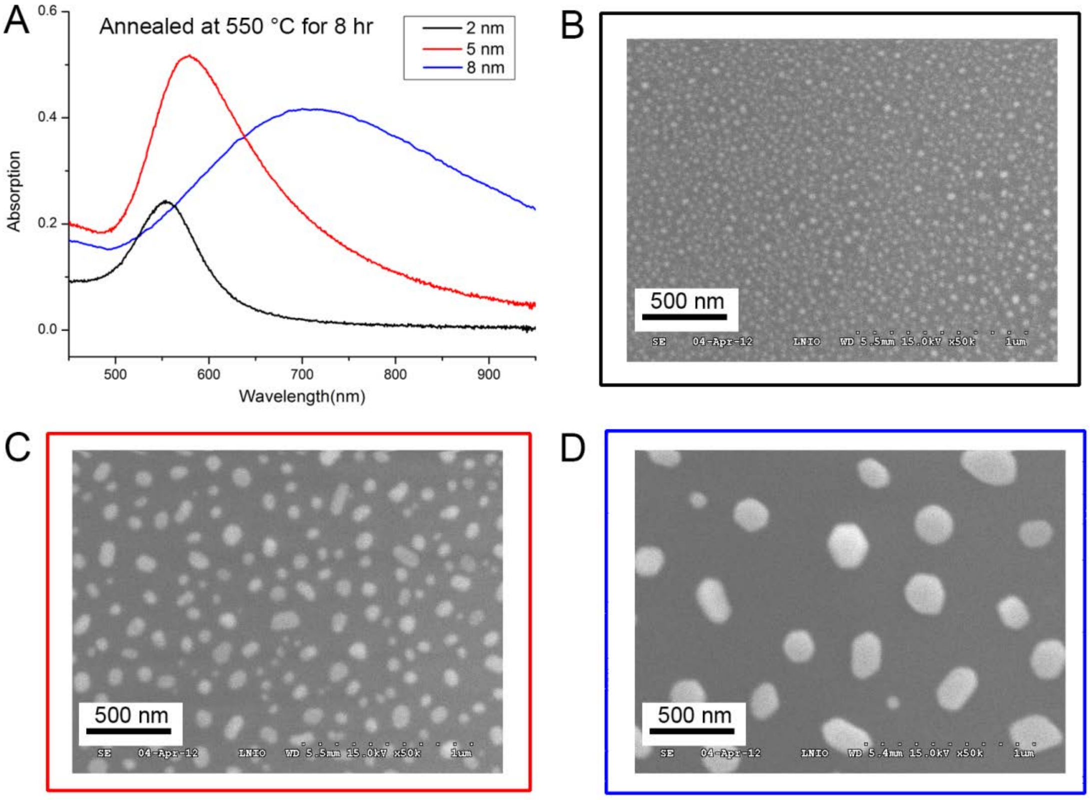

Figure 5.9 Spectres LSPR (A) des échantillons recuits avec différentes épaisseur initiales d’or évaporé et leurs images MEB, correspondant à 2 nm (B), 5 nm (C) et 8 nm (D), le recuit a été effectué en présence d'oxygène à 550 °C pendant 8 h.

La température de recuit a une influence plus complexe sur les spectres Au NPs en plasmonique il pourrait y avoir deux mécanismes différents impliqués. Comme le montre la **Figure 5.10**, les échantillons avec les épaisseurs initiales de film évaporé de 2 nm et 5 nm, présentent des pics plasmoniques qui connaissent une évolution similaire avec la température de recuit: à une température plus élevée de recuit, le pic plasmonique se décale vers le bleu avec une plus grande valeur de la densité optique. De façon plus détaillée, quand la température de recuit passe de 500 °C à 600 °C, le pic d'extinction est légèrement décalé vers le bleu, de 554 nm à 546 nm, avec une augmentation de 0,07 observable sur la densité optique pour la couche d'or évaporé la plus mince (2 nm). Dans le cas de l'échantillon obtenu à partir de 5 nm d’or évaporé (**Figure 5.10**B), les pics sont plus larges que ceux obtenus avec l'échantillon d’épaisseur initiale de 2 nm (**Figure 5.10**A) et l’intensité des pics est également plus importante d’un facteur voisin de 2. L’augmentation de la température de recuit se traduit également par un décalage vers le bleu mais plus important avec une excursion de 27 nm, et une excursion d’amplitude voisine de 0,06 pour la densité optique proche de celle observée sur l’échantillon précédent. Il convient de noter qu’une évolution différente des pics plasmoniques a été observée pour l'échantillon recuit de 8 nm d’épaisseur initiale par rapport à celles obtenues sur les 2 autres échantillons de 2 nm et de 5 nm d’épaisseur initiale (**Figure 5.10**D). Ainsi, l’augmentation de la température de recuit a conduit à un grand décalage des pics vers le rouge avec une excursion de 126 nm (de 654 nm à 500 ° C à 780 nm à 600 ° C recuit) et à une diminution de la valeur de la densité optique 0,04, entre les deux températures extrêmes de recuit (**Figure 5.10**C).

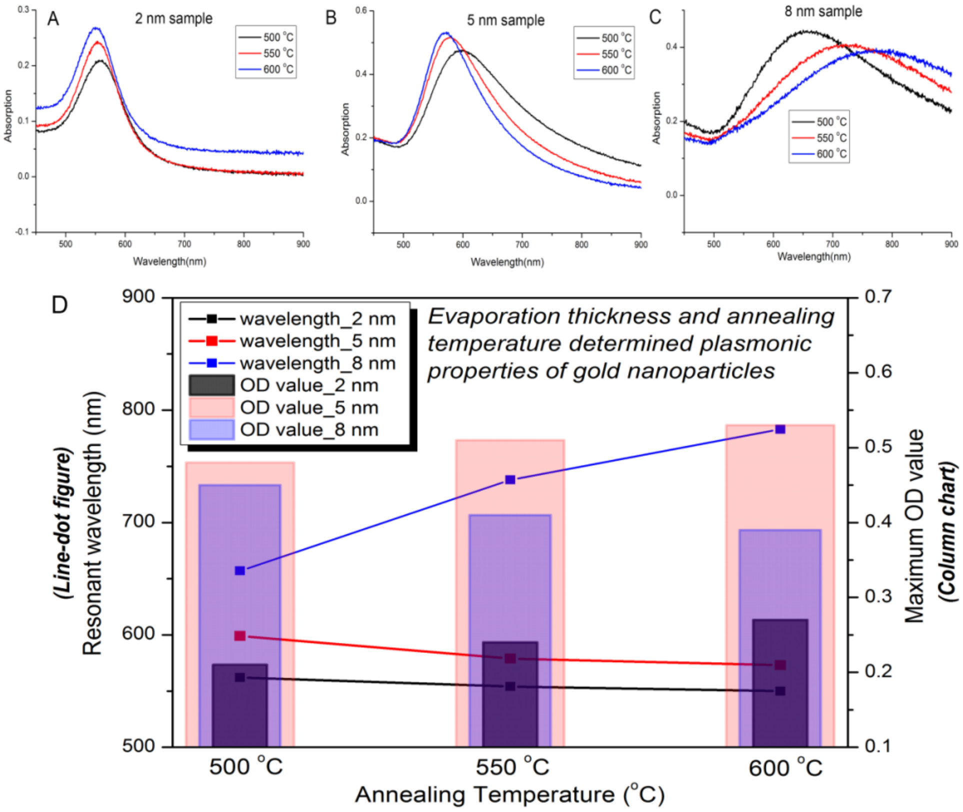

Figure 5.10 Spectres de LSPR pour les échantillons recuits à trois températures différentes (500 °C, 550 °C et 600 °C) avec une épaisseur de film évaporé initiale de 2 nm (A), 5 nm (B) et 8 nm (C), respectivement. Les propriétés plasmoniques caractéristiques ont été tracées en fonction de l'épaisseur initiale d'or évaporé et de la température de recuit. La longueur d'onde de résonance est représentée par la figure ligne-point, tandis que la valeur maximale de la densité optique est affichée sous forme de barres dans le panneau D.

5.3.2 Nanostructures d'or de tailles différentes, organisées en zones géographiques, sur un même substrat de verre

L'objectif est de disposer sur un même substrat de plusieurs zones de nanoparticules avec des tailles différentes et contrôlées. Ceci permettrait de tester rapidement et expérimentalement la taille de nanoparticules la mieux adaptée pour une cible spécifique, en terme de décalage de longueur d'onde et d'amplitude de la réponse.

Dans ce cadre, deux nouveaux protocoles sont présentés afin d'obtenir différentes zones de nanostructures d'or sur un substrat de verre unique par des techniques simples à mettre en œuvre et peu coûteuses.

Le premier protocole est basé sur l’utilisation de 4 cycles maximum d'évaporation d'or (épaisseur évaporée de 2 nm pour chaque cycle). Du ruban adhésif a été utilisé comme masque pour éviter que de l’or soit déposé sur certaines zones de verre. Par conséquent, on obtient en procédant ainsi des bandes avec du métal évaporé et des bandes sans métal disposées de façon alternée sur le verre rappelant la structure d’un code-barres.

Dans l’exemple étudié, on dispose de quatre bandes d’or d’épaisseur initiale respective de 2 nm, 4 nm, 6 nm et 8 nm. Ainsi, après un recuit à 550 °C, on a obtenu quatre zones avec des tailles de nanoparticules différentes. Une représentation schématique de cette répétition des cycles d'évaporation d'or sur verre avec le résultat après recuit est présentée sur la **Figure 5.11.**

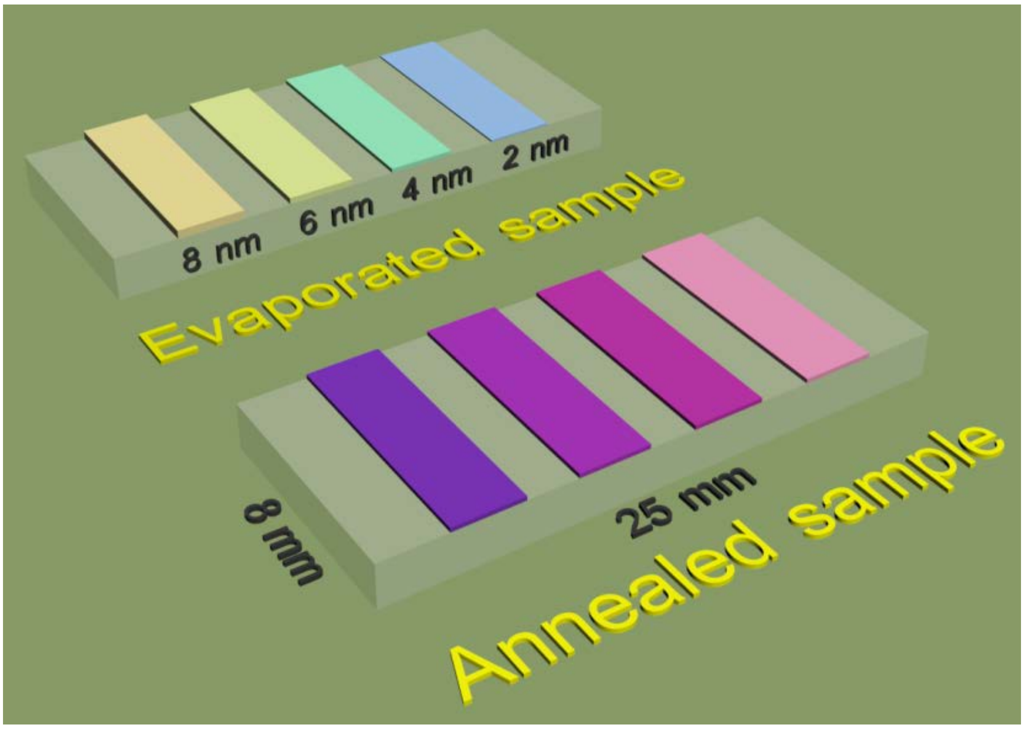

Figure 5.11 Structure de type "code-barres" obtenue à partir du premier protocole d'évaporation d'or sur des zones prédéfinies du substrat de verre, après recuit à 550°C. L'épaisseur d’or évaporé et les

dimensions de l'échantillon sont présentées sur la figure, il convient de noter que la figure n’est pas à l’échelle.

Les spectres LSPR et les images MEB pour les différentes zones Au NPs de ce substrat sont regroupés **Figure 5.12**. Conformément à ce qui a été trouvé précédemment, le pic de résonance plasmonique est toujours décalé vers le rouge avec l'augmentation de l'épaisseur initiale d’or évaporé. Le maximum de densité optique est obtenu pour la zone Au NPs obtenue à partir du recuit d’un film d’or évaporé de 6 nm. Les images MEB confirment que la taille des nanoparticules d’or augmente avec celle de l’épaisseur initiale d’or évaporé, ce qui se traduit par le décalage vers le rouge observé sur les spectres LSPR.

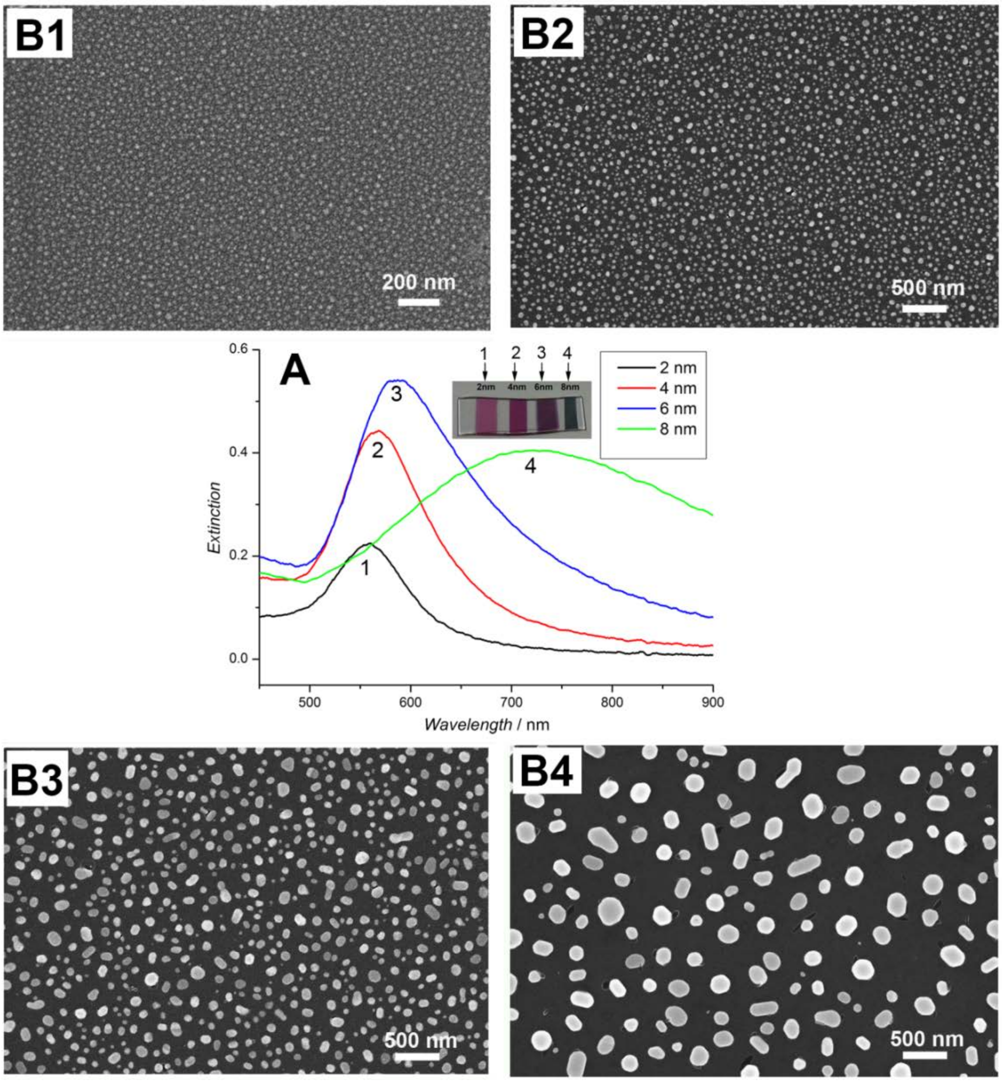

Figure 5.12 Spectres LSPR (A) et images MEB correspondantes de nanoparticules d'or obtenues à partir de films d’or évaporé (B) recuits à 550 °C avec une épaisseur initiale d’ordre 2 nm (B1), 4 nm (B2), 6 nm (B3) et 8 nm (B4), les nombres 1, 2, 3, 4 correspondent aux différentes d'épaisseurs d’or évaporé 2 nm , 4 nm, 6 nm et 8 nm avant recuit.

Dans le second protocole, des agrafes ont été fixées sur la partie supérieure d'un substrat de verre, laissant un vide entre le masque (agrafes) et le substrat (verre). Par un effet similaire à un effet d’ombrage, une zone à l’interface or-verre a été créée, où l'épaisseur de la couche d'or évaporée dans des directions transversales a été progressivement modulée, conduisant à des nanoparticules d'or de taille différente après recuit à haute température (550 °C). Une illustration pour les échantillons obtenus à partir de ce protocole est présentée **Figure 5.13**. Deux zones de transitions situées exactement à l'interface or-verre ont été observées pour l'échantillon recuit. Une observation à l'aide d'un microscope optique (voir l'encart) montre des différences de coloration de cette zone due à la variation de la taille des nanoparticules et des distances inter-particulaires.

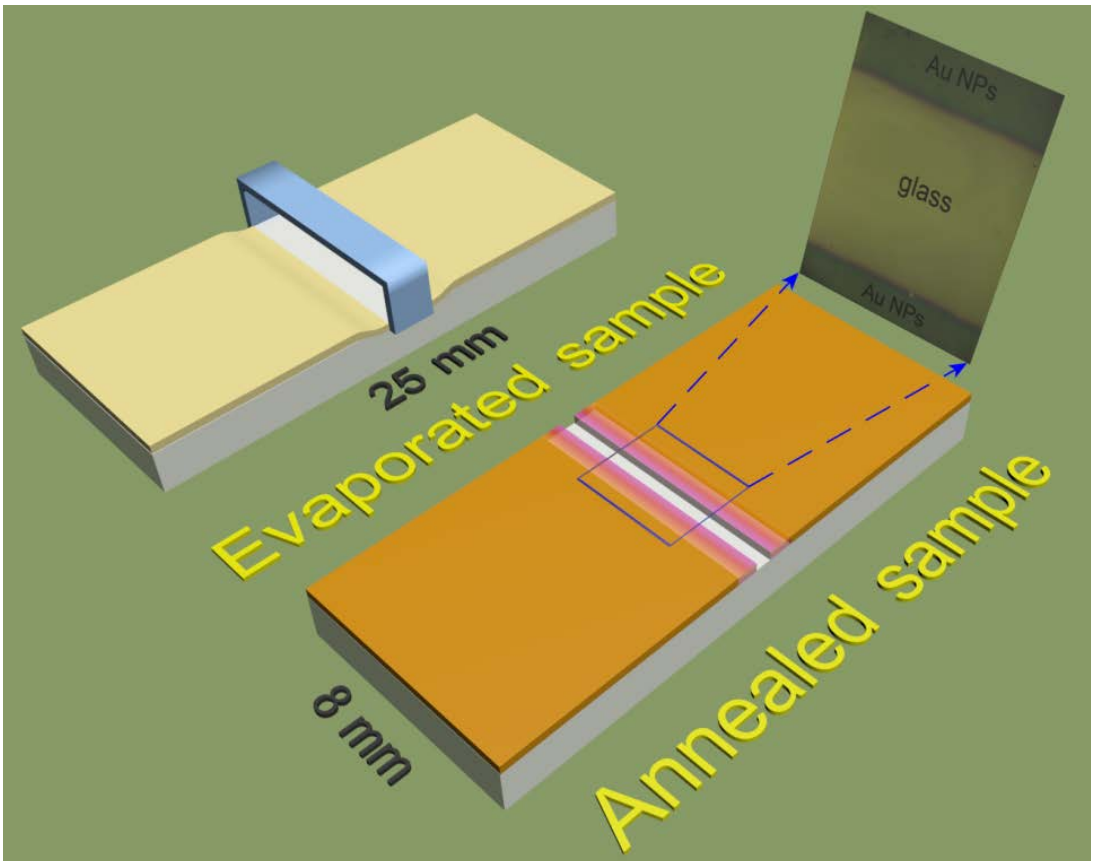

Figure 5.13 Echantillons préparés à partir du deuxième protocole utilisant des agrafes en tant que masque pour moduler progressivement l'épaisseur d'or évaporé. Une image typique observée au microscope optique des zones « d'ombre » (désignée par un rectangle bleu) est présentée dans l'encart.

L'activité plasmonique de cette surface et sa caractérisation au MEB ont été évaluées en choisissant quatre zones d'investigation de l'interface verre/or en partant du verre (flèche noire sur la **Figure 5.14**A). Les spectres LSPR pour les 4 différentes zones ont été enregistrés et présentés sur la **Figure 5.14** avec les images MEB correspondantes des nanoparticules d'or (B1-B4). Expérimentalement, lors du passage de la zone 1 à la zone 4 dans l'interface verre/or, la longueur d'onde est décalée vers le rouge et passe de 568 nm pour la courbe 1 à 677 nm pour la courbe 4, avec une augmentation de l’amplitude du pic associé qui passe de 0,2 à 0,475, respectivement. La taille des nanoparticules d'or augmente également en passant de 15 nm pour la zone 1 à 45 nm pour la zone 4.

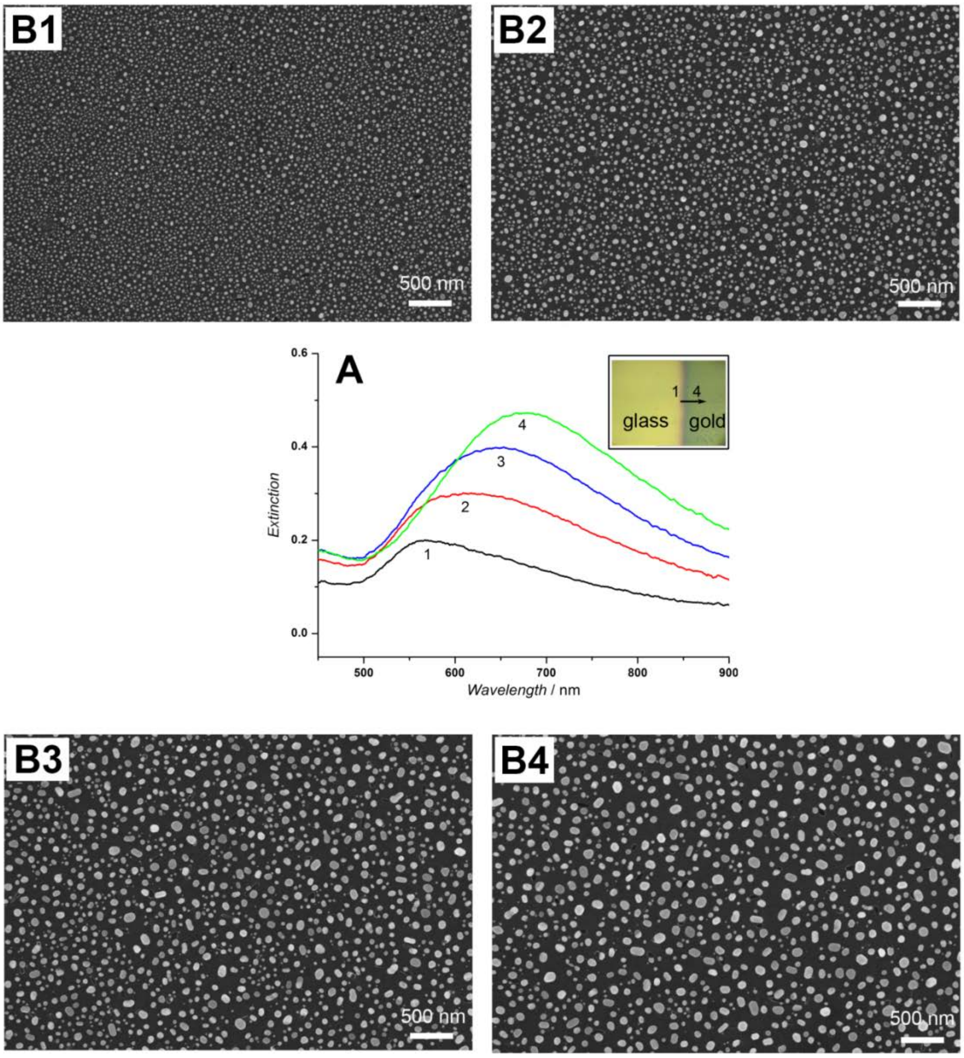

Figure 5.14 Spectres LSPR (A) des différentes zones de nanoparticules d'or dans l’interface verre-or interface (1 à 4) et images MEB correspondant (B1 à B4).

5.3.3 Organisation contrôlée sur un même substrat de zones de nanoparticules pour des applications de multidétection

Dans cette partie, une grille TEM de cuivre à motifs carrés est utilisée comme masque pour un dépôt sélectif du métal sur substrat de verre, afin de créer des nano/micro structures bien organisées, après recuit à haute température. Grace à cette grille, des zones homogènes d'or bien définies et de forme régulière sont obtenues après évaporation (**Figure 5.15**). Le film continu d'or est ensuite converti en nanoparticules d'or stables et régulièrement distribuées après recuit dans les différentes zones. Les résultats expérimentaux montrent que si la grille est soigneusement enlevée après avoir évaporé l'or, l'intégrité des motifs est conservée. Il a été également constaté expérimentalement que les motifs sont conservés après recuit à haute température, à l'exception de la couleur qui passe du bleu clair pour le film continu d'or évaporé au violet clair pour l'échantillon recuit.

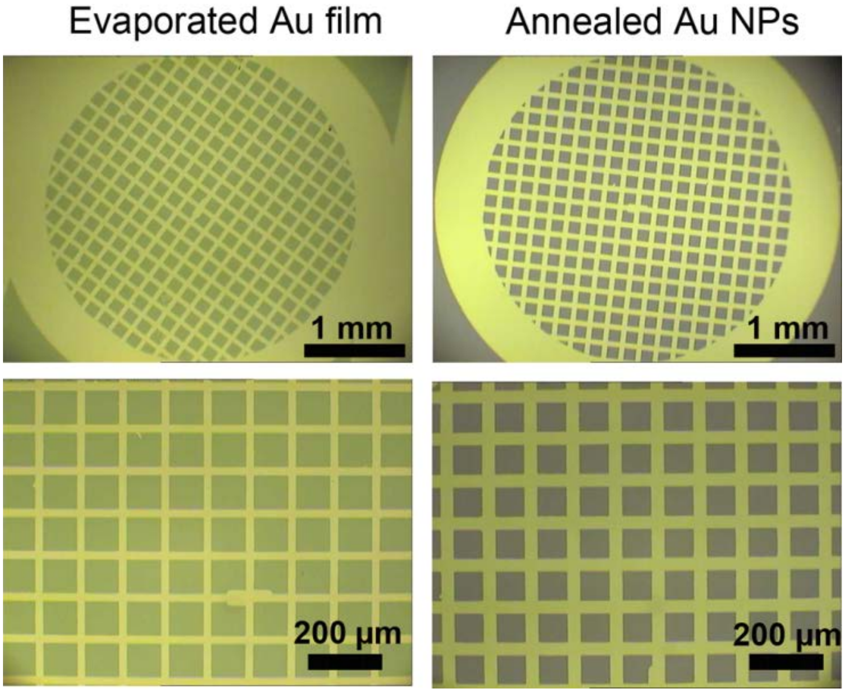

Figure 5.15 Images de microscopie optique de motifs obtenus à l'aide de la grille TEM sur un substrat de verre à l'aide de différents agrandissements (en haut: objectif 4x; bas: objectif 10x) avant recuit (à gauche) et après recuit (à droite).

5.3.4 Biomodification des nanoparticules d’or application à la détection de biomolécules spécifiques

La première étape dans un biocapteur LSPR est d'optimiser la morphologie des nanoparticules afin d’obtenir la meilleure réponse plasmonique, pour une cible donnée. Ainsi, les échantillons préparés à partir du deuxième protocole ont été utilisés pour déterminer expérimentalement et rapidement la dimension et la distance inter-particulaire optimales (voir **Figure 5.16**). L’optimisation s’est fait sur les anticorps anti-humain IgG facilement disponibles. Ces paramètres optimisés ont été utilisés pour réaliser un biocapteur de détection de l’atrazine (voir **Figure 5.17**) et de détection de protéines (voir la **Figure 5.18**).

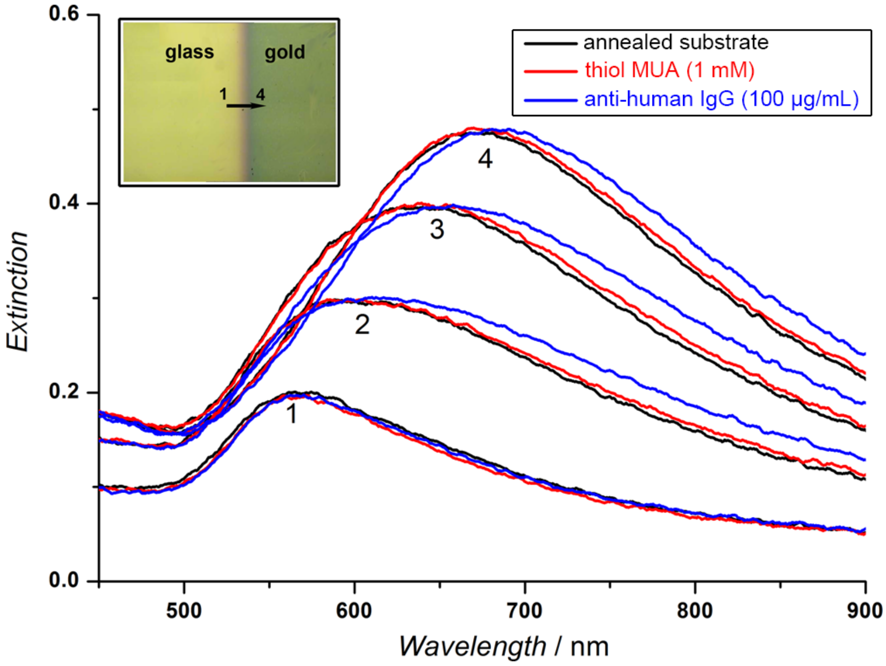

Figure 5.16 Réponses LSPR pour différentes zones en fonction des différentes étapes de la biomodification simultanée des nanoparticules d'or. L'échantillon est préparé en utilisant le protocole de masque agrafes décrit dans la **Figure 5.13**, et une image de microscopie optique de cet échantillon est représentée en insert.

On remarque que, après l'étape de fonctionnalisation par le thiol MUA, la longueur d'onde de la résonance est légèrement décalée vers le rouge. En outre, lorsque les biomolécules sondes (anticorps anti-humain) ont été immobilisées dans ces zones d'interface, en fonction de la zone, différents comportements ont été observés: décalage vers le rouge de 25 nm et 15 nm pour les zones 4 et 3, de 6 nm pour la zone 2 et pas de décalage observable pour la zone 1.

En conclusion, la sensibilité LSPR a pu être expérimentalement et simplement évaluée en fonction de la taille des nanoparticules et de la distance interparticulaire montrant que le meilleur résultat est obtenu pour les particules de la zone 4.

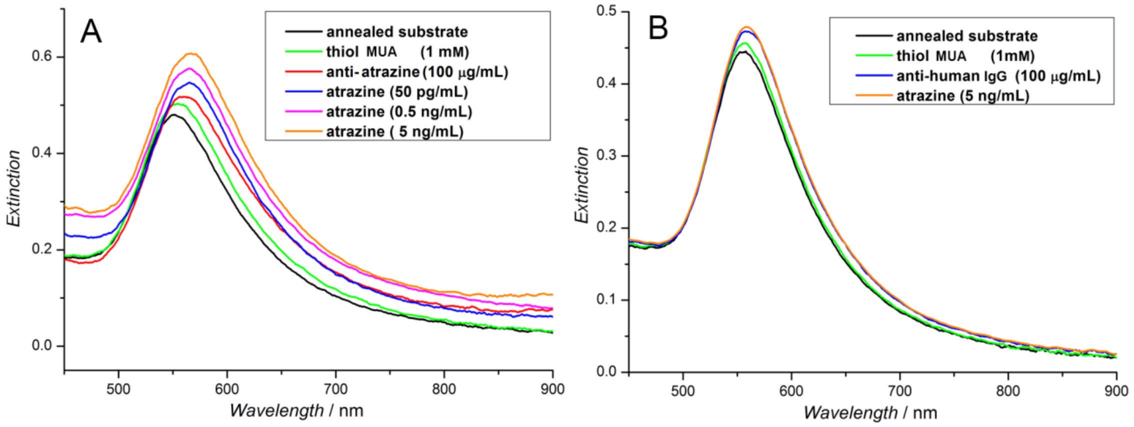

Figure 5.17 Biocapteur LSPR pour la détection spécifique de l'atrazine (A) et courbe expérimentale de contrôle en utilisant un anticorps anti-IgG humain non spécifique dans les mêmes conditions (B). L'épaisseur du film évaporé initial était de 5 nm suivie d'un recuit thermique à 550 °C pendant 8 h.

En se basant sur ce résultat, l'épaisseur initiale d'or évaporé a été choisie à 5nm pour développer un prototype de biocapteur LPSR dédié à la détection de l'atrazine. D'après la **Figure 5.17**, il apparaît que l'immobilisation de la couche d'alkanethiol MUA et des anticorps anti-atrazine conduit à un décalage de la longueur d'onde vers le rouge de 4 nm et 13 nm, respectivement (**Figure 5.17**A). La liaison de l'antigène (atrazine) avec son anticorps se traduit par un décalage très faible de la longueur d'onde (inférieure à 5 nm pour la concentration d'atrazine la plus élevée testée). Ce décalage est indépendant de la concentration en atrazine.

Par contre, il est observé une augmentation de la densité optique lorsque la concentration en atrazine augmente. Ainsi, la densité optique passe de 0,547 pour la concentration de 50 pg/mL à 0,576 pour celle de 0,5 ng/mL dilution et est maximale avec une valeur de 0.608 pour la concentration de 5 ng/mL. D'après les résultats obtenus, il apparaît que pour des molécules de petites tailles comme l’atrazine (environ 220 Da), c’est l’immobilisation d’une grande quantité d’anticorps sur les nanoparticules qui induit un décalage de longueur d’onde alors que la liaison entre l’antigène et l’anticorps se traduit surtout par une variation du signal de densité optique.

Afin de vérifier que l’augmentation de la densité optique est bien due à la liaison atrazine/anticorps anti-atrazine, un contrôle est réalisé en suivant par plasmonique l’interaction entre l’atrazine et l’anticorps anti-humain IgG (**Figure 5.17**B). Si la longueur d'onde du pic est décalée vers le rouge après modification des nanoparticules avec le thiol et l’immobilisation des anticorps IgG anti-humain, on observe par contre aucune modification significative de l’amplitude du pic après une exposition à 5 ng/mL atrazine. Par conséquent, les réponses LSPR illustrées à la **Figure 5.17**A correspondent bien à la liaison spécifique de l'atrazine avec son anticorps.

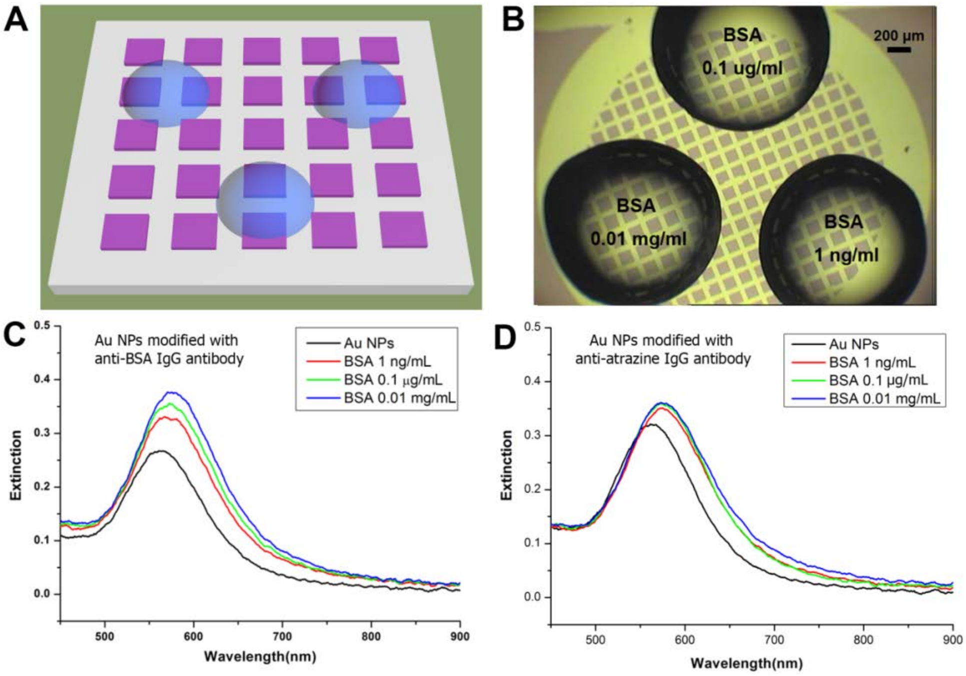

Figure 5.18 Illustration (A) et imagerie par microscopie optique (B) de trois gouttes de BSA de concentrations différentes déposées sur différents domaines du substrat actif en plasmonique: détection spécifique sur l'anticorps anti-BSA (C) et non spécifique sur l'anticorps anti-atrazine (D).

Le substrat optimisé a aussi été utilisé pour détecter la protéine d'albumine. Pour cela, trois gouttes de BSA avec des concentrations différentes sont déposées sur différentes zones de la puce LSPR (**Figure 5.18** A, B). Il convient de noter que le volume de chaque goutte de BSA est de 0,2 µL et que la puce LSPR est placée à 4 °C pendant 3 h dans une boîte humide scellée pour éviter l'évaporation des gouttes de BSA déposées sur le capteur. A partir des spectres LSPR présentés sur la **Figure 5.18**C, les différentes concentrations de BSA peuvent être à la fois distinguées par le décalage vers le rouge de la longueur d'onde du pic de résonance et par l'augmentation de la densité optique. Ainsi, lorsque la concentration en antigène augmente de 1 ng/mL à 0,01 mg/mL, le pic plasmonique est progressivement décalé vers le rouge de 567 nm à 580 nm avec une densité optique augmentée de 0,33 à 0,38. Au contraire, dans les expériences de contrôle en utilisant un anticorps non spécifique BSA (anti-atrazine IgG), les spectres LSPR correspondant à trois concentrations différentes de BSA se chevauchent et ne peuvent pas être différenciées comme le montre la **Figure 5.18**D.

5.3.5 Amélioration de la sensibilité du biocapteur LSPR

La sensibilité du biocapteur LSPR peut être encore renforcée à l'aide de deux protocoles indépendants: l'utilisation de nanoparticules bimétalliques Au/Ag et de revêtements fonctionnels à base de dopamine. Les réponses plasmoniques sont plus sensibles pour les nanoparticules bimétalliques, tandis que l'utilisation de revêtements de dopamine améliore l'immobilisation des anticorps. Comme conséquences directes de ces résultats, une limite de détection très basse de 0,01 ng/mL, pour le BSA est obtenue dans les conditions optimisées comme le montre la **Figure 5.19**.

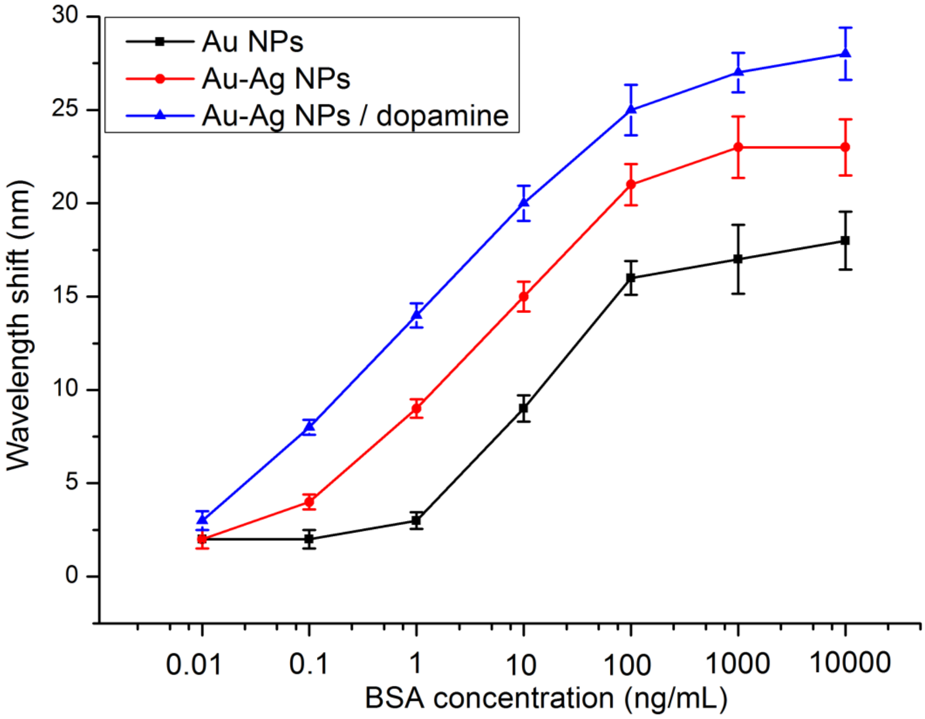

Figure 5.19 Courbes d'étalonnage pour la détection de BSA en utilisant différents substrats actifs en plasmonique à base de nanoparticules d'or (courbe noire), de nanoparticules bimétalliques Au/Ag (courbe rouge) et de nanoparticules bimétallique Au/Ag modifiées avec la dopamine (courbe bleue). L'épaisseur des films d'or et d'argent est de 4 nm et 2 nm, respectivement. Tous les échantillons ont été recuits à 500 °C pendant 8 h. Trois expériences ont été réalisées pour chaque substrat et la moyenne des résultats est présentée dans la figure ci-dessus.

5.4 Substrat SERS à base de dépôt d'or sur des cellules bactériennes utilisées comme motifs

L'idée de base est d'utiliser les cellules bactériennes *E. coli* comme motif pour contrôler la distribution des nanoparticules d'or sur le substrat à l'aide d'un recuit à haute température. La caractérisation MEB met en évidence une distribution de nanoparticules d'or plus dense à la surface du squelette des cellules bactériennes, avec une taille plus réduite (voir **Figure 5.20**B). Ce procédé a donc permis de créer des « points chauds » plasmoniques qui contribuent à amplifier de façon très efficace le signal SERS (**Figure 5.20**A).

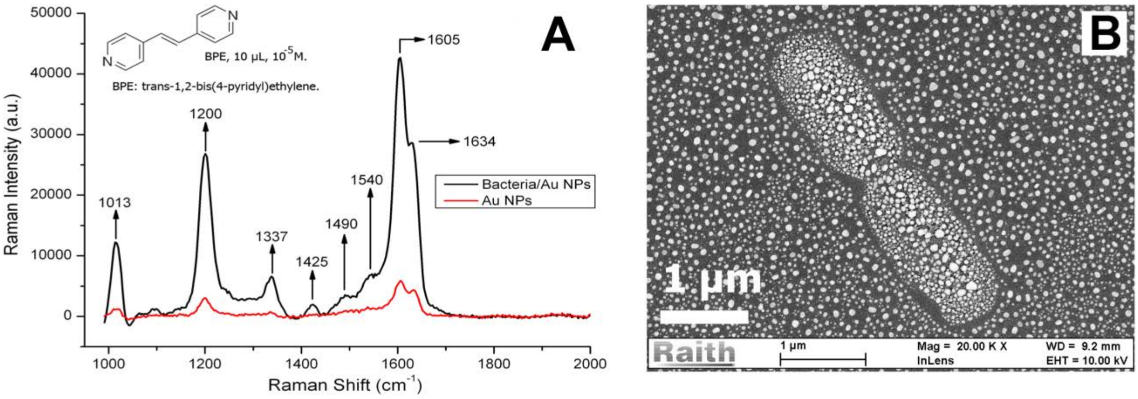

Figure 5.20 Spectres SERS (A) obtenus lors du dépôt d'une solution BPE (10^{-5} M) sur un substrat à base de nanoparticules et sur un substrat réalisé avec ce nouveau protocole et images MEB (B) des cellules bactériennes. Ces deux échantillons ont la même épaisseur initiale de film d'or (4 nm) et ont été recuits à 550 °C pendant 8 h pour former les nanoparticules, le temps d'intégration pour la mesure SERS est de 5 s.

Ce substrat SERS a été utilisé pour la détection d'une molécule de colorant Raman non résonante (BPE). Les réponses SERS pour une solution de BPE à différentes concentrations de 10^{-12} à 10^{-5} M ont été enregistrées et pour un dépôt de 10 µL ddH_2O sur le même substrat optimisé (**Figure 5.21**).

Lorsque l'intensité Raman du pic à 1605 cm^{-1} est tracée en fonction de différentes concentrations de solutions BPE, le substrat SERS optimisé permet d'atteindre une limite de détection BPE de 10^{-12} M, avec une plage de linéarité entre 10^{-7} et 10^{-12} M (coefficient de corrélation $R^2 = 0.9467$).

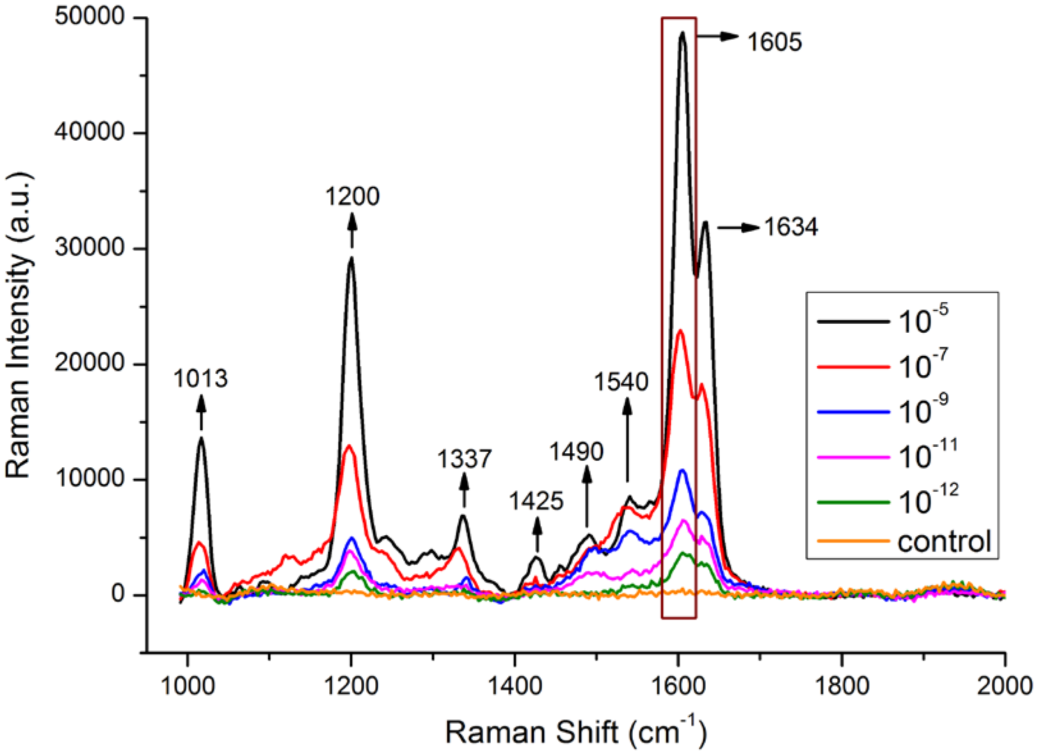

Figure 5.21 Spectres SERS obtenu après le dépôt de 10 µL d'une solution de BPE de différentes concentrations ou celui de10 µL ddH_2O. L'épaisseur initiale du film est de 4 nm, le temps d'intégration pour la mesure SERS est de 5 s pour la concentration BPE la plus élevée (10^{-5} M) et de 10 s pour les autres concentrations.

5.5 Conclusion et perspectives

Dans cette thèse, une présentation générale des biocapteurs optiques a été introduite dans le but d'expliquer les grands principes de fonctionnement et d'aboutir à une classification des biocapteurs basés sur le type de réactions mise en jeu. Les biorécepteurs à base de bactéries génétiquement modifiées pour être bioluminescentes et les biocapteurs utilisant la résonance des plasmons de surface ont été utilisés comme exemples.

Le chapitre 2 concerne le développement de protocoles originaux pour développer des biorécepteurs à base de bactéries bioluminescentes présentant une réponse linéaire en fonction du taux de produits toxiques. Il a été montré que ce résultat peut être atteint en contrôlant le métabolisme de la bactérie par une incubation à basse température ou par une régénération du milieu de culture après incubation.

Le chapitre 3 traite des biocapteurs LSPR pour objectif de développer des surfaces actives faciles à mettre en œuvre et peu coûteuses et permettant de faire de la multi-détection. Il a été montré qu'il était possible d'obtenir des nanoparticules métalliques à partir du recuit haute température d'un film obtenu par évaporation sur substrat de verre. L'épaisseur initiale déposée et la température de recuit permettent de contrôler facilement la taille des nanoparticules et la distance interparticulaire. L'utilisation de méthodes de masquage a par ailleurs permis de contrôler la répartition géographique de nanoparticules de taille donnée à la surface du substrat. Ceci a permis de mettre au point un protocole expérimental qui permet de choisir très rapidement la taille de nanoparticules qui donnera la réponse plasmonique la plus adaptée et de proposer une architecture d'immunocapteur sur substrat permettant la multi-détection. La sensibilité des biocapteurs a été améliorée en ayant recours à des nanoparticules bimétalliques ou à des modifications de surface spécifique comme la dopamine.

Le chapitre 4 est consacré au développement d'un substrat très actif en SERS. L'idée mise en œuvre a été d'utiliser les bactéries comme motifs pour contrôler la synthèse et la répartition de nanoparticules métalliques obtenus à partir d'un film métallique recuit. Il a été montré expérimentalement que les nanoparticules se développent de façon préférentielle à la surface du squelette des bactéries immobilisées sur le substrat et qu'elles présentent une plus petite taille que celles formées hors motif. Cela a permis de réaliser des « points chauds » très actifs en SERS. Le concept a été validé sur la détection d'une molécule modèle.

Les perspectives de ce travail concernent essentiellement une meilleure compréhension des mécanismes mis en jeu lors de la détection de polluants à l'aide de bactéries génétiquement modifiées mais également des travaux prospectifs sur les liaisons antigène-anticorps pour les exploiter au mieux afin de diminuer les limites de détection et d'augmenter la sensibilité. Il est également important de réfléchir sur l'intégration des différentes plateformes optiques et de poursuivre les travaux expérimentaux sur des échantillons issus de l'environnement.

Production scientifique

Articles de revues avec comité de lecture:

1. **K. Jia**, M. Y. Khaywah, Y. Li, J. L. Bijeon, P. M. Adam, R. Déturche, M. François, G. Louarn, R. E. Ionescu. Strong improvements of LSPR sensitivity by using Au/Ag bi-metallic nanostructures modified with poly-dopamine films. *ACS Applied Materials and Interfaces* **2014**, 6, 219-227.
2. **K. Jia**, P. M. Adam, R. E. Ionescu. Sequential acoustic detection of atrazine herbicide and carbofuran insecticide using a single micro-structured gold quartz crystal microbalance. *Sensors and Actuators B: Chemical* **2013**, 188, 400-404.
3. **K. Jia**, E. Eltzov, R. Marks, R. E. Ionescu. Bioluminescence enhancement through an added washing protocol enabling a greater sensitivity to carbofuran toxicity. *Ecotoxicology and Environmental Safety* **2013**, 96, 61-66.
4. **K. Jia**, J. L. Bijeon, P. M. Adam, R. E. Ionescu. A facile and cost-effective TEM grid approach to design gold nano-structured substrates for high throughput plasmonic sensitive detection of biomolecules. *Analyst* **2013**, 138, 1015-1019.
5. **K. Jia**, J. L. Bijeon, P. M. Adam, R. E. Ionescu. Sensitive localized surface plasmon resonance multiplexing protocols. *Analytical Chemistry* **2012**, 84, 8020-8027.
6. **K. Jia**, E. Eltzov, T. Toury, R. Marks, R. E. Ionescu. A lower limit of detection for atrazine was obtained using bioluminescent reporter bacteria via a lower incubation temperature. *Ecotoxicology and Environmental Safety* **2012**, 84, 221-226.
7. **K. Jia**, T. Toury, R. E. Ionescu. Fabrication of an atrazine acoustic immunosensor based on a drop-deposition procedure. *IEEE Transactions on Ultrasonics Ferroelectrics and Frequency Control* **2012**, 59, 2015-2021.

Proceedings:

8. **K. Jia**, J. L. Bijeon, P. M. Adam, R. E. Ionescu. Large scale fabrication of gold nano-structured substrate via high temperature annealing and their direct use for the LSPR detection of atrazine. *Plasmonics* **2013**, 8, 143-151.

9. R. E. Ionescu, **K. Jia**, E. Eltzov, T. Toury, R. Marks. Acoustic biosensors for medical and environmental purposes. *Proceedings of IEEE Transactions on Ultrasonics Ferroelectrics and Frequency Control*, 23-27 July **2011**, p1-4, Vancouver, Canada.

Brevet:

10. R. E. Ionescu, **K. Jia**, Procédé de fabrication d’un support d’analyse comprenant une matrice microbienne support associe et utilisations, 1353010, France.

Présentations orales dans des congrès internationaux:

11. **K. Jia**, E. Eltzov, R. S. Marks, R. E. Ionescu. Improved bioluminescence methodology for increased sensitive detection of pesticide. NanoSensorPhotonics-Optical biosensors, nanobiophotonics and diagnostics (symposium), 5-9 Novembre **2011**, Israel.

Présentations sous forme de poster dans des congrès internationaux

12. **K. Jia**, J. L. Bijeon, P. M. Adam, R. E. Ionescu. Plasmonic biosensors using high annealed controlled nanostructures. CREATE Water Thrust Symposium, 27 May **2013**, Beer-Sheva, Israel. 1p.

13. R. E. Ionescu, **K. Jia**, E. Eltzov, R. S. Marks. Bioluminescent detection of water pollutants by using novel protocols. CREATE Water Thrust Symposium, 27 May **2013**, Beer-Sheva, Israel. 1p.

14. R. E. Ionescu, **K. Jia**, T. Toury, R. S. Marks. Influence of micro-/nano-particles on the genetically engineered bioluminescence of Escherichia coli bacteria . Environmental Health 2013-Science & Policy to Protect Future Generations, 3-6 March **2013**, Boston, USA. 1p.

15. R. E. Ionescu, **K. Jia,** T. Toury, E. Eltzov, R. S. Marks. Acoustic biosensors for medical and environmental purposes. In: IONESCU, E.-R. Joint Conference on IEEE International Symposium on Applications of Ferroelectrics (ISAF/PFM)/ International Symposium on Piezoresponse Force Microscopy and Nanoscale Phenomena in Polar Materials , 24-27 July **2011** , Vancouver, Canada. 4p.

Présentations sous forme de poster dans des congrès nationaux

16. **K. Jia**, R. E. Ionescu. Fabrication and functionalization of nanoparticles, Nanoantenna Meeting Troyes, 23-24 October **2012**, France.

17. **K. Jia**, R. E. Ionescu. Large scale fabrication of plasmonic nanostructures and their functionalization for biosensing applications, Journée Nanofab du LNIO, 17 October **2012**, France.

18. **K. Jia**, E. Eltzov, T. Toury, R. S. Marks R. E. Ionescu. Bioluminescent assay for pesticide detection using engineered bacterial cells, France-Israel binational status seminar “Energy and Environment”, 13 December **2011**, Paris, France.

19. **K. Jia**, R. E. Ionescu. Detection of environmental pollutants using genetically modified E. coli bacteria. 6ème édition du Forum des Doctorants, 18 May **2011**, Université de Technologie de Troyes, France.

Contributions à des présentations orales

20. **K. Jia**, T. Toury, P. M. Adam, J. L. Bijeon, R. E. Ionescu. Multi-detection of (bio)molecules by using micro-structured quartz crystal microbalance. 6th European Workshop on Piezoelectric Materials, 11-13 July **2012**, Montpellier.

21. R. E. Ionescu, **K. Jia**, E. Eltzov, R. Marks. *Proceedings of Current Opinion in Biotechnology*, **2011**, 22 (1): S37, Istanbul, Turkey.

Kun JIA

Doctorat : Optique et Nanotechnologies

Année 2013

Détection Optique des (Bio)molécules

Les biocapteurs optiques ont connu une évolution sans précédent au cours des dernières années, principalement en raison de la forte interaction entre la biotechnologie, l'optique et la chimie des matériaux. Dans cette thèse, deux différentes plates-formes de biocapteurs optiques ont été conçues pour la détection sensible et spécifique des biomolécules. Plus précisément, le premier système de détection optique est construit sur la base de la bioluminescence de cellules bactériennes d'Escherichia coli génétiquement modifiées. L'émission de lumière induite par cette interaction peut donc être utilisée pour la détection des substances toxiques. Le second système utilise des nanoparticules de métaux précieux (or et argent) aux propriétés plasmoniques accordables qui permettent de sonder les interactions des biomolécules spécifiques à l'interface nano-bio par la résonance plasmonique de surface (LSPR). Ces nanoparticules ont été obtenues par traitement thermique à haute température d'un film métallique déposé sur du verre à l'aide d'une grille de TEM ou déposé sur une couche de bactéries fixée sur le verre. Après une optimisation appropriée des nanostructures métalliques en termes de morphologie et de fonctionnalisation, une sensibilité élevée et une grande spécificité peuvent être simultanément obtenues avec ces immunocapteurs plasmonique. Ces deux plateformes ont été utilisées pour détecter des pesticides comme le carbofuran et l'atrazine.

Mots clés : biocapteurs - bactéries luminescentes - oscillateurs à quartz - plasmons - nanostructures.

Optical Detection of (Bio)molecules

Optical biosensors have witnessed unprecedented developments over recent years, mainly due to the lively interplay between biotechnology, optical physics and materials chemistry. In this thesis, two different optical biosensing platforms have been designed for sensitive and specific detection of (bio)molecules. Specifically, the first optical detection system is constructed on the basis of bioluminescence derived from engineered Escherichia coli bacterial cells. Upon stressed by the toxic compounds, the bacterial cells produce light via a range of complex biochemical reactions in vivo and the resulted bioluminescent evolution thus can be used for toxicant detection. The bacterial bioluminescent assays are able to provide competitive sensitivity, while they are limited in the specificity. Therefore, the second optical detection platform is built on the localized surface plasmon resonance (LSPR) immunosensors. In this optical biosensor, the noble metal (gold and silver) nanoparticles with tunable plasmonic properties are used as transducer for probing the specific biomolecules interactions occurred in the nano-bio interface. These nanoparticles were obtained after a high temperature thermal treatment of an initially thin-metallic film deposited on a glass substrate through a TEM grid or on a bacteria layer fixed on the glass. After appropriate optimization on metal nanostructures morphology and surface biomodification, the applicable sensitivity and specificity can be both guaranteed in this LSPR immunosensor.

Keywords: biosensors - luminous bacteria - oscillators crystal - plasmon (physics) – nanostructures.

Thèse réalisée en partenariat entre :

Ecole Doctorale "Sciences et Technologies"